Neutron and Resonant X-ray Scattering Studies of Low Dimensional Quantum Magnets

Gheorghe Lucian Pascut

A thesis submitted to the School of Physics of Bristol University
for the degree of Doctor of Philosophy

School of Physics

Bristol University

September 2010

This thesis describes research on three different projects using the experimental techniques of resonant X-ray and elastic and inelastic neutron scattering. The first project focused on synchrotron X-ray measurements on the hexagonal metallic magnetic $AgNiO_2$ to explore the spontaneous transition below 365 K to a supercell crystal structure with periodic arrangements of expanded and contracted NiO_6 octahedra. The electronic energy levels of the Ni sites were probed by varying the X-ray energy through the Ni K-edge resonance (1s-4p) and a large enhancement of the supercell peak intensity was observed. An empirical model for the anomalous atomic scattering factors was developed to account quantitatively for all feature observed in the rich spectral linewidth (in absolute units) taking into account Kramers-Kronig relations between real and imaginary parts and a full modeling of the energy-dependent absorption effects. The empirically extracted form factors show an energy shift of $\sim$ 2.5 eV in the resonance for the different Ni sites. Comparison with LDA calculations that include quantitative shifts in the 4p-levels due to the structural hybridization with the surrounding oxygens, indicate a large contribution to the resonance energy shift due to a change in the 1s core level, a characteristic signature of different number of electrons between crystallographically different Ni sites. Measurements thus provide the first direct experimental evidence for spontaneous honeycomb charge order in triangular Ni lattice. The second project concerned the development of a microscopic model of the spin and orbital moment contributions to the magnetic ground state of Co^{2+} ions in the Ising magnet $CoNb_2O_6$, where field induced-Ising quantum critically was recently observed experimentally. The 28 fold degenerate energy levels for Co^{2+} were calculated in the presence of crystal-field, spin-orbit coupling and exchange mean-field. The crystal field effects were described by Steven's operator equivalent method including all terms allowed by the low local symmetry (monoclinic) at the Co sites. Crystal field parameters calculated theoretically using a point charge model, further refined to include hybridization effects were used as starting values in the empirical fits to the time-of-flight inelastic neutron scattering measurements of transitions to crystal field levels up to 800 meV. The fits were further constrained to reproduce the orientation of the easy-axis determined by neutron diffraction. A consistent description of all the data was obtained, including transitions to higher crystal field levels up to $\sim$ 1700 meV measured by optical experiments. The third project focused on time-of-flight neutron scattering measurements of the magnetic order and spin excitations near the field-induced quantum phase transition from spontaneous magnetic order to paramagnetic in the quasi-one dimensional spin 1/2 easy-plane antiferromagnet Cs_2CoCl_4. Neutron diffraction measurements observed that upon approaching the critical field the collinear antiferromagnetic structure stable at low field was replaced in a 1st order transition by an unexpected incommensurate spin-density-wave like order. This is stable over only a very narrow field range of 0.32(4) T and is suppressed in a continuous transition at 2.36 T. At much higher fields deep in the paramagnetic phase inelastic neutron scattering measurements reveal sharp and strongly dispersive magnon peaks as expected in this limit where spin are nearly ferromagnetically aligned. Detailed measurements of the dispersion relations along several non-equivalent directions in the **bc**-plane were quantitatively parameterized by a spin-wave model for an exchange Hamiltonian which confirmed the predominant one-dimensional interactions along **b**-axis and frustrated interchain interactions along **c**. Upon lowering the field to approach the critical point from above, in addition to the one-magnon signal a broad continuum scattering becomes visible already at 2.5 T and grows upon approaching B_C. This is attributed to multi particles scattering process which are allowed as quantum fluctuations are present in the paramagnetic phase due to strong easy-plane anisotropy effects in the region just above B_C.

ACKNOWLEDGMENTS

There are many people I would like to thank, who have contributed in some way towards this thesis. Firstly, I would like to extend my deepest gratitude to my supervisor Dr. Radu Coldea who has provided me with constant support and encouragement throughout the past four years. I am very grateful to the Bristol University and Harold Herbert Potter Fund which provided me with the scholarship. None of this work would have taken place without samples, so I am grateful to the crystal growers Z. Tylczynsli, T. S*ö*rgel and M. Jansen. I am grateful to all the instrument scientists who helped me with the neutron and X-ray scattering measurements at Diamond, ISIS, ILL and HMI especially Alessandro Bombardi, Franz Demmel, Mechthild Enderle and Jens-Uwe Hoffmann. The assistance and discussions offered by my collaborators have been very helpful, and I therefore wish to thank Paolo Radaelli and Igor Mazin. During my time in Bristol I received a lot of help from Ewa Wawrznska for which I am very grateful. I would also like to thank Martin Rotter for many good discussions on theoretical calculations of the crystal field levels during the tea time in Oxford. I also wish to thank Sunil Nair, Ciprian and Georgiana Plostinar, Federica Fabrizi, Graeme Johnstone, Amalia Coldea, Peter Babkevich and Andrew Boothroyd for reading chapters of this thesis. I would like to thank to all the people in Bristol and Oxford for making my time there very enjoyable. I am also very grateful for the good friends I made during my time in Bristol and Oxford.

I would like to thank my family, my relatives and my old friends for all their love and support.

I would like to thank to my dear wife for being very supportive and patient during stressed periods of this work.

"The important thing in science is not so much to obtain new facts as to discover new ways of thinking about them."

William Lawrence Bragg

"Science is a wonderful thing if one does not have to earn one's living at it."

Albert Einstein

DEDICATION

To my mother, my high school Professor Matei Bulc, my undergraduate tutor Marin Coldea and in memory of my Father.

Declaration of originality

I declare that the work in this dissertation was carried out in accordance with the requirements of the University's Regulations and Code of Practice for Research Degree Programmes and that it has not been submitted for any other academic award. Except where indicated by specific reference in the text, the work is the candidate's own work. Work done in collaboration with, or with the assistance of, others, is indicated as such. Any views expressed in the dissertation are those of the author.

SIGNED: ..... DATE: .....

Gheorghe Lucian Pascut

Contents

List of Figures

Chapter 1

Introduction

The behaviour of electrons in solids is responsible for many of the technologically-important properties of materials. A prominent example is superconductivity observed in certain materials where electrical current flows with no resistance below a certain critical temperature. Superconductivity is the result of the cooperative behaviour of all electrons correlating their motion with one another and acting in unison to avoid scattering by the crystal lattice and this phenomenon cannot be understood in terms of properties of un-correlated, independently moving electrons. Superconducting materials already have applications in the generation of high magnetic fields for medical research (magnetic resonance imaging-MRI), highly-sensitive magnetic sensors (Superconducting Quantum Interference Devices-SQUID), superconducting generators or motors, and might in the future also have further applications for energy storage or transport of electricity without energy loss. Effects of electron correlations leading to new material properties are abundant. Another important example is the colossal magneto-resistance (CMR) effect, discovered in transition metals oxides whereby the electrical resistance changes by several orders of magnitude upon the application of a modest magnetic field. This effect can be exploited in magnetic field sensors and might replace the giant magneto-resistance field sensors in the read heads of computer magnetic hard discs for data storage. The multiferroic effect describes the simultaneous occurrence of various

ferroic orders in certain materials, such as ferromagnetism and ferroelectricity (spontaneous electrical polarization). In certain multiferroic materials, the application of a magnetic field can switch the ferroelectric polarization or the application of an electric field can switch the magnetization of the material. Possible applications of multiferroic materials are in magnetic/electric switches and computer data storage. Metal-insulator transitions are also due to the strong electron correlations and could be exploited in electronic switches. The cooperative magnetic behaviour of electrons can also lead to important effects, such as a large temperature change in response to the application of a magnetic field (magneto-caloric effect); this could be used for magnetic refrigeration without moving parts or a cooling fluid.

The reason electrons act together in unison and correlate their motion and spin with one another is of course the result of inter-electron interactions, for the charges originating in the long-range Coulomb forces and for the spins originating in various forms of magnetic exchange interactions. In some materials electron correlation effects are rather weak, and can be treated as a small perturbation on the properties of essentially independent electrons. However, in other materials interactions are very strong and stabilize entirely new forms of electronic order with new properties, for example superconductivity is an emergent property of all electrons acting together and not simply the "sum of the parts". Often the cooperative behaviour cannot be easily anticipated from the local interactions among the electrons, and between the electrons and the lattice, and needs new concepts, as exemplified by the history of superconductivity, discovered experimentally in 1911 but only explained theoretically in a major tour de force culminating in 1957 after introducing the ideas of Cooper pairing of electrons mediated via exchange of lattice vibrations, with superconductivity arising from condensation of Cooper pair bosons. High-temperature superconductivity discovered in the layered copper-oxides in 1987 cannot be accounted for using the standard phonon-mediated mechanism and is still not yet theoretically explained! What makes strongly-correlated electron systems a research field at the very forefront of condensed matter research is the fact that properties

cannot be reliably predicted in particular if many degrees of freedom are involved, spins, charges and orbitals, with a large potential to discover novel forms of electronic order.

In order to study microscopically the electronic order and dynamics in correlated electron materials we need probes with atomic resolution which interact with the spins and charges. Both neutron and x-ray scattering are natural probes of the crystal structure, whereas neutrons are also scattered by the electron spins and can image magnetic structures (elastic scattering) and also probe the cooperative dynamics of spin fluctuations (via inelastic neutron scattering) and map the full dispersion relations in the three-dimensional Brillouin zone. X-rays are scattered by the electron cloud and by tuning the x-ray energy to resonance (to excite an internal electronic transition) the atomic scattering factor acquires an anomalous contribution which can provide detailed information about the electronic orbital and/or charge order, which are not accessible via neutron scattering. The experimental technology has benefited from significant advances over the recent years (new high-brilliance Diamond synchrotron in the UK and new suite of neutron instruments at the ISIS Target Station 2 in UK), and this is anticipated will lead to even more opportunities for detailed investigation of electronic order in the years to come.

The subject of this thesis is the investigation of electronic order and dynamics in three different correlated electron systems using synchrotron resonant X-ray and neutron scattering techniques. In the first system to be investigated, spontaneous charge order of electrons in a triangular lattice is probed using resonant x-ray scattering using the recently-commissioned magnetism beamline I16 at the Diamond synchrotron. The second system to be investigated is the Ising magnet $CoNb_2O_6$ where the spin and orbital components of the magnetic ground state are analysed in detail taking into account crystal field effects and the spin-orbit interaction and compared to transitions between energy levels observed via inelastic neutron scattering. The third project concerns the quantum easy-plane magnet Cs_2CoCl_4 where strong applied magnetic fields can suppress the transition temperature to spontaneous magnetic order all the way to essentially zero temperature thus

realizing a quantum phase transition between spontaneous magnetic order and paramagnetic, and experiments focused on changes to the magnetic structure and collective spin fluctuations upon crossing the critical point.

This thesis presents studies of the magnetic and structural properties of the low dimensional magnets $AgNiO_2$, $CoNb_2O_6$ and Cs_2CoCl_4 using x-ray resonant scattering and elastic (and inelastic) neutron scattering. The work presented here involves experimental results and theoretical calculations for $AgNiO_2$, only theoretical calculations for $CoNb_2O_6$ and experimental results for Cs_2CoCl_4.

This thesis has six chapters, starting with the introduction in Chapter 1. In the second and third chapter, I describe the x-ray and neutron scattering theory. The chapters 4, 5, and 6, describe the results on $AgNiO_2$, $CoNb_2O_6$ and Cs_2CoCl_4 respectively.

Each one of Chapters 4, 5, 6 is a comprehensive project, which includes detailed information about the studied system, concepts and phenomena which are useful for the reader to better understand the physics presented in that chapter. In the sections within each chapter, I will discuss the relevant experimental details, then I will present the data analysis followed by results and conclusions. The thesis ends with the references section, followed by the appendices, which contain information about the theoretical calculations done for $CoNb_2O_6$.

Chapter 4 presents single crystal x-ray resonant scattering measurements on the orbitally degenerate triangular metal $AgNiO_2$. Experimentally it is observed that this system has a structural transition which is accompanied by charge disproportionation at the Ni sites. From band structure calculations we learn that the the orbital degeneracy is lifted by charge disproportionation at the Ni sites. The aim of this project was to probe directly, using x-ray resonant scattering measurements, the proposed model for the charge disproportionation. If the system is in a state with charge disproportionation, different occupancy is expected for the d orbital of the Ni ions at inequivalent sites. This is turn would affect the energy position of the 1s-core level state with respect to the

Fermi level. To probe the charge disproportionation state, we performed an experiment where the energy difference between the 1s and 4p states, for different Ni ions, was directly measured (this energy difference is usually called edge energy). Charge disproportionation could exist, if there is a difference in the edge energy for inequivalent Ni ions. We can obtain the empirical edge energy for the Ni ions using a quantity called atomic scattering factor which is usually extracted from resonant scattering experiments. X-ray resonant scattering experiments were performed to measure supercell reflections which are related to atomic scattering factor for different inequivalent ions. The empirical edge energy difference for the inequivalent Ni ions in $AgNiO_2$, is 2.5 eV. Comparison of this value, with the energy shifts of the edge for Ni ions in oxides, suggest that there might be charge disproportion between the inequivalent Ni ions in $AgNiO_2$. The edge energy is a result of two effects: position in energy with respect to the Fermi energy of the 1s level (due to the occupancy of the d orbital) and the position in energy of the 4p states (due to the hybridization of the 3d(Ni) - 2p(O) states). The empirical edge energy difference is obtained because different Ni ions will have different edge energies. This is a consequence of different occupancies of the d orbital and different hybridizations effects with the neighbors. To understand how much of the edge shift is due the effects of the charge disproportionation and how much to the effects of the hybridization, I calculated the edge energy for the Ni ions in charge ordered state (using band structure calculations in the LDA approximation). I found that both charge disproportionation and structural distortions, contributes to the observed edge energy difference.

Chapter 4, contains a description of: the crystal structure and the structural transition; the proposed model for the charge disproportionation at the Ni sites; the possible mechanisms to lift the orbital degeneracy in insulating materials and the mechanism to lift the orbital degeneracy in $AgNiO_2$ (mechanism proposed by the band structure calculations). The structure factors in absolute units of electrons squared were extracted from the data corrected for absorption effects. A model was developed in order to extract the empirical atomic scattering factors for inequivalent

Ni ions. In addition I performed band structure calculations and the tensor analysis of the atomic scattering factors. We also present temperature dependent measurements of the resonant scattering, which show a strong correlation between the charge disproportionation and the structural transition.

Chapter 5 reports a study of the magnetic ground state and excited crystal field energy levels of Co^{2+} ions in the strong easy-axis magnet $CoNb_2O_6$. The aim of this chapter is to understand from a microscopic point of view the origin of the strong Ising-like anisotropy of the Co^{2+} ions and to determine the spin and orbital component of the magnetic ground state and of the excited levels taking into account spin-orbit interactions and crystal field effects from the distorted O_6 octahedron surrounding the Co^{2+} ions. The theoretical calculations give a quantitative description of the origin of the strong Ising anisotropy of Co^{2+} ions, attributed to the combined effect of crystal field from a largely-distorted octahedral ligand environment and a comparable spin-orbit coupling.

The challenging problem in this project was to find the "crystal field parameters" (CFP); these parameters take into account the interactions between the 3d electrons of the magnetic ion with the neighboring ligand. Due to the very low symmetry of the Co^{2+} local environment, there is a large number of unknown CFP in the expansion of the crystal field Hamiltonian (8 in total). Obtaining the CFP from direct fits to the experimental data, without having any starting parameters, is impossible due to the large search space spanned by them. In this chapter, I will describe a method to overcome this problem. The calculated CFP using a very simple model where the ligands are considered to be point charges fails to reproduce the energy scale found experimentally from time-of-flight inelastic neutron scattering measurements. To improve the method, the CFP are calculated including hybridization effects between the orbitals of the transition metal and the orbitals of the ligands. This new set of CFP gives a good agreement between the calculated and experimental excited crystal field energy levels, but fails to explain the two possible directions of the easy axis, obtained experimentally from neutron diffraction. Using the CFP (calculated

by including hybridization effects) as starting parameters, I performed fits to the data in order to obtain empirical CFP that can explain the direction of the easy axis. Two sets of the CFP were obtained from the fits to the data, which give a consistent description of the easy axis directions. In addition, they can also explain the low energy excited crystal field levels measured by time-of-flight inelastic neutron scattering and the high energy excited crystal field levels extracted from optical measurements.

Chapter 5, starts with an introduction presenting the importance of this project, followed by a detailed description of the crystal and magnetic structure of $CoNb_2O_6$ found using neutron diffraction. In the same section, there are discussions of the possibilities for the easy axis directions, which are indistinguishable to neutron diffraction experiments. The following sections describe: experimental details and extraction of the crystal field transition energies from the raw data; the total Hamiltonian for the magnetic ion, which includes effects such as electron-nucleus interaction, electron-electron interaction, spin-orbit interactions, crystal field interactions and interactions with an internal (molecular) and external magnetic field; phenomenologically the crystal field hamiltonian and the calculated CFP, using a simple point charge model and a more complicated model where hybridization effects are taken into account; comparison between the calculated and experimental quantities obtained using the calculated CFP; the fitting procedure which was used to obtain empirical CFP.

Chapter 6 reports elastic and inelastic time-of-flight single crystal neutron scattering experiments to explore the magnetic order and spin dynamics in the quasi-one-dimensional spin-1/2 easy-plane anisotropy antiferromagnet Cs_2CoCl_4 in a magnetic field applied close to the easy-plane. The scenario we investigate experimentally is that of spin-1/2 easy-plane anisotropy antiferromagnet chains in a magnetic field applied perpendicularly to the direction of the magnetic moments, a scenario which has not been explored experimentally before. Theoretical calculations predict that a transverse magnetic field introduces quantum fluctuations into the system, which

will destroy the long range order. The particular aim of this project was to test what happens to the magnetic order and spin excitations as the system undergoes a phase transition at high field where the antiferromagnetic order disappears. The main result is the observation of a new incommensurate magnetic phase which was not seen experimentally prior to this work and was also not predicted theoretically. The new phase is stable over a small field range just before the transition to the high field paramagnetic phase. The magnetic structure in this incommensurate phase at 2.1 T is a spin density wave, stabilized by the frustrated interchain exchange interactions. Sharp magnon modes were observed in the inelastic scattering data collected in a field of 4 T which is deep in the paramagnetic phase, where the spins are expected to be nearly ferromagnetically aligned along the field direction. Spin-wave theory was used to model the experimental dispersion and empirical exchange parameters were extracted, which confirmed the one-dimensional nature of this material. The excitation gap vs. field shows that the gap is closing at the paramagnet-incommensurate phase transition (within the experimental errors) which is consistent with a second order phase transition. At higher energies above the one-magnon dispersion, evidence for broad continuum scattering was observed in the paramagnetic phase for a finite field range above the critical field. Theoretical calculations of the accessible phase space for two and three magnon scattering processes suggest that the continuum scattering could be due to three magnon scattering processes.

Chapter 6 describes the crystal and magnetic structure in zero field and the necessary corrections performed to the data in order to obtain the magnetic moments on absolute scale. The following sections describe: the steps required to obtain the order parameters for the commensurate (antiferromagnetic) and incommensurate phase which were further used to obtain the temperature-field phase diagram; the results of the group theory which were used to determine the magnetic structure in the incommensurate phase; the results of the inelastic scattering; the quantitative parametrization of the hamiltonian in order to extract the empirical exchange parameters; the evolution of the excitation gap vs. field and the continuum scattering.

Chapter 2

Neutron scattering

Neutron scattering is a powerful tool to study the properties of matter [1] and it is based on the interaction between neutrons and matter. The advantages of using neutrons for studying matter are: they are neutral particles and can penetrate deep into matter, they are heavy particles whose changes in energy may be easily measured by changes in velocity and they possess a magnetic moment which interacts with unpaired electrons in solids, allowing the details of microscopic magnetism to be examined. Neutrons can interact with the matter in two ways: first, the interaction with the atomic nucleus via the so-called strong force, and secondly via magnetic forces.

The interaction via the strong force, extends only over distances of the size of the atomic nucleus and the mean free path of a thermal neutron is of the order of 1 cm. The neutron can be scattered either coherently or incoherently or it can be absorbed by the nucleus. The coherent scattering results from interference effects between the nuclei, and the observed elastic Bragg scattering in a neutron scattering experiment, allows one to obtain information about the crystal structure. The incoherent scattering is observed as an isotropic background, and is usually subtracted out of the coherent scattering before analyzing it. The incoherent scattering can also be very useful, for example incoherent scattering from a vanadium sample is used to obtain the detector efficiencies. Neutron diffraction experiments use neutrons with energies in the region of about 25 meV (thermal

neutrons) which is much less than the energy necessary to create nuclear excitations so the nucleus will be in the same quantum state during the scattering process. The reason why thermal neutrons are used in experiments is that they have energies similar to the energies of elementary excitations in solids [1].

In magnetic solids, there are unpaired electrons with magnetic moments that will interact with the neutron's magnetic moment. This interaction is weaker than the nuclear interaction, but extends over larger distances and the net result of this interaction gives rise to a similar mean free path of 1 cm as in the case of strong force. The importance of the mean free path (MFP) is that it gives the number of collisions (NC) experienced by a neutron along a path of length L, and thus by definition of the MFP, the average NC experienced by a neutron along a path of length L is L/MEP.

The neutron scattering processes can be quantitatively described by the *partial differential cross section*, *differential cross section* and *total cross section* (usually labeled by σ) [2, 3]. In order to define these quantities, one can use the schematic diagram of a scattering process shown in Figure 2.1. We assume a parallel neutron beam of flux I_0 (neutrons per unit area per second) and energy ε_0, incident on a sample with a very small cross-sectional area. In this case, the probability of scattering of a neutron by the sample is small (taking into account the MFP of neutron this approximation is valid). If some neutrons are scattered, then at large distances from the sample we detect neutrons with energies ε_f scattered in the solid angle covered by the detectors. The *partial differential cross section* is defined as the number of neutrons that are scattered per second into a certain direction with a certain range of energy values centered at the nominal value ε_f:

$$\frac{d^2\sigma_s}{d\Omega\, d\varepsilon_f} = \frac{\left(\dfrac{\text{number of neutrons scattered per second into the solid angle d}\Omega}{\text{with final energies between } \varepsilon_f \text{ and } \varepsilon_f + \text{d}\varepsilon_f}\right)}{I_0\, d\Omega\, d\varepsilon_f} \tag{2.1}$$

The *partial differential cross section* $\frac{d^2\sigma}{d\Omega d\varepsilon_f}$ is the basic quantity that is measured during a neutron scattering experiment and depends on the details of the interaction between the neutron and the sample; this is the quantity which can be related to theoretical model. Since the interaction of the

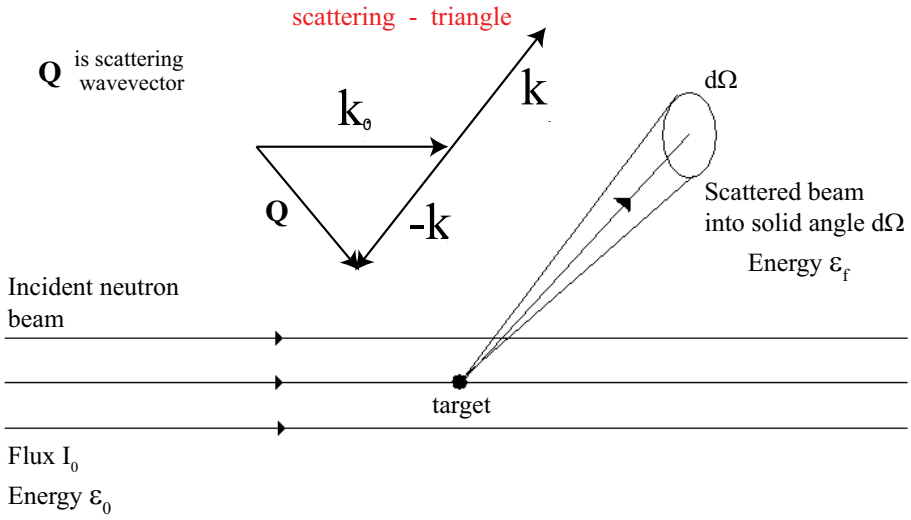

Figure 2.1 Schematic representation of the scattering process; a neutron beam with flux I_0 is incident on the sample. Neutrons with the initial wavevector $\mathbf{k}_i$ and energy ε_0 are scattered into the solid angle dΩ with the final wavevector $\mathbf{k}_f$ and energy ε_f.

neutron with the sample can be through the strong-force or through the magnetic-force, one can examine the form of the cross section for both nuclear and magnetic scattering. If the detector has an efficiency η, then the number of neutrons detected per second (counting rate) is:

$$\eta I_0 \frac{d^2\sigma_s}{d\Omega d\varepsilon_f} d\Omega d\varepsilon_f \tag{2.2}$$

Integrating $\frac{d^2\sigma_s}{d\Omega d\varepsilon_f}$ over dε_f, we obtain the number of neutrons per second scattered into the solid angle dΩ (regardless of energy ε_f) to be:

$$I_0 d\Omega \int_0^\infty \frac{d^2\sigma_s}{d\Omega d\varepsilon_f} d\varepsilon_f = I_0 \frac{d\sigma_s}{d\Omega} d\Omega \tag{2.3}$$

where $\frac{d\sigma_s}{d\Omega}$ is called the *differential cross section* and is defined as:

$$\frac{d\sigma_s}{d\Omega} = \frac{\text{number of neutron scattered per second into the solid angle d}\Omega}{I_0 d\Omega} \tag{2.4}$$

Integrating over the solid angle we find the number of neutrons scattered per second in any direction:

$$I_0 \int \frac{d\sigma_s}{d\Omega} d\Omega = I_0 \sigma_s \tag{2.5}$$

where σ_s is known as the scattering cross section. Neutrons can be either scattered or absorbed, and one can define the number of neutrons absorbed by the sample per second as $I_0\sigma_a$ (where σ_a is the absorption cross section). Finally the number of neutrons per second that have their momentum changed in the sample is $I_0\sigma_t$ (where $\sigma_t = \sigma_s + \sigma_a$, is the total cross section). The cross section has the dimension of area and is usually quoted in barns (1 barn = 10^{-28} m^2).

2.1 Neutron scattering cross-sections

The scattering cross section of the target can be calculated by quantum scattering theory. The Hamiltonian **H** of the system (neutron plus the sample) is:

$$\mathbf{H} = \mathbf{H}_0 + \frac{\mathbf{p}^2}{2m} + \mathbf{V} \tag{2.6}$$

where $\mathbf{H}_0$ is the Hamiltonian of the sample, $\varepsilon = \frac{\mathbf{p}^2}{2m}$ is the kinetic energy of the neutron and **V** is the Hamiltonian representing the interaction between the neutron and the sample (**V** is treated as a small perturbation). Without the interaction, the states of the system can be written as, $|\mathbf{k}(\varepsilon), \mathbf{s}, \Psi(E)\rangle = |\mathbf{k}(\varepsilon)\rangle\ |\mathbf{s}\rangle\ |\Psi(E)\rangle$, where **k** is the wavevector of the neutron with energy ε, **s** the spin of the neutron and $|\Psi(E)\rangle$ is a state of the sample corresponding to the energy E. Using Fermi's Golden Rule, one can calculate the probability of a transition, W_1 per second from the initial state of the system $|\mathbf{k}_0(\varepsilon_0), \mathbf{s}_0, \Psi_0(E_0)\rangle$ to the final state of the system $|\mathbf{k}(\varepsilon_f), \mathbf{s}, \Psi_f(E_f)\rangle$ as:

$$\begin{aligned} &W_1(|\mathbf{k}_0(\varepsilon_0), \mathbf{s}_0, \Psi_0(E_0)\rangle \rightarrow |\mathbf{k}(\varepsilon_f), \mathbf{s}, \Psi_f(E_f)\rangle) = \\ &\frac{2\pi}{\hbar} |\langle \mathbf{k}(\varepsilon_f), \mathbf{s}, \Psi_f(E_f)|\mathbf{V}|\mathbf{k}_0(\varepsilon_0), \mathbf{s}_0, \Psi_0(E_0)\rangle|^2\ \delta(E_f - E_0 - \varepsilon_0 + \varepsilon_f) \end{aligned} \tag{2.7}$$

where the δ function express the conservation of energy. Because the initial and final states of the sample can not be measured, the number of transitions per second, W_N, going from $|\mathbf{k}_0(\varepsilon_0), \mathbf{s}_0, \Psi_0(E_0)\rangle$

to $|\mathbf{k}_f(\varepsilon_f),\mathbf{s}_f,\Psi_f(E_f)\rangle$ is given by:

$$W_N(|\mathbf{k}_0(\varepsilon_0),\mathbf{s}_0,\Psi_0(E_0)\rangle \rightarrow |\mathbf{k}(\varepsilon_f),\mathbf{s},\Psi_f(E_f)\rangle) = \sum_{|\Psi_0(E_0)\rangle} p(|\Psi_0\rangle) \sum_{|\Psi_f(E_f)\rangle} W_1(|\mathbf{k}_0(\varepsilon_0),\mathbf{s}_0,\Psi_0(E_0) > \rightarrow |\mathbf{k}(\varepsilon_f),\mathbf{s},\Psi_f(E_f)\rangle) \tag{2.8}$$

Eq. 2.8 is averaged over all initial states $|\Psi_0(E_0)\rangle$ with their distribution p($|\Psi_0(E_0)\rangle$) and summed over all final states $|\Psi_f(E_f)\rangle$ allowed by the δ function. The number of transitions, W_N, per second from the initial state $|\mathbf{k}_0(\varepsilon_0),\mathbf{s}_0,\Psi_0(E_0)\rangle$ to the final state $|\mathbf{k}(\varepsilon_f),\mathbf{s},\Psi_0(E_0)\rangle$ is given by:

$$W_N(|\mathbf{k}_0(\varepsilon_0),\mathbf{s}_0,\Psi_0(E_0)\rangle \rightarrow |\mathbf{k}(\varepsilon_f),\mathbf{s},\Psi_f(E_f)\rangle) = \frac{2\pi}{\hbar}|\langle\mathbf{k}(\varepsilon_f),\mathbf{s},\Psi_f(E_f)|\mathbf{V}|\mathbf{k}_0(\varepsilon_0),\mathbf{s}_0,\Psi_0(E_0)\rangle|^2\,\rho(\varepsilon_f) \tag{2.9}$$

where $\rho(\varepsilon_f)$ is the density of final scattering states defined such that $\rho(\varepsilon_f)d\varepsilon_f$ is the number of final states with energy in the interval $d\varepsilon_f$ centered around ε_f. By combining Eqs. 2.4 and 2.9, we observe that the *differential cross section* is given by:

$$\frac{d\sigma_s}{d\Omega} = \frac{W_N(|\mathbf{k}_0(\varepsilon_0),\mathbf{s}_0,\Psi_0(E_0)\rangle \rightarrow |\mathbf{k}(\varepsilon_f),\mathbf{s},\Psi_f(E_f)\rangle)(d\Omega)}{I_0\,d\Omega} \tag{2.10}$$

where $W_N(|\mathbf{k}_0(\varepsilon_0),\mathbf{s}_0,\Psi_0(E_0)\rangle \rightarrow |\mathbf{k}(\varepsilon_f),\mathbf{s},\Psi_f(E_f)\rangle)(d\Omega)$ is the number of transition per second in dΩ.

Using Eq. 2.10 one can calculate the *partial differential cross section* for scattering from $|\mathbf{k}_0(\varepsilon_0),\mathbf{s}_0,\Psi_0(E_0)\rangle$ to $|\mathbf{k}(\varepsilon_f),\mathbf{s},\Psi_f(E_f)\rangle$ as follows [1–3]:

$$\frac{d^2\sigma_s}{d\Omega\,d\varepsilon_f} = \frac{|\mathbf{k}|}{|\mathbf{k}_0|}\left(\frac{m}{2\pi\hbar}\right)|\langle\mathbf{k}(\varepsilon_f),\mathbf{s},\Psi_f(E_f)|\mathbf{V}|\mathbf{k}_0(\varepsilon_0),\mathbf{s}_0,\Psi_0(E_0)\rangle|^2\,\delta(E_f-E_0-\varepsilon_0+\varepsilon_f) \tag{2.11}$$

In order to obtain practical formulae one has to know the interaction potential **V**. For example, the interaction potential for nuclear scattering is given by:

$$\mathbf{V} = \frac{2\pi\hbar}{m}b\delta(\mathbf{r}-\mathbf{R}) \tag{2.12}$$

where **R** is the nuclear position and **r** is the neutron's position. The quantity b has dimensions of length and is known as the *scattering length*. By calculating the scattering cross sections for the case of a single atom held fixed such that its quantum state does not change $|\Psi_0(E_0)\rangle = |\Psi_f(E_f)\rangle$ (equivalent with $E_0 = E_f$), we obtain [1]:

$$\frac{d^2\sigma_s}{d\Omega d\varepsilon_f} = \frac{|\mathbf{k}|}{|\mathbf{k}_0|} b^2 \delta(\varepsilon_f - \varepsilon_0) \tag{2.13}$$

$$\frac{d\sigma_s}{d\Omega} = \int \frac{d^2\sigma_s}{d\Omega d\varepsilon_f} d\varepsilon_f = b^2 \tag{2.14}$$

$$\sigma_s = \int \frac{d\sigma_s}{d\Omega} d\Omega = 4\pi b^2 \tag{2.15}$$

Using similar arguments but tedious calculations, the nuclear coherent elastic scattering cross-section, magnetic elastic scattering cross-section and magnetic inelastic scattering cross-section have been calculated in [1–3]. In this section, I will give only the final formulae which will be used throughout this thesis in order to convert the raw intensities into quantities that can be used in data analysis.

1) Nuclear coherent elastic scattering cross-section:

$$\begin{aligned}\left(\frac{d^2\sigma_s}{d\Omega d\varepsilon_f}\right)_{\text{nuclear-elastic}} &= \delta(\hbar\omega) \frac{d\sigma_{nuc}}{d\Omega}(\mathbf{Q}) = \\ &\frac{N(2\pi)^3}{V_0} |F_{nuc}(\mathbf{Q})|^2 \, \delta(\mathbf{Q} - \tau_{nuc}) \, \delta(\hbar\omega)\end{aligned} \tag{2.16}$$

with

$$F_{nuc}(\mathbf{Q}) = \sum_j b_j e^{i\mathbf{Q}\cdot\mathbf{R}_j} \tag{2.17}$$

where F_{nuc} is the nuclear structure factor (the sum is over all the atoms j in the unit cell at positions $\mathbf{R}_j$), b_j is the scattering length for atom j and **Q** is the scattering wavevector (see Figure 2.1). Nuclear coherent elastic scattering occurs when the scattering vector **Q** coincides with a reciprocal lattice vector τ_{nuc}.

2) Magnetic coherent elastic scattering cross-section: In magnetically ordered systems, magnetic coherent elastic scattering is observed as magnetic Bragg peaks (in an analogous way to

nuclear Bragg peaks). Magnetic Bragg peaks arise due to scattering from the average magnetic lattice, occurring when the scattering vector **Q** coincides with a reciprocal magnetic lattice vector τ_{mag}.

$$\left(\frac{d^2\sigma_s}{d\Omega d\varepsilon_f}\right)_{\text{magnetic-elastic}} = \delta(\hbar\omega)\frac{d\sigma_{mag}}{d\Omega}(\mathbf{Q}) = \frac{N_m(2\pi)^3}{V_{0m}}\left(\frac{\gamma r_0}{2}\right)^2 \sum_{\alpha\beta}\left(\delta_{\alpha,\beta} - \frac{Q_\alpha \cdot Q_\beta}{|\mathbf{Q}|^2}\right) F^\alpha(\mathbf{Q})F^{\beta *}(\mathbf{Q})\ \delta(\mathbf{Q}-\tau_{mag})\delta(\hbar\omega) \tag{2.18}$$

with

$$F^\alpha(\mathbf{Q}=\tau_{mag}) = \sum_j \mu_j^\alpha f_j(\mathbf{Q}) e^{i\mathbf{Q}\cdot\mathbf{R}_j} \tag{2.19}$$

where F^α is the magnetic structure factor (the sum is over all the magnetic ions j in the unit cell at positions $\mathbf{R}_j$), $f_j(\mathbf{Q})$ is the magnetic form factor [4] and μ_j^α is the α-component of the magnetic moment of the j ion.

3) Magnetic coherent inelastic scattering cross-section:

$$\left(\frac{d^2\sigma_s}{d\Omega d\varepsilon_f}\right)_{\text{magnetic-inelastic}} = \left(\frac{\gamma r_0}{2}\right)^2 f^2(\mathbf{Q}) \frac{|\mathbf{k}|}{|\mathbf{k}_0|} S(\mathbf{Q},\omega) \tag{2.20}$$

with $S(\mathbf{Q},\omega)$ known as the response function:

$$S(\mathbf{Q},\omega) = \sum_{\alpha\beta}\left(\delta_{\alpha,\beta} - \frac{Q_\alpha \cdot Q_\beta}{|\mathbf{Q}|^2}\right) S^{\alpha\beta}(\mathbf{Q},\omega) \tag{2.21}$$

where $S^{\alpha\beta}(\mathbf{Q},\omega)$ are the space and time Fourier transforms of the time-dependent spin-spin correlation functions, for non-localized magnetic excitations measured at low temperatures (0), where only the ground state $|GS\rangle$ with energy E_{GS} is populated:

$$S^{\alpha\alpha}(\mathbf{Q},\omega) = \sum_{|EX\rangle} |\langle EX|S^\alpha(\mathbf{Q})|GS\rangle|^2 \delta(\hbar\omega + E_{GS} - E_{EX}) \tag{2.22}$$

where the sum is over all the excited states $|EX\rangle$ of the system with energy E_{EX}. $S^\alpha(\mathbf{Q})$ is the Fourier transform of the α-component of the spin density, S^α.

Since in Chapter 5 we present studies of the crystal field excitations, it is useful to write the response function for localized excitations in the following form:

$$S(\mathbf{Q},\omega) = \sum_{|ex\rangle} |\langle ex|\mu_{\perp}|gs\rangle|^2 \delta(E_{gs} + \hbar\omega - E_{ex}) \tag{2.23}$$

where $\mu_{\perp}$ is the component of the magnetic moment perpendicular to $\mathbf{Q}$; $|gs\rangle$ and $|ex\rangle$ are the ground and excited crystal field states.

2.2 Neutron scattering instruments: OSIRIS

To define the neutron momentum and energy transfer we assume an incident neutron of well-defined wavevector $\mathbf{k}_0$, momentum $\hbar\mathbf{k}_0$ and energy $\mathrm{E}_0 = \frac{\hbar^2\mathbf{k}_0^2}{2m_N}$ that scatters from a sample, changing its momentum to $\hbar\mathbf{k}$ and energy to $E = \frac{\hbar^2\mathbf{k}^2}{2m_N}$ in the process (see Figure 2.1). Then the neutron momentum and energy transfers $\hbar\mathbf{Q}$ and $\hbar\omega$ are given by:

$$\begin{aligned} \hbar\mathbf{Q} &= \hbar\mathbf{k}_0 - \hbar\mathbf{k} \\ \hbar\omega &= \frac{\hbar^2\mathbf{k}_0^2}{2m_N} - \frac{\hbar^2\mathbf{k}^2}{2m_N} \end{aligned} \tag{2.24}$$

2.2.1 Elastic scattering

To introduce the idea of time-of-flight neutron scattering, only the particular case of elastic scattering $\hbar\omega = 0$, will be discussed in this section. In Figure 2.2 a) we show a hypothetical scattering experiment, where a monochromatic flux I_0 of neutrons with momentum $\mathbf{k}_0$ is incident on the sample. Neutrons transfer momentum $\hbar\mathbf{Q} = \hbar\mathbf{k}_0 - \hbar\mathbf{k}$ to the sample and scatter through an angle 2θ towards a detector bank with 13 detector elements (labeled from 1 to 13 using the following notation: $n = 1, ..., 13$). Each detector element is placed at an angle $2\theta_n$ and subtends a solid angle $\mathrm{d}\Omega_n$. Eq. 2.16 is telling us, that we have coherent scattering only when $\delta(\mathbf{Q} - \tau_{nuc})$ =1, which is equivalent to $\mathbf{Q} = \tau$. The condition, $\mathbf{Q} = \tau$ can also be written in the form: $2\,\mathrm{d}\sin\theta = \lambda$. Each

angle $2\theta_n$ corresponds to a wavevector transfer $\mathbf{Q}_n$. In this experiment one can probe 13 points in the sample reciprocal space. If any of these points satisfy the condition $\mathbf{Q}_n=\tau$, then for that particular detector, one will observe coherent scattering. In Figure 2.2 b) we show a hypothetical plot of the differential cross section vs. $2\theta_n$, where it is assumed that for the $2\theta_n$ angles corresponding to the detector elements n = 4 and 6, the condition $\mathbf{Q} = \tau$ is satisfied. For both detectors we observe coherent scattering. In conclusion, with this type of experiment one can probe lines in the reciprocal space. A detailed description of elastic and inelastic time-of-flight neutron scattering is found in [5–7].

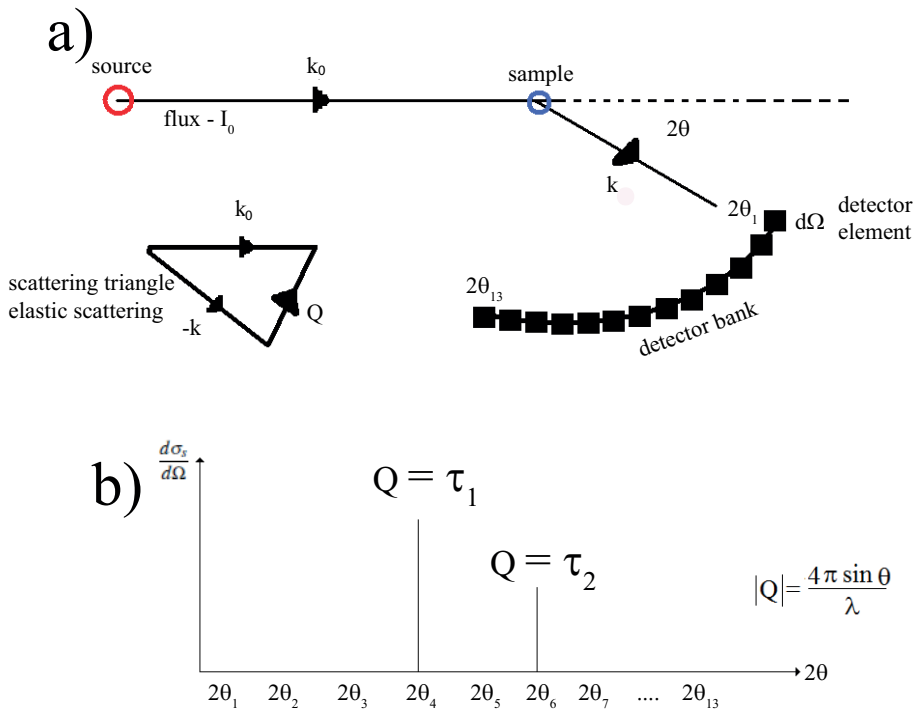

Figure 2.2 (a) Schematic diagram of a hypothetical diffraction experiment. Monochromatic neutrons of I_0, wavevector $\mathbf{k}_0$ and energy E_0 emanating from a source. The incident neutrons transfer momentum $\hbar\mathbf{Q} = \hbar\mathbf{k}_0 - \hbar\mathbf{k}$ ($\hbar\omega = 0$) to the sample and are scattered through an angle 2θ towards the detector bank. (b) Plot of the differential cross section vs. $2\theta_n$, where it is assumed that for the $2\theta_n$ angles corresponding to the detector elements n = 4 and 6, $\mathbf{Q} = \tau$ is satisfied.

In the experiment described above, the incident flux used is monochromatic and constant in

time. Next we will assume the same experiment as the one in Figure 2.2 a), but this time we will assume a pulsed flux, where each pulse will have neutrons with energies in a range E to E+ΔE. Each neutron will have a different wavelength $\lambda_i = 9.044\ \sqrt{E_i}$, where E_i is the energy of neutron i. If we assume the case of only one detector element but a pulsed incident flux, one can observe using the relation, $|Q| = 4\ \pi \sin\theta/\lambda$, that in this special case, lines in the reciprocal space are probed. If all detectors are used with an incident pulse flux, one can probe surfaces in the reciprocal space. For real instruments, pulses of neutrons with different energies are emanated at the same time t_0. Recording the arrival time t of the neutron at the detector, one can calculate the wavevector transfer. The advantages of the time-of-flight neutron scattering technique, compared with the one described above where the incident flux was monochromatic, is that for the same instrument setting one can probe surfaces in the reciprocal space.

2.2.2 OSIRIS - ISIS pulsed neutron source

A schematic diagram of the OSIRIS instrument at ISIS pulsed neutron source, used for the single crystal elastic and inelastic time-of-flight neutron scattering experiment is shown in Figure 2.3. Details about the instrument can be found in Ref. [8].

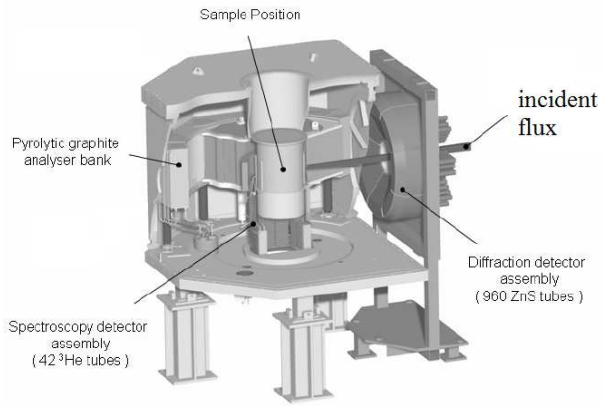

Figure 2.3 Schematic diagram of the instrument used for the elastic and inelastic time-of-flight neutron scattering experiment.

Chapter 3

X-ray scattering

This chapter presents a brief description of the classical and quantum-mechanical formalism used to describe the interaction of X-ray radiation (XR) with matter. The detailed derivation of all the formula given in this section can be found in many books [9–14]. XR is a transverse electromagnetic radiation with the electric and magnetic fields, **E** and **B**, perpendicular to each other and to the direction of propagation **k**. XR is described classically by using plane waves for the electric and magnetic fields, **E**(**r**,t) and **B**(**r**,t), and the flux of a classical X-ray beam is proportional to the square of the electric field amplitude. In quantum mechanics, a monochromatic X-ray beam is viewed as being quantized into photons, each having a well defined energy and momentum; in this case the flux of the beam is given by the number of photons passing through a given area per unit time. The XR can be scattered by matter (X-ray scattering - XS) or can be absorbed (X-ray absorption - XA); both XS and XA will be discussed in the following sections. Before a microscopic description of the interaction between XR and matter, I will give a brief description of quantities that we actually measure during the experiments, such as the *scattered intensity* I_{sc}, *differential cross-section*, $(d\sigma/d\Omega)$ and *total cross-section*, σ_{tot} (these concepts were explained for the case of neutron scattering in Chapter 2).

Assuming that an X-ray beam, of flux Φ_0 is incident on a sample with a smaller cross-sectional

area, one wants to calculate the intensity of the scattered beam I_{sc} in a direction defined by the unit vector $\mathbf{u}$. Here, I_{sc} is defined as the number of X-ray photons scattered per second into a detector that subtends a solid angle $\Delta\Omega(\mathbf{u})$. I_{sc} will be proportional to Φ_0, to the solid angle $\Delta\Omega(\mathbf{u})$, to the total number of particles in the sample, N, and most importantly, it is proportional to the *differential cross-section*, $(d\sigma/d\Omega)(\mathbf{u})$ (which describes how efficiently an atom from the sample scatters the XR). So we can write for the scattered intensity [11]:

$$I_{sc} = \Phi_0 N \Delta\Omega \left(\frac{d\sigma}{d\Omega}\right)(\mathbf{u}) \tag{3.1}$$

Thus the *differential cross-section* per scattering particle is defined by:

$$\left(\frac{d\sigma}{d\Omega}\right)(\mathbf{u}) = \frac{\textit{No. of X-ray photons per second into } \Delta\Omega(\mathbf{u})}{\Phi_0 N \Delta\Omega(\mathbf{u})} \tag{3.2}$$

In quantum mechanics the scattering process is described by time-dependent perturbation theory. The interaction between the XR and the sample is specified by the interaction Hamiltonian $\mathbf{H}_{int}$, which produces transitions between the initial $|i\rangle$ and final $|f\rangle$ states. Here, $|i\rangle$ and $|f\rangle$ refer to the combined states of the XR and the electrons from the system. The number of transitions, W, per second between $|i\rangle$ and $|f\rangle$ is given in the first-order perturbation theory by *Fermi's Golden Rule* [3]:

$$W = \frac{2\pi}{\hbar}|M_{if}|^2 \rho(\varepsilon_f) \tag{3.3}$$

where the matrix elements are defined as $M_{if} = \langle f|\mathbf{H}_{int}|i\rangle$ and $\rho(\varepsilon_f)$ is the density of states, defined such that $\rho(\varepsilon_f)\,d\varepsilon_f$ is the number of final states with energy in the interval $d\varepsilon_f$ centered around ε_f. In order to evaluate the *differential cross-section*, $\left(\frac{d\sigma}{d\Omega}\right)$ we have to calculate the number of transitions per second, I_{sc}, into the solid angle $\Delta\Omega$ using Eq. (3.3). From the calculations of the *differential cross-section* using Eq. (3.3) [10], it is observed that it is more convenient to define a new quantity called scattering length b, which characterizes the scattering power of the atom, with b being the only quantity that can be determined experimentally for any atom. Usually b is a complex number and it becomes real only when the XR absorbtion effects in the atom

are negligible. The *differential cross-section* is equal with the square of the scattering-length: $(d\sigma/d\Omega)(\mathbf{u}) = |b(\mathbf{u})|^2$. We defined the *total scattering cross-section* per particle $\sigma_{scatt-tot}$ as the total number of photons scattered per second, normalized to Φ_0 and N, $\sigma_{scatt-tot} = \int (\frac{d\sigma}{d\Omega})(\mathbf{u}) d\Omega$, where the integration is carried out over all the directions defined by unit vector **u**. In terms of scattering length, $\sigma_{scatt-tot} = 4\pi |b|^2$. Because any atom absorbs parts of the XR without scattering it, we also have to define the *absorption cross-section*, σ_{abs}. The sum of cross-section of all the interaction processes (absorption, elastic and inelastic scattering) gives the *total cross-section*, $\sigma_{tot} = \sigma_{scatt-tot} + \sigma_{abs}$ [10, 11].

3.1 Classical treatment of X-ray scattering

In a first approximation, we can describe the electric component of the monochromatic XR by a plane-wave with an electric field **E** that has constant modulus |**E**| everywhere in a plane perpendicular to the direction of propagation. For example, the spatial and temporal variation of a plane-wave, propagating along the **z**-axis (one-dimensional case) can be described by a simple expression, such as $E_0 e^{i(\omega t - kz)}$, where E_0 is the amplitude of the electric field wave. In the three-dimensional case if we write the polarization of the electric field as a unit column vector, ε, and the wavevector along the direction of propagation as **k**, then the electric field plane-wave is described by:

$$\mathbf{E}(\mathbf{R}, t) = \ \varepsilon \ E_0 e^{i(\omega t - \mathbf{k}\cdot\mathbf{r})} \tag{3.4}$$

When the electric field described by the Eq. (3.4) falls on a charged particle with charge q, a force **F** = **E**q will act on the particle producing accelerations of the charged particle. From classical electromagnetic theory, we know that an accelerated charge radiates. This radiation which spreads out in all directions from the atoms, has the same frequency as the primary beam and it is called scattered radiation. In the classical theory of scattering atoms are considered to scatter as dipole oscillators with definite characteristic atomic angular frequencies ω_0, which are identified with the

absorption angular frequencies of the atoms. The bound electrons of the atoms undergo harmonic oscillations when the incident *XR* falls on them and will emit XR as a result of the oscillations. The scattering process is modeled by considering that the atom is a single harmonic oscillator.

The equation of motion for a single harmonic oscillator of mass m, restoring constant κ and damping coefficient Γ is given by [9, 11, 12]:

$$m\ddot{\mathbf{r}} + \Gamma\dot{\mathbf{r}} + \kappa\mathbf{r} = 0 \tag{3.5}$$

where $\ddot{\mathbf{r}}$ ($\dot{\mathbf{r}}$) is the second (first) time derivative of the displacement $\mathbf{r}$. When the oscillator, approximated by a particle with an effective charge (-e) and mass m (vibrating about a massive positive charge which we may consider at rest), is exposed to an oscillating electric field of angular frequency ω, whose electric vector at the time t_0 and at the position of the electron is given by $\mathbf{E}_{in} = \varepsilon_{in} E_0 e^{i\omega t_0}$, the equation of motion becomes [9, 11, 12]:

$$m\ddot{\mathbf{r}} + \Gamma\dot{\mathbf{r}} + \kappa\mathbf{r} = (-e)\varepsilon_{in} E_0 e^{i\omega t_0} \tag{3.6}$$

The restoring force and damping coefficient Γ are used to model the binding energy of the electron to the atom. The damping is the result of the radiation which is emitted by the electron, or of the energy transferred to other electrons. We will first consider the scattering from a single free electron, which is simple, and presents the main characteristics of the scattering by an atom.

Let us assume that we have a free electron of mass m, which we may consider at rest. This is equivalent with setting Γ and κ to zero in Eq. (3.6). When the electron is exposed to the oscillating electric field, it will be forced to oscillate and will act as a source that will radiate as a small dipole antenna. The radiated electric field at large distances ($\mathbf{k}\cdot\mathbf{r} \gg 1$) is given by [9, 11, 12]:

$$\mathbf{E}_{sc}(\mathbf{R}, t = t_0 + |\mathbf{r}|/c) = -b(\varepsilon_{sc}, \varepsilon_{in}) E_0 \varepsilon_{sc} \frac{e^{i(\omega t - \mathbf{k}\cdot\mathbf{r})}}{|\mathbf{r}|} \tag{3.7}$$

with the scattering-length b defined as [10]:

$$b(\varepsilon_{sc}, \varepsilon_{in}) = r_0 \varepsilon^*_{sc} \cdot \varepsilon_{in} \tag{3.8}$$

where $r_0 = e^2/(4\pi\varepsilon_0 mc^2) = 2.82\,10^{-5}$ Å is known as the classical electron radius; P = $\varepsilon^*_{sc} \cdot \varepsilon_{in}$ is a polarization factor which depends on the X-ray source; ε^*_{sc} is the transpose of ε_{sc}; all the other quantities have their usual meaning. If the incident polarization is normal (or parallel) to the plane of scattering, the outgoing one is also normal (parallel) to the plane. These polarization modes are called sigma (labeled σ), when perpendicular to the plane of scattering, and pi (labeled π) when parallel, see Figure - 3.1. The process described above is the so-called Thomson scattering. The

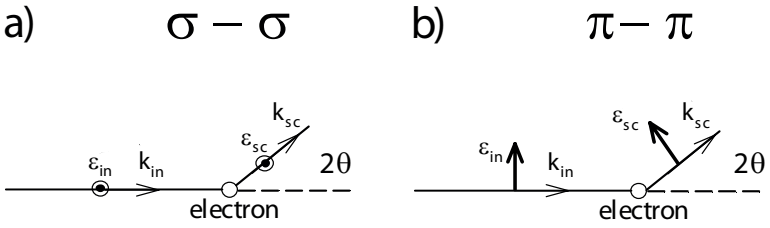

Figure 3.1 Directions of incident and scattered polarizations for a) σ-σ mode and b) the π-π mode. The polarization factor P of the scattering length is 1 for σ-σ scattering and $cos2\theta$ for for π-π scattering, where θ is the scattering angle.

simple result of the Thomson scattering is a good approximation even for the bound electrons of an atom, as far as the frequency of the XR is large compared to the characteristic atomic frequencies, ω_0. In order to calculate the scattering from an atom, it is necessary to take into account both the number of electrons and their position in the electronic cloud. Every point of the electronic cloud is considered to scatter independently from the others and the scattered amplitudes add coherently. As in any interference calculation within the Born approximation, one obtains the total scattering length by the Fourier transform of the electron density $\rho(\mathbf{r})$ [10]:

$$b(\varepsilon_{sc}, \varepsilon_{in}) = r_0 \varepsilon^*_{sc} \cdot \varepsilon_{in} f^{Thomson}(|\mathbf{Q}|) \tag{3.9}$$

where $\mathbf{Q}$ is the scattering vector and the quantity $f^{Thomson}(|\mathbf{Q}|)$ is called the Thomson scattering factor and is given by:

$$f^{Thomson}(|\mathbf{Q}|) = \int \rho(\mathbf{r}) \cdot e^{i\mathbf{Q}\mathbf{r}}\, dV(\mathbf{r}) \tag{3.10}$$

For forward scattering, the integral of $\rho(\mathbf{r})$ over all $\mathbf{r}$ values must be equal to the number of electrons in the atom, $f^{Thomson}(|\mathbf{Q}| = 0)$ = Z. Values of the Thomson scattering factors have been numerically calculated for most of the chemical elements. Analytical functions of the form given by Eq. (3.11), which reproduce the numerical calculations, are used to calculate the atomic Thomson scattering factors; the coefficients a_i, b_i and c are given in Ref. [15]:

$$f^{Thomson}(|\mathbf{Q}|) = \sum_{i=1}^{4} a_i e^{-b_i(|\mathbf{Q}|/4\pi)^2} + c \tag{3.11}$$

We want to mention that throughout this chapter Thomson scattering factors refer to the values calculated using Eq.(3.11), with the appropriate coefficients.

We can improve our model for X-ray scattering by considering the full classical model, *Eq.* (3.6). This model yields the following scattering length [10]:

$$b(\varepsilon_{sc}, \varepsilon_{in}) = r_0 \frac{\omega^2}{\omega^2 - \omega_0^2 - i\Gamma\omega/m} \varepsilon_{sc}^* \cdot \varepsilon_{in} \tag{3.12}$$

where $\omega_0^2 = \kappa/m$. We observe from *Eq.* (3.12), that when we consider the classical model for an atom, the scattering length is a complex number; we can separate b into real and imaginary parts by multiplication of both the numerator and the denominator by $\omega^2 - \omega_0^2 + i\Gamma\omega/m$. The result is:

$$b(\varepsilon_{sc}, \varepsilon_{in}) = r_0 \frac{\omega^2 \cdot (\omega^2 - \omega_0^2)}{(\omega^2 - \omega_0^2)^2 + (\Gamma\omega/m)^2} \varepsilon_{sc}^* \cdot \varepsilon_{in} + r_0 \frac{i(\Gamma/m)\omega^3}{(\omega^2 - \omega_0^2)^2 + (\Gamma\omega/m)^2} \varepsilon_{sc}^* \cdot \varepsilon_{in} \tag{3.13}$$

The anomalous contribution to the real part of the scattering length can be separated by subtraction of the classical Thomson scattering, r_0 from the first term of *Eq.* (3.13). Then the anomalous contributions to the scattering length are given by:

$$b(\varepsilon_{sc}, \varepsilon_{in})_{real}^{resonant} = r_0 \frac{\omega_0^2 \cdot (\omega^2 - \omega_0^2) - (\Gamma/m)^2 \omega^2}{(\omega^2 - \omega_0^2)^2 + (\Gamma\omega/m)^2} \varepsilon_{sc}^* \cdot \varepsilon_{in} \approx r_0 \left(\frac{\omega_0}{\omega - \omega_0}\right)_{\frac{\Gamma}{m} \to small} \varepsilon_{sc}^* \cdot \varepsilon_{in} \tag{3.14}$$

and

$$b(\varepsilon_{sc}, \varepsilon_{in})_{imaginary}^{resonant} = r_0 \frac{(\Gamma/m)\omega^3}{(\omega^2 - \omega_0^2)^2 + (\Gamma\omega/m)^2} \varepsilon_{sc}^* \cdot \varepsilon_{in} \tag{3.15}$$

Further we will call the anomalous contribution as resonant contributions due to the that fact that the anomalous contributions become significant only when the angular frequency ω of the incoming XR is close to the characteristic angular frequency of the oscillator ω_0. From $Eqs.$ (3.14) and (3.15), we see that for an atom which is modeled as a single harmonic oscillator, the real part of the resonant scattering length of an oscillator is negative below the absorption edge, where $\omega < \omega_0$, and positive above the edge, while the imaginary part of the resonant scattering length is positive everywhere. We define the resonant atomic scattering factors as the scattering length divided by r_0:

$$f' = \frac{\omega_0^2 \cdot (\omega^2 - \omega_0^2) - (\Gamma/m)^2\,\omega^2}{(\omega^2 - \omega_0^2)^2 + (\Gamma\,\omega\,/\,m)^2}\,\varepsilon_{sc}^* \cdot \varepsilon_{in} \tag{3.16}$$

and

$$f'' = r_0\,\frac{(\Gamma/m)\,\omega^3}{(\omega^2 - \omega_0^2)^2 + (\Gamma\,\omega\,/\,m)^2}\,\varepsilon_{sc}^* \cdot \varepsilon_{in} \tag{3.17}$$

Now we can write down the total atomic scattering factor, f (including resonance effects) for an atom as [10, 11]:

$$f(E,\mathbf{Q}) = (\ f^{Thomson}(|\mathbf{Q}|) + f'(\omega) + if''(\omega)\ )\ \varepsilon_{sc}^* \cdot \varepsilon_{in} \tag{3.18}$$

We mentioned earlier that during the interaction process between XR and matter part of the radiations is not scattered but absorbed. The absorption cross-section for a single oscillator model is [11]:

$$\sigma_{abs} = 4\pi r_0 c\,\frac{(\Gamma/m)\,\omega^2}{(\omega^2 - \omega_0^2)^2 + (\Gamma\,\omega\,/\,m)^2} \tag{3.19}$$

We stop at this point to anticipate one of the limitations of the single-oscillator model. The imaginary part of the resonant scattering represents the dissipation in the system or in other words the absorption. f'' and σ_{abs} for a forced harmonic oscillator display a resonance when the driving angular frequency ω is close to the characteristic angular frequency ω_0, with the width of this resonance being proportional to the damping constant Γ. It follows from $Eqs.$ (3.17) and (3.19) that the single oscillator model can be expected to yield at best a peak in f'' and σ_{abs}. Far away

from the resonance, at frequencies ω much larger then the resonance frequency ω_0, according to *Eq.* (3.19), $\sigma_{abs} \sim \omega^{-2}$ [11]. This result doesn't resemble the experimentally determined absorption cross sections which have a discontinuous jump at an absorption edge, followed by an ω^{-3} fall-off [11]. In order to model this behavior for an atom one must instead assume a superposition of oscillators with relative weights, called oscillator strengths, $g(\omega_0) \sim \sigma_{abs}(\omega = \omega_0)$. In this case the resonant scattering factors become [9, 11]:

$$f'(\omega) = \sum_{\omega_0} g(\omega_0) \frac{\omega^2 \cdot (\omega^2 - \omega_0^2)}{(\omega^2 - \omega_0^2)^2 + (\Gamma \omega / m)^2} \tag{3.20}$$

and

$$f''(\omega) = \sum_{\omega_0} g(\omega_0) \frac{(\Gamma/m)\, \omega^3}{(\omega^2 - \omega_0^2)^2 + (\Gamma \omega / m)^2} \tag{3.21}$$

This classical model, although simple, can describe most of the phenomena. Nevertheless, the values of the resonance frequencies and of the damping coefficient are not calculable within this framework and are left arbitrary. This theory does not give much indication about the **Q** dependence of the scattering factor at resonance. Therefore the only coherent and completely exact description is given by the quantum theory of the interaction between the radiation and atoms, summarized in the following section.

3.2 Quantum mechanical treatment of X-ray scattering

From a quantum mechanical perspective, a monochromatic X-ray beam is viewed as being quantized into photons, each having an energy $\hbar\omega$ and momentum $\hbar\mathbf{k}$. In the absence of any interaction between the XR and the electrons in the atom, the Hamiltonian of the system is given by [11]:

$$\mathbf{H}_0 = \mathbf{H}_{electron} + \mathbf{H}_{radiation} \tag{3.22}$$

where $\mathbf{H}_{electron}$ and $\mathbf{H}_{radiation}$ refer to the electrons and XR respectively.

Classically it is shown that the interaction between an electromagnetic field and a charge q is allowed by replacing the momentum operator **p** by **p**-q **A**, where **A** is the vector potential operator of the radiation. To obtain the interaction Hamiltonian we consider first the case of a free electron for which $\mathbf{H}_{electron} = \mathbf{p}^2/2\mathrm{m}$. This allows us to write down the Hamiltonian of the interacting system as [11, 12]:

$$\mathbf{H}_0 = \frac{(\mathbf{p}+e\mathbf{A})^2}{2m} + \mathbf{H}_{radiation} = \frac{\mathbf{p}^2}{2m} + \frac{e\mathbf{A}\cdot\mathbf{p}}{m} + \frac{e^2\mathbf{A}^2}{2m} = \mathbf{H}_{electron} + \mathbf{H}_{int} + \mathbf{H}_{radiation} \tag{3.23}$$

where $\mathbf{H}_{int}$ is the interaction Hamiltonian:

$$\mathbf{H}_{int} = \frac{e^2\mathbf{A}^2}{2m} + \frac{e\mathbf{A}\cdot\mathbf{p}}{m} \tag{3.24}$$

The vector potential operator of XR is linear in photon creation and annihilation operators [11]. Keeping this in mind and observing that the second term in $\mathbf{H}_{int}$ is linear in **A**, we conclude that first order in perturbation theory, Eq. (3.3), can either create or destroy a photon, but not both. This term gives rise to the photoelectric absorption $\left(\sigma_{abs}^{PE}\right)$. The first term in $\mathbf{H}_{int}$ is quadratic in **A** and we conclude that in first order perturbation theory it can first destroy and then create a photon, while leaving the electron in the same atomic state $|\Psi_0\rangle$ (we want to mention here that $|\Psi_0\rangle$ is the ground state of the electron, while $|i\rangle$ is the ground state of the combined system, photon plus electron). This term therefore describes elastic Thomson scattering. To obtain resonant scattering terms it is necessary to take the calculations to higher order. In second order perturbation theory the transition probability from Eq. 3.3 is described as [11]:

$$W = \frac{2\pi}{\hbar}\left|\langle f|\mathbf{H}_{int}|i\rangle + \sum_{n=1}^{\infty}\frac{\langle f|\mathbf{H}_{int}|n\rangle\langle n|\mathbf{H}_{int}|i\rangle}{\varepsilon_i - \varepsilon_n}\right|^2 \rho(\varepsilon_f) \tag{3.25}$$

where the sum is over all possible excited states with energy ε_n. Using $Eq.$ (3.25) it can be shown that the **A**·**p** term from the interaction Hamiltonian, $Eq.$ (3.24), which is linear in creation and annihilation operators, can produce scattering via an intermediate state. Reading the matrix element that appears in the numerator of the second term in $Eq.$ (3.25), from right to left the scattering process can be described in the following way: the incident photon is first absorbed and the electron

makes a transition from the ground state, $|\Psi_0\rangle$, to an intermediate state, $|\Psi_n\rangle$. Then the electron makes a transition from $|\Psi_n\rangle$ back to $|\Psi_0\rangle$ giving away its excess energy to a photon. The resonant behaviour arises when the denominator in Eq. 3.25 tends to zero. This occurs when the total energy, $\varepsilon_i = \hbar\omega_{in} + E_0$, is equal to the energy of the electron in the intermediate state, ε_n. Here, $\hbar\omega_{in}$ is the energy of the incident photon, E_0 is the energy of the electron in the atomic ground state $|\Psi_0\rangle$, and $\varepsilon_n = E_n$ is the energy of the electron in the atomic excited state $|\Psi_n\rangle$.

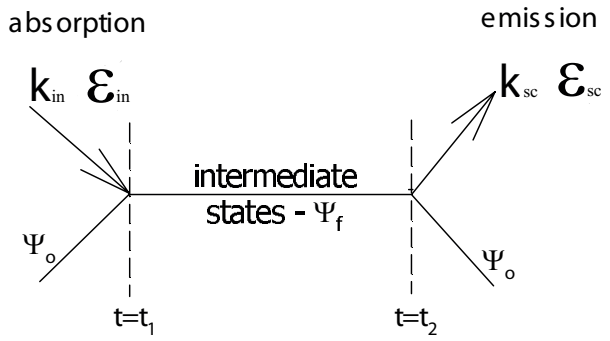

Figure 3.2 Schematic diagram of the resonant process where an incident photon with ($\mathbf{k}_{in}$, ε_{in}) is absorbed by a core electron Ψ_0 which is promoted to the intermediate state Ψ_f and after a short time is reemitted with ($\mathbf{k}_{sc}$, ε_{sc}) when the electron and core-hole recombine.

The resonant scattering process to the intermediate states is controlled by two considerations. The Pauli exclusion principle requires that only unoccupied intermediate states can be accessed, while the usual quantum mechanical selection rules imply that electric dipole transitions dominate. Quantum theory predicts that in solids the resonant corrections become dependent on the polarization of the incoming and scattered photons, when the symmetry of the intermediate state $|\Psi_n\rangle$ is lowered due to its involvement in chemical bonding. It also predicts that resonant scattering becomes a probe of magnetic order in the solids, when the intermediate state is split by magnetic interactions. The two terms described above in the interaction Hamiltonian, Eq. (3.24), give rise

to terms b_{disp1} and b_{disp2} in the scattering length expression [10]:

$$\begin{aligned} b(\vec{\varepsilon}_{sc},\vec{\varepsilon}_{in}) =& r_0 \langle\Psi_0|\varepsilon_{sc}^* e^{+i\mathbf{k}_{sc}\cdot\mathbf{r}}\cdot\varepsilon_{in} e^{-i\mathbf{k}_{in}\cdot\mathbf{r}}|\Psi_0\rangle - \\ & - r_0\sum_c \frac{\langle\Psi_0|\varepsilon_{sc}^*\cdot\mathbf{p}\cdot e^{+i\mathbf{k}_{sc}\cdot\mathbf{r}}|\Psi_n\rangle\langle\Psi_n|\varepsilon_{in}^*\cdot\mathbf{p}\cdot e^{+i\mathbf{k}_{in}\cdot\mathbf{r}}|\Psi_0\rangle}{m(E_n-E_0-\hbar\omega_{in}+i\Gamma_n/2)} - \\ & - r_0\sum_c \frac{\langle\Psi_0|\varepsilon_{in}^*\cdot\mathbf{p}\cdot e^{-i\mathbf{k}_{in}\cdot\mathbf{r}}|\Psi_n\rangle\langle\Psi_n|\varepsilon_{sc}^*\cdot\mathbf{p}\cdot e^{+i\mathbf{k}_{sc}\cdot\mathbf{r}}|\Psi_0\rangle}{m(E_n-E_0+\hbar\omega_{in})} = \\ & = b_{Thomson}+b_{disp1}+b_{disp2} \end{aligned} \tag{3.26}$$

Here $|\Psi_0\rangle$ and $|\Psi_n\rangle$ stand for the ground and excited electron states. For elastic scattering the states $|i\rangle$ and $|f\rangle$ in Eq. (3.25) are identical. $\mathbf{p}$ and $\mathbf{r}$ are the electron momentum and position operator. In the last two terms from *Eq.* (3.26) the sum is taken over all excited states $|\Psi_n\rangle$ (empty bound or continuous states). $E_n - E_0$ represents the energy of the excitation and $\hbar\omega_{in}$ ($\hbar\omega_{sc}$) is the energy of the incident (scattered) photon. In elastic scattering $\hbar\omega_{in} = \hbar\omega_{sc}$. Here $2\pi\hbar/\Gamma_n$ is the life time of the $|\Psi_n\rangle$, and Γ_n is the quantum counterpart of the damping factor Γ, *Eqs.* (3.5)-(3.6), in the classical theory.

The first term in Eq. (3.26) will give rise to Thomson scattering, also found in the classical theory of XR scattering, Eq. (3.10). The last two terms, b_{disp1} and b_{disp2}, define the dispersive part of the scattering. As mentioned earlier, the numerator in the second term of (3.26) suggests that the incoming photon transfers momentum to the electron in the ground state, $|\Psi_0\rangle$, and promotes the electron from its ground state into the excited state, $|\Psi_n\rangle$. We can say that the scattering b_{disp1} is obtained by the excitation, $|\Psi_0\rangle$ -> $|\Psi_n\rangle$, then de-xcitation, $|\Psi_n\rangle$ -> $|\Psi_0\rangle$. This order is reversed in b_{disp2} since the $|\Psi_n\rangle$ state, which is virtual, is destroyed before being created. From Eq. (3.26) we observe that close to resonance, the denominator of the dispersion term b_{disp1} becomes very small compared to the denominator of the dispersion term, b_{disp2}, leading to the conclusion that the most significant term close to resonance is b_{disp1}. In order to calculate the resonant scattering factors we will only consider b_{disp1} from Eq. (3.26). Scattering operators of the form $e^{\mp i\mathbf{k}\cdot\mathbf{r}}$, as occuring in

Eq. (3.26), can be developed in a power series [12]:

$$e^{\mp i\mathbf{k}\cdot\mathbf{r}} = 1 \mp i\mathbf{k}\cdot\mathbf{r} - (\mathbf{k}\cdot\mathbf{r})^2/2 \mp ... \tag{3.27}$$

The approximation in which only the leading term in the Eq.(3.27) is retained is referred to as the dipolar approximation. The dipolar approximation works very well for the case where $|\mathbf{k}| = 2\pi/\lambda$ is small (longer wavelengths as visible light) and for the case where the scattering object is compact relative to the wavelength used (that is, if either the initial state or the final state has a compact core-type wave function). The dipolar approximation (only the first term is retained in Eq.(3.27), $e^{\mp i\mathbf{k}\cdot\mathbf{r}} = 1$) works very well in case of K-edge, where an electron from the core 1s level is promoted to the empty 4p states above the Fermi energy. For the K-edge, $|\Psi_0\rangle = |\Psi_{1s}\rangle$, $|\Psi_n\rangle = |\Psi_{4p}\rangle$, $E_0 = E_{1s}$, $E_n = E_{4p}$ and $\Gamma_n = \Gamma_{4p}$.

We obtain the resonant scattering factor (in units of classical electron scattering, r_0) in the dipolar approximation using the first dispersive term b_{disp1} in Eq. (3.26), by replacing $e^{\mp i\mathbf{k}\cdot\mathbf{r}} = 1$, using $\mathbf{p}_\alpha = -i\hbar\frac{d}{d\alpha}$, where $\alpha = x,y,z$, for the components of the momentum operator $\mathbf{p}$ and using $\frac{\mathbf{p}_\alpha}{m} = \frac{i}{\hbar}[\mathbf{H}_{electron}, \alpha]$; the resonant scattering factor becomes [12]:

$$f'(E) + if''(E) = -\frac{m}{\hbar^2}\sum_{4p}(E_{4p} - E_{1s})^2 \left[\frac{\langle\Psi_{1s} \mid \varepsilon^*_{sc}\cdot\mathbf{r} \mid \Psi_{4p}\rangle\langle\Psi_{4p} \mid \varepsilon_{in}\mathbf{r} \mid \Psi_{1s}\rangle}{E_{4p} - E_{1s} - \hbar\omega_{in} + i\Gamma_{4p}/2}\right] \tag{3.28}$$

We can separate the real and imaginary parts of the quantum resonant scattering factor, $Eq.(3.28)$ using the same steps used to separate the real and imaginary parts of the classical resonant scattering , $Eqs.(3.16)$-(3.17).

$$f'(E) = -\frac{m}{\hbar^2}\sum_{4p}(E_{4p} - E_{1s})^2(E_{4p} - E_{1s} - \hbar\omega_{in})\frac{\langle\Psi_{1s} \mid \varepsilon^*_{sc}\cdot\mathbf{r} \mid \Psi_{4p}\rangle\langle\Psi_{4p} \mid \varepsilon_{in}\cdot\mathbf{r} \mid \Psi_{1s}\rangle}{(E_{4p} - E_{1s} - \hbar\omega_{in})^2 + \Gamma^2_{4p}/4} \tag{3.29}$$

$$f''(E) = \frac{m}{\hbar^2}\sum_{4p}(E_{4p} - E_{1s})^2(\Gamma_{4p}/2)\frac{\rangle\Psi_{1s} \mid \varepsilon^*_{sc}\cdot\mathbf{r} \mid \Psi_{4p}\rangle\rangle\Psi_{4p} \mid \varepsilon_{in}\cdot\mathbf{r} \mid \Psi_{1s}\rangle}{(E_{4p} - E_{1s} - \hbar\omega_{in})^2 + \Gamma^2_{4p}/4} \tag{3.30}$$

When the $4p$ states are isotropic, the quantum mechanical form of the resonant scattering factors depends on the incident and scattered polarization directions through a unique factor, $\varepsilon^*_{sc}\cdot\varepsilon_{in}$, and

the total atomic scattering factor is independent of the orientation of the scattering object, with respect to the incident and scattered polarization directions. This result is equivalent to the one obtained by classical methods, Eq.(3.18), and we can represent the atomic scattering factor by a scalar. In the case when the 4p states are anisotropic due to the interaction with the neighboring atoms, the resonant atomic scattering factor will be dependent on the orientation of the scattering object with respect to the incident and scattered polarization directions, and in this case the atomic scattering factor is represented by a second-rank tensor (3x3 matrix) [12–14]. We are writing this tensor using a reference frame (**x**,**y**,**z**) attached to the crystal:

$$
\begin{aligned}
f =& (\varepsilon_{sc}^{x}\ \varepsilon_{sc}^{y}\ \varepsilon_{sc}^{z}) \cdot \hat{f}_{atomic} \cdot \begin{pmatrix} \varepsilon_{in}^{x} \\ \varepsilon_{in}^{y} \\ \varepsilon_{in}^{z} \end{pmatrix} = f^{Thomson}(|\mathbf{Q}|) \cdot \begin{pmatrix} 1 & 0 & 0 \\ 0 & 1 & 0 \\ 0 & 0 & 1 \end{pmatrix} (\varepsilon_{sc}^{x}\ \varepsilon_{sc}^{y}\ \varepsilon_{sc}^{z}) \cdot \begin{pmatrix} \varepsilon_{in}^{x} \\ \varepsilon_{in}^{y} \\ \varepsilon_{in}^{z} \end{pmatrix} \\
&+ (\varepsilon_{sc}^{x}\ \varepsilon_{sc}^{y}\ \varepsilon_{sc}^{z}) \cdot \begin{pmatrix} f'_{xx} & f'_{xy} & f'_{xz} \\ f'_{xy} & f'_{yy} & f'_{yz} \\ f'_{xz} & f'_{yz} & f'_{zz} \end{pmatrix} \cdot \begin{pmatrix} \varepsilon_{in}^{x} \\ \varepsilon_{in}^{y} \\ \varepsilon_{in}^{z} \end{pmatrix} \\
&+ i \cdot (\varepsilon_{sc}^{x}\ \varepsilon_{sc}^{y}\ \varepsilon_{sc}^{z}) \cdot \begin{pmatrix} f''_{xx} & f''_{xy} & f''_{xz} \\ f''_{xy} & f''_{yy} & f''_{yz} \\ f''_{xz} & f''_{yz} & f''_{zz} \end{pmatrix} \cdot \begin{pmatrix} \varepsilon_{in}^{x} \\ \varepsilon_{in}^{y} \\ \varepsilon_{in}^{z} \end{pmatrix}
\end{aligned}
\tag{3.31}
$$

where $(\varepsilon_{sc}^{x}\varepsilon_{sc}^{y}\varepsilon_{sc}^{z})$ and $\begin{pmatrix} \varepsilon_{in}^{x} \\ \varepsilon_{in}^{y} \\ \varepsilon_{in}^{z} \end{pmatrix}$ are the projections of the scattered, ε_{sc}^{*} and incident, ε_{in} polarizations in the (**x**,**y**,**z**) reference frame; the tensor components are defined as:

$$
f'_{\alpha\beta}(E) = -\frac{m}{\hbar^2}(E_{4p}-E_{1s})^2(E_{4p}-E_{1s}-\hbar\omega_{in})\left[\frac{\langle\Psi_{1s} \mid \mathbf{r}_\alpha \mid \Psi_{4p}\rangle\langle\Psi_{4p} \mid \mathbf{r}_\beta \mid \Psi_{1s}\rangle}{(E_{4p}-E_{1s}-\hbar\omega_{in})^2+\Gamma_{4p}^2/4}\right] \tag{3.32}
$$

and respectively

$$
f''_{\alpha\beta}(E) = \frac{m}{\hbar^2}(E_{4p}-E_{1s})^2(\Gamma_{4p}/2)\left[\frac{\langle\Psi_{1s} \mid \mathbf{r}_\alpha \mid \Psi_{4p}\rangle\langle\Psi_{4p} \mid \mathbf{r}_\beta \mid \Psi_{1s}\rangle}{(E_{4p}-E_{1s}-\hbar\omega_{in})^2+\Gamma_{4p}^2/4}\right], \tag{3.33}
$$

with $\alpha, \beta = x, y, z$. The (**x**,**y**,**z**) reference frame is chosen such that **z**||**c**-axis (parallel with the 3-fold axis), **x**||**a**-axis and **y** orthogonal to **x** and **z**. In the most general case, the resonant scattering tensor is a second-order tensor with nine independent components, see *Eq*. (3.31). In order to obtain the form of the resonant scattering tensors at the Ni sites, we are taking into account the fact that the scattering tensor should be invariant under all symmetry transformations which belong to the space group of the crystal. Using only the local symmetry of the Ni ions in $AgNiO_2$, we learn that all the off diagonal terms of the resonant scattering tensor are zero and that $f'_{(xx)} = f'_{(yy)} \neq f'_{(zz)}$ and $f''_{(xx)} = f''_{(yy)} \neq f''_{(zz)}$. In the given space group the atomic scattering tensor for the Ni ions have the following diagonal form:

$$\hat{f}_{atomic} = \begin{pmatrix} f_\perp & 0 & 0 \\ 0 & f_\perp & 0 \\ 0 & 0 & f_\parallel \end{pmatrix} \tag{3.34}$$

where $f_\parallel$ and $f_\perp$ are the eigenvalues of $\hat{f}_{atomic}$ in the direction parallel to the **z**-axis and perpendicular to the **z**-axis, respectively $f_\parallel = f^{Thomson}(|\mathbf{Q}|) + f'_{zz} + if''_{zz}$ and $f_\perp = f^{Thomson}(|\mathbf{Q}|) + f'_{xx} + if''_{xx} = f^{Thomson}(|\mathbf{Q}|) + f'_{yy} + if''_{yy}$. To simplify we will write the atomic scattering tensor as the sum between an isotropic and an anisotropic part:

$$\hat{f}_{atomic} = \begin{pmatrix} f_\perp & 0 & 0 \\ 0 & f_\perp & 0 \\ 0 & 0 & f_\perp \end{pmatrix} + \begin{pmatrix} 0 & 0 & 0 \\ 0 & 0 & 0 \\ 0 & 0 & f_\parallel - f_\perp \end{pmatrix} = f_\perp \begin{pmatrix} 1 & 0 & 0 \\ 0 & 1 & 0 \\ 0 & 0 & 1 \end{pmatrix} + \begin{pmatrix} 0 & 0 & 0 \\ 0 & 0 & 0 \\ 0 & 0 & \Delta f_{anis} \end{pmatrix} \tag{3.35}$$

We observe from *Eq*. (3.35), that when the anisotropy component of the atomic scattering tensor is very small or the geometry of experiment is such that the polarizations of the incident and scattered *XR* don't see the anisotropic component, the atomic scattering tensor reduces to a scalar as in the classical theory, *Eq*. (3.18), with $f = f_\perp$.

During the interaction process called absorption, the radiation is absorbed instead of being scattered (the photon completely disappears). As we discussed in the previous paragraphs, this process

is modeled by the first order perturbation theory using the linear term in **A** from the interaction Hamiltonian, Eq. (3.24). This process is called *photoelectric absorption*. The *photoelectric absorption* cross-section derived from the interaction Hamiltonian at the lowest level of perturbation theory is given by [10]:

$$\sigma_{abs}^{PE} = \frac{constants}{\hbar\omega_{in}} \sum_{4p}(E_{4p} - E_{1s})^2(\Gamma_{4p}/2)\frac{\langle\Psi_{1s} \mid \varepsilon_{sc}^* \cdot \mathbf{r} \mid \Psi_{4p}\rangle\langle\Psi_{4p} \mid \varepsilon_{in} \cdot \mathbf{r} \mid \Psi_{1s}\rangle}{(E_{4p} - E_{1s} - \hbar\omega_{in})^2 + \Gamma_{4p}^2/4} \tag{3.36}$$

From equations *Eqs*. (3.19) and (3.36) we observe that the imaginary part of the resonant scattering factors, calculated for forward scattering (**Q** = 0), is related to the *photoelectric absorption* cross-section σ_{abs}^{PE} at the photon energy $E = \hbar\omega$ by [16]:

$$f''(|\mathbf{Q}| = 0) = \frac{E\sigma_{abs}^{PE}(E)}{2hcr_e} \tag{3.37}$$

The absorption cross section per atom, σ_{abs}, is an easy quantity to measure. When a monochromatic X-ray beam with incident intensity, I_0, passes through a homogeneous plate of uniform thickness, z, the transmitted intensity (I) can be modelled using the Lambert-Beer law, which states that [17]:

$$A_{eff} = \frac{I}{I_0} = e^{-\mu(E)z} \tag{3.38}$$

where $\mu(E)$ is the energy dependent linear absorption coefficient. For a homogenous material made of a single element the absorption coefficient $\mu(E)$ is related to $\sigma_{abs}(E)$ through [17]:

$$\mu(E) = (\frac{\rho N_A}{A})\sigma_{abs}(E) \tag{3.39}$$

where N_A, ρ and A are Avogadro's number, the mass density and the atomic mass number respectively. We want to mention here that during the transmission experiments, most of the beam is lost due to the photoelectric effects (σ_{abs}^{PE}), but a small part of the beam is lost due to coherent(σ_{coh}) and incoherent scattering (σ_{inc}). In the vicinity of the absorption edge, the σ_{coh} and σ_{inc} are less than two percent of $\left(\sigma_{abs}^{PE}\right)$ and we can approximate $\sigma_{abs} = \sigma_{abs}^{PE}$.

In practice we are interested in obtaining the mass absorption coefficient μ/ρ from which we can obtain $f''(|\mathbf{Q}|=0)$ through the following relation [12]:

$$\mu/\rho = \frac{4.20784 \cdot 10^7 f''}{AE} \tag{3.40}$$

Theoretical values of the mass absorption coefficients, μ/ρ, and resonant scattering factor, f'', were calculated and tabulated in [16] for energies away from the resonance. To a reasonable approximation, the mass absorption coefficient is independent of the physical state of the absorber and $(\mu/\rho)_{compound}$ for a compound is additive with respect to the $(\mu/\rho)_i$ of its elements [17, 18]:

$$(\frac{\mu}{\rho})_{compound} = \frac{1}{MW}\Sigma_j(\frac{\mu}{\rho})_j A_j \tag{3.41}$$

where MW = $\sum_j x_j A_j$ is the molecular weight of the compound and x_j is the number of atoms of type j per formula unit.

3.3 Practical formulas used for the data analysis

In the most general case the atomic scattering factor is a tensor, Eq. (3.35), dependent on the scattering wavevector, $\mathbf{Q}$, and on the photon energy, E = $\hbar\omega$. In the dipolar approximation the $\mathbf{Q}$ dependence comes from the Thomson scattering factor, Eq. (3.11), and the energy dependence, E, comes from the resonant scattering factors, Eqs. (3.20), (3.21), (3.28). Further in our calculations we will ignore the anisotropic part, Δf_{anis}, of the scattering tensor in Eqs. (3.35) and we consider that the atomic scattering factors for Ni ions are scalars (verifications for this approximation will be given in Section 4.8). The real and imaginary part of the resonant atomic scattering factors, f' and f'', are not independent quantities but (at constant $\mathbf{Q}$) are related by their mutual Kramers-Kronig relationships [12, 19]:

$$f'(E_0) = \frac{2}{\pi}P\int_0^\infty \frac{Ef''(E)}{E_0^2 - E^2}dE \quad f''(E_0) = -\frac{2E_0}{\pi}P\int_0^\infty \frac{f'(E)}{E_0^2 - E^2}dE, \tag{3.42}$$

where P indicates principal part, which means that the term for which $E_0^2 = E^2$ is excluded from the integrals. By performing RXD experiments we aim to obtained experimentally the resonant scattering factors which are crystallographically site-selective, can be used to contrast oxidation states in mixed-valence materials and can be also used to learn about the local environment of the ions. Empirical determination of the distribution of valence states in compounds containing ions with two different oxidation states relies upon the rapid change in the shape of f'' close to the absorption edge for the two distinct ions; f'' also shifts to higher energies by a few eV per oxidation state unit (see Fig. 4.11). Thus, close to the resonance, the shape of f'' will vary significantly between ions with different oxidation states. One would also expect differences in the shape of f'' for elements in a single oxidation state but with markedly dissimilar coordination environment [20]. The intensity of XR diffracted by crystals depends on the structure factor F(E,**Q**) and thus on the atomic scattering factors, f_j:

$$F(E,\mathbf{Q}) = \sum_j f_j(E,|\mathbf{Q}|)\ T_j(|\mathbf{Q}|)\ e^{i\mathbf{Q}\cdot\mathbf{R}_j}, \tag{3.43}$$

The sum extends over all atoms at position $\mathbf{R}_j$ in the unit cell. $T_j(|\mathbf{Q}|) = e^{-\frac{1}{2}U_j|\mathbf{Q}|}$ is the temperature Debye-Waller factor for the j atom and U_j is the temperature dependent isotropic atomic displacement. In order to extract $f_j(|\mathbf{Q}|,E)$ for each atom from the measured structure factors $F(E,|\mathbf{Q}|)$, the structure $\mathbf{R}_j$, the temperature factor T_j and the Thomson scattering factor $f_j^{Thomson}(|\mathbf{Q}|)$ have to be known. In our calculations we used the crystal structure determined by earlier neutron diffraction, the Thomson scattering factors calculated using Eq. (3.11) and Debye-Waller factors calculated using the isotropic atomic displacement U_j from [21]. In addition, a number of corrections have to be applied to the measured intensities:

$$I(E,\mathbf{Q}) = C\ |F(\mathbf{Q},E)|^2\ Abs(S,\mu(E),O)\ L(E,2\theta)\ E_{xtin}, \tag{3.44}$$

where C is a scaling constant including constant terms like the sample mass, incident flux, etc.; *Abs* is the absorption coefficient of the beam through the sample, μ is the energy-depended lin-

ear absorption coefficient for $AgNiO_2$, the terms S and O characterize the sample shape and the orientation of the sample in the laboratory reference frame, 2θ is the total scattering angle, and the last term $L(E, 2\theta)$ is the Lorentz factor which, for the particular instrument geometry of the instrument used to perform the experiment, is $\sim \frac{1}{E^3 \sin 2\theta}$ [22]. E_{xtin} is called extinction factor and for this particular experiment is approximated with 1; we neglect the extinction due to the fact that our crystal is very small.

To understand the extinction effects we define two type of crystals: perfect crystal (as the crystal without lattice defects) and the imperfect crystal (which is usually viewed as one comprised of very small mosaic blocks). The integrated intensity of a reflection from a small perfect crystal is $|F|^2$ [23]. The integrated intensity of a reflection from a large perfect crystal is $|F|$ (derivation of this proportionality is called dynamical theory of diffraction), and the integrated intensity of a reflection from an imperfect large crystal is $|F|^2$ (derivation of this proportionality is called kinematical theory of diffraction) [23]. In general, the integrated intensity of a reflection is appreciably larger for the ideally imperfect crystal than for one which is ideally perfect. The experimentally measured values fall between these two extremes, depending upon the state of imperfection in the crystal. Because most crystals are rather imperfect, it is customary to interpret the integrated intensity measurements using the imperfect crystal approximation (which state that the integrated intensity $|F|^2$). Usually the crystals are imperfect but not ideally imperfect, therefore the measured integrated intensity is somewhat less than the value predicted by the ideally imperfect approximation. We describe the situation by saying that there is extinction in the crystal, the term extinction meaning that the integrated intensity is less than predicted by the ideally imperfect crystal approximation. In our case due to the fact that the crystal is very small, we work in the approximation where the integrated intensity $|F|^2$ and the extinction is negligible, E_{xtin} =1.

We mentioned earlier in section 3.2 that the attenuation of transmitted XR beam through a homogenous polycrystalline sample of given thickness is given by the Beer's law, $Eq.$ (3.38).

Thus if the sample has a non-uniform thickness across its area, the measured absorption, A_{eff}, will differ from the nominal value. Defining $P(z)$ as the fraction of the sample area that is of thickness z, where $\int_0^{z_{max}} P(z)dz = 1$, the effective absorption factor becomes $A_{eff} = \int P(z)e^{-\mu(E)\,z}dz$ [24]. In our case the absorption is affected by regions of the sample with zero thickness and by a distribution of thicknesses. In a first approximation we assume that we have a leakage (zero thickness) fraction f, together with a Gaussian distribution in thicknesses centered around a nominal values z_0 with width γ; then

$$P(z) = f\delta(z) + (1-f)\frac{1}{\gamma\sqrt{2\pi}}e^{-\frac{(z-z_0)^2}{2\gamma^2}} \tag{3.45}$$

for which the effective absorption factor becomes [25]:

$$A_{eff} = f + (1-f)e^{(-\mu(E)\,z_0 + \frac{\mu(E)^2\,\gamma^2}{2})} \tag{3.46}$$

The formula we are using to calculate the linear absorption coefficient for $AgNiO_2$ at energies away from the resonance energy was calculated using $Eq.$ (3.41):

$$\begin{aligned}\mu^{AgNiO_2} =& \frac{\rho_{AgNiO_2}}{MW}(\frac{\mu_{Ag}}{\rho_{Ag}}A_{Ag} + \frac{\mu_{Ni}}{\rho_{Ni}}A_{Ni} + 2\frac{\mu_O}{\rho_O}A_O) = \\ &= 0.036238\ (\ 10.274\ \mu_{Ag}\ +\ 6.5944\ \mu_{Ni}\ +\ 22535\ \mu_O)\end{aligned} \tag{3.47}$$

Using $Eq.$ (3.47) and $Eq.$ (3.40) we derived the relation between the linear absorption coefficient and the total imaginary part of the resonant scattering factor:

$$\mu^{AgNiO_2}[cm^{-1}] = \frac{1.5249\,10^6}{E[eV]}f''_{total} \tag{3.48}$$

where

$$f''_{total} = f''_{Ag} + 2f''_O + \frac{f''_{Ni1} + f''_{Ni2} + f''_{Ni3}}{3} \tag{3.49}$$

is the total contribution for one formula unit. These formulas are used for the data analysis in Chapter 4.

3.4 X-ray scattering instruments: I16

3.4.1 I16 - Diamond Light Source

A schematic diagram of the I16 instrument at Diamond Light Source used for the single crystal x-ray resonant scattering experiment is shown in Figure 3.3. Experiments on this instrument are performed using monochromatic incident flux. Some advantages of this instrument are that the wavelength of the incident photons can be tuned and the fact that the sample can be oriented in any direction with respect to the laboratory reference frame, such that we can probe a large region of the reciprocal space. Details about this instrument can be found in Ref. [26].

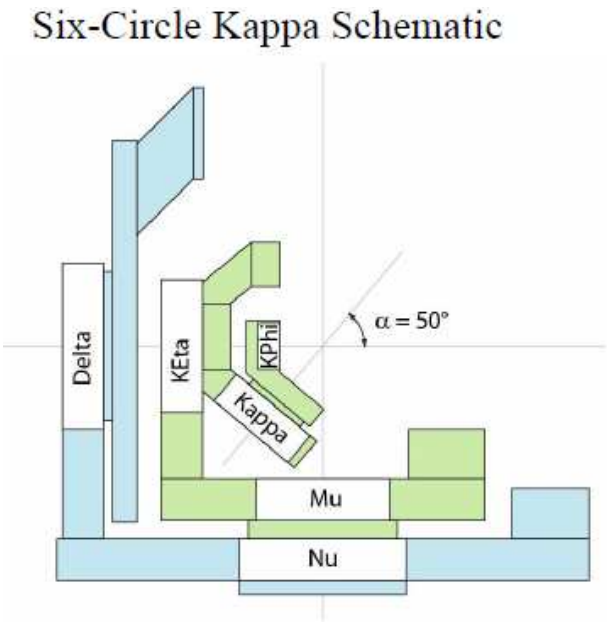

Figure 3.3 Schematic diagram of the instrument used for the x-ray resonant scattering experiment where delta, Keta, etc. are variable angles.

.

Chapter 4

Honeycomb Charge order in triangular metallic $AgNiO_2$ probed by single crystal resonant X-ray scattering

The layered hexagonal magnet $AgNiO_2$ realizes a rare example of a triangular antiferromagnetic metal with orbital degeneracy. It undergoes a structural transition below 365 K to a supercell crystal structure with a periodic arrangement of expanded and contracted NiO_6 octahedra, see Figure - 4.1, proposed to indicate spontaneous charge order at the Ni sites into electron-rich and localized sites arranged in a triangular lattice, surrounded by a honeycomb of itinerant Ni sites [27]. This chapter reports synchrotron single-crystal resonant x-ray scattering measurements to probe the Ni electronic states. A strong resonant enhancement of the scattering intensity is observed for supercell reflections as the x-ray energy is tuned through the Ni K-edge. A rich structure with multiple peaks is observed as a function of x-ray energy, attributed to interference scattering from the distinct (expanded/contracted) Ni sites. The empirically extracted atomic resonant scattering factors show an edge shift of 2.5 eV between the crystallographically distinct sites which is in very

good quantitative agreement with the expected shift in the presence charge order estimated using band structure calculations in the LDA approximation. Order parameter measurements show a strong correlation between the spontaneous charge order and the structural response in temperature of oxygen displacements which indicate that the charge order and the structural distortion are strongly linked.

4.1 Introduction

The presence of orbital degrees of freedom in addition to spin opens up rich and largely unexplored possibilities for complex electronic order patterns. If the electrons are mobile, even richer possibilities exist as the tendency to lift the orbital degeneracy via the symmetry-lowering local Jahn-Teller (JT) distortions competes with the tendency to remove the degeneracy by charge transfer between sites and therefore more complex order patterns can occur [28]. Recent studies of the hexagonal antiferromagnetic metal 2H-$AgNiO_2$ with orbitally-degenerate Ni^{3+} ($t_{2g}^6 e_g^1$) ions arranged in triangular layers revealed no JT distortions, but an unexpected oxygen order pattern below T_S=365 K, consisting of a periodic arrangement of expanded and contracted NiO_6 octahedra, see Figure - 4.1. The oxygen order pattern was proposed to be a consequence of charge disproportionation (CD) at the Ni sites of the form $3e_g^1 \rightarrow e_g^2 + 2e_g^{0.5}$ [27]. This is in sharp contrast to the related nickelate $NaNiO_2$ [29], where the NiO_2 layers are essentially identical with only subtle differences in the interlayer bonding along **c** axis (mediated by Na^+ trigonal bonds with 3 Oxygens below and 3 above as opposed to linear O-Ag^+-O bonds). Despite the similarities, $NaNiO_2$ is an insulator with a charge gap estimated at ~ 0.6 eV [30] and at T_S = 480 K undergoes a structural transition to a monoclinic structure due to cooperative JT ferro-orbital order [29]. The very different behavior between Na- and Ag-nickelates is not well understood and may be ultimately due to the subtly different inter-layer bonding which stabilizes an insulating state in Na-nickelate (where subsequently

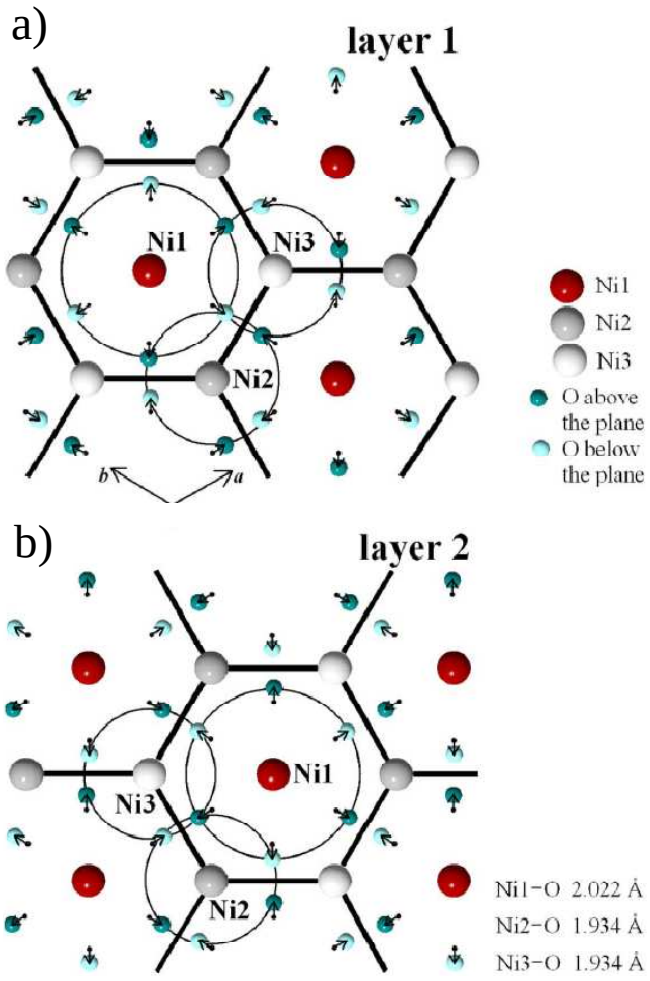

Figure 4.1 Schematic diagram of the NiO_2 layers in the low symmetry phase of the hexagonal 2H-$AgNiO_2$ system. a) schematic diagram of a NiO_2 layer at z = 1/4 showing how the displacements (small arrows) of the oxygen ions (small balls) lead to a periodic arrangement of expanded (large circle, Ni1) and contracted (small circles, Ni2,3) NiO_6 octahedra. Thick hexagonal contour shows the honeycomb network of contracted sites. The origin of the coordinate system is at the circled Ni2 site. b) The expanded site Ni1 has a staggered zigzag arrangement between even and odd layers stacked along the **c** axis. Layer 2 in the unit cell (z = 3/4 and -1/4) is obtained from layer 1 by 180° rotation around the central (1/2, 1/2, z) axis followed by a **c**/2 translation. The different Ni-O distances have been proposed to occur as a consequence of a net electron transfer between the contracted sites to the expanded sites, leading to electron-rich $Ni1^{3-\delta}$ expanded sites and electron-depleted $Ni2,3^{3+\delta/2}$ contracted sites, where $0<\delta\leq 1$ is the net amount of charge transfer.

orbital degeneracy is lifted by JT distortions) whereas a metallic state persists in Ag-nickelate. Band-structure calculations proposed that this metallic screening is key in reducing the energy cost for charge transfer and this combined with the gain in Hund's rule coupling for the doubly occupied Ni sites, gain in covalency effects from closer proximity Ni-O and gain in kinetic energy for the itinerant electrons on the contracted Ni sites favor CD as the preferred mechanism to lift orbital degeneracy as opposed to conventional JT distortions [27].

In order to test if the oxygen displacements are accompanied by CD at the Ni sites, we used resonant x-ray diffraction (RXD) and x-ray absorption spectroscopy (XAS) techniques to probe directly the oxidation state of Ni ions. Both techniques were successfully used before to probe charge disproportionation patterns [31, 32] and oxidation states [20, 33] of resonant ions, in transition metals and their oxides. RXD and XAS rely on the measurement of the energy difference (also called edge energy, E_{K-edge}) between a core state and a continuous energy band of empty states above the Fermi energy. In the process of RXD and XAS at the K-edge, the core level state is 1s and the empty states above the Fermi level are the 4p states. The different edge-energies for the Ni ions ($E^{Ni1}_{K-edge} \neq E^{Ni2}_{K-edge}$), are a result of different positions in energy (with respect to the Fermi energy) of the 1s states ($E^{Ni1}_{1s} \neq E^{Ni2}_{1s}$ but $E^{Ni1}_{4p}=E^{Ni2}_{4p}$) , or of the 4p states ($E^{Ni1}_{4p} \neq E^{Ni2}_{4p}$ but $E^{Ni1}_{1s}=E^{Ni2}_{1s}$) or of both 1s and 4p states ($E^{Ni1}_{1s} \neq E^{Ni2}_{1s}$ and $E^{Ni1}_{4p} \neq E^{Ni2}_{4p}$) [34, 35].

A schematic description of the changes expected at the Ni K-edge when the structural transition occur in $AgNiO_2$ is given in Figure - 4.2. In the high temperature phase all the Ni sites are equivalent and they have the same edge-energy E_{K-edge}, see Figure 4.2 a). As a consequence the intensity for all the supercell reflections which are dependent on the edge-energy difference, ΔE_{K-edge} is zero. This is not the case in the low temperature phase where Ni ions sits in three crystallographically inequivalent sites; each site has different Ni - O bond lengths and because of that the energy position of the 4p states will be different due to different hybridizations ($E^{Ni1}_{4p} \neq E^{Ni2}_{4p} \neq E^{Ni3}_{4p}$). As a result the edge-energy E_{K-edge} for Ni1,2,3 ions will be different; if at the structural transition

a charge disproportionation occurs in the system, the position in energy of the 1s states will also be different for the Ni1,2,3 ions. If we combine the changes in energy of the 4p and 1s states, due to the hybridization effects and charge disproportionation, we expect a large difference in the edge-energies for Ni1 and Ni2,3 ions, see Figure 4.2 b) (we assume that Ni2 and Ni3 ions are in a similar electronic state because the local enviroment is equivalent). In this case the intensity of all the supercell reflections which are dependent on the edge-energy difference ΔE_{K-edge} (between Ni1 and Ni2,3 ions) will have a finite intensity. If at the structural transition there is no charge disproportionation (only oxygen displacements), then there will be an energy difference between the edges only due to shift of the 4p states, which comes as a result of different hybridizations between the Ni4p states and O2p states (different Ni-O bond lengths), see Figure 4.2 c). Hypothetically, if at the structural transition the hybridizations due to oxygen distortions are so small that the energy shifts of 4p states are very small (≈ 0), but there is a charge disproportionation, then there will be an energy difference between the edges due only to the shift of the 1s states, which comes as a result of different effective valences states for Ni ions, see Figure 4.2 d).

Our aim is to test experimentally the proposed charge disproportionation model; we are doing this by determining from (RXD) and (XAS) measurements the edge energy shift between Ni ions inside the contracted (Ni1) and expanded (Ni2,3) octahedra and comparing it with the calculated edge energy shift for the charged order state in the LDA approximation.

This chapter is organized as follows: section 4.2 presents the crystal structure above and below the T_S; section 4.3 discusses possible mechanisms to lift the orbital degeneracy of Ni^{3+} sites; section 4.4 explain the experimental details and how the raw intensities were obtained; section 4.5 presents the steps taken in order to extract the structure factors squared in absolute units; section 4.6 discusses the steps taken to extract experimentally the edge energies for the different Ni ions; section 4.7 presents the experimental results; section 4.8 shows theoretical calculations of the edge energies and a comparison with the experimentally extracted values; section 4.9 presents the

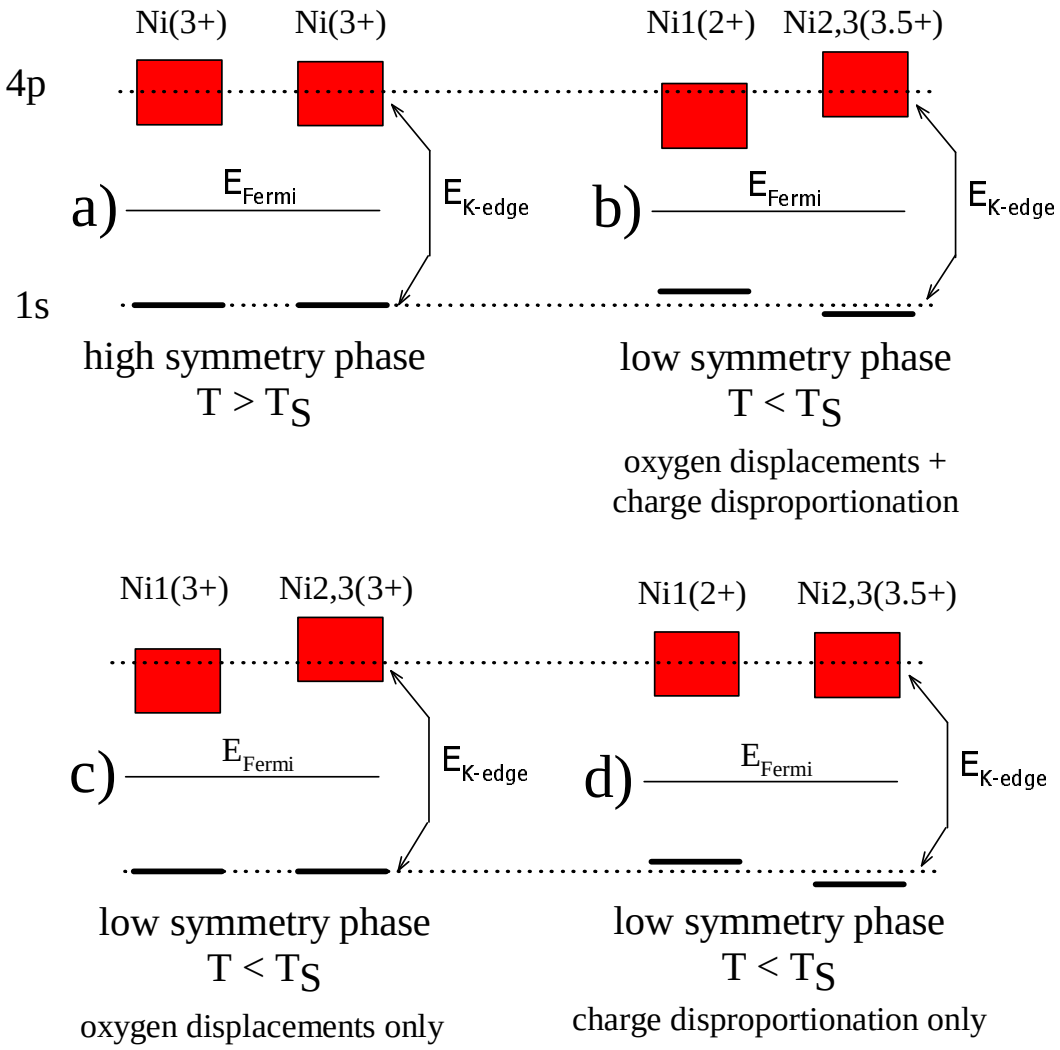

Figure 4.2 Schematic diagram of the atomic energy levels probed by RXD process (the red rectangular shapes represents the 4p density of states and the thick lines the positions of the 1s energy levels): a) energy level scheme of the 1s and 4p states in the high symmetry phase ($T > T_S$), where all the Ni ions are equivalent (Ni ions are in the 3+ effective valence state); b) energy level scheme in the low symmetry phase ($T > T_S$), where the Ni ions have different effective valence states (2+ and 3.5+) in crystallographically inequivalent positions. Hypothetical scenarios: c) no CO but only oxygen displacements; d) CO but no oxygen displacements.

temperature dependence of the charge disproportionation and order parameter for the structural distortions; the conclusions are summarized in the last section.

4.2 Crystal structure

Both high- and low- temperatures crystal structure of $AgNiO_2$ have been measured by neutron diffraction [36]. The high temperatures, $T > T_S$, crystal structure is shown in Figure - 4.3 a); each unit cell contains two identical NiO_2 layers which are related by a mirror plane reflection through the Ag layer; within each individual layer Ni ions are arranged in a triangular lattice. In Figure - 4.3 b) we show the tripling of the unit cell in the distorted phase, using schematic projections of the unit cell in the **ab**-plane. The local environment of Ni ions is a distorted O_6 octahedra and octahedra from different layers are connected through a O-Ag-O linear bond. From considerations of charge neutrality in the system we conclude that the ions are in the following effective oxidation states Ag^{1+}, O^{2-} and Ni^{3+} (we mention these values here because the effective oxidation state of Ni ions is important when Ni^{3+} ions are placed inside an ideal octahedra; ions with the $3d^7$ configuration placed inside an ideal octahedra leads to orbital degeneracy due to the fact that there is only one electron in the e_g double degenerate orbital, see - Figure 4.4).

If one asks the question: "What is the nature of the oxygen distortions with respect to an ideal octahedra for the Ni^{3+} ion?", one the answer can be found using Figures - 4.3 c) d), e) and f). Figure - 4.3 c) shows the local environment of the Ni^{3+} ions (distorted O_6 octahedra) in the crystal reference frame; Figures - 4.3 d), e) and f) show schematically how can one (starting from an ideal octahedra) obtain a distorted octahedra with the same local symmetry as the one of the Ni^{3+} ions in $AgNiO_2$. The symmetry of the local environment of the Ni^{3+} ions in $AgNiO_2$ is such that even with the distortions from an ideal octahedra present, the orbital degeneracy of the e_g orbital is not lifted and Ni^{3+} ions with the $3d^7$ configuration are orbitally degenerate, see Figure - 4.5. In the

low temperatures crystal structure, changes will occur in the Ni environment due to the oxygen distortions; due to the distortions, there will be 3 distinct Ni sites in the unit cell, see Figure - 4.1. At the structural transition, the small distortions of the oxygen ions occurring in the crystal, are found only in the **ab**-plane. Each three identical octahedra in the high temperature phase will correspond to, one expanded - (Ni1) and two contracted - (Ni2,3) octahedra, see Figure - 4.1.

4.3 Mechanisms to lift the orbital degeneracy

When a free transition metal (TM) ion with the d^1 configuration is placed in a crystal, the orbital degeneracy will be lifted due to the interaction of the electron in the *d*-orbitals with the ligand ions from the environment of the TM ion [37]. Depending on the symmetry of the environment the orbital degeneracy can be completely or partially lifted. When there is more then one electron in the *d*-orbitals the electron-electron interactions have to be taken into account to determine ground state and the orbital degeneracy. The ground state of a free TM ion with the d^7 configuration is schematically shown in Figure 4.4 d). When this ion is placed inside an octahedra (we assume the strong crystal field approximation), the interaction between the *d* electrons and the ligand ions from the corners of the octahedra will split the *d*-orbitals into a triplet (t_g) and doublet (e_g) state, see Figure 4.4 e). To minimize the energy of the system, six electrons will occupy the triplet state and one electron will occupy the doublet state. In the case when an ion with the d^7 configuration is placed inside an octahedra the ion will be in an orbitally degenerate state due to the fact that there is only one electron in the doublet state. The well known mechanism to lift the orbital degeneracy in insulating materials is the Jahn-Teller distortion [38].

When an ion with the d^7 configuration is placed inside an ideal octahedra, see Figure 4.4 b), in order to lift the orbital degeneracy, the ions on the Z_{cubic}-axis will distort in opposite direction, see Figure 4.4 c). This distortion of the environment will create a crystal field which will lift the

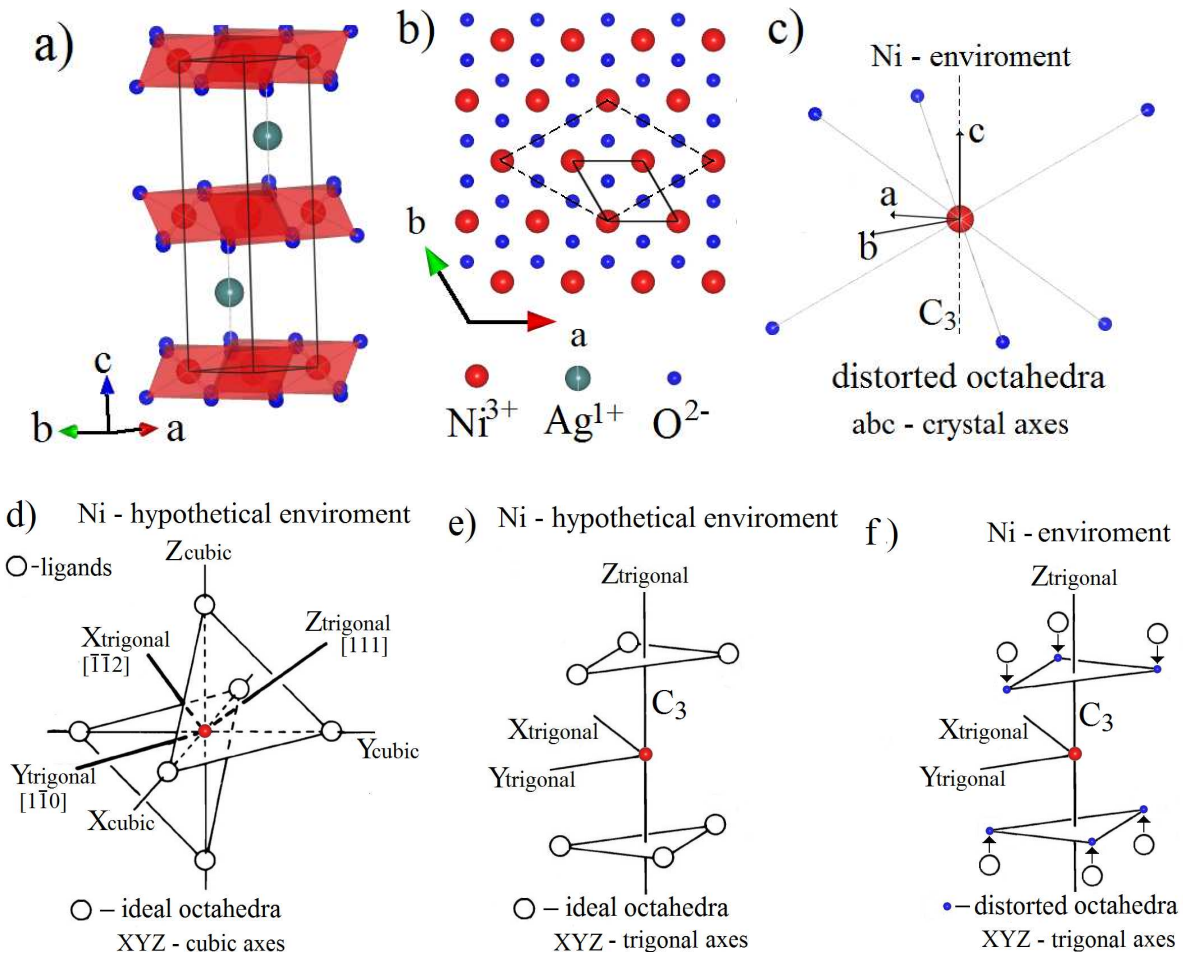

Figure 4.3 (a) Crystal structure of $AgNiO_2$ at high temperatures, $T > T_S$. (b) Basal plane showing the triangular network of Ni ions (red balls) coordinated by oxygens (blue balls). The thick solid line contour shows the unit cell and the dashed line shows the unit cell tripling in the distorted structure. (c) schematic view of the O_6 distorted octahedra in the crystal axis; this environment preserves the double degeneracy of the e_g state, see Figure - 4.5 (the degeneracy could be lifted by lowering the point group symmetry of the environment which means the three fold rotation C3 ∥ c is broken). (d) ideal octahedra in the cubic and trigonal axis; representation of the trigonal axes ($X_{trigonal}$, $Y_{trigonal}$, $Z_{trigonal}$) with respect to the cubic axes (X_{cubic}, Y_{cubic}, Z_{cubic}). (e) view of the octahedral arrangement of oxygen ions when the trigonal $Z_{trigonal}$ axis is vertical; the six oxygen ions are grouped into two triangles whose planes are perpendicular to the $Z_{trigonal}$ axis; (f) displacement of the oxygen triangles through equal distances along the $Z_{trigonal}$ axis as shown by the arrows; when the $Z_{trigonal}$ axis is oriented parallel with the crystal **c** axis, the distorted environment from the trigonal axes (red and blue balls) is similar with the Ni^{3+} environment in $AgNiO_2$, panel-(c).

.

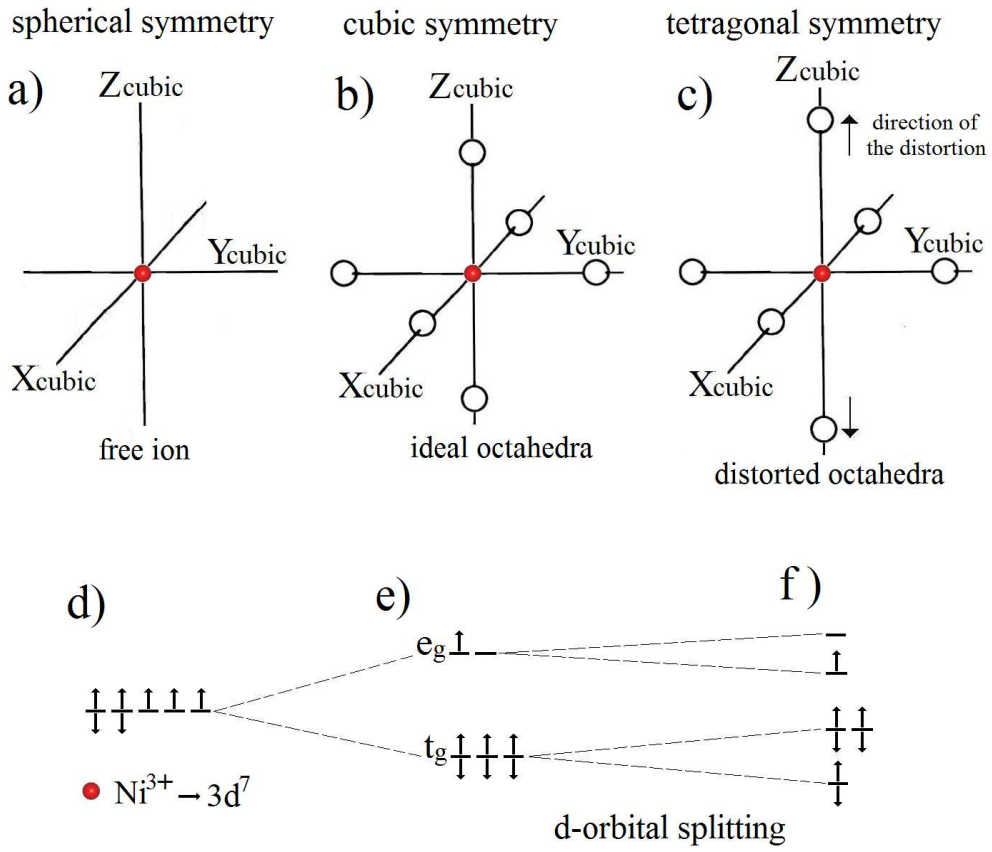

Figure 4.4 Schematic representation of different ligands environments and the corresponding splitting of the five fold orbital degeneracy of the 3d orbitals; the crystal field goes from spherical symmetry to lower symmetries. (a) free ion - spherical symmetry, (b) ideal octahedra - cubic symmetry. (c) distorted octahedra; the distortion is indicated by arrows - tetragonal symmetry. (d) degeneracy and occupancy of the d orbital when the ion is free. (e) when the ion is placed in the environment indicated in panel-(b) and (f) when the ion is placed in the environment indicated in panel-(c). When a distortion of the type indicated in panel-(c) occurs for an ideal octahedra the doubly degeneracy of the e_g orbital is lifted.

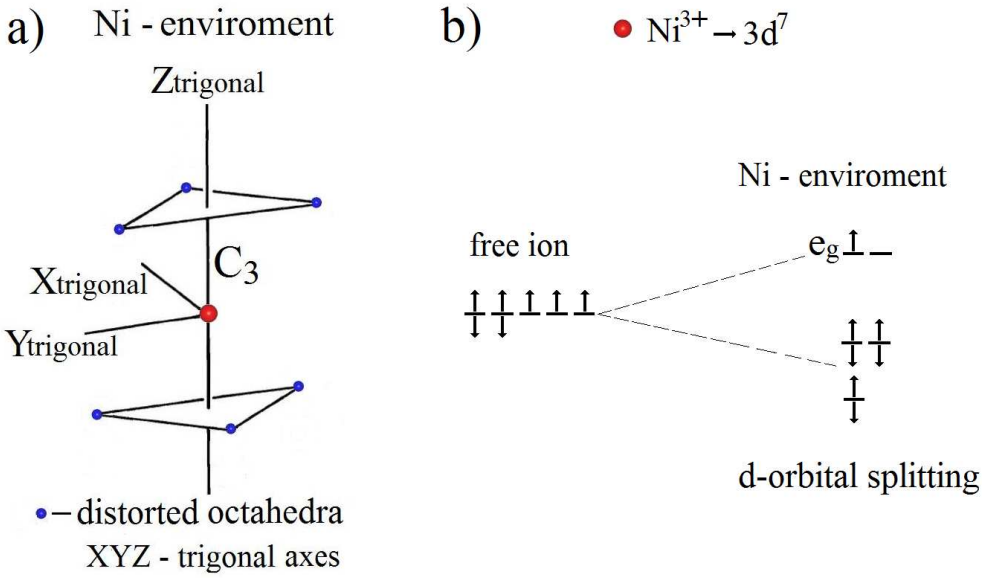

Figure 4.5 (a) Schematic representation of the local environment (distorted octahedra) for the Ni^{3+} ions in the high temperature phase using the trigonal axis. (b) splitting of the five fold degenerate d orbital and their occupancy for the Ni^{3+} ions in the high temperature phase; from panel-(b) we can see that Ni^{3+} ions are orbitally degenerate in the high temperature phase.

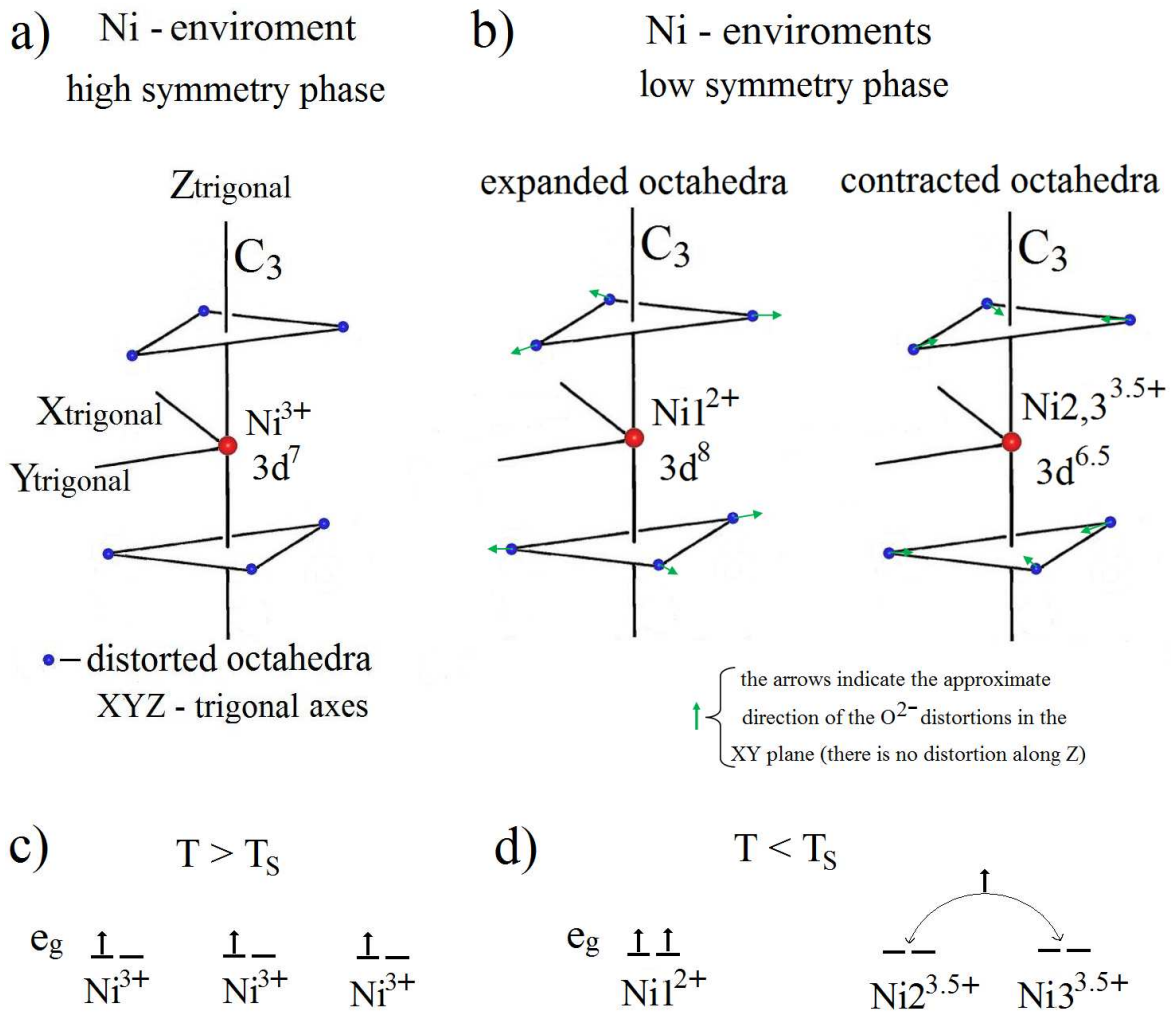

Figure 4.6 (a) local environment for Ni^{3+} ion in the high temperature phase. (b) local environment for $Ni1^{2+}$ and $Ni2,3^{3.5+}$ ions in the low temperature phase. (c) Electronic configuration of the Ni ions in the high temperature phase. (d) Electronic configuration of the Ni1 and Ni2,3 ions in the low temperature phase.

orbital degeneracy of the doublet state, see Figure 4.4 e) and f). This is the mechanism which lifts the orbital degeneracy of Ni^{3+} ions in the insulator system $NaNiO_2$ (a structural transition occurs in the system upon lowering the temperature which lifts the orbital degeneracy of the e_g orbital).

Further we will discuss the possible mechanism to lift the orbital degeneracy of Ni^{3+} ions in $AgNiO_2$. In the high temperature phase, the NiO_6 octahedra are already distorted, but the distortion doesn't lift the orbital degeneracy of the doublet state, see Figure 4.5. One expects that upon lowering the temperature the system will suffer a distortion such that the orbital degeneracy is lifted. Indeed a structural transition occurs in $AgNiO_2$ at T_S = 365 K but the new distortions of the NiO_6 octahedra do not lift the orbital degeneracy (the three fold symmetry axis which has to be broken if the degeneracy of the doublet state is lifted, is found in both high and low temperature phase, see Figure 4.6). The mechanism proposed to lift the orbital degeneracy in the weakly metallic $AgNiO_2$ system, based on charge ordering [27], is shown schematically in Figure 4.6 c) and d). Each Ni^{3+} ion in the high temperature phase will have one electron in the doublet (e_g) state; at the structural transition one of three ions will received an extra electron (Ni1) and the other two ions (Ni2,3) will share the remaining electron in a "metallic bond"; the ion which received an electron has a fully occupied doublet state and due to the surplus of charge the oxygen environment will expand (Ni1). The other two ions have a deficit of charge, and so the surrounding oxygen environment will contract (Ni2,3). We see that the well known mechanism, Jahn-Teller distortion, is not present at all in $AgNiO_2$ and therefore can not be used to explain the origin of the observed structural distortion. Instead, the observed structural transition has been proposed to be a response to an electronic instability of the system to charge order, as a mechanism of lifting orbital degeneracy. In the CO scenario there is an energy gain due to Hund's rule coupling and kinetic energy which is larger than the loss in energy due to the on-site coulomb repulsion (which is largely reduced due to the metallic screening) and lattice distortions [27, 28].

4.4 Experimental details and data collection

This experiment was performed using the I16 magnetism beam-line at the Diamond Light Source, United Kingdom operated with a Si (111) double-crystal monochromator to select photons with energy near the Ni K-edge of 8.35 keV. RXD measurements were done on a small crystal platelet with a diameter of $\sim$70 μm using photons with energies in the range 8.3 - 8.4 keV. XAS measurements were recorded in transmission mode on a powder sample using photons with energies in a wider range 8.25 - 8.42 keV. For a given instrument setting ($\mathbf{k}_{in}$, $\mathbf{k}_{sc}$, η), where $\mathbf{k}_{in}$, $\mathbf{k}_{sc}$ are the wave-vectors of the incident and scattered beam respectively and η is the angle between the scattering wave vector $\mathbf{Q}$ and $\mathbf{k}_{in}$, the scattered intensity was collected in a 2D pixelated area detector normal to $\mathbf{k}_{sc}$, see Figure - 4.7 a). The integrated intensity of the reflection was obtained by summing up all the counts in a region around the reflection (red dash-box) and subtracting the background counts which was obtained by summing up all the counts in a region surrounding the peak (the region between the red and the green dash-boxes). Due to the mosaicity of the sample, we measured rocking curve scans (RCS) for each reflection, at fixed incident energy, to make sure that we recorded the total number of scattered counts. When we say RCS scan we mean that the intensity was collected in the following way: the 2D detector was fixed at the nominal scattering angle of a reflection, 2θ and then the sample was rotated within a range of 2° around an axis perpendicular to $\mathbf{Q}$, using a step of 0.02 ° and counting 1 s/step; an example of such RCS is shown in *Figure* - 4.7 b) for one of the main reflections. The energy scans were obtained by integrating the RCS-scans at each energy (area under peak in *Figure* - 4.7 b)). The instrument geometry is such that in the laboratory reference frame (X_{lab}, Y_{lab}, Z_{lab}) the linear polarization of the incident beam is in the $X_{lab}Y_{lab}$ plane and the scattering plane is parallel to the $Y_{lab}Z_{lab}$ for all the measured reflections; $X_{lab} \| \mathbf{k}_{in}$, Y_{lab} is in the horizontal plane ($Y_{lab} \perp X_{lab}$), Z_{lab} is in the vertical plane ($Z_{lab} \perp X_{lab}$).

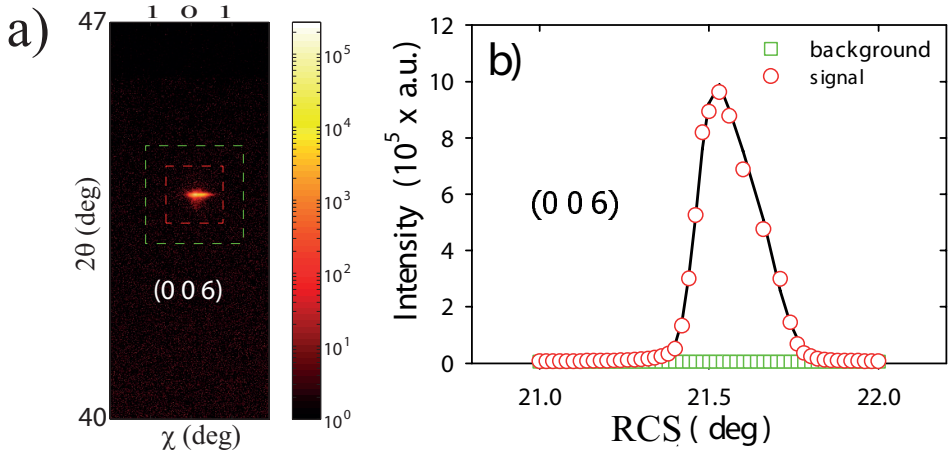

Figure 4.7 (a) raw counts for the (0 0 6) main reflection near resonance collected in a 2D pixelated area detector normal to $\mathbf{k}_f$. The integrated intensity was obtained by summing up all the counts in the read dash-box and subtracting the background (the integrated intensity in the region between the green and red dash-box). (b)RCS scan for the (0 0 6) main reflection.

4.5 Data Corrections

In this section we explain the steps involved in the data analysis, in order to obtain the experimental structure factors squared $|F(\mathbf{Q},E)|^2$ in absolute units of electrons squared. From Eq. (3.44), we observe that using the measured intensity $I(\mathbf{Q},E)$, we can obtain $|F(\mathbf{Q},E)|^2$ if the scale constant C, the absorption factor Abs(E) and the Lorentz factor L(E,2θ) are known quantities. The Lorentz factor can easily be calculated for any reflection at any energy but the main problem is the absorption factor.

To correct the data for absorption: - we have to propose a model for absorption and then use this model and the experimental data, to obtain the effective dimensions of the sample shape; - we have to obtain the energy dependence of the linear absorption coefficient over energies close to the resonance, using the transmission measurements on powder .

Once we obtain the effective dimensions of the sample and the energy dependence of the linear

absorption coefficient, we can use the absorption model to correct all the data for absorption effects.

In the first step, we will describe how we obtained the linear absorption coefficient from transmission measurements on powder. The experimental "effective absorption spectrum" is plotted in Fig. -4.8(a) (open circles). There are two necessary steps to extract $\mu(E)$ from the data: the first step is to obtain the empirical values of f, γ and z_0 used in Eq. (3.46). We obtain these values using only quantities measured away from the resonance. In the second step we introduce the obtained empirical values f, γ and z_0, back into Eq. (3.46) together with the measured absorption spectrum over all energies and extract $\mu(E)$ for the whole experimental energy range. We can write Eq. (3.46) at two different energies E_{below} = 8.3 keV and E_{above}=8.419 keV far away from the resonance energy where μ is approximated very well by analytical calculations. The linear absorption coefficients $\mu(E_{below})$ and $\mu(E_{above})$ for $AgNiO_2$ were calculated using Eq. (3.47). Assuming a very narrow distribution $\gamma \approx 0$ in Eq. (3.46), the calculated values $\mu(E_{below})$ and $\mu(E_{above})$, the measured values of the absorption coefficients $A_{eff}(E_{below})$ and $A_{eff}(E_{above})$, we obtain by solving the system of equations formed from Eq. (3.46) at the two energies E_{below} and E_{above}, a unique solution for the empirical values of (f, z_0). Using these values and the experimental absorption spectrum plotted in Fig. 4.8(a), we obtain a temporary solution for the linear absorption coefficient $\mu(E)_{temp}$. In the case where $\gamma \neq 0$, because the parameters in Eq. (3.46) are correlated, we don't obtain a unique solution (f, z_0,γ), but for all solutions, the extracted $\mu(E)$ is the same to within 1%. At this point in the data analysis an average value was chosen for the linear absorption coefficient.

In the second step, we will describe how we obtained the effective dimensions of the sample using the experimental data. The absorption model consist of a numerical Monte Carlo integration method for a disk-shaped sample (cylinder) of effective dimensions obtained by fits to the data as described below. The structure factor is related to the atomic positions in the unit cell and depending on the scattering wavevector **Q**, the structure factor can have contributions from all the

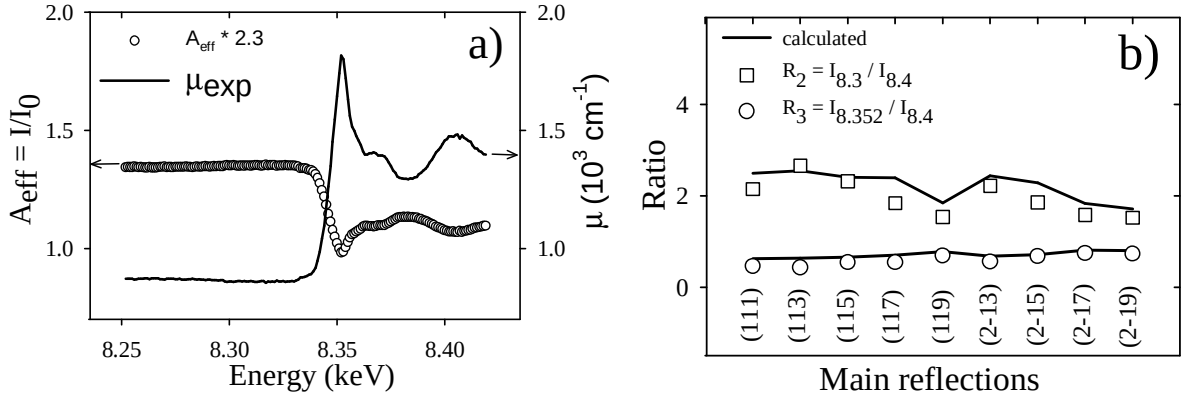

Figure 4.8 (a) Energy dependence of the absorbtion near Ni K-edge (open circles) measured in transmission mode on a powder sample and the experimental linear absorption coefficient (solid line) obtained as described in the text. (b) Experimental (symbols) and calculated (solid line) ratios of the absorption coefficients at different energies (8.3, 8.4 keV off-resonance and 8.352 keV at-resonance).

atoms in the unit cell or only from a smaller number. Our strategy was to measure a number of main reflections with no Ni contribution, because according to Eqs. (3.44), (3.43) and (3.42), for all the main reflections with no Ni contribution, the ratios of the intensities (corrected for Lorentz factor) at different energies (E1, E2 and E3) give us the experimental ratios of the absorptions. At this point we define the following absorption ratios: $R1_{exp} = I_{E1}/I_{E2}$, $R2_{exp} = I_{E1}/I_{E3}$ and $R3_{exp} = I_{E2}/I_{E3}$). In total we measured 9 main reflections at three energies, two off resonance E1 = 8.3 keV, E3 = 8.4 keV and one close to the resonance E2 = 8.352 keV. From all these, only two reflections, (2, -1, 7) and (2, -1, 5), were measured for the whole energy range in order to test the absorption model. Next, we calculated the absorbtion coefficients A_{eff} at E1, E2 and E3 and using these values we calculated further the theoretical ratios of absorptions, $R1_{the}$, $R2_{the}$ and $R3_{the}$ using the numerical Monte Carlo integration method, by taking into account the orientation of the sample with respect to the incident and scattered beams, the calculated value for $\mu(E1)$, the experimentally obtained values $\mu(E2)_{temp}$ and $\mu(E3)_{temp}$ in the first step and the experimentally measured sample dimensions ($R_{exp} \sim 35\mu m$, $t_{exp} \sim 20\mu m$; the theoretical ratios were compared with the ex-

perimental ones and the agreement between them was not acceptable. Further we tried to obtained the effective dimensions of the cylinder (from fits of the theoretical ratios to the experimental ones) in order to get a better agreement between the the theoretical and experimental ratios. Analyzing the effective path of the beam through the sample for different orientations corresponding to the measured reflections, we observed that for some reflections the absorption coefficient is sensitive just to the thickness of the sample t, others are sensitive only to the radius R, and others to both R and t. We calculated the theoretical ratios of the absorptions, R_{the} and we compared them with the experimental ratios, R_{exp} (for all 9 main reflections with no Ni contribution) in a fitting function where the input parameters are the sample size (R, t). We found a solution (R_{temp}, t_{temp}) which give a much better agreement than the previous solution (R_{exp}, t_{exp}).

When we extracted the sample dimensions, we were using the temporary linear absorption coefficients obtained from the transmission measurements on powder. In order to optimize all parameters obtained experimentally we constructed a fitting function where we include both steps described in the previous paragraphs in order to obtain improved values for the the energy dependence of the linear absorption coefficient and the sample dimensions. The starting parameters for this fitting function were $\mu(E)_{temp}$ and (R_{temp}, t_{temp}).

From the final fits, we observed that the linear absorbtion coefficient μ shown in Figure 4.8 a) (solid line) and the effective thickness t = 18 μm and radius R = 34 μm gave the best fit between the calculated and experimental absorbtion ratios, see Figure 4.8 b). All the measured data was further corrected for absorption using the Monte Carlo code with fixed: effective radius and thickness of the sample, orientation of the sample with respect to the incident and scattered beam and experimentally-estimated linear absorption coefficient over the whole energy range. The accuracy of the absorption correction procedure is shown in Fig. 4.9; the raw intensity of the (2, -1, 7) and (2, -1, 5) main reflections is shown in panel (a); the intensity after absorption corrections is shown in panel (b). We observe from panel (b) that the intensity of the main reflections is nearly constant

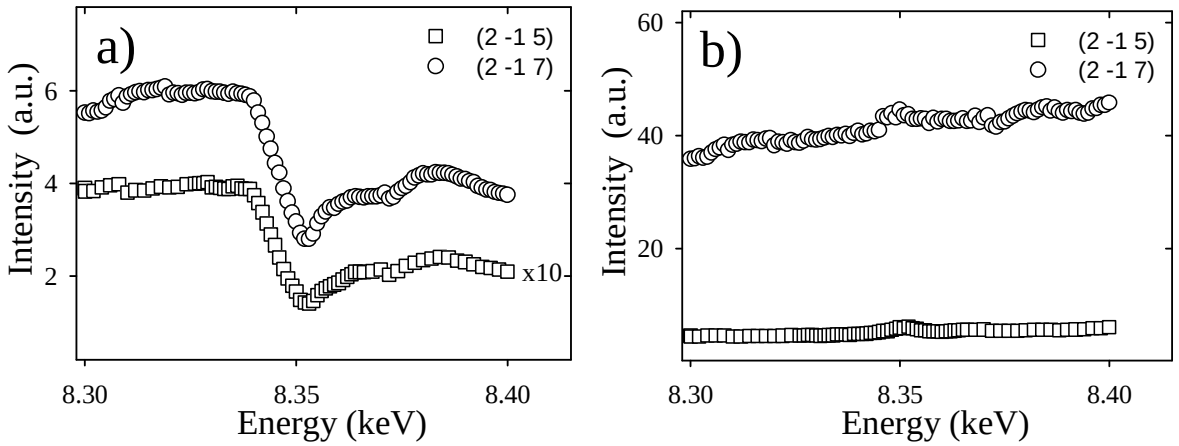

Figure 4.9 (a) Energy dependence of the raw intensity of the reference main reflections (2, -1, 7) and (2, -1, 5); the structure factors have no Ni contribution and the change in the intensity vs. energy is due only to the absorption effects. (b) Raw intensity corrected for absorption effects showing a linear energy dependence as expected for reflections with no Ni contributions.

(to within 10%) as expected for reflections which have no Ni contribution to the structure factor. To put the structure factors in absolute units of electrons, we extracted the absolute scaling constant C, by comparison of the experimental structure factors with the calculated structure factors at two energies, 8.3 keV and 8.352 keV. In Fig. 4.10 we show the agreement between the calculated and experimental structure factors off resonance, at 8.3 keV. Using the scale constant, the calculated Lorentz factors and absorbtion coefficient vs. energy, we have extracted the energy dependence of the experimental structure factors squared in absolute units of electrons squared, see Fig. 4.12 (open circles).

4.6 Data analysis

We measured three different families of supercell reflections in the energy range 8.3-8.4 *keV*, in order to probe the electronic states of Ni ions with different phase factors for the different Ni sites.

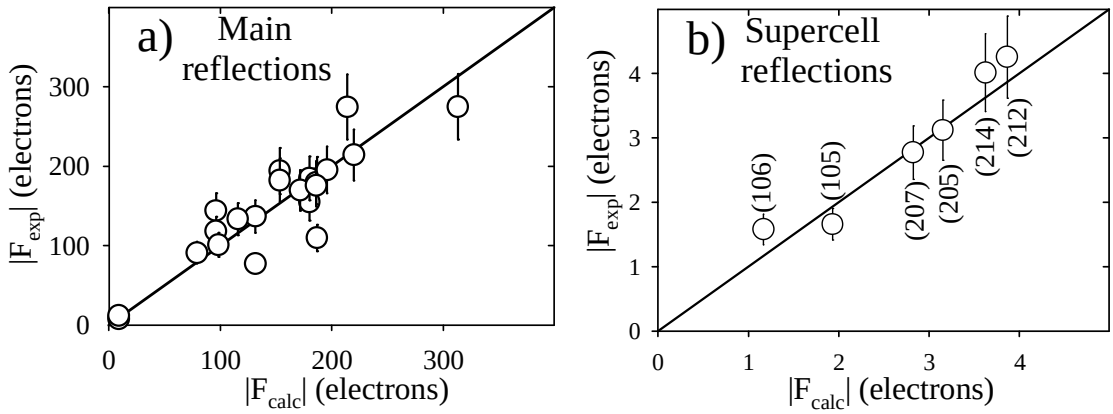

Figure 4.10 Observed vs. calculated structure factors for main (a) and supercell (b) reflections off-resonance (8.3 KeV). Solid line is guide for the eye.

The analytical formulas for the measured $|F|^2$ are given below.

$$|F_{109}|^2 = 3[\Delta f_{Ni}^{Thomson}(|\mathbf{Q}|) + \Delta f_{Ni}^{'}(E) + c_{109} \cdot f_{O}^{Thomson}(|\mathbf{Q}|)]^2 + 3[\Delta f_{Ni}^{''}(E)]^2 \tag{4.1}$$

$$|F_{203}|^2 = 3[\Delta f_{Ni}^{Thomson}(|\mathbf{Q}|) + \Delta f_{Ni}^{'}(E) + c_{203} \cdot f_{O}^{Thomson}(|\mathbf{Q}|)]^2 + 3[\Delta f_{Ni}^{''}(E)]^2 \tag{4.2}$$

$$|F_{105}|^2 = 3[\Delta f_{Ni}^{Thomson}(|\mathbf{Q}|) + \Delta f_{Ni}^{'}(E) + c_{105} \cdot f_{O}^{Thomson}(|\mathbf{Q}|)]^2 + 3[\Delta f_{Ni}^{''}(E)]^2 \tag{4.3}$$

$$|F_{205}|^2 = 3[\Delta f_{Ni}^{Thomson}(|\mathbf{Q}|) + \Delta f_{Ni}^{'}(E) - c_{205} \cdot f_{O}^{Thomson}(|\mathbf{Q}|)]^2 + 3[\Delta f_{Ni}^{''}(E)]^2 \tag{4.4}$$

$$|F_{207}|^2 = 3[\Delta f_{Ni}^{Thomson}(|\mathbf{Q}|) + \Delta f_{Ni}^{'}(E) - c_{207} \cdot f_{O}^{Thomson}(|\mathbf{Q}|)]^2 + 3[\Delta f_{Ni}^{''}(E)]^2 \tag{4.5}$$

$$\begin{aligned} |F_{106}|^2 =& [f_{Ni1}^{Thomson}(|\mathbf{Q}|) - 2f_{Ni2}^{Thomson}(|\mathbf{Q}|) + f_{Ni3}^{Thomson}(|\mathbf{Q}|) + f_{Ni1}^{'}(E) - 2f_{Ni2}^{'}(E) + f_{Ni3}^{'}(E) + \\ &+ c_{106} \cdot f_{O}^{Thomson}(|\mathbf{Q}|)]^2 + [f_{Ni1}^{''}(E) - 2f_{Ni2}^{''}(E) + f_{Ni3}^{''}(E)]^2 \end{aligned} \tag{4.6}$$

where $\Delta f_{Ni}^{'}(E) = f_{Ni1}^{'}(E) - f_{Ni3}^{'}(E)$, $\Delta f_{Ni}^{''}(E) = f_{Ni1}^{''}(E) - f_{Ni3}^{''}(E)$ and c_{hkl} are positive structural constants. We observe from these equations that there are two main contributions which give rise to scattering intensity for the supercell reflections: one contribution comes from x-ray scattering by the O displacements (energy independent) and the other comes from x-ray scattering by the Ni ions (energy dependent). The scattering from O displacements is represented by the

terms like $f_O^{Thomson}(|\mathbf{Q}|)$ [see first bracket in Eqs. (4.1)-(4.6)], whereas scattering from the Ni ions comes through the energy-independent factor $f_{Ni\xi}^{Thomson}(|\mathbf{Q}|)$ and energy-dependent terms $f'_{Ni\xi}(E)$ and $f''_{Ni\xi}(E)$, where $\xi = 1,2,3$. In the ideal structure oxygens are in the high-symmetry position with no displacement and all Ni sites are equivalent, and as a consequence all structure factors of the supercell reflection cancel out. If there is a small displacement of the O ions and if we assume hypothetically that the Ni electronic structure doesn't change ($f_{Ni\xi}^{Thomson}(|\mathbf{Q}|)$, $f'_{Ni\xi}(E)$ and $f''_{Ni\xi}(E)$ for different sites are identical), all the structure factors become non-zero due to x-ray scattering from the oxygens, which is energy independent. Looking at measured intensity vs. energy (Figure 4.12), we observe a strong modulation of intensity with energy which is due to the fact that the anomalous atomic scattering factors for Ni1 (inside the expanded octahedra) and Ni2,3 (inside the contracted octahedra) have a different behavior vs. energy. Using the system of equations, Eqs. (4.1)-(4.6) together with f''_{total} extracted from the linear absorption coefficient, Eq. (3.49) we obtain f'(E) and f"(E) for the Ni1 and Ni3 sites, by the method described below.

Before explaining the method we have to discuss Q-dependent terms in the equations Eqs. (4.1)-(4.6). From Fig. 4.10(b), we see that the fit of the experimental $|F|^2$ for the supercell reflections is good to within 10%. If in our equations, we use the calculated scattering factors at energies off resonance we introduce discrepancies which can influence in a biased way the extraction from the data of f'(E) and f"(E). To avoid the propagation of these errors, we replace in the Eqs. (4.1)-(4.6), the Q-dependent terms by the corresponding experimental values extracted from the $|F|^2$ at 8.3 keV (i.e. Q-dependent term for the (2, 0, 5) reflection is $f_{Ni1}^{Thomson}(|\mathbf{Q}|)$ - $f_{Ni3}^{Thomson}(|\mathbf{Q}|)$ - c205 $\cdot f_O^{Thomson}(|\mathbf{Q}|)$).

Using the modified equations, we solve the system of equations, where the unknown parameters are f' and f" for Ni1 and Ni3; we subtract the $|F|^2$ of different families (i.e. $|F|^2_{109}$-$|F|^2_{105}$) and from these subtractions we obtain experimental values for $\Delta f'_{Ni} = f'_{Ni1}(E) - f'_{Ni3}(E)$; replacing the calculated average values for $\Delta f'_{Ni}$ back in the $|F|^2$ formulas we are able to extract

$\Delta f''^2_{Ni} = [f''_{Ni1}(E) - f''_{Ni3}(E)]^2$; using f''_{total} and $\Delta f''^2_{Ni}$ we solved the system formed by these two equations and we obtained a few possible solutions for $(f''_{Ni1-temp}, f''_{Ni3-temp})$. For each solution $(f''_{Ni1-temp}, f''_{Ni3-temp})$ we use the Kramers-Kronig relationships $Eq.$ (3.42) to obtain the corresponding $(f'_{Ni1-temp}, f'_{Ni3-temp})$. The $|F|^2$ were calculated for each solution $(f'_{Ni1-temp}, f'_{Ni3-temp}, f''_{Ni1-temp}, f''_{Ni3-ten}$ using $Eqs.$ (4.1)-(4.6) and compared to the experimental $|F|^2$. We found that there is a unique solution which gives an acceptable agrement between the experimental and calculated structure factors squared (we call this temporary solution). By analyzing the first neighborhood of the $Ni2$ and $Ni3$ ions we observe the we can make the following assumption: $f''_{Ni2-temp} = f''_{Ni3-temp}$. To obtain the best solution for the resonant scattering factors we constructed a fitting procedure

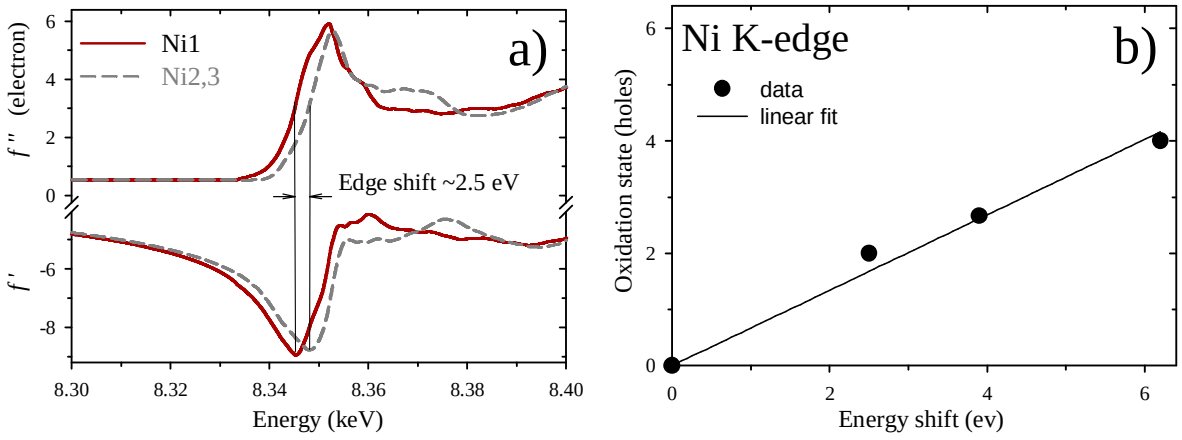

Figure 4.11 (a) Energy -dependence of empirically-extracted real and imaginary anomalous atomic scattering factors for Ni1 (solid line) and Ni2,3 (dashed line) obtained from a best fit to the measured spectra such as in Fig. 4.12. (b) shift of the Ni K-edge energy vs. oxidation state taken from [33].

where the input parameter was $f''_{Ni1-temp}$. The steps for the fitting procedure are: the curve $f''_{Ni1-temp}(E)$ is changed a little bit, then $f''_{Ni3-temp}(E)$ is obtained using f''_{total}; in the following step $f'_{Ni1-temp}(E), f'_{Ni3-temp}(E)$ curves are obtained using the Kramers-Kronig relationships. Finally the structure factors squared $|F|^2(E)$ were calculated using Eqs. (4.1)-(4.6) and they were compared with the experimental ones. This procedure was done until we obtained the best agree-

ment between the calculate and experimental |F|^2; we call best agreement, the fit which minimizes the following function: $\sum[|F|^2_{exp} - |F|^2_{the}]^2$. The solution, $(f'_{Ni1}, f'_{Ni3}, f''_{Ni1}, f''_{Ni3})$ which gives the best agreement with the data is shown in Fig. 4.11 a).

4.7 Discussions

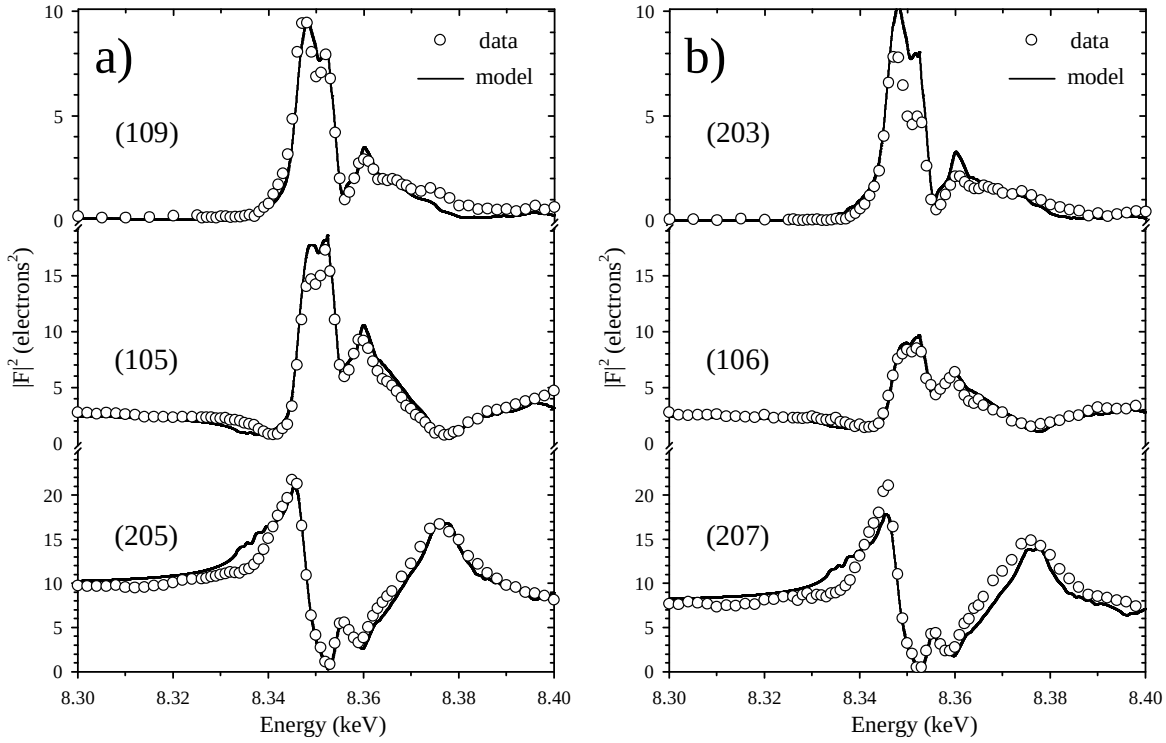

Figure 4.12 Structure factors of several reflection at 300 K as a function of x-ray energy near the Ni K-edge. The rich structure arises from interference scattering from the distinct Ni sites [Fig. 4.1] with energy-shifted anomalous atomic scattering factors shown in [Fig. 4.11]. Pre-edge values of the structure factors in middle and bottom panels is due to the scattering from oxygen displacements.

In total we measured three different families of supercell reflections: 1) the energy independent contribution to the $|F|^2$ is almost zero, this is the case for (1, 0, 9) and (2, 0, 3) supercell reflections; 2) the energy independent contribution to the structure factors has a finite positive value, this is the

case for (1, 0, 5) and (1, 0, 6); 3) the energy independent contribution to the structure factors has a finite negative value, this is the case for (2, 0, 5) and (2, 0, 7) supercell reflections. In Fig. 4.12 we show the experimental (open circles) and the calculated (solid line) structure factors squared. From this figure we observe that using the experimentally extracted curves for $(f'_{Ni1}, f'_{Ni3}, f''_{Ni1}, f''_{Ni3})$, we obtained a good agrement between the experiment and calculations and we can reproduce all the main features seen in the experimental data around the edge. This give us the confidence that we can use the the energy dependent $(f'_{Ni1}, f'_{Ni3}, f''_{Ni1}, f''_{Ni3})$ curves to extract the edge energy for the Ni ions at different sites. The edge energy was chosen at the energy where $f'(E)$ is minimum (see Figure 4.11) or where we have the first maximum in the first derivative of the $f''(E)$ curves (see Figure 4.16). Based on this criteria, we can see that there is a shift of about ~ 2.5 eV between the edges for Ni1 and Ni3 ions, which suggest that there is a change in the edge energy between the two Ni sites. Using experimental results for the edge shift vs. oxidations states, which shows that there is linear dependence between the Ni valence and the K-edge energy shift [33], we can estimate a maximum charge disproportionation of about 1.5 electrons between Ni1 and Ni3 ions. However, this needs further clarification because the edge shift measured experimentally is a combination of two effects. As described in the previous sections,(see Fig. 4.2), during the microscopic process in the resonant scattering, an electron from the core 1s-level is promoted to the empty 4p-states above the Fermi level, so the K-edge energy is determined by the position of the 1s-core level and the 4p-states with respect to the Fermi energy. In the high temperature phase all the Ni ions are sitting at equivalent positions (ideal-octahedra), so the energy for the 1s$\longrightarrow$4p transition is the same for all ions. When we lower the temperature, the structure distorts around T_S = 365 K and the Ni sites become inequivalent; one third of the ideal-octahedra expand and two thirds of them contract when we cross the structural transition temperature. The 4p-states for Ni ions inside the expanded and contracted octahedra will change their position in energy with respect to the Fermi energy because of the different hybridization with the neighboring oxygen ions. Examples where the edge shift

is different due to the distortions of the first neighborhood and not charge disproportionation have been published in the literature [39]. From this we learn that the edge shift between Ni1 and Ni3 ions could come from the oxygen distortions and not charge disproportionation between these two sites.

The proposal for charge disproportionation at Ni sites in $AgNiO_2$ comes from neutron diffractions experiments, which found that at lower temperatures than T_S the system order magnetically with a large magnetic moment at the Ni1 sites and no magnetic moment at the Ni2,3 sites. This suggested that at the structural transition electrons are transferred from the Ni2,3 sites to the Ni1 sites, so that the Ni1 sites (expanded octahedra) become e^- rich compared to Ni2,3 sites (contracted-octahedra). The proposed model for the charge disproportionation was supported by band structure calculations [27].

We see from these simple arguments that there are two possible models that could explain the experimental edge-shift. The first scenario is that the edge-shift is due only to the oxygen distortions (different shift of the 4p-states with respect to the Fermi energy) and at the structural transition there is no charge transfer between the Ni1 and Ni2,3 sites. The second scenario is that the edge-shift is due to the oxygen distortions and charge transfer between the Ni sites at the structural transition (see Figure 4.2). In order to find the correct model we have calculated the energy of the 1s-core level and the energy of the 4p-states with respect to the Fermi energy, in the charge ordered state. The results of the theoretical calculations are discussed in the following section. From $Eq.$ (4.6) we see that the $|F|^2$ for the (1, 0, 6) supercell reflection depends on the anomalous scattering factors from the all inequivalent Ni sites (Ni1, Ni2 and Ni3); inspection of the first neighborhood for Ni1,2,3 suggest that Ni2 and Ni3 are in very similar electronic state; assuming that Ni2 and Ni3 have the same electronic configuration in the charge ordered state, we calculated the structure factors for this reflection using the same anomalous scattering factors for Ni2 and Ni3; the result is given in Fig. 4.12; we can see that the agreement between the

experimental and calculated $|F|^2$ for the (1, 0, 6) supercell reflection is good and we conclude that Ni2 and Ni3 are in a very similar charge state. This argument justifies our assumption made during the fitting procedure used to obtain the resonant scattering factors.

4.8 Tensor analysis and band structure calculations

In section 3.2, we showed that the atomic scattering factor is a second-rank tensor which in the most general case has nine independent components that reduce upon taking into account the local site symmetry of the ion site. Using the space group of $AgNiO_2$, the atomic scattering tensor $\hat{f}_{atomic}$ for Ni ions, expressed in an orthogonal reference system (**x**, **y**, **z**) connected to the crystal, has the following form:

$$\hat{f}_{atomic} = \begin{pmatrix} f_\perp & 0 & 0 \\ 0 & f_\perp & 0 \\ 0 & 0 & f_\parallel \end{pmatrix} = f_\perp \begin{pmatrix} 1 & 0 & 0 \\ 0 & 1 & 0 \\ 0 & 0 & 1 \end{pmatrix} + \begin{pmatrix} 0 & 0 & 0 \\ 0 & 0 & 0 \\ 0 & 0 & \Delta f_{anis} \end{pmatrix} \tag{4.7}$$

When we take into account the tensorial form of the atomic scattering factor, the structure factor becomes a tensor and thus the scattered intensity depends on the orientation of the crystal with respect to the polarization of the incident and scattered *XR* beams. The direction of linear polarization of the incident *XR* beam is denoted by unit vectors, which are always expressed in the orthogonal (**x**, **y**, **z**) reference system. Thus, our reference frame is the crystal, not the laboratory, and from this point of view, changing the crystal orientation means a change in the direction of the polarization. Thus, each reflection will have a different polarization. We show in section 3.3 that when the atomic scattering factor is a scalar quantity, the scattered intensity is proportional $|F|^2$ and the polarization factor $P = 1$. When the atomic scattering factor is a tensor, the scattered intensity is proportional to $|\varepsilon_{in}^* \cdot \hat{F} \cdot \varepsilon_{sc}|^2$, where ε_{in} and ε_{sc} are the unit vector polarizations of the incident and scattered XR beam and $\hat{F}$ is the structure factor tensor. Instead of using arbitrary

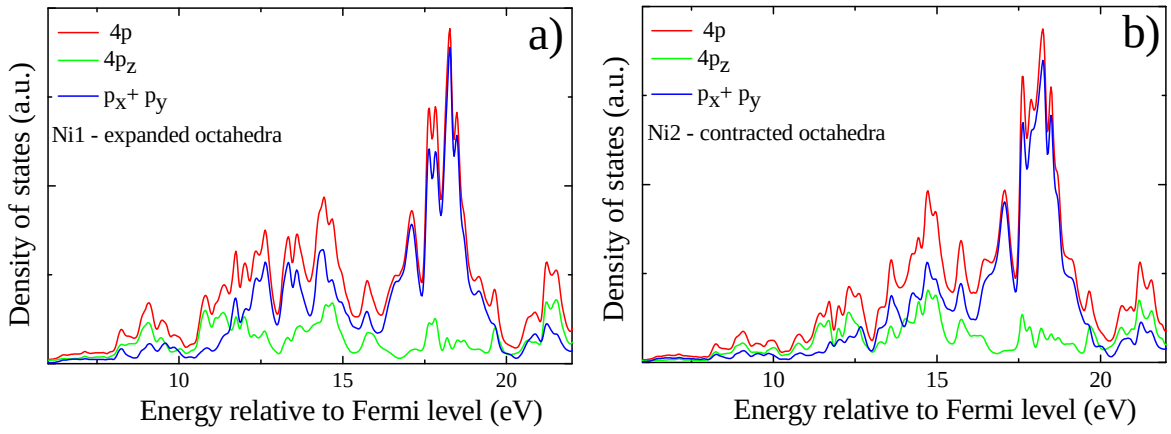

Figure 4.13 LDA calculation of density of states (DOS) for final electron states. The difference between the $p_x = p_y$ and p_z DOS is giving us two independent components of the atomic scattering tensor.

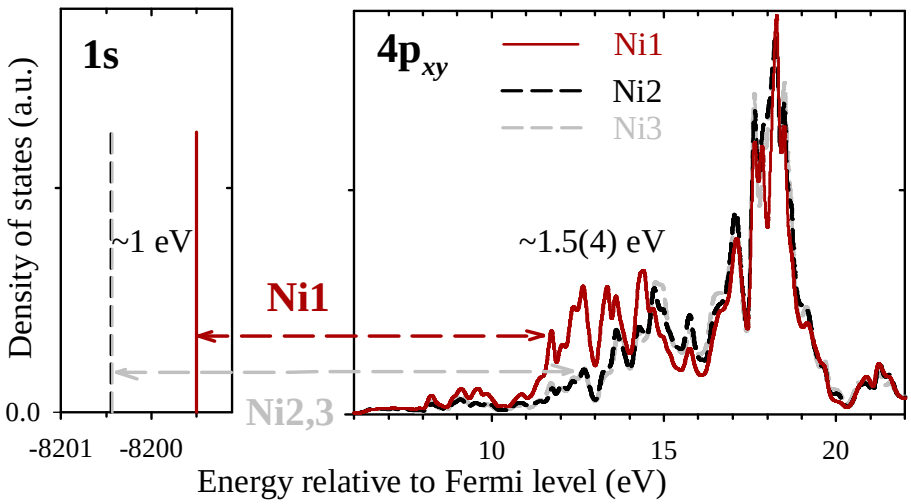

Figure 4.14 LDA calculation of density of states (dos) for the initial and final electron states in the transition $1s \rightarrow 4p_{xy}$ (horizontal dashed arrows) probed by the present resonant Ni K-edge scattering experiments. Solid/dashed curves show the dos for electron-rich/depleted Ni1/Ni2,3 sites. Due to fewer electrons in Ni2,3 the binding energy per electron is stronger and the $1s$ core level is deeper in energy (dashed vertical line in left panel) compared to Ni1. The closer proximity of the oxygens promotes a stronger hybridization with the O $2p$ levels for Ni2,3 sites and this pushes the $4p_{xy}$ band higher in energy compared to the expanded Ni1 site. The combined effect is a predicted transition energy shift of $2.5(4)$ eV higher for Ni2,3 compared to Ni1.

polarizations ε_{in} and ε_{sc} we use the conventional σ and π polarizations defined in section 3.1. The linear polarization of the incident beam, which is perpendicular to the scattering plane (see section 4.4), is expressed in the crystal reference frame (**x**, **y**, **z**) and is called σ_{in}-polarization. We also define the polarizations of the scattered beam as σ_{sc} when the polarization is perpendicular to the scattering plane and as π_{sc} when the polarization is in the scattering plane perpendicular to $\mathbf{k}_{sc}$. For an incident XR beam with σ_{in} polarization ($I_{\sigma_{in}}$), the scattered intensity can have σ_{sc} ($I_{\sigma_{in}\sigma_{sc}}$) or π_{sc} ($I_{\sigma_{in}\pi_{sc}}$) polarizations; we can now write the total scattered intensity as:

$$I_{sc} = I_{\sigma_{in}\sigma_{sc}} + I_{\sigma_{in}\pi_{sc}} \tag{4.8}$$

where

$$I_{\sigma_{in}\sigma_{sc}} \sim |\sigma^*_{sc} \cdot \hat{F} \cdot \sigma_{in}|^2 \quad I_{\sigma_{in}\pi_{sc}} \sim |\pi^*_{sc} \cdot \hat{F} \cdot \sigma_{in}|^2 \tag{4.9}$$

To see the distribution of the scattered intensity between $\sigma\sigma$ and $\sigma\pi$ polarizations we have calculated the analytical form of the $|\sigma^*_{sc} \cdot \hat{F} \cdot \sigma_{in}|^2$ and $|\pi^*_{sc} \cdot \hat{F} \cdot \sigma_{in}|^2$ terms for the (109) supercell reflection. Using

$$\sigma_{in} = \begin{pmatrix} \sigma^x_{in} \\ \sigma^y_{in} \\ \sigma^z_{in} \end{pmatrix} \quad \sigma_{sc} = \begin{pmatrix} \sigma^x_{in} \\ \sigma^y_{in} \\ \sigma^z_{in} \end{pmatrix} \quad \pi_{sc} = \begin{pmatrix} \pi^x_{in} \\ \pi^y_{in} \\ \pi^z_{in} \end{pmatrix} \tag{4.10}$$

for the polarizations of the incident and scattered beams, we obtain the following formulas for the structure factors squared:

$$\begin{aligned} |\sigma^*_{sc} \cdot \hat{F} \cdot \sigma_{in}|^2_{(109)} =& 3[(\Delta f^{Thomson}_{Ni} + f'_{\perp-Ni1} - f'_{\perp-Ni3} + \sigma^z_{in} \cdot \sigma^z_{in} \cdot (\Delta f'_{anis-Ni1} - \Delta f'_{anis-Ni3}) + \\ & + c_{109} f^{Thomson}_{O})^2 + (f''_{\perp-Ni1} - f''_{\perp-Ni3} + \sigma^z_{in} \cdot \sigma^z_{in} \cdot (\Delta f''_{anis-Ni1} - \Delta f''_{anis-Ni3}))^2] \end{aligned} \tag{4.11}$$

$$|\pi^*_{sc} \cdot \hat{F} \cdot \sigma_{in}|^2_{(109)} = 3(\sigma^z_{in} \cdot \pi^z_{sc})^2[(\Delta f'_{anis-Ni1} - \Delta f'_{anis-Ni3})^2 + (\Delta f''_{anis-Ni1} - \Delta f''_{anis-Ni3})^2] \tag{4.12}$$

$\sigma^z_{in} \cdot \sigma^z_{in}$ and $(\sigma^z_{in} \cdot \pi^z_{sc})^2$ coefficients that prefactor the anisotropic part in the above equations, have been evaluated for all the supercell reflections we measured in our experiment and they have values

smaller than 10^{-2}. Based on these arguments we can safely conclude that during the experiment we are only sensitive to the $f_\perp$ components of the atomic scattering tensor. The scalar atomic scattering factors, f extracted from the experiment (see Figure 4.11), are equivalent to $f_\perp$.

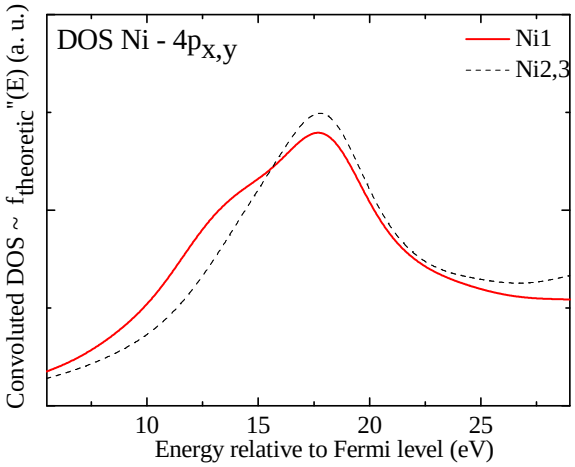

Figure 4.15 . Convolution of the density of states with a Lorentzian to take into account the lifetime of the excited state. The value of the Lorentzian width is optimized to obtain the best agreement between the theoretical and experimental spectra in the vicinity of the absorption edge, i.e. in the region from -10 to 15 eV around the first inflection point of the edge. The value obtained for the FWHM is 4.5 eV. The calculations don't take into account that the final-state life time is energy-dependent

To show that the atomic scattering factor is a tensor and in order to compare the empirically-extracted edge shift, Figure 4.11, with theoretical calculations for the CO state, we have computed using LDA band-structure calculations described in [27], the shift in the energy levels probed by the resonant experiments, namely the core 1*s* level and empty 4p band. In Figure 4.13 we show the total, $p_x + p_y$ (p_x=p_y by symmetry) and p_z density of states for Ni1 and Ni2; from the difference between the p_x=p_y and p_z DOS and Eq. (3.25) we can conclude that the atomic scattering factor is a tensor (having only three non-zero components) with two independent components as expected from the symmetry analysis.

The results of the theoretical calculations for energy positions of the 1s and 4p states, are shown

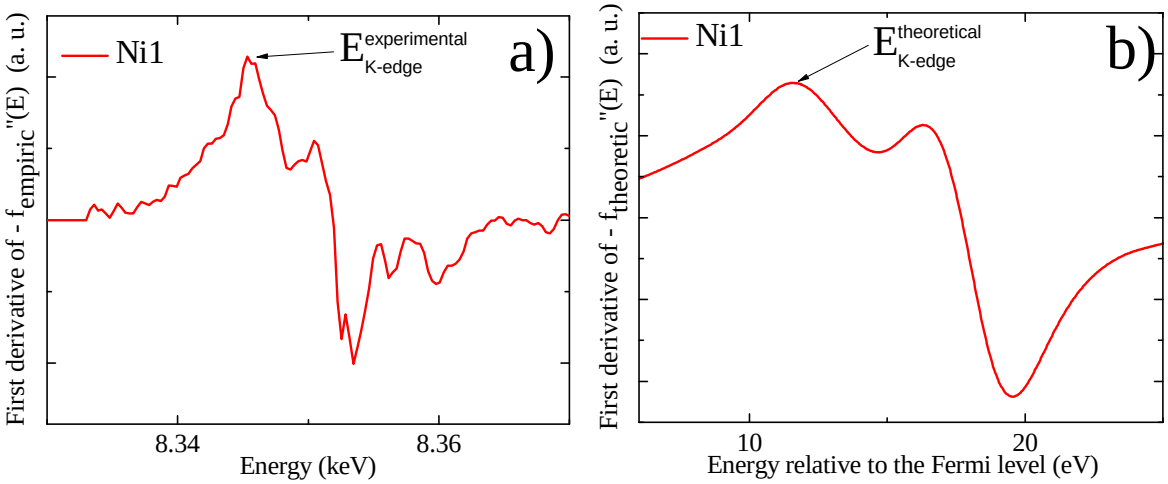

Figure 4.16 First derivative of the imaginary part of the atomic scattering factors f" for Ni1 ions; the first maximum in the first derivative is identified with the absorption edge; a) first derivative of the empirically extracted f", see Figure 4.11; b) first derivative of the theoretically calculated f", see Figure 4.15.

in Figure 4.14. Only the $4p_{xy}$ (degenerate) bands are shown as only transitions from 1s to those bands are induced by the in-plane component of the scattering factor $f_{\perp}$, as probed in the present experiments. For the electron-rich Ni1 site, the 1s core level is higher in energy, as the binding energy of the core electrons is smaller due to inter-electron Coulomb repulsion with the extra 3d electron, and the $4p_{xy}$ bands are lower in energy, as the hybridization with the oxygen 2p band is weaker as oxygens are displaced further away (compared to Ni2,3). The combined effect is an edge shift for the transition 1s - $4p_{xy}$ for Ni1 compared to Ni2,3 of +2.5(4) eV (estimation of the uncertainty depends on the precise definition of the lower boundary edge for the 4p band, see Figure 4.16). The experimentally extracted shift of 2.5(3) eV compares well with the theoretical prediction and shows that both contributions to the edge shift need to be included to explain the data (the core level shift due to CO and the oxygen hybridization of the excited 4p band). In Figure 4.15 we show the convoluted density of states with a Lorentz function (we work in the constant matrix elements approximation) to take into account the life time of the excited state. The FWHM

of the Lorentz function was optimized until the best agreement with the experimental data was obtained (for comparison see Figures 4.11 and 4.15).

4.9 Temperature dependence

In order to learn more about the temperature dependence of the charge order state and about its relation with the structural transition, we have measured the temperature dependence of reflections which are mostly sensitive to the charge order state and reflections which are mostly sensitive to the oxygen distortions. We also measured the energy profile of reflections (from two different families) at two different temperatures to learn more about the type of the phase transition. In Figure 4.17 we show the order parameter extracted from two supercell reflections. The reflections were measured at fixed energy 8.347 keV, close to the resonance energy, with increasing temperature. From these results, we learn that there is strong correlation between the two states and that the transition to the charge order state happens at the same time with the structural transition, as predicted by the band structure calculations. The transition temperature obtained from the order parameter measured in this experiment is slightly smaller than the transition temperature extracted from neutron diffraction measurements of the displacement order parameter due to the sample heating in the beam. In Figure 4.18 we show the temperature dependence of the profile for the structure factors squared of two different supercell reflections (black circles and blue squares): (1, 0, 9) which is directly related to the charge disproportionation (it has no contribution from the oxygen displacements out of the resonance regime) and (1, 0, 5) which has contribution from both, charge disproportionation and oxygen displacements.

From a careful inspection of the supercell reflections profile we observe that the only differences between the profiles at the two different temperatures is a scale constant; the shape of the profile is almost the same, Figure 4.18. At 300 K the charge order is saturated and the oxygen atoms

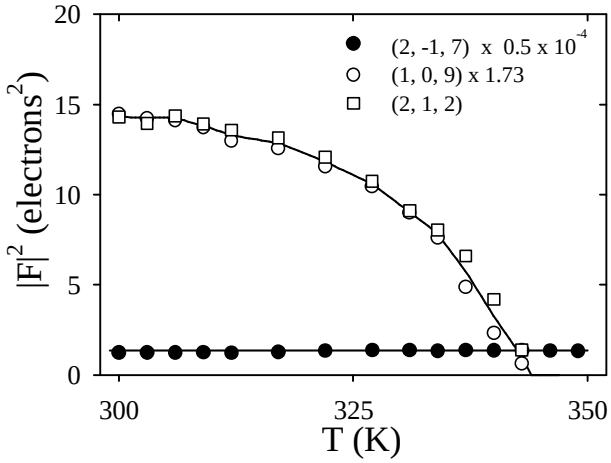

Figure 4.17 Order parameter of the oxygen displacement(open squares) and charge order (open circles) extracted from the (2, 1, 2) and (1, 0, 9) supercell refections; the solid circles show the temperature dependence of the (2, -1, 7) main reflection. The solid lines are guide for the eye.

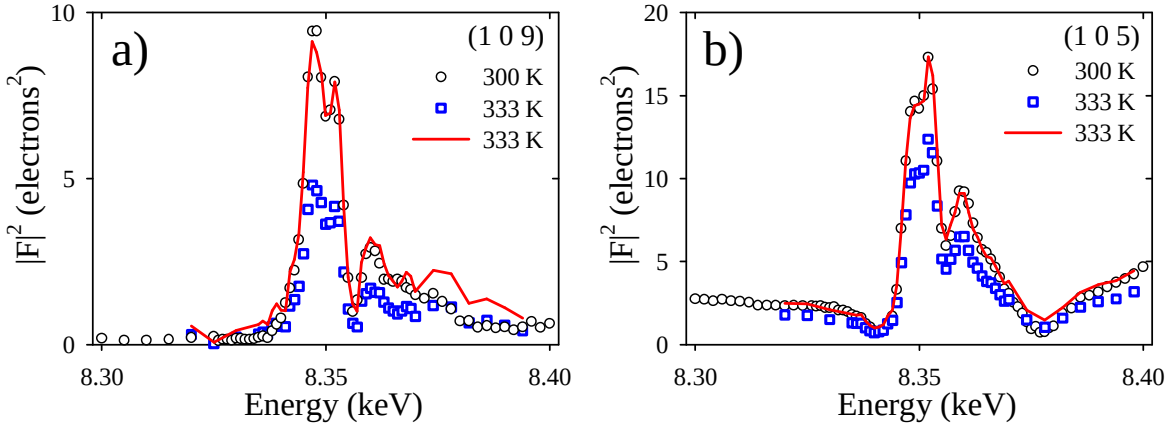

Figure 4.18 Temperature dependence of the experimental structure factors vs. energy for the (a) charge order (1, 0, 9) and (b) oxygen displacements (1, 0, 5) supercell reflections. The red lines represent the 333 K data (green squares) multiplied by 1.4 for (1, 0, 9) and 1.9 for (1, 0, 5) supercell reflections.

are in equilibrium at the maximum displacement in the whole sample volume; at 333 K when we are closer to the transition, a fraction of the volume sample is in the normal state (with the high temperature crystal structure). This scenario will give us a decrease in intensity and no change in the profile shape. The case mentioned above is consistent with a first order phase transition, as it includes a coexistence of two phases.

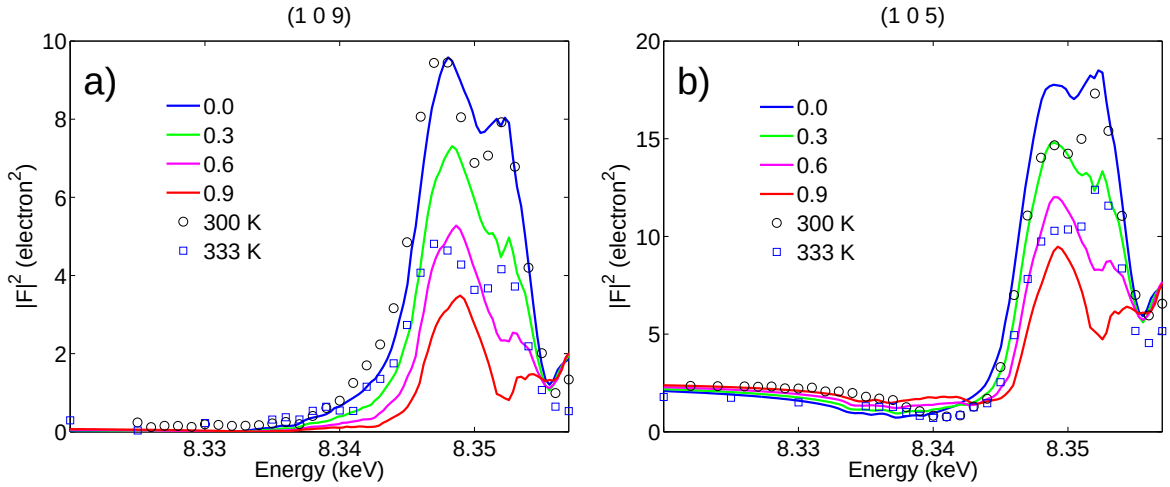

Figure 4.19 Calculations of the $|F|^2$ to simulate the temperature dependence of the experimental structure factors vs. energy for the (a) charge order (1, 0, 9) and (b) oxygen displacements (1, 0, 5) supercell reflections. Blue color (zero shift) represents the calculations of the structure factors using f''_{Ni1-0} and f''_{Ni3-0} curves which are equivalent with the curves f''_{Ni1} and f''_{Ni3} curves from Figure 4.11; red color represents the calculations of the structure factors using $f''_{Ni1-0.9}$ and $f''_{Ni3-0.9}$ curves which are obtained by shifting the f''_{Ni1} to right by 0.9 eV and f''_{Ni3} to left by 0.45 eV. Symbols represent experimental data.

A second scenario would be that the transition is of second order. In this case at 300 K the charge order is saturated and the oxygen atoms are in equilibrium at the maximum displacement in the whole sample volume; while increasing the temperature, the charge disproportionation and, the oxygen displacements are decreasing continuously and at the transition temperature T_S, the oxygen displacement would be zero and all the Ni ions are equivalent. Assuming a linear relation between the amount of charge disproportionation and the shift of the f'' curves for the Ni1 and Ni3

ions, we calculated the profile of the supercell reflections for different shifts of the f''; the results of such calculations for different shifts are shown in Figure 4.19. We see that these calculations also give a decrease in intensity without a significant change in the profile for energies close to the edge energy. The assumption made in order to do these calculations was that the profile of the f'' for the two Ni ions does not change with the increase of temperature. These arguments show that the data is consistent with both models; further measurements are needed in order to distinguish between the two.

4.10 Conclusions

In conclusion, we have reported resonant X-ray scattering measurements on a single-crystal of the triangular lattice metal $2H$-$AgNiO_2$, which undergoes a spontaneous honeycomb charge order pattern. We have observed a large resonant enhancement of charge order reflections as the x-ray energy was tuned through the Ni K-edge and the rich structure as a function of energy can be quantitatively accounted for by interference scattering from the electron-rich and -depleted Ni sites. We did all the necessary corrections to bring the data in absolute units and we extracted the energy dependence of the atomic resonant scattering factors for the three distinct Ni ions which gave the best fit to the data. Taking into account the full tensor component of the anomalous scattering factors and the hybridization with the oxygen orbitals we obtained a good agreement between the empirically extracted edge shift between the distinct Ni sites and the microscopic band-structure calculations of charge ordering. Measurements of the order parameters shows that there is a strong correlation between the charge order transition and the structural transition, as predicted by band structure calculations. Measurements and calculations of the energy profile at different temperatures show that both models, first order and second order phase transition, are consistent with the data.

Chapter 5

Magnetic ground state and crystal field energy levels of Co^{2+} ion in the Ising ferromagnet $CoNb_2O_6$

This chapter reports a study of the magnetic ground state and excited energy levels of Co^{2+} ions in the strong easy-axis magnet $CoNb_2O_6$. This material has recently attracted interest as Co ions form nearly-decoupled ferromagnetic Ising chains with a sufficiently small exchange interactions such that the spontaneous long rage magnetic order can be suppressed in a quantum phase transition by a strong external transverse applied magnetic field. This is the first experimental realization of the quantum critical Ising chain. The aim of this chapter is to understand from a microscopic point of view the origin of the strong Ising-like anisotropy of the Co^{2+} ions and to determine the spin and orbital component of the magnetic ground state and of the excited levels, taking into account spin-orbit interactions and crystal field effects from the distorted O_6 octahedron surrounding the Co2+ ions. The crystal field is parameterized using the Steven's equivalent operator method and starting values for all the allowed crystal field parameters given the low local symmetry (mon-

oclinic C_2 point group) are obtained using a point charge model calculation. The obtained energy levels scheme is compared with the previously measured inelastic time-of-flight neutron scattering data on crystal field energy levels. A good agreement is found between the calculated and experimentally measured values of the excited energy levels, magnitude of the magnetic moment and the direction of the easy-axis.

5.1 Introduction

Ising magnets have been important in studies of thermally induced phase transitions partly due to much theoretical progress starting from Onsager (exact solution for the two dimensional Ising model [40]), and partly due to detailed experimental studies of a range of Ising-like magnets via neutron scattering, which have enabled detailed studies of critical scattering to be made and to test theoretical predictions [41]. More recently Ising magnets are attracting interest for the study of collective quantum effects introduced by an external magnetic field perpendicular to the Ising axis. The applied magnetic field allows quantum tunneling fluctuations between the up and down spin orientations and make fluctuations become sufficiently strong such that they "melt" the spontaneous long-range magnetic order in a continuous phase transition to a paramagnetic phase [42]. One of the theoretically most studied paradigms for such a quantum phase transition is the 1D ferromagnetic Ising chain in transverse field whose theoretical solution has inspired the general theory of quantum criticality. The insulating magnet $CoNb_2O_6$ has been proposed to be a good realization of a quasi-1D Ising ferromagnet, based on neutron scattering measurements observing sheets of diffuse scattering perpendicular to the chain direction [43]. Magnetic structure [44, 45], susceptibility measurements [46] and magnetization measurements [47] also show evidence for a strong Ising-like anisotropy with the easy axis in the crystallographic **ac**-plane. Recent neutron scattering measurements in applied magnetic field along b-axis, i.e. perpendicular to the Ising axis,

have observed that spontaneous magnetic order is suppressed in a continuous phase transition at a critical field of 5.5 T [48]. Detailed measurements of the spin dynamics show direct evidence for a transformation of quasiparticles across this critical point, between pairs of solitons (domain walls excitations interpolating between the two degenerate ground states in the ordered phase) and spin flip quasiparticles, a key prediction of 1D ising quantum criticality [48]. At the same time measurements of the spin excitation spectrum in zero field confirmed that the main Hamiltonian was that of Ising spins coupled ferromagnetically along the chain with a small (2%) interchain exchange and also showed evidence for significant ($\sim$15%) subleading interactions beyond the dominant Ising term $S_i^z S_{i+1}^z$ between the S^x and S^y spin components of the neighbouring spins on the same chain which affects the dispersion of solitons already in zero field.

The aim of the study reported here is to understand microscopically the origin of the dominant Ising like anisotropy and the strength and form of the subleading perturbations. The origin of the magnetic anisotropy is the spin-orbit coupling $\lambda\ \mathbf{L}\cdot\mathbf{S}$ [49] which prefers collinear arrangements of the total spin **S** and total orbital angular momentum **L**, where the orbital angular momentum of magnetic electrons is strongly affected by the crystal electric field potential created at the positions of the magnetic electrons by the surrounding negatively charged O^{2-} ligands [50]. Applying Hund's rules [51] to the Co^{2+} free ion (electronic configuration $3d^7$ in the last shell), to obtain the ground state that minimizes electron-electron interactions constrained by the Pauli principle leads to L = 3 and S = 3/2 for the total orbital and spin quantum numbers, giving in total a multiplet of $(2L + 1)(2S + 1) = 28$ states [52]. The orbital degeneracy $(2\,L + 1) = 7$ will be lifted when the magnetic ion is included in a crystal. For example the crystal electric field potential of an ideal O_6 octahedron with Co^{2+} ion in the center, lifts the orbital degeneracy of the free ion states of Co^{2+} ion and splits the orbital energy levels in a triplet, triplet and singlet (in order of increasing energy) [37], see Figure - 5.8. In $CoNb_2O_6$ the crystal electric field of the distorted O_6 octahedra completely lifts the orbital degeneracy and splits the orbital energy levels into 7 orbital singlets.

The crystal field of the distorted octahedra together with the spin-orbit coupling perturbation splits (and mixes) the 28 states of the multiplet and lifts the multiplet degeneracy into a set of Kramer doublets, where the remaining two-fold degeneracy of each level is due to the fact that there are odd number of electrons. In $CoNb_2O_6$, the O_6 octahedron is in fact strongly distorted from cubic symmetry, see Figure 5.2(a); the local symmetry is monoclinic (C_2 point group) with as many as 8 symmetry allowed terms (B_q^k) in the crystal field perturbation energy expansion in the basis of angular momentum operators as described later. Values for all these crystal field parameters are calculated in the point charge model (PCM) approximation B_q^k(PCM), where the electronic cloud of each of the surrounding oxygens is approximated by a point charge of $2e^-$. Including hybridization effects we obtain a better estimate for the crystal field parameters B_q^k(SOM). Those values are then used as starting point in a comprehensive fit of the model (including spin-orbit coupling and the exchange mean-field due to the long range magnetic order) to the excited energy levels, magnitude of the ordered magnetic moment and easy axis direction obtained from previous measurements to obtain a consistent description of all those measurements.

The rest of the chapter is organized as follows: section 5.2 presents the crystal and magnetic structure at low temperatures; section 5.3 briefly mentions the details of the the experiments performed previously to measure the crystal field levels [53]; the data is then fully analyzed and experimental quantities extracted are presented in section 5.4; a brief description of the theoretical model used in the data modeling is given in section 5.5; section 5.6 presents calculations of the crystal field parameters before and after hybridization effects are included in the model; section 5.7 discusses the steps taken in refining empirical crystal field parameters from fits to data; the best fit model and the final comparison with the experimental data is presented in section 5.8; section 5.9 shows the calculations of the higher energy crystal field levels and comparison with optical measurements; finally the conclusions are summarized in section 5.10. The Appendices give detailed information about how to obtain the form of the crystal field Hamiltonian in the operator equivalent

approach and how to calculate numerically all the relevant crystal field parameters using the point charge model.

5.2 Crystal and Magnetic Structure of $CoNb_2O_6$

$CoNb_2O_6$ crystallizes in the orthorhombic system with space group Pbcn (No. 60). The lattice parameters of the chemical unit cell at T = 1.67 K are $|\mathbf{a}|$ = 14.1475 Å , $|\mathbf{b}|$ = 5.7120 Å and $|\mathbf{c}|$ = 5.0446 Å [54]. The fractional atomic coordinates of the atoms in the unit cell, together with the ion type and Wyckoff positions are given in Table - 5.1. There are four crystallographically-

Table 5.1 Structural parameters for $CoNb_2O_6$ at T = 1.65 K [54].

Atom name	Ion type	Wyckoff position	x/a	y/a	z/a
Co	Co^{2+}	4c	0.0000	0.1818	0.2500
Nb	Nb^{5+}	8d	0.1616	0.3242	0.7445
$O1$	O^{2-}	8d	0.0952	0.3966	0.4329
$O2$	O^{2-}	8d	0.0753	0.1153	0.8884
$O3$	O^{2-}	8d	0.2523	0.1238	0.5693

equivalent Co^{2+} ions in the unit cell, see Figures - 5.1 and - 5.2(c), occupying the 4c Wyckoff positions with fractional coordinates, Co1: (0, y, $\frac{1}{4}$), Co2: (0, $\bar{y}$, $\frac{3}{4}$), Co3: ($\frac{1}{2}$, $\frac{1}{2}-y$, $\frac{3}{4}$) and Co4: ($\frac{1}{2}$,$\frac{1}{2}$ + y, $\frac{1}{4}$), with y = 0.1818. Each Co^{2+} ion is placed inside an oxygen distorted octahedral environment with the local symmetry point group C_2. The twofold symmetry axis is parallel with the crystallographic **b** axis, see Figures - 5.2(b). It is important to understand the distortions of the O_6 octahedron surrounding the Co^{2+} ions using as starting point an ideal octahedron because these distortions combined with the effects of the spin-orbit coupling are ultimately responsible for the

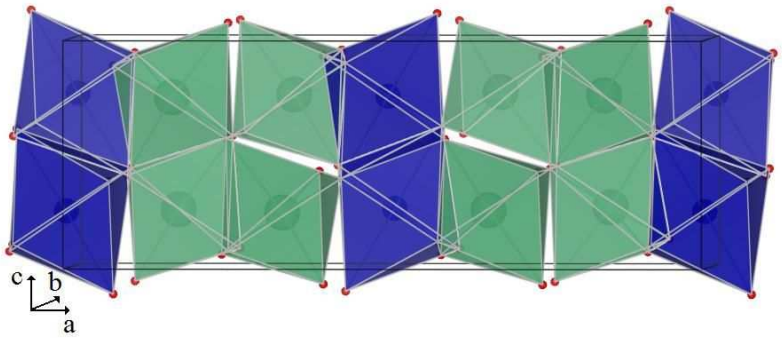

Figure 5.1 Unit cell of $CoNb_2O_6$ system; the CoO_6 octahedra are colored blue and the NbO_6 octahedra are colored green.

magnetic anisotropy effects. All four Co sites are related by symmetry and if we understand the first neighborhood of one of them (for example Co1), it is easy to understand the first neighborhood for all the others.

The first step in understanding the environment of the Co1 ion is to find the "closest" ideal octahedron from which only minimal displacements are needed to generate the actual distorted octahedron. The procedure we used to obtain the ideal octahedron is explained in Ref. [55] and results are given in Table - 5.2 and illustrated in Figure - 5.2(a) (this procedure uses a fitting algorithm to minimize the relative displacements of O ions from the ideal octahedra to actual octahedron). The ideal octahedron has the **Y** axis along **b** and **Z** axis in the **ac**-plane at an angle γ with respect to the **c**-axis. The ideal octahedron has $|\mathbf{d}_{Co-O}|$ = 2.103 Å and for Co1 γ_{Co1} = -32.07°, see Figure - 5.2(a) (positive angles are defined as clockwise rotations). The ideal and distorted octahedra together with the axes for the local and crystallographic reference frames are shown in Figure - 5.2(a). The vectors with the origin at the corners of the ideal octahedron show the oxygen displacements, and their components d_x, d_y, d_z (in Å) are given in Table - 5.2. For example, the displacement vector for O1 ion is: $\mathbf{d}_{O1} = d_x\,\mathbf{i} + d_y\,\mathbf{j} + d_z\,\mathbf{k}$, where **i**, **j** and **k** are the unit vectors of the local **XYZ** coordinate system. A detailed analysis of the local symmetry of the Co^{2+} ions suggest that the calculations of the crystal field parameters B_q^k (which will be defined later in Appendix -

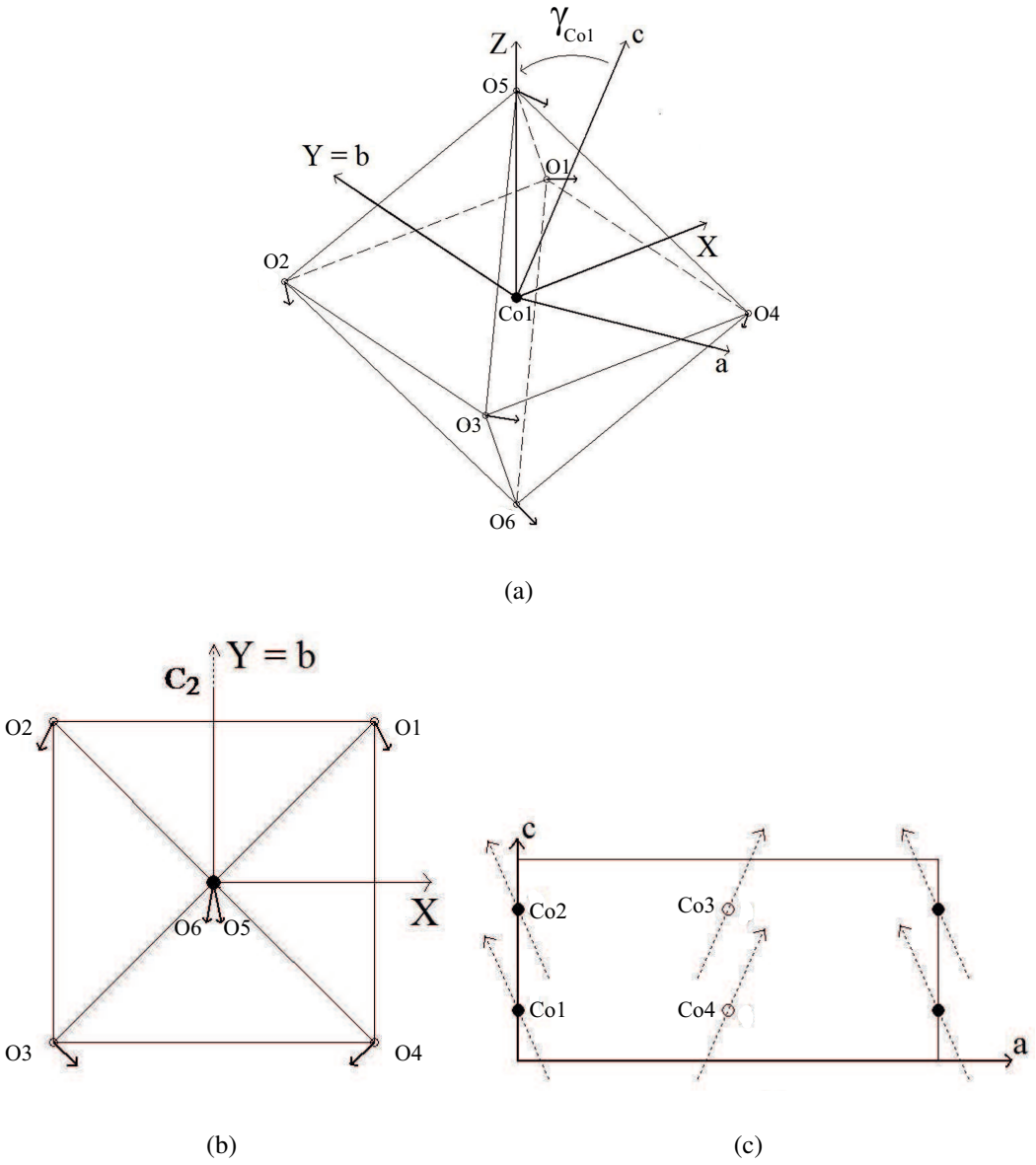

Figure 5.2 (a) schematic representation of the orientation of the local coordinate system **xyz** of the ideal octahedron around Co1 with respect to the crystallographic axes **abc**. Solid arrows at each vertex are oxygen displacements from the ideal position. (c) Projection of the local **Z** axis for the four Co ions in the **XY**-plane; (b) Projection of the oxygen distortions in the **XY**-plane; the filled central black circle represent the Co1 ion and open circles are oxygen ions surrounding it.

Table 5.2 Displacements (in Å) of oxygen around the Co1 relative to an ideal octahedron as shown in Figure - 5.2(a).

Name	d_x	d_y	d_z
$O1$	0.1441	-0.2601	0.0667
$O2$	-0.1441	-0.2601	-0.0667
$O3$	0.2136	-0.2099	-0.0260
$O4$	-0.2136	-0.2099	0.0260
$O5$	0.0657	-0.3798	0.0083
$O6$	-0.0657	-0.3798	-0.0083

A, Eq. - A.20) would be simplified if we work in the local coordinate system **XYZ** instead of the crystallographic coordinate system **abc**. In Figure - 5.2(c) we show the direction of the local **Z** axis for each of the four Co^{2+} ions in the unit cell; we observe the **Z** axis is at γ = -32.07° for ions Co1 and Co2 and at -γ for Co3 and Co4. We will show in the next paragraphs that reports of the magnetic structure found from neutron diffraction measurements [44] find that the directions of the magnetic moments are very close to directions of the local **Z** axes for each Co^{2+} ion.

As a consequences of the 2_y twofold symmetry axis parallel with the crystallographic **b**-axis the oxygen ions have the following symmetry: 2_y $O_5 \rightarrow O_6$, 2_y $O_1 \rightarrow O_2$, 2_y $O_3 \rightarrow O_4$ which can be expressed mathematically as the following relations between the spherical angles θ and α (defined in the **XYZ** local coordinate system, see Figure - 5.3):

$$\begin{aligned} \theta_{O_x} + \theta_{O_{x+1}} &= \pi \\ \alpha_{O_x} + \alpha_{O_{x+1}} &= g\pi, \quad x = 1,3,5 \end{aligned} \tag{5.1}$$

where g is an odd number. We show in Appendix - B that due to these special relations all the imaginary terms in the crystal field expansion B'^{k}_{q} (which will be defined later in Appendix - A, Eq.

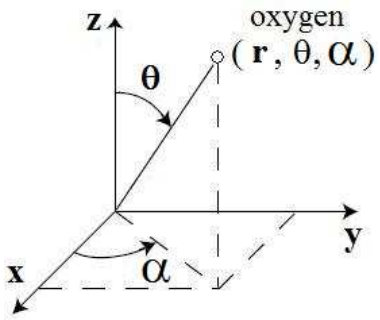

Figure 5.3 Spherical coordinates system used to define the spherical angels θ and φ of the oxygen ions in the **XYZ** local coordinate system.

- A.20) will be zero. The crystal field parameters B'^{k}_{q} are called imaginary crystal field parameters because they are prefactors of purely imaginary operators in the expansion of the crystal field Hamiltonian. The fact that in our case $B'^{k}_{q} = 0$ makes the calculations easier.

Reports of the specific heat and ac-susceptibility measurements in Ref. [46] find that a strong anisotropy exists in this system; reports of the magnetization measurements on single crystal in Ref. [47] find that the magnetic moments are in the **ac**-plane at $\sim \pm 34^\circ$ to **c** axis. Reports of the magnetic structure measured using neutron diffraction find that magnetic moments are in the **ac**-plane at angles of $\pm 31^\circ$ to the **c** axis. Heid [44] reported the magnetic structure with the direction of the magnetic moment for Co1 at 31° and Scarf [45] reported the magnetic structure with the direction of the magnetic moment for Co1 tilted in the opposite direction at -31° from the **c** axis, see Figure - 5.4. Once the direction of the magnetic moment is chosen for the Co1 ion, the direction of the magnetic moments at the other four sites is obtained form group theory considerations [44]. From the reported magnetic structures we learn that there are two possibilities for the directions of the easy axis at the Co1 site. In terms of the local coordinate system **XYZ**, the easy axis would be nearly along the **z**-axis $\xi_{Co1} \cong 0^\circ$ (model S2) or at $\xi_{Co1} = 62^\circ$ (model S1) from the **Z** axis in the **XZ**-plane. Figure - 5.4 shows that in fact the two magnetic structure are related by a shift of (1/2, 1/2, 0) and so would have the same structure factors and they would be indistinguishable in

neutron diffraction measurements.

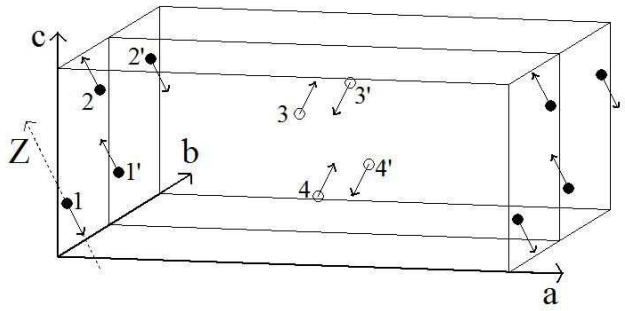

(a) scenario S2: $\xi_{Co1} \cong 0°$

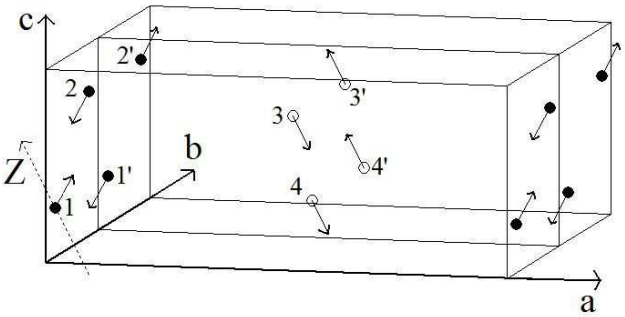

(b) scenario S1: ξ_{Co1} = - 62°

Figure 5.4 Magnetic unit cell of $CoNb_2O_6$ below 1.95 K in the antiferromagnetic phase according to model S1 (a) Heid [44] and S2 (b) Scharf [45]. The black and open circles represent the Co ions with the fractional coordinate x/a = 0 and x/a = 0.5 respectively; the dotted line represents the **Z** axis of the ideal octahedron in the local coordinate reference frame. One can see that the two magnetic structures are related by a shift of $\mathbf{t}_{14}$ (Co1 $\rightarrow$ Co4) = (1/2, 1/2, 0) so would give an identical signature in neutron diffraction.

5.3 Experimental Details

This section gives brief details of the neutron scattering measurements of the excited crystal field levels performed earlier [53]. Measurements were performed using the time-of-flight direct-geometry spectrometer, HET, on the pulsed neutron source ISIS at the Rutherford Laboratory. This technique was used to investigate the transitions from the ground state of Co^{2+} ions to higher crys-

tal field levels. A spinning Fermi chopper placed before the sample is phased to the pulsed source such as to produce pulses of nearly monoenergetic neutrons; in this experiment several incident neutron energies were used, E_{in} = 25, 75, 170, 250, 350, 550 and 1200 meV to cover the lowest band of excitations. This instrument has two banks of detectors: a low-angle bank of position sensitive detectors covering scattering angles between 3° and 9° at a distance of 4 m from the sample and a larger-angle bank, covering angles between 10° and 30° at a distance of 2.5 m. Due to the different distances between the two detectors banks and the sample position, the energy resolution will be different for measurements in the two different detector banks. If an instrument is said to have a resolution ΔE it means that we are not able to resolve experimentally transition energies separated by an energy interval < ΔE. The neutron scattering technique used here is based on the measurements of the time of flight from the source through the sample to the detector banks. In order for the neutrons to arrive at the low-angle bank they have to travel a larger distance, 4 m than for the high-angle bank which means that they will better separated in time when arriving at the detector; this is equivalent with saying that at fixed incident energy E_{in} there is a better resolution for the low-angle bank than for the high-angle bank, $\Delta E_{low-angle\,bank} < \Delta E_{high-angle\,bank}$. A single crystal of $CoNb_2O_6$ was mounted on the instrument such that the **b** axis was perpendicular to horizontal scattering plane. The measurements were made at a base temperature of 5 K with the incident beam oriented along the crystal **a*** axis. The intensity was recorded as a function of time of flight then converted to energy transfer.

The time-of-flight spectra were converted to energy transfer and normalized to the scattering from a standard vanadium sample to correct for the energy dependence of the incident flux. Only the data from the small-angle horizontal detector bank was used in the current study (we will justify this in the next section 5.4). Since the transitions are not dispersive in momentum, see Figure - 5.7, the intensity for a range of scattering angles is averaged to produce spectra as a function of energy transfer, see Figure - 5.5. The position in energy of the crystal field excitations were obtained from

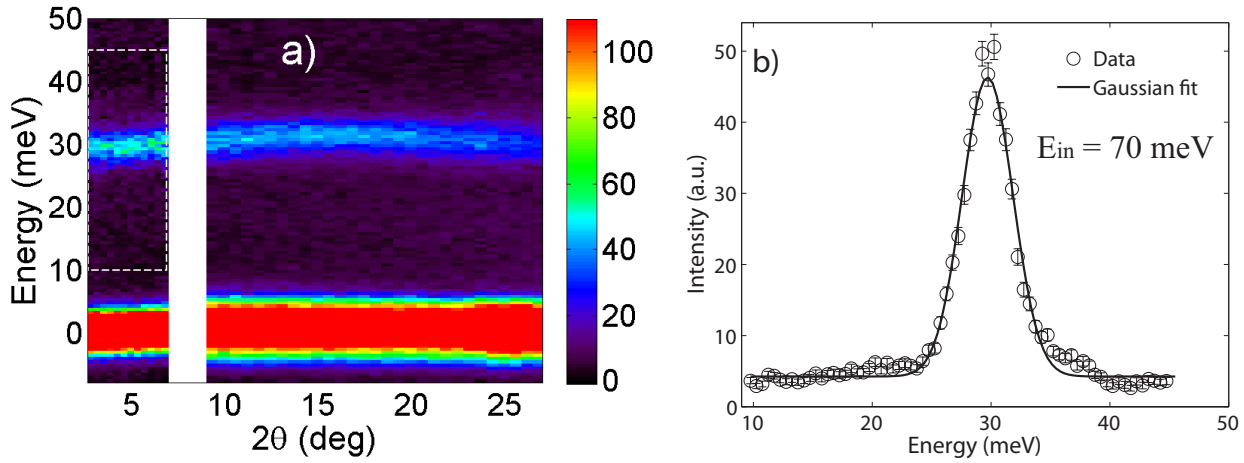

Figure 5.5 (a) Color intensity map of the inelastic neutron intensity observed at 5K for an incident energy of E_{in} = 75 meV; the elastic line is at zero energy transfer as expected; a crystal field excitation is seen near 30 meV. (b) Intensity vs. energy transfer (open circles) and Gaussian fit (solid line). Data points are obtained by averaging the counts in the first detector bank covering the range of scattering angles 3° and 9°; The dashed white box in panel (a) represent the area of the energy cut.

the data measured with the horizontal low-angle bank of detectors which covered scattering angle, $3° < 2\theta < 9°$. Gaussian functions were fitted to the observed peaks in order to find the centers of the peak positions, $\varepsilon_n^{exp}(E_{in})$ and the integrated areas I_{area}^{exp} at various incident energies E_{in}, see Figure - 5.5(b). The excitation energy is given by $\varepsilon_n^{exp} = E_n - E_0$, where E_n and E_0 are the energies of the nth excited state and the energy of the ground state of Co^{2+} ions respectively.

5.4 Experimental Results

Because the measurements were done using different incident energies the same crystal field excitation was measured more than once. To obtain the average experimental energies of the crystal field excitations $\varepsilon_n^{exp}(E_{in})$ for each incident energy E_{in}, the data from the horizontal low-angle bank of detectors was averaged and the peak positions in energy was extracted by fitting the peaks with

single Gaussian functions, see Figure - 5.5(b). Then, the values $\varepsilon_n^{exp}(E_{in})$ corresponding to the same crystal field excitation were averaged and the error bars were chosen such that all the values are included in the confidence interval, see Table - 5.3. Gaussian fits of the peak positions for the transition energies used in this project at different energies are given in Figure - 5.6. The reason we have slightly different values for the same transition energy could be the following: in theory each excitation is represented by a $\delta(E - \varepsilon_n^{exp})$ function (FWHM=0) centered at the energy ε_n^{exp}, but from the experimental point of view, due to the resolution of the instrument, each excitation has a finite width (FWHM$\neq$0) and in general the peak shape can be modeled by a Gaussian function. We will show in the theory section that the energy levels of the Co^{2+} ions are separated in groups of doublets which are very close in energy (see Figure - 5.8). The energy splitting between the doublets is much smaller then the instrument resolution (ΔE) and because of that the level splitting cannot be resolved experimentally. The resolution of the instrument (FWHM) broadens with increasing the incident energy E_{in}. This broadening could be responsible for the small differences in the nominal energy of the same excitation ε_n^{exp} for different incident energies E_{in}.

Table 5.3 Experimental energies of the crystal field excitations, extracted as described in the text, for Co^{2+} ion.

$\varepsilon_{n=1,\ldots,6}^{exp}$	ε_1^{exp}	ε_2^{exp}	ε_3^{exp}	ε_4^{exp}	ε_5^{exp}	ε_6^{exp}
meV	30(2)	50(3)	107(7)	136(4)	170(3)	737(15)

The integrated intensity of the excitations is not affected by the resolution effects but instead is strongly affected by the absorption effects which are energy dependent. Before the absorption effects are discussed, it is important to explain the decrease in intensity with increasing the scattering angle, 2θ see Figure - 5.5(a) or with increasing the wavevector transfer $|\mathbf{Q}|$ see Figure - 5.7(b), for a fixed incident energy and fixed transfer energy where the absorption factor is constant. From

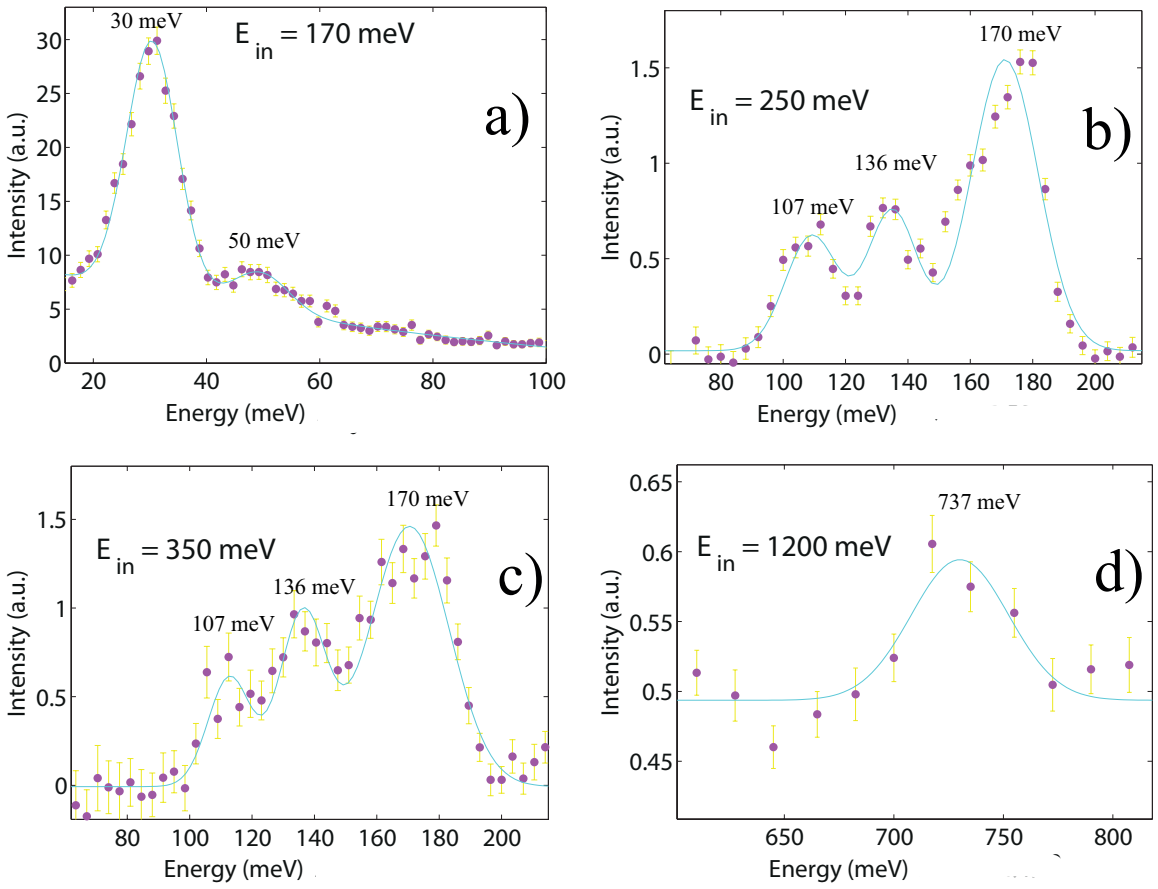

Figure 5.6 Gaussian fits of the peak positions from which the experimental crystal field transition energies ε^{exp} were extracted, see Table - 5.3.

Eq. (5.2) (section 5.5) we see that the scattered intensity is proportional with the squared magnetic form factor, $f(|\mathbf{Q}|)$ which is $|\mathbf{Q}|$-dependent, see Figure - 5.7(a). The magnetic form factor $f(|\mathbf{Q}|)$ is obtained from the Fourier transform of the magnetization density distribution of a single magnetic atom. When the magnetization arises from electrons in a single 3d open shell the magnetic form factor can be calculated from the radial distribution of the electrons in that shell. Numerical calculations have been done for the 3d metals using Hartree-Fock wave-functions and analytical parameterizations have been fitted to the numerical calculations; the fitted coefficients are listed in literature [4] for the transition metals and their ions. The approximation used in the Hartree-Fock calculations (dipole approximation) uses the assumption of a magnetization density distribution of spherical symmetry (free magnetic ion); when the magnetic ion is placed in a crystal the magnetization distribution doesn't have spherical symmetry anymore and the true form factors deviates from their calculated values in dipolar approximation. These deviations became important for high values of the wave vector transfer |**Q**| [56].

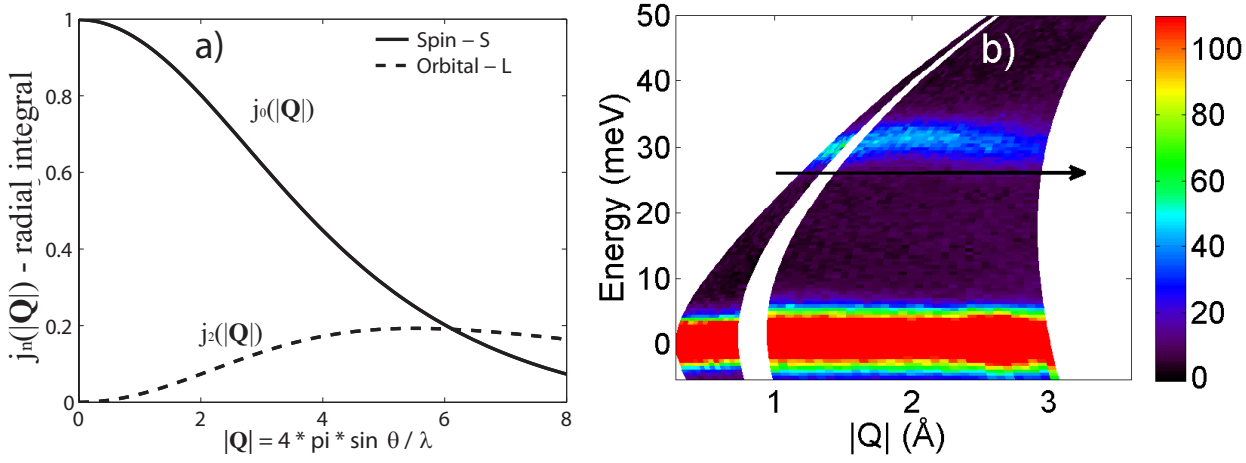

Figure 5.7 (a) radial integral, j_0 (solid line) and j_2 (dash line); in dipolar approximation, the spin magnetic from factor is $f_S(|\mathbf{Q}|) = j_0(|\mathbf{Q}|)$ and the orbital from factor is $f_L(|\mathbf{Q}|) = 0.5 * [\, j_0(|\mathbf{Q}|) + j_2(|\mathbf{Q}|)]$; (b) color intensity map of the inelastic neutron intensity for an incident energy of $E_{in} = 75$ meV showing the |**Q**| dependence of the intensity for the crystal field excitation at 30 meV. The solid arrow show the direction of intensity decrease.

Figure - 5.7(a) shows the spin and orbital magnetic form factor for Co^{2+} ion calculated in the dipolar approximation; the coefficients of the analytical functions have been taken from [4]. We observe that there is a strong decrease of the magnetic form factor with increasing the wave vector transfer |**Q**|. Based on the discussion above, we conclude that the intensity decrease as |**Q**| is increasing is mainly due to the magnetic form factor. The reason why we use only the data from the horizontal low-angle bank of detectors is that the wavevector transfer for measurements using this detector bank is smaller than the wavevector transfer for measurements using the larger-angle bank of detectors where the intensity is much more sensitive to the detailed form of the magnetic form factor.

Due to the complicated sample shape we could not model the absorption effects precisely and because of that the data was not corrected for the absorption effects. To get an idea about how strong the absorption effects are, approximate calculations of the absorption coefficients have been done for a cylindrical sample of an effective radius (chosen by taking into account the size of the sample) for all the incident neutron energies. We found that there could be a decrease in intensity up to 40% for E_{in} = 75 meV and up to 15% for E_{in} = 1200 meV. Because of the absorption effects we only compare the ratio of the calculated intensities with the ratio of the experimental intensities measured at the same incident energy where the absorption factors are approximately the same. Also due to the dipolar approximation used in our calculations, the calculated intensity can be compared with the experimental intensity only for small values of the wave vector transfer |**Q**|. There are only two crystal field excitations which satisfy all these conditions; the excitations at energy transfer of $\varepsilon^{exp}_{\Psi_1}$ = 30 meV and $\varepsilon^{exp}_{\Psi_2}$ = 50 meV, measured with the same incident energy of E_{in} = 170 meV. The intensities for these two crystal field excitations are given in Table - 5.4. The ratio of these two intensities, $I^{exp}_{area}(E_{in}=30)$ / $I^{exp}_{area}(E_{in}=50)$ = 4.8(1.4) will be compared later with the calculated value in order to test theoretical predictions.

The orbital magnetic form factor is very small for the values the wave vector transfer |**Q**| of the

Table 5.4 Intensities of the crystal field excitations.

E_{in}	$\varepsilon^{exp}_{\Psi_{n=1,\ldots,2}}$	$\lvert\mathbf{Q}_x\rvert$	$\lvert\mathbf{Q}_y\rvert$	$\lvert\mathbf{Q}_z\rvert$	$\lvert\mathbf{Q}\rvert$	I^{exp}_{area}
meV	*meV*	Å^{-1}	Å^{-1}	Å^{-1}	Å^{-1}	*a.u.*
170	30	0.8982	0	0.6818	1.1276	240(20)
170	50	1.4767	0	0.6335	1.6068	50(10)

two excitations given in Table - 5.4; for this reason we will only use the spin magnetic form factors in the calculations of the neutron intensities.

5.5 Theory review of formulas used to interpret inelastic the neutron scattering data

The magnetic inelastic neutron scattering for unpolarized neutrons is proportional with [2]:

$$\frac{d^2\sigma}{d\Omega dE} = b_m^2 \frac{k_f}{k_i} |f(|\mathbf{Q}|)|^2 \sum_{\alpha,\beta} \left(\delta_{\alpha\beta} - \frac{Q_\alpha Q_\beta}{\mathbf{Q}^2}\right) S_{\alpha\beta}(\mathbf{Q},\hbar\omega) \tag{5.2}$$

where $\hbar\omega$ is the energy transfer, $\mathbf{Q}$ is the wavevector transfer, b_m is the magnetic scattering length and $f(|\mathbf{Q}|)$ is the magnetic form factor [4]. The prefactor $\delta_{\alpha\beta} - \frac{Q_\alpha Q_\beta}{\mathbf{Q}^2}$ is the polarization factor and $S_{\alpha\beta}(\mathbf{Q},\hbar\omega)$ is the response function of the magnetic operator given by:

$$S_{\alpha\beta}(\mathbf{Q},\hbar\omega) = \sum_n p_0 \langle\Psi_0|M_\alpha(\mathbf{Q})|\Psi_n\rangle \langle\Psi_n|M_\beta(\mathbf{-Q})|\Psi_0\rangle \delta(E_0 - E_n - \hbar\omega) \tag{5.3}$$

where $|\Psi_0\rangle$ and $|\Psi_n\rangle$ are the initial (ground) and final states of the system with energies E_0 and E_n and the initial state has probability p_0. Within the dipole approximation the magnetization operator $\mathbf{M}(\mathbf{Q})$ is given by:

$$\mathbf{M}(\mathbf{Q}) = \sum_i (\mathbf{L}_i + 2\mathbf{S}_i) e^{i\mathbf{Q}\cdot\mathbf{R}(i)} \tag{5.4}$$

where the sum runs over all ions in the unit cell. Combining the Eqs. 5.2 to 5.4 we learn that the intensity of the inelastic scattering for a transition from the ground state, $|\Psi_0\rangle$ to an excited state, $|\Psi_n\rangle$ is proportional to:

$$|\langle\Psi_n|L_\perp + 2S_\perp|\Psi_0\rangle|^2 \tag{5.5}$$

where $\mathbf{L}_\perp$ and $\mathbf{S}_\perp$ are the components of orbital and spin operator momentum perpendicular to the wavevector transfer $\mathbf{Q}$. In order to calculate the neutron scattering intensities for crystal field transition one needs to know explicitly the wavefunctions of all the energy levels, Ψ_n. To find the wavefunctions one needs to write down the total Hamiltonian of the magnetic ion, including the terms for all the relevant interactions and then solve the Schrödinger's equation to find the eigenfunctions and eigenvalues of the Hamiltonian.

5.5.1 Theoretical Model for the Magnetic Hamiltonian

To describe the magnetic ground state one needs to solve the Schrödinger's equation of the system $\mathbf{H}\Psi = E\Psi$ in order to get the energies, E and the eigenfunctions, Ψ of the ground state and excited states. Using the calculated eigenfunctions, one can calculate the expectation values for other quantities such as magnetic moments, neutron scattering cross-sections and compare them with the corresponding values measured experimentally. The total Hamiltonian used in the Schrödinger's equation for transition metals with the configuration d^n can be written as [57]:

$$\mathbf{H} = \mathbf{H}_0 + \mathbf{V}_{ee} + \mathbf{V}_{so} + \mathbf{V}_{cf} + \mathbf{V}_m + \mathbf{V}_{ext} \tag{5.6}$$

where the first term $\mathbf{H}_0$ describes the interaction of each electron with the nucleus (unperturbed Hamiltonian), the second term $\mathbf{V}_{ee}$ describes the interaction of the electrons with each other (Coulomb interaction), the third term $\mathbf{V}_{so}$ describes the interaction between the orbital $\mathbf{l}$ and spin $\mathbf{s}$ moments (spin-orbit interaction), the fourth term $\mathbf{V}_{cf}$ describes the effects of the electrostatic crystal field of the ligands surrounding the magnetic ion (crystal-field interaction). The last two terms

$\mathbf{V}_m$ and $\mathbf{V}_{ext}$ describe the interaction with an internal effective magnetic field (exchange) created by the neighboring ions if the system spontaneously orders magnetically (molecular field interaction) and the interaction with an external magnetic field. In terms of single electron operators, the terms $\mathbf{H}_0, \mathbf{V}_{ee}, \mathbf{V}_{so}$ in Eq. 5.6 are written as follows [58]:

$$\mathbf{H}_0 = -\frac{\hbar^2}{2m}\nabla_i^2 + \frac{1}{4\pi\varepsilon_0}\frac{Ze^2}{\mathbf{r}_i} \tag{5.7}$$

$$\mathbf{V}_{ee} = \frac{1}{4\pi\varepsilon_0}\sum_{i,j}\frac{e^2}{\mathbf{r}_{ij}} \tag{5.8}$$

$$\mathbf{V}_{so} = \sum_i \zeta_i \mathbf{l}_i \cdot \mathbf{s}_i \tag{5.9}$$

where the sum runs over all the electrons in the ion, Z is the nuclear charge, r_i is the distance separating the ith electron from the nucleus, r_{ij} is the distance between the ith and jth electrons, ζ_i is the spin-orbit coupling for single electron and all the other quantities have their usual meaning. ζ_i is a positive quatity which increases with the nuclear charge of the atom and decreases with the radius r of the electron moving around the nucleus [49].

The first three terms in Eq. 5.6, ($\mathbf{H}_0$, $\mathbf{V}_{ee}$, $\mathbf{V}_{so}$) represent the Hamiltonian of the free ion, the following two terms ($\mathbf{V}_{cf}$, $\mathbf{V}_m$) are added to the total Hamiltonian when the free ion is put into a crystal and the last term is added to the total Hamiltonian if an external magnetic field is applied. The total Hamiltonian $\mathbf{H}$ is very complex and in order to solve the eigenvalues problem of this Hamiltonian we have to apply perturbation theory. The first term in the total Hamiltonian Eq. 5.6 is considered as the unperturbed Hamiltonian $\mathbf{H}_0$ and all the other terms will be treated as perturbations. The order in which these perturbations are considered is not critical, but the best results are obtained most easily if the perturbations are treated in order of descending magnitude. It is well known that for transition metal ions the magnitude of the perturbing Coulomb interaction is much larger than the magnitude of all the other perturbations [37]. Thus we can solve first the eigenvalues problem for the free ion Hamiltonian without the spin-orbit interaction

$$\mathbf{H}_{free-ion} = \mathbf{H}_0 + \mathbf{V}_{ee} \tag{5.10}$$

and then we can use eigenfunctions of the free ion Hamiltonian, $\mathbf{H}_{free-ion}$ as zero-order functions to find the splitting of the energy levels in the perturbing Hamiltonian

$$\mathbf{H}_{pert} = \mathbf{V}_{cf} + \mathbf{V}_{so} + \mathbf{V}_{m} + \mathbf{V}_{ext} \tag{5.11}$$

It is well known that the Schrödinger equation with the Hamiltonian given by Eq. 5.10 cannot be solved exactly because of the presence of the electrostatic repulsion between the electrons, $\mathbf{V}_{ee}$. To find the eigenstates and eigenvalues of the $\mathbf{H}_{free-ion}$ one must first solve the the Schrödinger equation for $\mathbf{H}_0$ and then use the first order perturbation theory to find the eigenvalues and eigenfunctions of the $\mathbf{H}_{free-ion}$.

In order to solve the problem it is assumed that the potential field generated by the system's components (electrons and nuclei) has spherical symmetry (central-field approximation). This means that the potential field at any point depends only on its distance from the origin. In this approximation the Schrödinger's equation with the Hamiltonian $\mathbf{H}_0$ can be solved by the method of separation of variables. The eigenfunctions of the Hamiltonian $\mathbf{H}_0$ are Slater determinants and the correspondent eigenvalues depend only on the electronic configuration (n_i, l_i), where n_i is the principal quantum number and l_i is the angular momentum quantum number [52]. Since the eigenvalues of $\mathbf{H}_0$ do not depend on m_{l_i} and m_{s_i}, there is a high degeneracy of the eigenstates. Consequently, many different sets of energy eigenfunctions can be chosen. Taking into consideration that $\mathbf{H}_0$ commutes with $\mathbf{l}_i$, $\mathbf{L} = \sum_i \mathbf{l}_i$ and with $\mathbf{s}_i$, $\mathbf{S} = \sum_i \mathbf{s}_i$ ($\mathbf{H}_0$ does not involve spin operators) the eigenfunctions of the operator $\mathbf{H}_0$ can be classified by the set of quantum numbers L, S, M_L and M_S; the $\mathbf{V}_{ee}$ Hamiltonian which introduces a non-central spherical potential does not commute with $\mathbf{l}_i$ but commutes with $\mathbf{L}$ [59]. Since $\mathbf{H}_{free-ion} = \mathbf{H}_0 + \mathbf{V}_{ee}$ has no spin components, $\mathbf{H}_{free-ion}$ will commute with both $\mathbf{L}$ and $\mathbf{S}$. Hence $\mathbf{H}_{free-ion}$, $\mathbf{L}^2$, $\mathbf{L}_z$, $\mathbf{S}^2$, $\mathbf{S}_z$ form a commuting set of operators so the eigenfunctions of $\mathbf{H}_{free-ion}$ are classified by quantum numbers L, S, M_L and M_S.

The eigenfunctions of the free ion Hamiltonian $\mathbf{H}_{free-ion}$ are described by the quantum numbers L, S, M_L and M_S and they are designated by $|LSM_LM_S\rangle = |LM_L\rangle \bigotimes |SM_S\rangle$ (the product of the

orbital states $|LM_L\rangle$ and the spin states $|SM_S\rangle$), where L is the total orbital quantum number, S is the total spin quantum number, M_L and M_S are the projections of the **L** and **S** along a quantization axis. The energy levels of the free ion Hamiltonian $\mathbf{H}_{free-ion}$ can be described using the spectroscopic notation. For each value of the quantum number L the the electronic state is described by a term symbol $^{2S+1}$L, where 2S+1 is the spin multiplicity (for example electronic states with the orbital quantum number L = 0, 1, 2, 3, 4, 5 are labeled by the letters S, P, D, F, G, H) [52]. A very nice example where the eigenvalues and eigenfunctions are calculated for the Hamiltonian of a free ion with the configuration d^3 is given in [60].

For transition metals ions the interaction with the crystal field $\mathbf{V}_{cf}$ (which affects only the orbital degree of freedom) is much larger than the $\mathbf{V}_{SO}$ interactions, so to a good approximation L and S remain good quantum numbers and one first solves the orbital level splitting of the free ion in the presence of $\mathbf{V}_{cf}$, then applies $\mathbf{V}_{SO}$ as a perturbation.

Co^{2+} has the electronic configuration $3d^7$. The spectroscopic terms for this configuration are: ^2P, $2x$ ^2D, ^2F, ^2G, ^2H, ^4P and ^4F with the last term being the ground state according Hund′s rules. From a simple calculation of the term energies using the formulas given in [61] we see that the energy splitting between the ground state term ^4F and the first excited term ^4P is of the order 10^3 meV; this energy splitting is about ten times larger than the energy splitting due to the perturbation interactions included in the perturbation Hamiltonian H_{pert} in Eq. 5.11; the order of magnitude of the energy splitting due to the crystal field, spin-orbit and molecular field interaction has been reported in [62].

Because we are interested in the low-energy level splitting of the Co^{2+} ions (energies < 1 eV) and as a consequence of the large energy splitting between the ground state term ^{4}F and the excited term ^{4}P we can perform our calculations of finding the splitting of the energy levels due to the perturbation Hamiltonian H_{pert} within the $|LSM_LM_S\rangle$ basis with $L = 3$ and $S = 3/2$ corresponding to the ground state term ^4F of degeneracy (2L+1) x (2S+1)=7 x 4=28. The low-energy electronic

structure results from the lifting of the 28-fold degeneracy of the lowest term ^4F. The 28 levels, originating from the ^4F term, and their eigenfunctions will be calculated by direct diagonalization of the Hamiltonian $\mathbf{H}_{pert}$ within the $|L = 3\ S = 3/2,\ M_L M_S\rangle$ basis as follows (shorthand notation $|M_L M_S\rangle$).

The explicit form of the terms in the perturbation hamiltonian $\mathbf{H}_{pert}$ expressed using the total orbital $\mathbf{L} = \sum_i \mathbf{l}_i$ and spin $\mathbf{S} = \sum_i \mathbf{s}_i$ operators, is given below [49]: Spin-orbit interaction Hamiltonian:

$$\mathbf{V}_{so} = \lambda \mathbf{L} \cdot \mathbf{S} \tag{5.12}$$

Molecular Field Hamiltonian:

$$\mathbf{V}_m = \mathbf{H}_m \cdot \mathbf{S} \tag{5.13}$$

External Zeeman Hamiltonian:

$$\mathbf{V}_{ext} = \mu_B(\mathbf{L} + 2\mathbf{S}) \cdot \mathbf{B} \tag{5.14}$$

Crystal Field Hamiltonian (derived in Appendix B):

$$\mathbf{V}_{cf} = B_0^2\mathbf{O}_0^2 + B_1^2\mathbf{O}_1^2 + B_2^2\mathbf{O}_2^2 + B_0^4\mathbf{O}_0^4 + B_1^4\mathbf{O}_1^4 + B_2^4\mathbf{O}_2^4 + B_3^4\mathbf{O}_3^4 + B_4^4\mathbf{O}_4^4 \tag{5.15}$$

where B_m^n are the crystal field coefficients, $\mathbf{O}_m^n$ are the Stevens operators (see Appendix - C), $\lambda = -\zeta/2S$ is the total spin-orbit coupling [49] (S = 3/2 for Co^{2+}), $\mathbf{H}_m$ is the molecular field (due to magnetic order), μ_B is the Bohr magneton and $\mathbf{B}$ is the external magnetic field. For an ion with the configuration d^n, λ is positive when the d-electron shell is less than half-filled (n<5) and negative if the shell is more than half-filled (n>5); ζ is positive for any occupation of the d-electron shell.

Using the operators from the equations 5.11, 5.12 to 5.15 one can calculate matrix elements of the form $\langle M'_L M'_S|\mathbf{H}_{pert}|M_L M_S\rangle$ and diagonalize the total matrix to obtain the 28 energy levels $E_{n=1,\ldots,28}$ and eigenfunctions $\Psi_{n=1,\ldots,28} = \sum_j c_j |M_L M_S\rangle_j$ which are used to describe the ^4F multiplet.

5.5.2 Crystal field Parameters

Even though the operator equivalent form of the crystal field Hamiltonian Eq. A.20, in Appendix A was derived in the point charge model approximation, it is valid in general. It can be derived using symmetry considerations alone and the Wigner-Eckart theorem which says that the matrix elements of any operator between states of a multiplet $|M_L>$ can be expressed as matrix elements of a function of components of the angular momentum operator [63]. The local point group symmetry of the central ion imposes severe constraints as to which crystal field parameters are allowed in the expansion of the crystal field Hamiltonian Eq. A.20; the higher the symmetry the fewer the number of terms. For example for an ideal octahedron (in the local XYZ reference frame, see Figure - 5.2(a)) the crystal field (cubic point group symmetry) depends essentially on a single variable parameter, the distance between the central ion and one of the vertices. Indeed the crystal field Hamiltonian Eq. A.20 contains only one independent parameter.

$$H_{cf}^{Cubic} = B_0^4 O_0^4 + B_4^4 O_4^4, \; with \; B_4^4 = -5B_0^4, \;\; B_0^4 < 0 \tag{5.16}$$

and the 7-fold degenerate orbital level L = 3 of the Co^{2+} free ion (with the absolute energy E) is split into a lower triplet at absolute energy E - 360 $|B_0^4|$, a middle triplet at absolute energy E + 120 $|B_0^4|$ and an upper singlet at absolute energy E + 720 $|B_0^4|$ (the crystal field parameter B_0^4 change sigh with $\pi/4$ rotations around the **Z** axis). Furthermore if the symmetry is lowered to tetragonal (say by elongation of the ideal octahedron along the z axis) the Hamiltonian becomes:

$$H_{cf}^{Tetragonal} = B_0^2 O_0^2 + B_0^4 O_0^4 + B_4^4 O_4^4, \;\; B_0^2 > 0 \tag{5.17}$$

and the lowest triplet is further split into a doublet and a singlet. Lowering the symmetry further to the orthorhombic point group more terms are allowed and the Hamiltonian becomes:

$$H_{cf}^{Orthorhombic} = B_0^2 O_0^2 + B_2^2 O_2^2 + B_0^4 O_0^4 + B_2^4 O_2^4 + B_4^4 O_4^4, \;\; B_2^2 < 0, \; B_2^4 > 0 \tag{5.18}$$

(with 5 independent terms) and this lifts completely the orbital degeneracy into 7 orbital singlets (6 energy spacing between levels). Lowering the symmetry even further allows for even more

terms in the Hamiltonian. The effect of these additional terms (in principle variable) is not to split the levels any longer (as they are singlets already) but to allow for more solutions with different wavefunction content that give the same energy level splitting, so in an empirical comparison of the measured transition energies to the calculated transition energies using the crystal field Hamiltonian one needs additional information sensitive to the wavefunction of the levels not just the energies relative to the ground state in order to narrow down the possibilities.

The Co^{2+} ions in $CoNb_2O_6$ sit in a crystal environment of a very low point group symmetry, monoclinic C_2. In this case in principle a maximum number of 8 crystal field parameters in the crystal field Hamiltonian are allowed (both real B_q^k and complex B'^k_q parameters). The B'^k_q are prefactors of complex operators in the crystal field expansion of the Hamiltonian and because of the complex operators the complex calculations have to be done to solve the eigenvalues problem of the Hamiltonian. The choice of the reference frame can simplify the expansion and Appendix B shows that by choosing the **y** axis of the local reference frame along the C_2 local 2-fold rotation axis and the **z** axis along the axis of the ideal octahedra closest to the actual distorted octahedra, all complex prefactors B'^k_q vanish. An equivalent analysis can be performed by choosing a different coordinate system such as the crystal orthorhombic axes **abc**, or putting the **Z** axis along the C_2 direction but in this case some of the B'^k_q become finite. This is because not all terms in the full expansion are independent, and in fact a rotation of the coordinate system along **Z** axis, say by angle α leads to a new expansion in the new coordinate frame **X'Y'Z'** where the coefficients B are linearly dependent on the parameters in the **XYZ** reference frame, and by choosing the right angle α some coefficients cancel [64].

So the expansion Eq. 5.15 for Co^{2+} ion in the convenient local **XYZ** frame can be regarded as close to the "minimal" parametrization of the crystal field Hamiltonian with a minimal number of independent terms. The phase space spanned by the eight variable parameters is enormous and there are in principle many different ways in which they can combine to give a very similar looking

energy levels scheme. In order to narrow down the number of possible empirical parameters of the Hamiltonian one needs to use additional constraints and independent information not just the level scheme. The strategy adopted here was to obtain approximate values for the B_q^k terms using the PCM to obtain the most relevant terms and the order of magnitude of their relative strength, then refine this with the SOM to account for the hybridization in a first approximation, then use those values as starting values for the fits to the energy levels obtained in both optical and neutron scattering data and also wavefunction specific information such as the magnitude of the ordered magnetic moment in the ground state and the direction of the easy axis. The phase space spanned by the 8 parameters B_q^k is enormous and we cannot in principle rule out the possibilities that another set of parameters exists that we may have missed and which could give similar results.

However the strategy adopted by constructing the fitting procedure and in choosing realistic starting values for the parameters should very strongly reduce the possibilities of another (physically meaningful) set of B_q^k parameters that could give and equivalent description.

5.6 Predictions of the Point Charge Model and Hybridization effects

A model to calculate to a first approximation the B_q^k used in the crystal field Hamiltonian, Eq. (5.15) is the point-charge model (PCM) described in this section. The parameters calculated in the PCM are important as they are used as starting values in the fits to the experimental data to obtain the empirical crystal field parameters that give the best agreement to the experimental data such as the energy levels, magnitude of the magnetic moment, direction of the magnetic moment and neutron intensities of the transitions. For all the quantities calculated further in this chapter we are using only the information regarding the distorted environment of Co1 ion (the **XYZ** local coordinate system defined in Figure - 5.2(a)), apart from the case where the neutron intensities are

calculated and where we have to use information about the environment of all four Co sites. The number of crystal field parameters necessary to fully describe the crystal field Hamiltonian for the low symmetry environment of Co^{2+} ion in $CoNb_2O_6$ is equal to eight, see Eq. (5.15). This is in principle a very large phase space of parameters and one can not independently fit all those 8 parameters to the data and expect to converge to a unique solution. In principle not all 8 parameters are independent and the strategy adopted here is to use theoretical models such as Point Charge Model (PCM) and Simple Overlap Model (SOM) (which is a further refinement of the PCM), to calculate approximate values for B_q^k, and use those as starting values in the direct fits to the data.

The simplest and most common model used to theoretically estimate the crystal field parameters is the PCM. This only takes into account the electrostatic interaction between the electrons of the magnetic ion and the charged ions in the first neighborhood with the following two main assumptions: the charge density of the ligands is assumed to be -Z_{eff} |e| (where Z_{eff} is the effective oxidation state) and this is considered to be concentrated in a point situated at the nominal position of the ligand ion [59]. In order to calculate the crystal field parameters, B_q^k in the PCM model all we have to know are the effective oxidation states of the ligands and the relative position of the ligands with respect to the transition metal ion. In Section 5.2 we discussed the environment of the Co^{2+} ions and showed that the first neighborhood is a distorted octahedron (the local symmetry of the environment is monoclinic of point group C_2); we also showed that for Co1 ion we can model the distorted octahedron by an ideal octahedron plus small distortions as shown in Figure - 5.2(a). To understand the crystal field Hamiltonian and how the crystal field lifts the degeneracy of the free-ion ground state we consider first the case the ideal octahedron with d_{Co-O}=2.103 Å. The orbital degeneracy, (2L+1)=7 , is lifted by the crystal field interactions to result in two orbital triplet states and a singlet state as shown in Figure - 5.8 (the spin degeneracy, (2S+1)=4 , is lifted only if spin-obit interactions or other internal molecular or external magnetic fields are present). The crystal field for an environment of cubic symmetry is described by a single parameter so the crystal

field Hamiltonian is $H_{cf}^{cubic} = B_0^4(O_0^4 - 5O_4^4)$; the number of necessary crystal field parameters to describe the electric effects of the ligands, increases with lowering the symmetry of the environment [64]. Considering the ideal octahedron defined in the **XYZ** local coordinate system, Figure - 5.2(a), we calculated analytically the expressions for the two crystal field parameters and we obtained $B_0^4 = -\frac{Dq}{60}$ (with $B_4^4 = -5B_0^4$), where $Dq = \frac{1}{4\pi\varepsilon_0}\frac{Z_{eff}e^2\langle r^4\rangle_{3d}}{6d_{Co-O}}$, Z_{eff} is the effective oxidation state of ligands, d_{Co-O} is the distance between the Co^{2+} and the $O^{Z_{eff}-}$ ions in the ideal octahedron, and $\langle r^4\rangle_{3d}$ is the average r^4 for the radial integral of the magnetic ion, as defined in [59], all the other quantities have their usual meaning. Direct calculations give B_0^4 = -0.56 meV and the resulting orbital levels splitting are shown in Figure - 5.8). We see that the cubic crystal field partially

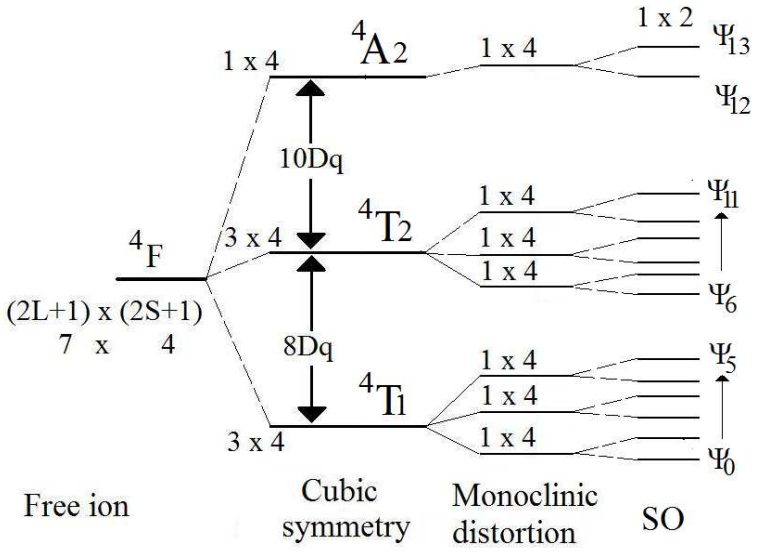

Figure 5.8 From left to right we show a schematic diagram of the energy levels when the Co^{2+} ($3d^7$) ion is placed inside an environment of spherical, cubic and monoclinic symmetry. We see that the ligands arranged in a cubic symmetry lifts only partially the orbital degeneracy; when the local symmetry is monoclinic the orbital degeneracy is lofted complectly. The addition of SO interaction lifts the remanning spin degeneracy to result in a set of Kramers doublets (6 for the lowest manifold).

.

lifts the orbital degeneracy; the seven-fold orbital degenerate ground state for the free ion is split in

a triplet ground state, followed by another triplet state at energies of 8Dq = $480|B_0^4|$ = 268.8 meV and a singlet state at very high energies of 18Dq = $1080|B_0^4|$ = 604.8 meV [37]. Further lowering the symmetry to monoclinic the orbital degeneracy is completely lifted, resulting in seven orbital singlets, see Figure - 5.8. The 4-fold spin degeneracy of each orbital singlet level is further lifted by spin-orbit coupling to results in a set of 14 doublets as confirmed by Kramer's theorem which states that for an odd number of electrons in the presence of only electric fields the energy levels remain at least doubly degenerate [37]. The remaining degeneracy is lifted only when internal molecular or external magnetic fields are present. Using Kramers' theorem and the results of the PCM calculations shown in Figure 5.8, we conclude that the 28 degenerate energy levels of the free Co^{2+} ion will split be into 14 two-fold degenerate energy levels. Usually in transition metals the crystal field effects are much stronger than spin-obit effects [62] and due to this difference in the interaction strength, we expect that the 14 energy levels will be split into three energy groups, the first group centered around the orbital triplet $^4T_1$ ground state, the second group centered around the orbital triplet $^4T_2$ state at 8Dq and the the third group centered around the orbital singlet $^4A_2$ state at 18Dq (see Figure - 5.8). From Table 5.3 we see that the experimentally observed transition energies can be split in two groups, first group centered around 85 *meV* and second group centered around 737 *meV*. The first group of experimental transition energies centered around 85 *meV* is associated with transition between the ground state Ψ_0 and to the levels inside the $^4T_1$ multiplet ($\Psi_{n=1,\ldots,5}$), see Figure - 5.8 and - 5.10; due to the fact that in transition metals the effects of the crystal field are strong we associate the second group of experimental transition energies centered around 737 *meV* with transition between the ground state Ψ_0 and the states $\Psi_{n=6,\ldots,11}$ coming from the $^4T_2$ orbital triplet manifold state at 8Dq (typical values of Dq obtained experimentally for Co^{2+} ions in ideal and distorted O_6 octahedron are in the range 75-90 meV [65, 66]); using an experimental average values for Dq $\approx$ 85 meV , we observe that transitions to the states coming from $^4A_2$ singlet-orbital state would be at much higher energies, 1530 meV. Using the mapping

discussed above between the experimental and calculated groups of transition energies we obtain an approximate experimental value for $Dq_{exp}^{neutrons} = 81.5\,meV$ for the Co^{2+} ion in $CoNb_2O_6$ which is slightly smaller than the values obtained from optical measurements of $Dq_{exp}^{optic} = 90.5\,meV$ [67]. The calculated value in the PCM is $Dq_{calc}^{PCM} = 33.6\,meV$; this value was obtained using: the distance between Co^{2+} and $O^{Z_{eff}-}$ ions in the regular octahedra $d_{Co-O} = 2.1032$ Å, the value of the radial integral calculated in the literature [37] $\langle r^4 \rangle_{3d} = 0.28661$ Å^4 and assuming an effective oxidation state $Z_{eff} = 2$ for the oxygen ions in the first neighborhood. We observe that there is a large difference between the absolute magnitude of Dq predicted by the PCM and the experimental value (underestimated by a factor of 2-3). This difference is due to the fact that the PCM model doesn't take into account hybridization effects. In real materials the charge of the ligands is not concentrated in a point at the ligand position but is distributed in a region around the ligand position due to the hybridization effects between the ligand and transition metal orbital. We can say that the crystal field parameters predicted by the point charge model are underestimated due to the fact that this model doesn't include hybridization effects.

To further improve on the crystal field parameters we used the Simple Overlap Model (SOM) which takes into account the hybridization effects [68, 69]. The SOM takes into account in a first approximation the chemical bonding and it may be regarded as a starting point to obtain more realistic values for the crystal field parameters which will be further used in the crystal field Hamiltonain, Eq. 5.15 to calculated the transition energies and compare them with the experimental transition energies. This model has been successfully applied to reproduce phenomenological (empirical) crystal field parameters for a large number of lanthanides as well as for some transition metals elements [70–73]. The basic idea is the same as that of the PCM and in both methods the crystal field parameters are calculated from the atomic positions of the ligands relative to the magnetic ion. In the PCM the purely electrostatic potential of the perturbation is produced by the point charges located at the ligands sites situated at a distance R from the transition metal ion (the

point charges Z_{eff} are equal with the effective oxidation state of the ligand). In the SOM the purely electrostatic potential of perturbation is produced by effective charges uniformly distribution over a small region situated around the mid point of the metal-ligand distance. The total charge in each region is equal to $-Q_{eff}\,|e|\,\rho$, where Q_{eff} is the number of effective charges and ρ is the orbital overlap between the 3d orbitals of the central magnetic ion and the s and p orbitals of the ligand ion; the values of ρ varies as a function of the metal-ligand distance, R, according to the power low $\rho = \rho_0\,(\frac{R_0}{R})^{3.5}$, R_0 being the shortest metal-ligand distance [70]. In this model Q_{eff} and ρ_0 are variable parameters obtained from fits to the data. Within a first-order approximation the relation between the crystal field parameters calculated in the PCM and SOM, B_q^k(PCM) and B_q^k (SOM) is a simple scale law [71]:

$$B_q^k(SOM) = \rho\left(\frac{2}{1-\rho}\right)^{k+1}\left(\frac{Q_{eff}}{Z_{eff}}\right)B_q^k(PCM) \tag{5.19}$$

For illustrative purposes Eq. 5.19 is given for the case when all the distances ligand-transition-metal-ion are equivalent (in this case all the coefficients B_q^2(PCM) should be multiplied by the same constant factor, $\rho\left(\frac{2}{1-\rho}\right)^{k+1}$, in order to obtain B_q^2(SOM)). In our case the distances ligand-transition-metal-ion are different and Eq. 5.19 becomes more complicated. From numerical calculations of the overlap integrals for transition metals ions it is found that the overlap parameters ρ_0 could have values between 0.10 and 0.30 [74, 75]. Using the SOM model to other systems where Co^{2+} ions are found in environments such as distorted octahedra, it was observed that the overlap parameter has values between $0.12 < \rho_0 < 0.16$ ($\Delta\rho_0$ = [0.12, 0.16]) and the effective charge takes values in the range $0.6 < Q_{eff} < 1$ (ΔQ_{eff} = [0.6, 1]) [70–72]. From Eq. (5.19) we observe that we can improve on the values of B_q^k if we know the values of Q_{eff} and ρ_0 for the Co^{2+} in the system under study. We observe that using the crystal field Hamiltonian, Eq. (5.15) with the crystal field parameters given by Eq. (5.19) where Q_{eff} and ρ_0 are variable parameters in the experimental range found in the literature ΔQ_{eff} and ΔQ_{eff} for Co^{2+} ions, we can calculate the transition energies and compare them with the experimental transition energies, to get an idea about how well

the SOM predicts the overall energy scales.

A fitting function was constructed where the fitting parameters were Q_{eff} and ρ_0 and only the crystal field Hamiltonian, Eq. 5.15 and the spin-orbit Hamiltonian, Eq. 5.12 were included in the calculations of the transition energies. The calculations were done for the distorted octahedra of the Co1 ion including all eight non-zero crystal field parameters calculated using on Eq. 5.19; the spin-orbit constant used in the calculations was set to the value extracted from optical measurements, $\lambda = -18.7meV$ [76]. Only the first five energies, ε_1^{exp} to ε_5^{exp} from Table - 5.3 (transitions in the $^4T_1$ sixtuplet of doublets, see Figure - 5.10) were used in the fits; the criteria to obtain the best values for Q_{eff} and ρ_0 was the minimization of the function: $f(Q_{eff},\rho_0) = \sum_i(\varepsilon_i^{cal}/\varepsilon_i^{exp} - 1)^2$, where ε^{cal} and ε^{exp} are the calculated and experimental transition energies. The search space for the input parameters Q_{eff} and ρ_0 were limited to the experimental limits found in the literature for Co ion, Q_{eff} and ρ_0. $Q_{eff} = 0.67$ and $\rho_0 = 0.13$ gave the crystal parameters (see Table - 5.5) which gave the best overall agreement between the calculated and experimental transition energies, see Table - 5.6.

Table 5.5 Crystal field parameters(for the distorted octahedron) calculated in the PCM and SOM.

Method	$(Z/Q)_{eff}$	ρ_0	B_0^2	B_1^2	B_2^2	B_0^4	B_1^4	B_2^4	B_3^4	B_4^4
PCM	2.00	-	2.791	-7.920	-0.058	-0.496	0.014	0.168	0.302	2.498
SOM	0.67	0.13	2.678	-3.707	-0.900	-1.149	0.138	0.501	0.756	6.346

Reasonably close agreement is obtained for the sequence of levels apart from the last one, identified with $\Psi_0 \rightarrow \Psi_6$ transition from the ground state to the first excited $^4T_2$ orbital triplet state largely underestimated, however this may mean only one parameter is underestimated B_0^4 which gives the large $^4T_1 \rightarrow {}^4T_2$ split, see Figure - 5.10. The calculated transition energies given in

Table 5.6 Energies of transitions between the ground state Ψ_0 to the excited $\Psi_{n=1,...,5}$ levels of the $^4T_1$ orbital manifold, and the transition E_6 from Ψ_0 to the lowest state of the $^4T_2$ orbital manifold (see Figure - 5.8).

Method	ε_1	ε_2	ε_3	ε_4	ε_5	ε_6
PCM	23.7	61.2	100.4	108.1	129.3	302.8
SOM	25.7	59.9	102.2	142.4	157.9	625.7
Exp	30.0	50.0	107.0	136.0	170.0	737.0

Table 5.6 are to the excited doublet levels. In the presence of magnetic order (which only occurs below 3K in $CoNb_2O_6$) the degeneracy of the doublets is lifted. Due to the exchange interactions between the neighboring Co^{2+} ions there is a molecular field present at each Co^{2+} site which will lift the doublet degeneracy (we will show later the splitting is of the order of a few meV only). From measurements of the magnetic structure we know that there are two possibilities for the direction of the easy axis, see Figure - 5.4. The easy axis could be in the **XZ**-plane, either very close to the local **Z** axis (scenario S2) or at $\sim$62 $^\circ$ from the **Z**-axis (scenarios S1), see Figure - 5.4. In order to determine the direction of the easy axis from the our calculations we apply the following procedure: first step is to include a very small external magnetic field $|\mathbf{B}|=10^{-5}$ T, such that the transition energy levels are unaffected. This small magnetic field would split the doubly degenerate states insignificantly but would help us to choose the ground state wave function ($\Psi_{0\downarrow}$, see Figure - 5.10); using the ground state wave function we can further calculate quantities such as the magnitude of the magnetic moment along the direction of the applied external magnetic field. Second step is the variation of the orientation of the external magnetic field **B** (defined by the angles θ and α) and finding the magnitude of the magnetic moment along the field direction, in each case and plotting the results as a 2D map in (θ, α). The direction where the total magnetic moment has largest value defines the easy axis. Such a two dimensional magnetization map is

shown in Figure - 5.9 (color is proportional to the magnitude of the total magnetic moment in the (θ, φ) direction, when the field is applied in the (θ, φ) direction) for the crystal field parameters obtained in the SOM, Table - 5.5. We observe that the magnetic moment has largest values when

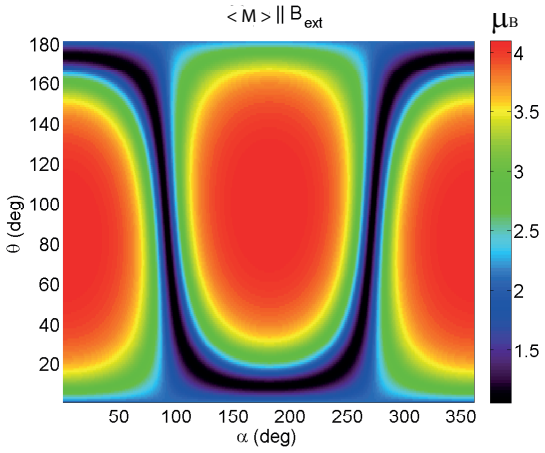

Figure 5.9 Magnetization map calculated using the crystal field parameters obtained in the SOM, Table 5.5. The color represent the magnitude of the magnetic moment <M> along the external field direction, **B** defined by the spherical angles (θ, α) in the local reference frame **xyz**.

.

the field is along (θ= 90 °, α = 0) and (θ= 90 °, α = 180 °); this is consistent with an easy axis along the local **X** axis which is not in agreement with the two possibilities found experimentally (θ= 0 ° or 62 °) for the easy axis, see Figure - 5.4. From the calculations of the magnetization map we learn that the crystal field parameters calculated in the SOM don't correctly predict the orientation of the easy axis which means that they can not entirely account for all the hybridization effects. In order to account for all the hybridization effects we are trying to obtain the empirical crystal field parameters from fits to the data. The crystal field parameters calculated in the SOM, see Table - 5.5, will only be used as starting values for the fitting procedure.

5.7 Empirical crystal field parameters

In order to refine the obtained crystal field parameters and the spin-orbit constant empirically by fits to the data we constructed a fitting function where the input parameters are the crystal field parameters and the spin-orbit coupling. In the previous function we calculated the transition energies and the direction of the easy axis using the crystal field parameters calculated in the SOM and we compared the calculated results with the experimental results; we have seen that using the crystal field parameters calculated in the SOM we obtain an acceptable agreement for the transition energies but we can not explain the direction of the easy axis seen experimentally. The total Hamiltonian in our fitting function includes the crystal field Hamiltonian Eq. 5.15, the spin-orbit Hamiltonian Eq. 5.12 and the Hamiltonian of interaction with an external field Eq. 5.14, $\mathbf{B}_{ext}$ ($|\mathbf{B}_{ext}| = 10^{-5}$ T). First step in our data analysis is to obtain the crystal field parameters by varying them around the values obtain in the SOM (see Figure - 5.10 for a schematic representation of the transition energies). Only the first 5 experimental transition energies from Table - 5.3 were used in the fits. For each set of crystal field parameters the theoretical transition energies are calculated and compared with the experimental transition energies; the best solution for the empirical crystal field parameters is found when the following function is minimum,

$$f(B,\lambda) = \sum_i (\frac{\varepsilon_i^{cal}}{\varepsilon_i^{exp}} - 1)^2 \tag{5.20}$$

The second step in our data analysis is to add new constraints to our fitting function such as the direction of the easy axis measured experimentally by neutron diffraction. As we discussed in section 5.2, we definitely know that the easy axis is in the **ac** plane, but there are two possibilities for the direction of the easy axis in the plane (neutron diffraction measurements can not distinguish between these two direction). The first scenario (S1) is the one where the easy axis for Co1 is at 31 $^\circ$ with respect to the **c** axis (see Figure - 5.4(a)); the second scenario (S2) is the one where the easy axis for Co1 is at -31° with respect to the **c** axis (see Figure - 5.4(a)). Because it is easier to work

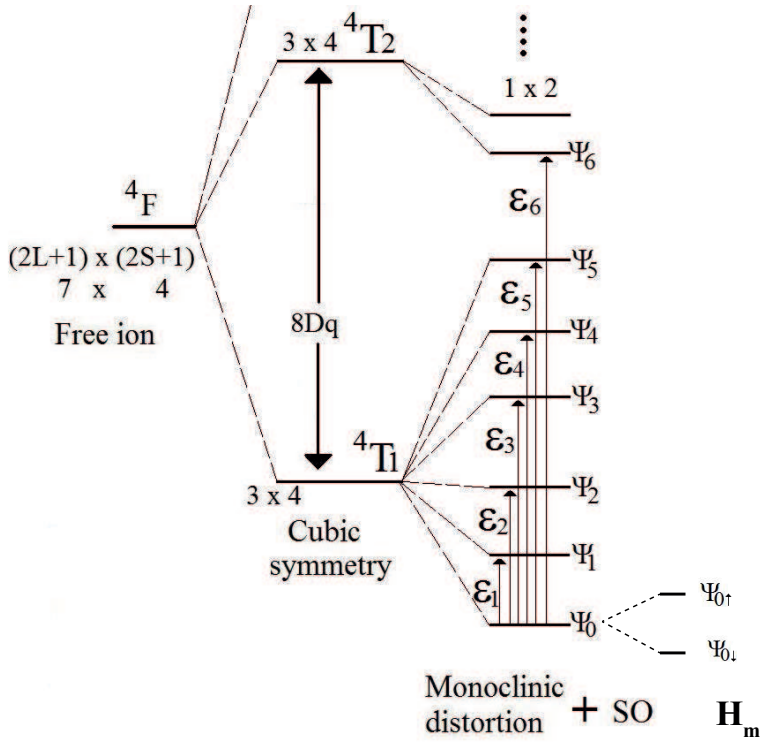

Figure 5.10 From left to right we show a schematic diagram of the energy levels when the Co^{2+} ($3d^7$) ion is placed inside an environment of spherical, cubic and monoclinic symmetry. monoclinic local symmetry together with the SO interaction lifts the remanning spin degeneracy to result in a set of Kramers doublets (6 for the lowest manifold. Only an additional molecular field can further lift the degeneracy of the Karmers doublets as is shown only for the ground state

.

in the local coordinate system, we define the easy axis in the local **XYZ** coordinate system: for the first scenario (S1) the easy axis is in the **XZ** plane, at $\theta = 62^\circ$ clockwise with respect to the **Z** axis and for the second scenario (S2) the easy axis is along the **Z** axis. To obtain the best empirical crystal field parameters we used the fitting criteria to minimize differences of the calculated and experimental transition energies to the experimental transition energy, the function $f(B's, \lambda)$, Eq. 5.20 but with additional terms as explain below. For scenario S1 we added to $f(B's, \lambda)$ the term $[\frac{\arctan\left(\frac{M_x}{M_z}\right)}{62} - 1]^2$ and for the second scenario S2 we added the term $[cos\left(\arctan\left(\frac{M_x}{M_z}\right)\right) - 1]^2 + (M_x)^2$. In the pervious section we have seen that the easy axis is along the local **X** axis for the crystal field parameters obtains in the SOM; with the new constraints (by varying the crystal field parameters) we force the easy axis to be along one of the two directions found from neutron diffraction measurements.

Table 5.7 Empirical crystal field parameters B_q^k found starting from the SOM values and belonging to the best fit to reproduce the orientation of the easy axis in models S1 and S2, Figure 5.4.

Method	B_0^2	B_1^2	B_2^2	B_0^4	B_1^4	B_2^4	B_3^4	B_4^4	λ
SOM	2.678	-3.707	-0.900	-1.149	0.138	0.501	0.756	6.346	-18.7
*S*1	3.500	-4.400	-0.031	-1.250	0.042	0.220	1.840	8.010	-19.9
*S*2	0.600	-5.000	-7.000	-1.100	0.000	0.000	0.100	7.200	-21.1

The new constraints for the easy axis are explain below:

Scenario S1: if we apply very small external magnetic field $\mathbf{B}_{ext}$ along the experimental easy axis direction (in this case the experimentally easy axis is found in the **XZ** plane at 62° from the **X** axis) then $\mathbf{B}_{ext}$ will induce a magnetic moment along the magnetic field direction, |**M**|(S1) proportional to |**B**| but there will still be a component of magnetic moment, M_x along the **X** axis due to the strong anisotropy created by the crystal field parameters obtained in the SOM model, see Figure -

Table 5.8 Transition energy levels calculated using the empirically determined crystal field parameters in Table 5.7, that give closest agreement to the measured transition energies within models S1 and S2. The empirically obtained spin-orbit coupling constant is λ = 19.9 meV.

Method	ε_1	ε_2	ε_3	ε_4	ε_5	ε_6
SOM	25.7	59.9	102.2	142.4	157.9	625.7
*S*1	29.8	53.9	98.1	142.9	154.8	642.0
*S*2	29.8	53.9	98.1	142.9	154.8	642.0
Exp	30.0	50.0	103.0	136.0	170.0	737.0

5.9. With the additional condition imposed in this model we force the crystal field parameters to converge to values for which when we apply a small magnetic field $\mathbf{B}_{ext}$ along the experimentally determined easy axis, the expectation values of M_x and M_z are such that they correspond to a naturally occurring easy axis, found in the **XZ** plane at the correct angle from the **Z**-axis which is this case is 62° to the local **Z** axis. In this scenario we don't impose any direct constraint on the values of the the magnetic moment components.

Scenario S2: if we apply very small external magnetic field $\mathbf{B}_{ext}$ along the experimental easy axis direction (in this case along the **Z** axis) then $\mathbf{B}_{ext}$ will induce a magnetic moment along the magnetic field direction, |**M**|(S2) proportional to |**B**| but there will still be a strong component of the magnetic moment, M_x along the **X**-axis due to the strong anisotropy along the easy axis created by the crystal field parameters obtained in the SOM model, see Figure - 5.9. With the additional conditions imposed in this model we force the crystal field parameters to converge to values for which when we apply a small magnetic field **B** along the experimentally determined easy axis, the expectation values of M_x and M_z are such that they correspond to a naturally occurring easy axis(along **Z**). In this scenario we impose the constrain that the value of the the magnetic moment

component $M_x = 0$.

The values of the crystal field parameters found from fits to the data for the two scenarios are given in Table 5.7. The calculated energies for the corresponding crystal field parameters are given in Table 5.8.

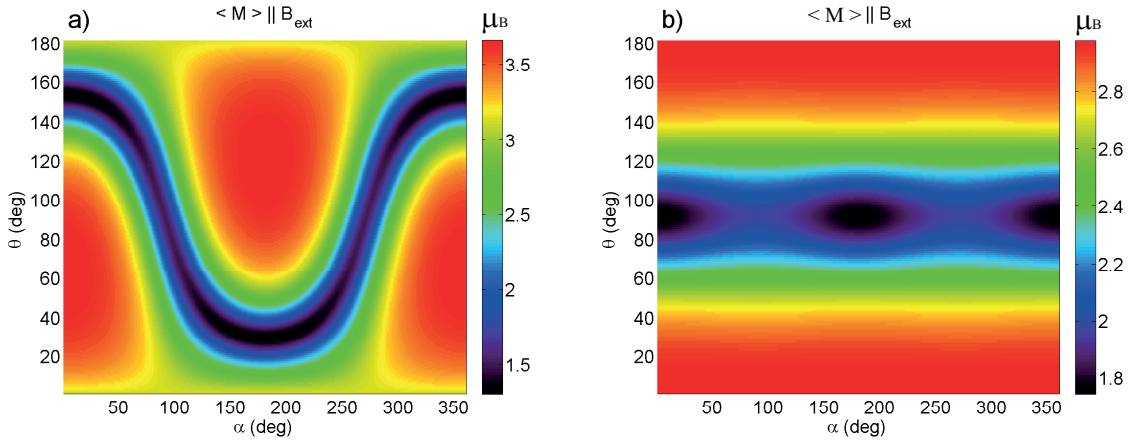

Figure 5.11 Magnetization maps as a function of direction in spherical coordinates, angles (θ, φ) calculated using the empirical crystal field parameters, Table 5.7: (a) scenario S1 and (b) scenario S2. The color represent the magnitude of the magnetic moment <M> along the external field direction, $\mathbf{B}_{ext}$.

.

In Figure 5.15 we plot the magnetization map obtained using the two sets of empirically extracted crystal field parameters: (a) using the constraints for the scenario S1 and (b) using the constraints for the scenario S2.

At this point it is important to summarize what we have done so far. In the first approximation the crystal field parameters were calculated in the PCM model, B_q^k(PCM). Using the crystal field parameters B_q^k(PCM) the transition energies for Co^{2+} ions have been calculated and compared with experimental transition energies. This comparison showed that the PCM underestimate the energy scales involved in the process. To improve the agreement between the calculated and experimental transition energies we included hybridization effects in our calculations by obtaining rescalled

crystal field parameters using the SOM model, B_q^k(SOM). Using the B_q^k(SOM) the agreement between the calculated and experimental transition energies becomes satisfactory. The experimental energy scale is reproduced by calculations in the SOM model, but calculations of the expected direction for the easy axis using B_q^k(SOM) shows that this model is inconsistent with the possibilities allowed for the easy axis obtained by the analysis of the neutron diffraction measurements of the magnetic structure. Further we tried to obtain the crystal field parameters empirically from fits to data including the constraints for the direction of the easy axis (the starting values for the crystal field parameters in the fits, were B_q^k(SOM) values). Two solutions were obtained for the crystal field parameters B_q^k(S1) and B_q^k(S2) each of them corresponding to one of the two experimentally determined directions for the easy axis. The values of crystal field parameters B_q^k(S1) are similar to those obtained in the SOM model (except B_2^2 and B_1^4 which are much smaller) but the values crystal field parameters B_q^k(S2) differ much more (B_2^2 is very large compared with the negligible value in the calculations). The comparison off all the crystal field parameters calculated in the PCM, SOM and empirically extracted from fits to the data reveal different magnitudes but all them have the same sign. This might be expected because in a first approximation hybridization effects lead to a rescaling of the overlap integrals. Further discussions of the resulting energy levels for the two sets of the empirical crystal field parameters B_q^k(S2) or B_q^k(S2) is given in the next section.

5.8 Discussions and Results

The previous section described the fitting procedures to extract empirical B_q^k parameters from fits constrained to reproduce the easy-axis direction. We used a very small external magnetic field (10^{-5} T) to lift the two fold degeneracy of the ground state in order to calculate quantities such as the total magnetic moment along the field direction. The splitting in energy of the two fold degenerate states due to the external magnetic field was basically insignificant but using the calculated

magnetic moment along the field direction was useful in determinations of the easy axis. We know that this system orders magnetically(below 3K) which means that there is an exchange interaction between the spin component of the neighboring Co^{2+}. The effect of this exchange interaction can be taken into account in our calculations by the molecular field Hamiltonian given by Eq. 5.13, where the approximate magnitude of the molecular field $|\mathbf{H}_m|$ is determined experimentally from the present measurements. We already know that in the absence of an external field (magnetic or molecular field) the energy levels of Co^{2+} ions in $CoNb_2O_6$ have two fold degeneracy. Due to exchange interactions between the spin components of the neighboring Co^{2+} ions this two fold degeneracy is lifted. The experimental energy splitting of the two fold degenerate ground state to be of the order of 2.9 meV, see Figure - 5.12. In order to find experimentally the value of the molecular field constant for the two possible scenarios, S1 and S2, we apply a variable $|\mathbf{H}_m|$ in the direction of the corresponding easy axis (for S1 and S2) until the splitting of the two fold degenerate ground state is very close the splitting observed experimentally of 2.9 meV. The obtained values for the molecular fields in the two scenario are $|\mathbf{H}_m|(S1) = 1.2meV$ and $|\mathbf{H}_m|(S2) = 1.4meV$.

Using the two sets of empirical parameters (B_q^k, λ, $|\mathbf{H}_m|$) for scenario S1 and S2, two dimensional maps are calculated (for all angles θ and α) for quantities such the total magnetic moment along the molecular field, the spin and orbital component of the ground state $\Psi_{0\downarrow}$, the energy of the first excited state $\Psi_{0\uparrow}$ (see Figure - 5.10) and the total energy of the system (with respect to the energy of the free ion chosen to be zero on the energy scale). Form Figure - 5.13 we see that the crystal field parameters obtained in scenario S1 are giving a much more stable ground state with the energy $E_{GS}(S1) \cong -594meV$, compared to the crystal field parameters obtained in scenario S2 where $E_{GS}(S2) \cong -538meV$. The results presented in Figure - 5.14 shows that the values chosen for the molecular fields are such that when the molecular field occurs along the easy axis direction (due to the long range magnetic order) the energy splitting of the ground state doublet has approximately the same values as the one obtained from inelastic neutron scattering. The results presented

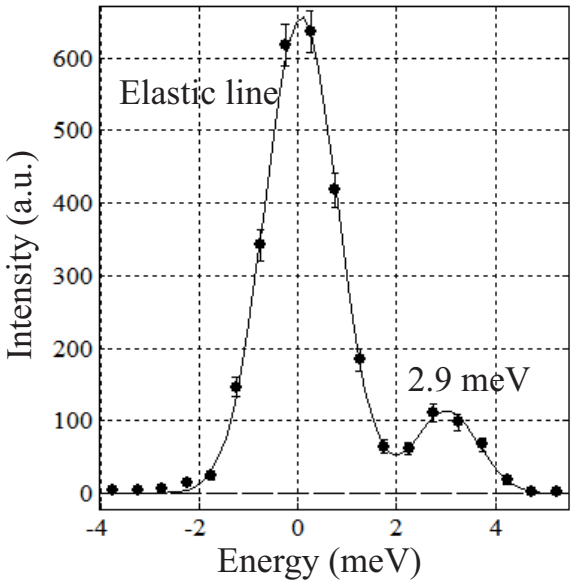

Figure 5.12 Experimental splitting of the lower doublet due to the molecular field $\mathbf{H}_m$. The solid line is guide to the eye.

.

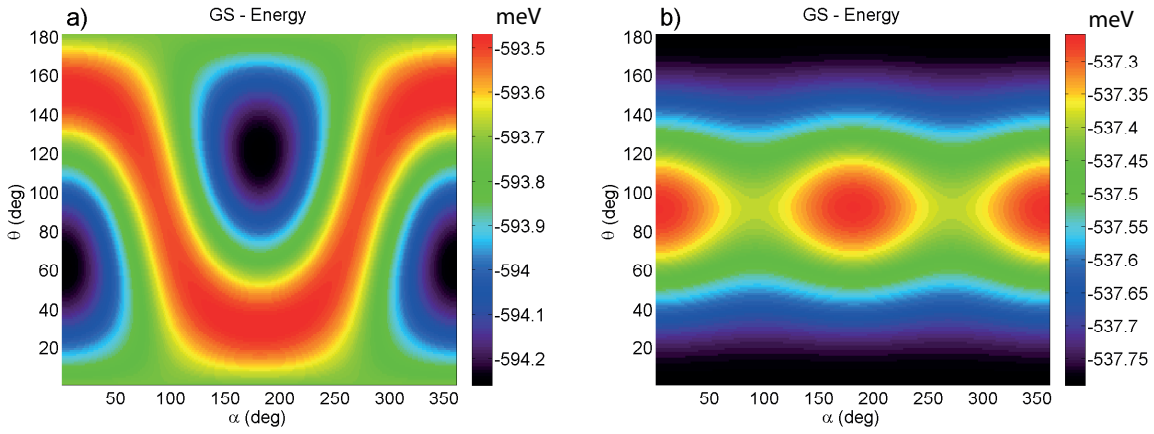

Figure 5.13 Two dimensional maps of the ground state energy for different directions of the H_m field; (a) for scenarios S1 and (b) for scenario S2. The color represent the values of the ground state energy with respect to the energy of the free ion (which is chosen to be at zero on the energy axis).

.

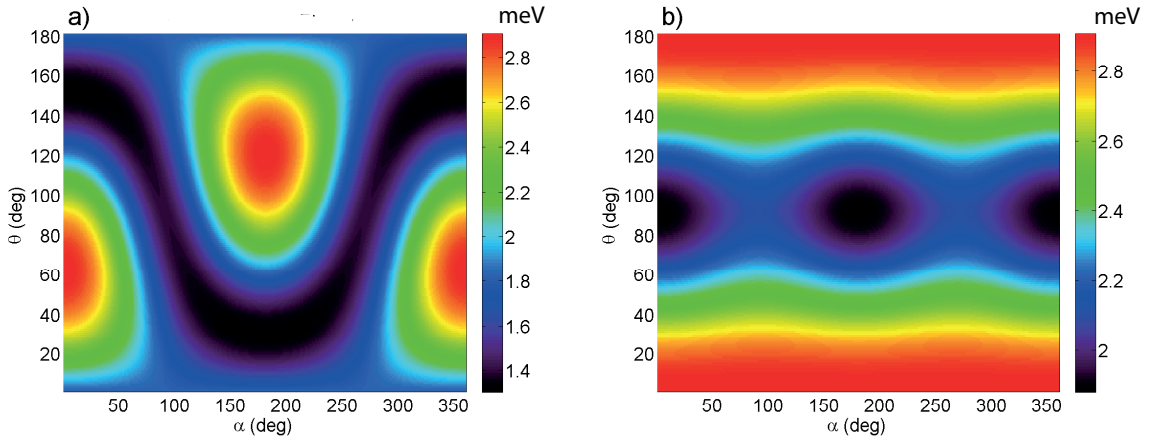

Figure 5.14 Two dimensional maps of the ground state doublet splitting for different directions of the H_m molecular field; (a) S1 and (b) S2. The color represent the energy value of the first excitation relative to the ground state (transitions inside the doublet $\Psi_0 \uparrow$ to $\Psi_0 \downarrow$).

.

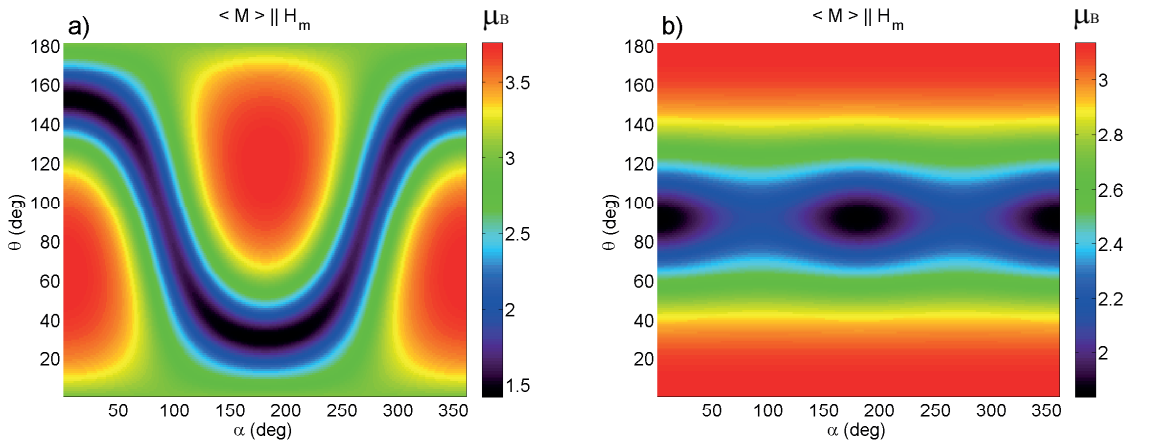

Figure 5.15 Magnetization maps calculated using the empirical crystal field parameters in Table 5.7 and the molecular field H_m: (a) S1 and (b) S2. The color represent the magnitude of the magnetic moment $\langle M \rangle$ along the molecular field direction, $\mathbf{H}_m$.

.

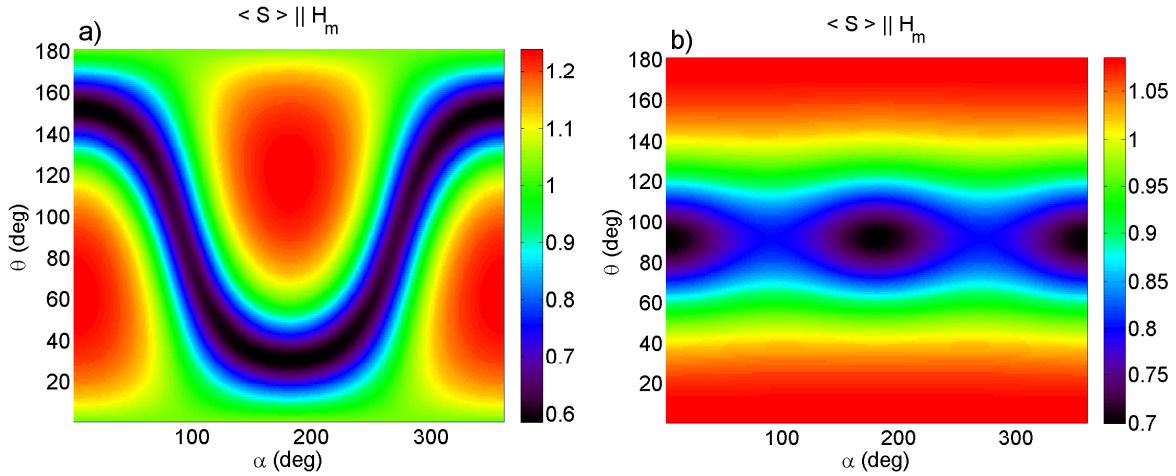

Figure 5.16 Expectation value of the spin only part of the magnetic moment in the ground state $\langle S \rangle$ calculated along the molecular field $\mathbf{H}_m$ using the empirical crystal field parameters in (a) S1 and (b) S2. The color represent the magnitude of the $\langle S \rangle$ along the external field direction, $\mathbf{H}_m$.

.

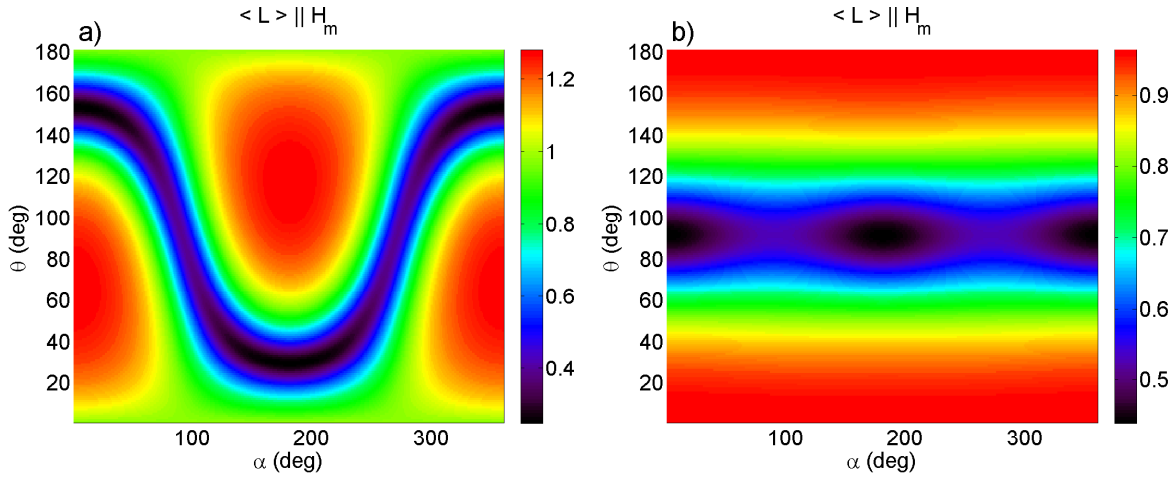

Figure 5.17 Expectation value of the orbital only part of the magnetic moment in the ground state $\langle L \rangle$ calculated along the molecular field $\mathbf{H}_m$ using the empirical crystal field parameters in (a) scenario S1 and (b) scenario S2. The color represent the magnitude of the $\langle L \rangle$ along the external field direction, $\mathbf{H}_m$.

.

in Figure 5.15 shows that the easy axis direction is as expected for the two sets of crystal field parameters; it also gives the magnitude of the magnetic moments in the ground state: $\langle \mathrm{M}_{GS}(\mathrm{S1}) \rangle$ = 3.756 μ_B and $\langle \mathrm{M}_{GS}(\mathrm{S2}) \rangle$ = 3.133 μ_B which compare reasonably with the value obtained experimentally for the ordered moment of 3.2 μ_B, from neutron diffraction experiments [44, 45]. The orbital and spin contributions to the ground state magnetic moment can be seen in Figures 5.17 and 5.16; from these figures we learn that in the ground state the expectation value of the **L** and **S** operators have finite values, showing the the orbital momentum is not quenched and it contributes to the value of the magnetic moment ($|\langle \mathrm{L}_{GS}(\mathrm{S1}) \rangle|$ = 1.280, $|\langle \mathrm{S}_{GS}(\mathrm{S1}) \rangle|$ = 1.238) and ($|\langle \mathrm{L}_{GS}(\mathrm{S2}) \rangle|$ = 0.963, $|\langle \mathrm{S}_{GS}(\mathrm{S2}) \rangle|$ = 1.085). The experimental ratio of the intensities for the first two transitions at 30 and 50 meV, is $(I_{30}/I_{50})_{exp}$ 4.8(1.4); the calculated values within S1 and S2 models, are $(I_{30}/I_{50})_{calc}(\mathrm{S1}) \sim 2.91$ and $(I_{30}/I_{50})_{calc}(\mathrm{S1}) \sim 2.54$, consistent within a factor of 2 which can be regarded as reasonably satisfactory given that data has not been corrected for absorption effects and non-spherical magnetic form factor.

From the discussion above we observe that both sets of parameters obtained for the two scenarios, S1 and S2 can explain to a certain approximation all the quantities extracted experimentally. The only calculated quantity in both scenarios, S1 and S2, which is not measurable experimentally is the absolute value of total energy of the ground state for Co^{2+} ions, see Figure 5.13, which is lower for scenario S1 than scenario S2. To try and distinguish further between these two sets of parameters we compare our calculated transitions energies with the ones obtained by optical measurements in the following section section.

For completeness Tables 5.10 and 5.11, lists explicitly the coefficients of the wavefunction for the ground state doublet (for both models S1 and S2), in the basis $|M_L, M_S\rangle$, in the local **XYZ** reference frame.

5.9 Comparison with Optical measurements

Optical transitions are conventionally discussed using the so-called Tanabe-Sugano energy level diagrams calculated for high symmetry environments for all the electronic configurations [61]. The Tanabe-Sugano diagram for the $3d^7$ electronic configuration for a ideal octahedral environment (cubic symmetry) is shown in Figure 5.18. The Tanabe-Sugano diagram is a diagram which plots the (normalized) transition energies of an electronic transition (in units of E/B, B is the Racah parameter which reflects the electrostatic repulsion between the electrons in the 3d orbitals) on the vertical axis and the (normalized) crystal field splitting energy (in units of Dq/B) on the horizontal axis for all possible electronic states of the system. Dq is the crystal field splitting energy defined earlier. The lowest energy state is usually placed at the origin, and all other states are plotted relative to it. The number of curves intersected by a vertical line for a given pair of Dq and B, gives the number of possible transitions and therefore the number of expected spectral absorption features. For a free ion (Dq = 0) with incomplete shell there are many possibilities of arranging electrons in orbitals leading to different electronic states, called Russell-Saunders states. We discussed earlier that these states are labeled by the term symbol, $^{2S+1}$L, where where 2S+1 is the spin multiplicity and for each quantum number L which shows the orbital degeneracy, the term symbol is replaced by a letter (for example L=0, 1, 2, 3, 4 ,5 corresponds to S, P, D, F, G, H). A few of the free ion states are labed on the left side of the Tanabe-Sugano diagram, Figure 5.18. Once the ion is placed in a crystal (Dq $\neq$ 0) the new states describing the electronic configuration are labeled by the molecular term borrowed from the group theory of levels according to symmetry; the letters $^{2S+1}A_p$, $^{2S+1}E_p$ and $^{2S+1}T_p$ refer to a single, doubly and triply degenerate state; the left superscript (2S+1) represents the spin multiplicity of the state and the right subscripts p represents an index used in the group theory classification. For values of Dq/B < 2.2 (left side of the dashed vertical line in Figure - 5.18) the system is in the high spin (HS) state (S = 3/2) with a triplet orbital ground state ($^4T_1$) and for values of Dq/B > 2.2 (right side of the dashed vertical line in Figure - 5.18)

the system is in the low spin (LS) state (S = 1/2) a with a doublet orbital ground state (^{2}E). If the symmetry of the environment is lower than cubic, the degeneracy of all the molecular states showed in the Tanabe-Sugano diagram, Figure 5.18 will be lifted but the energy splitting within the doublets(E) and triplets(T) will be small compared with the energy difference between the molecular states in the cubic symmetry. In general these diagrams are used to identify the individual or groups of transitions energies seen experimentally between the molecular states.

From optical measurements on this system it is found that Dq/B $\sim$ 0.96 [67] (the solid line in Figure - 5.18 represents this system on the Tanabe-Sugano diagram). Assuming that Co^{2+} ions are inside an ideal octahedra (Oh symmetry) and using the experimental value Dq/B together with Tanabe-Sugano diagram (see Figure 5.18) it is possible to identify all the transitions energies seen experimentally in optical measurements [67]. In the Oh symmetry, the ground state of the Co^{2+} ion is $^4T_1$ (this state comes from the atomic term ^{4}F, Figure 5.8, red circles); because the photon operator does not change the spin components during the transition, only transitions between states with the same spin component are possible; spin allowed d-d transition from the $^4T_1$ ground state are towards $^4T_2$, $^4A_1$ (states which come from the atomic term ^{4}F) and towards $^4T_1$ (state which comes from the atomic term ^{4}P), see the intersection of the solid line at Dq/B $\sim$ 0.96 with the higher energy levels (with the same spin multiplicity as the ground state) in Figure 5.18. The ground state term and the first two excited states in the Tanabe-Sugano diagram corresponds to the triplet orbital ground state and the two excited states separated by 8Dq and 18Dq from Figure 5.19; by taking into account the distortion of the octahedron we see in Figure 5.19 that the orbital degeneracy is completely lifted. In Ref. [67] transition energies from the ground state to all the excited states extracted experimentally from optical measurements (these transitions are shown schematically in Figure - 5.19); using a different approach than the one used here the transition energies extracted from the optical data were modeled in [67]; these transitions are shown schematically in Figure 5.19. In Table 5.9, first and second column show the experimental ($\varepsilon_{optic}^{obs}$) and calculated ($\varepsilon_{optic}^{calc}$)

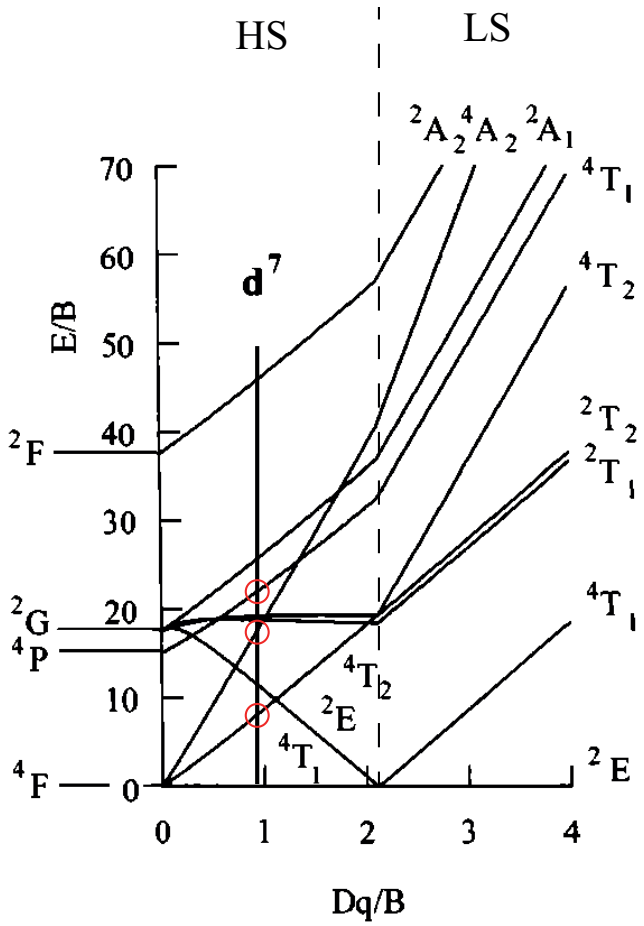

Figure 5.18 Tanabe-Sugano diagram for the $3d^7$ configuration for an octahedral environment. For Dq/B = 0 the states are labeled using the spetroscopic symbol notation (left side of the diagram Dq =0) and for Dq/B > 0 the states are labeled using the molecular term notation.

.

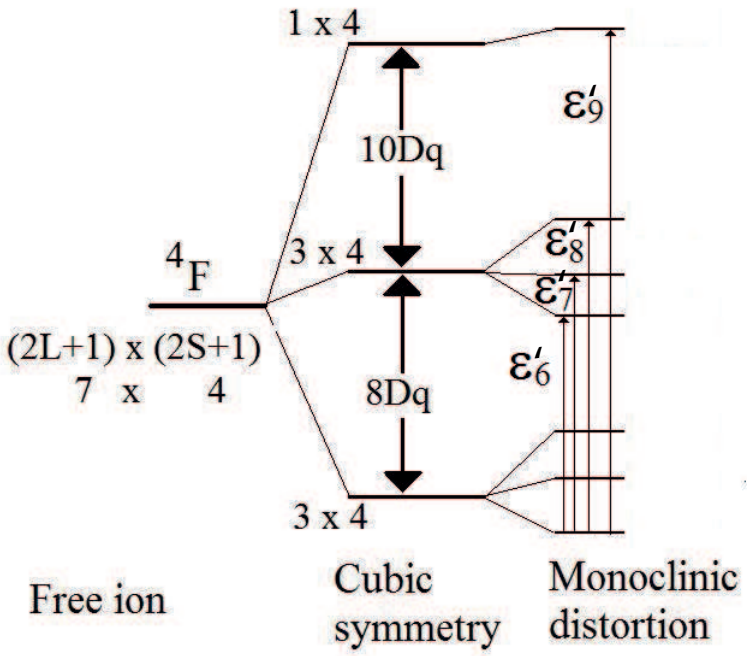

Figure 5.19 From left to right we show a schematic diagram of the energy levels when the Co^{2+} ion is placed inside an environment of spherical, cubic and monoclinic symmetry. The transitions obtained from optical measurements are shown by the vertical arrows.

.

transition energies taken from [67]. We calculated these transition energies using the present crystal

Table 5.9 Transition energies(see Figure - 5.19) from optical measurements and obtained in various models.

$Transition-energy(meV)$	$\varepsilon^{obs}_{optic}$	$\varepsilon^{calc}_{optic}$	ε^{calc}_{S1}	ε^{calc}_{S2}	$\varepsilon^{obs}_{neutrons}$
ε'_6	787	780	644(8)	571(8)	737(15)
ε'_7	818	817	816(5)	702(5)	–
ε'_8	843	875	849(10)	803(7)	–
ε'_9	1698	1728	1608(3)	1444(3)	–

field modeling in scenarios, S1 and S2. Because in our case we included in the calculations the spin-orbit and exchange effects, the orbital and spin degeneracy is completely lifted (the orbital singlet states with spin multiplicity equal with four shown in Figure 5.10 for monoclinic symmetry will be split into four states very close in energy due to the spin-orbit and molecular field effects). In order to compare the calculated transition energies using our approach with the ones obtained from optical measurements, we have averaged the four transition energies coming from lifting the spin degeneracy of the orbital singlet state. The calculated average transition energies are shown in table 5.9, third column for the empirical crystal field parameters obtained in scenario S1 and forth column for empirical crystal field parameters in scenario S2. The error bar interval for the calculated values is chosen such that the energy of all four states coming from lifting the spin degeneracy of an orbital singlet state are include in the confidence interval. The values in both models are reasonably consistent with the optical data with S1 favoring slightly better for the ε'_6 and ε'_7.

5.10 Conclusions

The energies of the crystal field transitions measured using time-of-flight inelastic neutron scattering in the Ising ferromagnetic $CoNb_2O_6$ have been analyzed using a microscopic model for all relevant interactions. The terms included in the total Hamiltonian were the crystal field, the spin-orbit and the molecular exchange mean- field. Two different approaches, a point charge model (PCM) and a simple overlap model (SOM), have been used to obtain initial theoretical values for the crystals field parameters B_q^k. The parameters in the PCM largely underestimated the overall energy scales for crystal field splitting obtained experimentally; this was attributed to neglect of hybridizations effects as the electrostatic energy is sensitive to the overlap of the finite-extent orbitals at the transition-metal and the ligands site. The SOM model includes these hybridizations effects in a first approximation and can reproduce to a good approximation the overall energy scales seen experimentally, but predicts an easy axis orientation at a large angle away from the allowed directions found by neutron diffraction measurements (in the ac plane at $\xi_{Co1} = 31\ ^\circ$ (model S1) or at -ξ_{Co1} (model S2)). Using the crystal field parameters calculated in the SOM model as starting values in our fits to the data, we obtained empirically (including constraints to the direction of the easy axis), two sets of crystal field parameters (for models S1 and S2). Both models gave a consistent description of not only the transition energies levels observed in neutron measurements up to 800 meV (including the trends in intensity for transitions to higher levels), but also optical transitions (to higher crystal field levels up to 1.6 eV), furthermore the magnitude of the ordered moment in the ground state is also reproduced and indicates a large component from the unquenched orbital moment. This analysis provides a natural explanation and quantitative description of the origin of the strong Ising anisotropy of Co^{2+} ions, attributed to the combined effect of crystal field from a largely-distorted octahedral ligand environment and a comparable spin-orbit coupling λ. The quantitative microscopic models presented here for the magnetic Hamiltonian of Co^{2+} ions taking into account all terms allowed by the low local symmetry with realistic values obtained from

the PCM/SOM models and constraints to reproduce quantitatively a wide range of very different experimental measurements such as the transition energies obtained from neutron/optical measurements, the magnitude of the ordered moment and the direction of the easy axis; these results are considerable improvement to previous proposals of the magnetic Hamiltonian [77], which included an over-simplified model for the crystal field, fitted only to magnetization data and largely inconstant with the crystal field level scheme measured with neutron scattering. The explicit values of the wavefuctions of the ground state doublets (Table **??**) is the starting point in deriving a microscopic effective hamiltonian for the exchange-driven spin dynamics in the lowest doublet. Already high-resolution neutron scattering have shown that in addition to the dominant Ising interaction $J\sigma_i^z\sigma_{i+1}^z$ there are significant (~ 15 %) other terms in the spin Hamiltonian which are responsible for the soliton dispersion and bound state formation, not predicted by the pure Ising $J\sigma_i^z\sigma_{i+1}^z$ term. Knowing explicitly the true spin and orbital component of the ground state doublet should allow an explicit derivation of all such subleading term and provide a macroscopic understanding of why they occurs and what their magnitude is. It may well be the case that when this is done only one of the two models presented here (S1 or S2) will be consistent with the observed magnitude of the soliton band width dispersion and bound state energies and that would uniquely define the microscopic Hamiltonian. This is important because $CoNb_2O_6$ is one a the very few systems that can be driven experimentally through a continuous quantum phase transition by transverse magnetic fields (in fact illustrates the key paradigm of the 1D Ising criticality) and detailed comparison of data with theory of quantum criticality requires including the subleading (beyond Ising) terms in the Hamiltonian.

Table 5.10 Wave function coefficients $c_{j\downarrow}$ and $c_{j\uparrow}$ of the lowest doublet $\Psi_{0\downarrow}$ and $\Psi_{0\uparrow}$ for model S1, where $\Psi_{0\downarrow\uparrow} = \sum_{j=1,\ldots,28} c_{j\downarrow\uparrow} |M_L M_S\rangle_j$.

$\Psi_{0\downarrow\uparrow}$ - S1	$c_{j\downarrow} - S1$	$c_{j\uparrow} - S2$	$\Psi_{0\downarrow\uparrow}$	$c_{j\downarrow}$	$c_{j\uparrow}$
$\|+3,+1.5\rangle_1$	-0.19656	-0.45541	$\|-3,-1.5\rangle_{28}$	0.45541	-0.19656
$\|+3,+0.5\rangle_2$	0.18258	-0.29474	$\|-3,-0.5\rangle_{27}$	-0.29474	-0.18258
$\|+3,-0.5\rangle_3$	-0.01265	-0.10716	$\|-3,+0.5\rangle_{26}$	0.10716	-0.01265
$\|+3,-1.5\rangle_4$	0.04753	-0.03459	$\|-3,+1.5\rangle_{25}$	-0.03459	-0.04753
$\|+2,+1.5\rangle_5$	0.00919	-0.03242	$\|-2,-1.5\rangle_{24}$	-0.03242	-0.00919
$\|+2,+0.5\rangle_6$	0.00705	-0.00981	$\|-2,-0.5\rangle_{23}$	0.00981	0.00702
$\|+2,-0.5\rangle_7$	-0.00735	-0.00085	$\|-2,+0.5\rangle_{22}$	-0.00085	0.00735
$\|+2,-1.5\rangle_8$	0.02316	0.01439	$\|-2,+1.5\rangle_{21}$	-0.01439	0.02316
$\|+1,+1.5\rangle_9$	0.04035	0.06585	$\|-1,-1.5\rangle_{20}$	-0.06585	0.04035
$\|+1,+0.5\rangle_{10}$	-0.09408	0.05187	$\|-1,-0.5\rangle_{19}$	0.05187	0.09408
$\|+1,-0.5\rangle_{11}$	0.25664	0.2119	$\|-1,+0.5\rangle_{18}$	-0.2119	0.25664
$\|+1,-1.5\rangle_{12}$	-0.38449	0.17357	$\|-1,+1.5\rangle_{17}$	0.17357	0.38449
$\|0,+1.5\rangle_{13}$	-0.00289	0.16471	$\|0,-1.5\rangle_{16}$	0.16471	0.00289
$\|0,+0.5\rangle_{14}$	0.25658	0.46623	$\|0,-0.5\rangle_{15}$	-0.46623	0.25658

Table 5.11 Wave function coefficients $c_{j\downarrow}$ and $c_{j\uparrow}$ of the lowest doublet $\Psi_{0\downarrow}$ and $\Psi_{0\uparrow}$ for model S2, where $\Psi_{0\downarrow\uparrow} = \sum_{j=1,\ldots,28} c_{j\downarrow\uparrow} |M_L M_S\rangle_j$.

$\Psi_{0\downarrow\uparrow}$ - S2	$c_{j\downarrow} - S1$	$c_{j\uparrow} - S2$	$\Psi_{0\downarrow\uparrow}$	$c_{j\downarrow}$	$c_{j\uparrow}$
$\|+3,+1.5\rangle_1$	-0.00041	0.66465	$\|-3,-1.5\rangle_{28}$	-0.66465	-0.00041
$\|+3,+0.5\rangle_2$	-0.28519	-0.00054	$\|-3,-0.5\rangle_{27}$	-0.00054	0.28519
$\|+3,-0.5\rangle_3$	0.00185	-0.03895	$\|-3,+0.5\rangle_{26}$	0.03895	0.00185
$\|+3,-1.5\rangle_4$	0.06269	-0.00031	$\|-3,+1.5\rangle_{25}$	-0.00031	-0.06269
$\|+2,+1.5\rangle_5$	-0.02532	0.01107	$\|-2,-1.5\rangle_{24}$	0.01107	0.02532
$\|+2,+0.5\rangle_6$	-0.00407	-0.00964	$\|-2,-0.5\rangle_{23}$	0.00964	-0.00407
$\|+2,-0.5\rangle_7$	0.01194	-0.00241	$\|-2,+0.5\rangle_{22}$	-0.00241	-0.01194
$\|+2,-1.5\rangle_8$	0.00248	-0.02430	$\|-2,+1.5\rangle_{21}$	0.02430	0.00248
$\|+1,+1.5\rangle_9$	-0.00115	0.04089	$\|-1,-1.5\rangle_{20}$	-0.04089	-0.00115
$\|+1,+0.5\rangle_{10}$	-0.02117	-0.00422	$\|-1,-0.5\rangle_{19}$	-0.00422	0.02117
$\|+1,-0.5\rangle_{11}$	0.00354	-0.26376	$\|-1,+0.5\rangle_{18}$	0.26376	0.00354
$\|+1,-1.5\rangle_{12}$	0.49747	-0.00088	$\|-1,+1.5\rangle_{17}$	-0.00088	-0.49747
$\|0,+1.5\rangle_{13}$	-0.01037	0.00841	$\|0,-1.5\rangle_{16}$	0.00841	0.01037
$\|0,+0.5\rangle_{14}$	-0.00471	-0.38786	$\|0,-0.5\rangle_{15}$	0.38786	-0.00471

Chapter 6

Phase diagram and magnetic excitations in quantum XY-antiferromagnet Cs_2CoCl_4 in transverse field

This chapter describes elastic and inelastic time-of-flight single crystal neutron scattering experiments to explore the magnetic order and spin dynamics in the quasi-one-dimensional spin-1/2 XY antiferromagnet Cs_2CoCl_4 in a magnetic field applied close to the XY plane which drives a transition from spontaneous long-range magnetic order to a gapped quantum paramagnet. The commensurate antiferromagnetic order observed at low field is stable over a wide field range but is replaced by an incommensurate magnetic order (spin density wave) just below the transition to paramagnetic. Deep in the paramagnetic phase the excitations are sharp, gapped magnons with minima at the incommensurate wavevectors of the magnetic order below B_C = 2.36(2) T and the dispersion relations give values for the intra- and inter-chain couplings. In addition to one-magnon excitations at high energies we also observe weak magnetic continuum scattering, which becomes stronger upon approaching the critical field from above and is attributed to multi-magnon

scattering processes.

6.1 Introduction

Quantum fluctuations become significant as the system lowers its dimensionality and the value of the spin quantum number. In the extreme case of 1D quantum magnets with S = 1/2, quantum fluctuations are very strong and may stabilize novel ground states or spin dynamics; because magnetic fields have a direct influence on the quantum fluctuations especially when the magnetic field is applied perpendicular to the direction of the magnetic moments (transverse field effects), the field "can" control the quantum fluctuations to stabilize novel ordered phases or phase transitions [42]. The purpose of the work presented here was to investigate the phase diagram of the quasi-one dimensional spin-1/2 easy-plane antiferromagnet Cs_2CoCl_4 in magnetic fields using single crystal neutron scattering. The particular aim was to see how magnetic order and spin excitations evolve as the system undergoes a phase transition at high field where the spontaneous magnetic order is suppressed. Spins in Cs_2CoCl_4 have a dominant nearest-neighbor antiferromagnetic exchange interaction along the crystallographic **b** axis and also the local crystal field environment is such the spins have strong easy-plane anisotropy. Although Co^{2+} ions have a free spin of $\tilde{S} = 3/2$ inside the lattice, crystal field effects + spin-orbit interaction split the 28 fold degenerate free ion manifold for spin ($\tilde{S}$ = 3/2) and orbital (L = 3) states in a set of Kramers doublets (as in previous chapter), and here the lowest doublet can be described by an "effective" S = 1/2 spin with strong easy-plane anisotropy (as opposite to easy-axis in $CoNb_2O_6$) and at low temperature the dynamics inside the lowest doublet can be modeled by an effective spin S = 1/2 and XXZ antiferromagnetic interactions. The scenario we investigate experimentally is that of the 1D spin-1/2 XXZ model in a magnetic field applied at an angle with respect to the XY-plane, with the following Hamiltonian:

$$\mathbf{H} = \mathbf{H}_{XXZ} + \mathbf{H}_{XZ} \tag{6.1}$$

where $\mathbf{H}_{XXZ}$ is the Hamiltonian describing the XXZ antiferromagnetic interactions

$$\mathbf{H}_{XXZ} = J\sum_{n}\left(\mathbf{S}_n^x\mathbf{S}_{n+1}^x + \mathbf{S}_n^y\mathbf{S}_{n+1}^y + \Delta\mathbf{S}_n^z\mathbf{S}_{n+1}^z\right) \tag{6.2}$$

and $\mathbf{H}_{XZ}$ is the Hamiltonian describing the interaction of the system with the external magnetic field

$$\mathbf{H}_{XZ} = g_x\mu_B B_x\sum_{n}\mathbf{S}_n^x + g_z\mu_B B_z\sum_{n}\mathbf{S}_n^z \tag{6.3}$$

J > 0 is the antiferromagnetic (AF) exchange constant and Δ = 0.25 is the anisotropy parameter in the limit where the exchange J is much smaller than the energy separation between the first two Kramer doublets. The operators $\mathbf{S}_n^\alpha$, where α = x, y, z, are the usual spin operators for the spin-1/2 and $\mathbf{H}_{XZ}$ doesn't commute with the exchange Hamiltonian, [H_{XXZ}, H_{XZ}] $\neq$ 0 for $B_x \neq 0$, so S_x is not a conserved quantity. It was proposed [78] that low-energy properties of Cs_2CoCl_4 is described by Eq. 6.2 with J = 0.23 meV and Δ = 0.25, therefore the physics should be well approximated by the famous XY model (Δ = 0) [79].

The physics of the non-interacting 1D chains described by the $\mathbf{H}_{XXZ}(\Delta)$ with Δ = 0 is well known in the scenario where there are no magnetic fields $B_x = B_z = 0$ and in the scenario where we only have a commutating magnetic field $B_z \neq 0$ [80]. In contrast, the physics of $\mathbf{H}_{XXZ}(\Delta = 0)$ with field along x, $B_x \neq 0$ and B_z = 0, is neither trivial nor widely known. The action of a non-commuting field B_x have been considered theoretically in [81, 82]. From these theoretical studies is was found that the in-plane field B_x has two effects: 1) to lower the symmetry of the XY model to Ising-like and 2) to introduce quantum fluctuations into the system. At high fields, quantum fluctuations destroy the long range order. This disordering field is below that where the system reaches its saturation point. This phase transition is therefore a nontrivial quantum phase transition through a quantum critical point with noncommuting field as control parameter. More complicated theoretical calculations have been recently done [83], for the 1D chains described by the $\mathbf{H}_{XXZ}(\Delta)$ with Δ = 0.25 in noncommuting field, including small interchain exchange interactions. The results are summarized in Figure - 6.1. From these calculations it was found that: 1) the main effect of

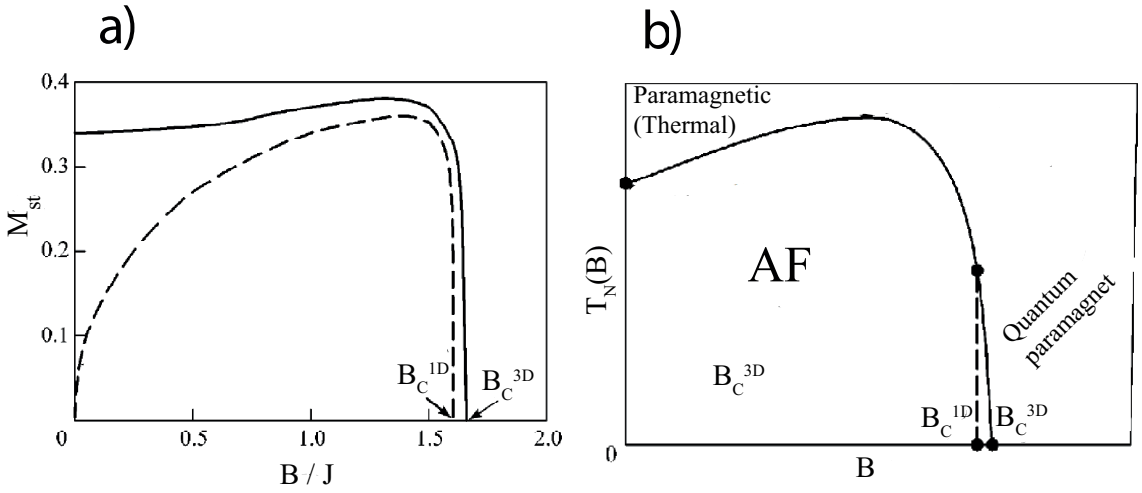

Figure 6.1 (a) The dependence of the long range magnetic order pramater M_{st} (staggered magnetization) on magnetic field B_x ($B_z = 0$) for the 1D chain (dashed line) and quasi-1D system (colid line) for $\Delta = 0.25$. (b) Expected phase diagram for the model descibed by Eq. 6.1 with $\Delta = 0.25$ and $B_z = 0$. These two plots are taken from [83].

interchain coupling on the system of coupled XXZ chains consists in extending of the AF ordered phase to finite temperatures, see Figure - 6.1 a); 2) in the presence of transverse magnetic field the 3D effects become less pronounced. They lead to a small shift of the critical field, see Figure - 6.1 b). The consideration of small interchain interactions implies that the properties of the model given by Eq. 6.1 with $\Delta = 0.25$ and $B_z = 0$, in transverse magnetic field B_x are similar to that of 1D quantum ising model in a magnetic field. One of the aims of this chapter is to present a detailed study of the experimental phase diagram of Cs_2CoCl_4. We will show that the presence of frustrated interchain interactions stabilize a new incommensurate magnetic phase close to the critical field which is not predicted by the theoretical phase diagram shown in Figure - 6.1 b).

6.2 Crystal Structure and zero field magnetic structure

The crystal structure of Cs_2CoCl_4 in shown in Figure - 6.2 a); it has orthorhombic space group Pnma (No. 62) with the lattice parameters at T = 0.3 K, a = 9.71 Å, b = 7.27 Å, and c = 12.73

Å [84]; the relative atomic coordinates used for the calculation of the nuclear structure factors are given in Table - 6.1. The chemical unit cell contains four equivalent Co^{2+} ions at sites 4c, surrounded by a tetrahedron of the chlorine ions, see Figure - 6.2. Small distortions from a perfect

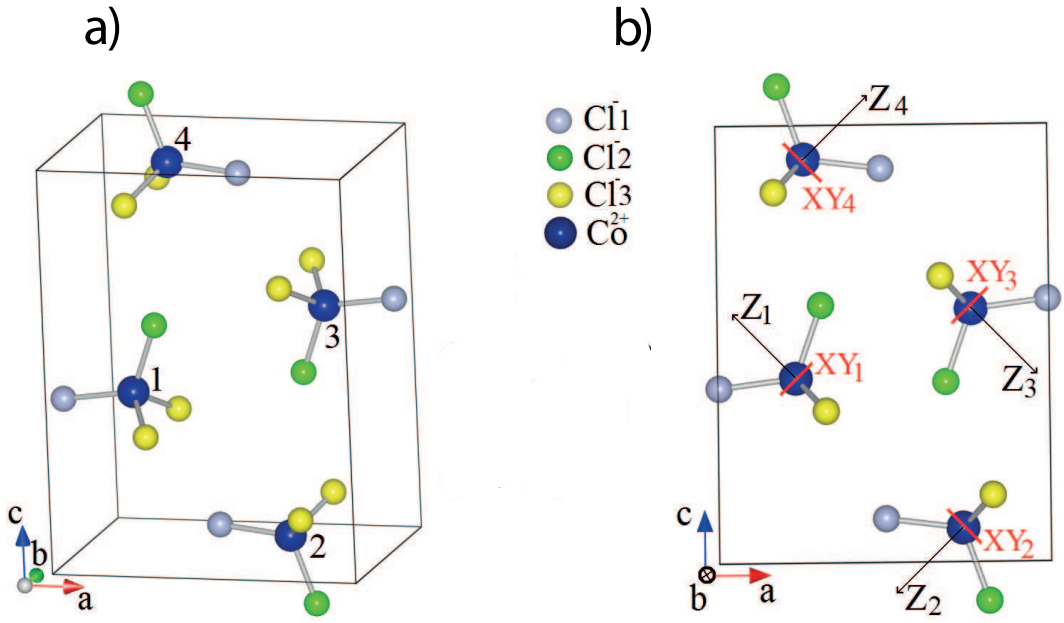

Figure 6.2 (a) 3D view of the crystal structure of Cs_2CoCl_4; there are four Co^{2+} ions in the unit cell (4c sites) labeled from 1-4. (b) Projections onto the **ac**-plane showing the orientation of the local XY planes for each Co^{2+} ion in the unit cell; magnetic chains run along **b** axis perpendicular to plane of the paper; the local Z axis is normal to the XY planes and bisect the largest angle of the distorted tetrahedrons.

tetrahedron lead to a splitting of the orbital singlet with true spin $\tilde{S}$ = 3/2 into two Kramers doublets with a separation 2D = 1.3(1) meV. The magnetic exchange energy is much lower than the inter-doublet separation and therefore only the lowest-lying doublet states $\tilde{S}_z = \pm 1/2$ participate in the low-energy dynamics at low temperatures (k_BT « 2D, D is the parameters which characterize the plane anisotropy). Projecting the Heisenberg exchange (Eq. 6.4), between the true spins, onto the lowest-lying doublet of $\tilde{\mathbf{S}}_z = |\pm 1/2\rangle$ states, gives an effective spin S = -1/2 Hamiltonian H_{XXZ}

Table 6.1 Atomic positions in the unit cell for Cs_2CoCl_4.

Atom name	Ion type	Wyckoff position	x/a	y/a	z/a
$Cs1$	$Cs1^{1+}$	4c	0.14013	0.25000	0.10074
$Cs2$	$Cs2^{1+}$	4c	0.47776	0.25000	0.82360
$Co1$	Co^{2+}	4c	0.73514	0.25000	0.07772
$Cl1$	$Cl1^{1-}$	4c	0.50372	0.25000	0.09993
$Cl2$	$Cl2^{1-}$	4c	0.81234	0.25000	0.91120
$Cl3$	$Cl3^{1-}$	8d	0.17400	0.00180	0.84720

with XY-like exchange which is described by the Eq. 6.1 with $\Delta = 0.25$ in the limit I « 2D.

$$\mathbf{H} = I\tilde{\mathbf{S}}_1\tilde{\mathbf{S}}_2 + D(\tilde{\mathbf{S}}_1^z)^2 + D(\tilde{\mathbf{S}}_2^z)^2 \tag{6.4}$$

Rotations of the $CoCl_4$ tetrahedra in the unit cell lead to different orientations of the XY easy plane between sites (1, 3) and (2, 4) and give the **b** axis as the only common in-plane direction for all sites. The geometrical distortions from a perfect tetrahedron environment are mostly angular; there is no significant difference in any of the respective Co - Cl bond lengths. The main distortion from a ideal tetrahedron is due to one of the four Cl^- ions being rotated by several degrees around the **b**-axis with respect to the central Co^{2+} ion and previous studies [85] proposed that the normal to the XY easy plane (local Z-axis) bisects this angle; see Figure - 6.2 (b). Neighboring Co^{2+} ions interact via superexchange interaction involving a bridge of two Cl^- ions with the path Co^{2+}-Cl^--Cl^--Co^{2+}. The shortest Cl^--Cl^- distance is between neighbours along the **b**-axis separated by $d_{Cl3^-Cl3^-} =$ 3.61 Å, see Figure - 6.3 a), giving a planar path Co^{2+}-Cl^--Cl^--Co^{2+}. As this is close to twice the ionic radius of Cl^- a sizeable overlap of electron wave functions contributing to the exchange integral is expected. Thus the important interaction is assumed to be the intrachain exchange J, between the two nearest - neighbors (NN) ions along the **b**-axis. Among other possible exchange

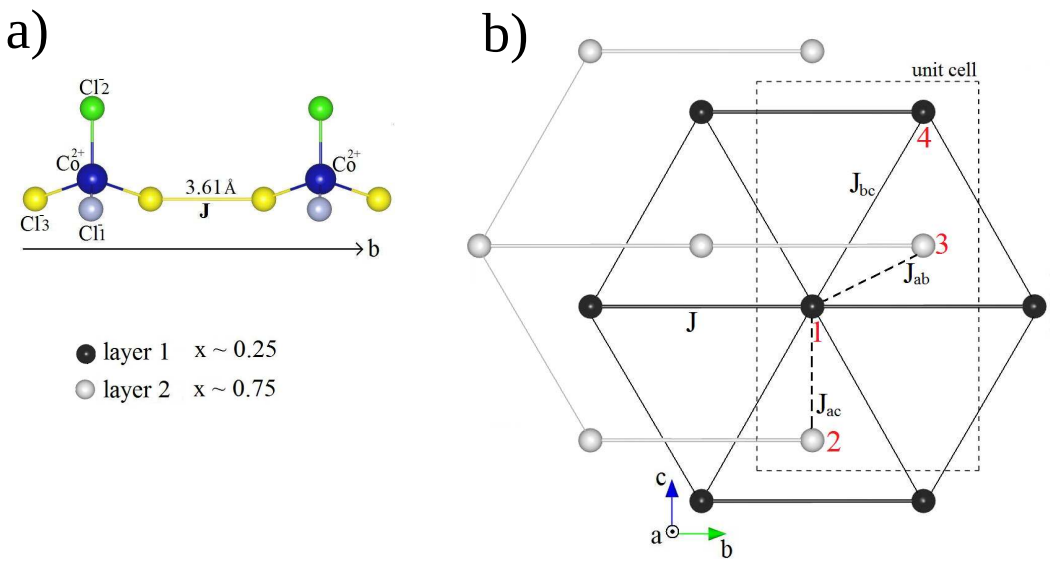

Figure 6.3 (a) the superexchange path Co^{2+}-Cl^{-}-Cl^{-}-Co^{2+} along the **b** axis; Co^{2+} ions are separated by two chlorine ions with the shortest distance between them suggesting that the Co^{2+} ions interact mainly via an AF superexchange interaction J along the **b** axis, forming AF spin chains which interact weakly via superexchange. (b) Crystal structure of Cs_2CoCl_4 projected onto the **bc**-plane showing the possible exchange paths (only the Co^{2+} ions are shown).

paths we have J_{bc} between Co1 - Co4 ($d_{Cl3^- - Cl2^-}$ = 3.99 Å), J_{ac} between Co1 - Co2 ($d_{Cl3^- - Cl1^-}$ = 4.03 Å) and J_{ab} between sites Co1 - Co3 ($d_{Cl2^- - Cl3^-}$ = 4.04 Å); in terms of these exchange integrals a Co1 ion is interacting with two Co1 ions through J, with four Co4 ions through J_{bc}, with four Co3 ions through Jab and with two Co2 though J_{ac}. Using the measured dispersion relation at 4 T we obtained a quantitative Hamiltonian parametrization in terms of these exchange integrals. Since these exchange paths are non-collinear, the orbital overlap is expected to be small than for the J path, and subsequently the interaction to be smaller J_{ab}, J_{bc}, J_{ac} « J [86,87]. Previous neutron scattering measurements in zero field [78] already showed that interchain couplings stabilize long-range order (LRO) below T_N = 217 mK with the spins ordered antiferromagnetically along the chain direction and the moments confined in the bc-plane very close to the b axis.

6.3 Experimental details and Data Analysis

In the resent study we performed elastic and inelastic neutron scattering measurements using the time-of-flight neutron scattering spectrometer OSIRIS at the pulsed neutron source ISIS. The sample was a 9 g flat plate crystal of approximate 5 mm along the b axis thickness optimized to minimize neutron absorption. The sample was aligned with the **bc** scattering plane horizontal and nuclear and magnetic peaks in the **bc** plane were measured using the two horizontal diffraction backscattering banks of detectors, which are placed in a ring around the incident beam, covering the range of scattering angles 2θ from 150^o to 171^o. When the instrument was used in diffraction mode the wavelength defining choppers were running at a frequency of 25 Hz, producing a selectable, 4 Å wide wavelength band at the sample position. By changing the phase of the choppers we were able to select different wavelength bands. The total d-spacing range covered during the experiment was from 1.7 to 11 Å. The raw diffraction intensities are registered as a function of arrival time at the detector and the position of the detector element. These intensities as a function of

time of flight and position of the detector element were converted to intensity as a function of neutron wavelength and scattering angle 2θ, thus allowing two dimensional maps, of the Bragg peak intensity in the horizontal plane to be collected, see Figure - 6.4. The two dimensional integrated

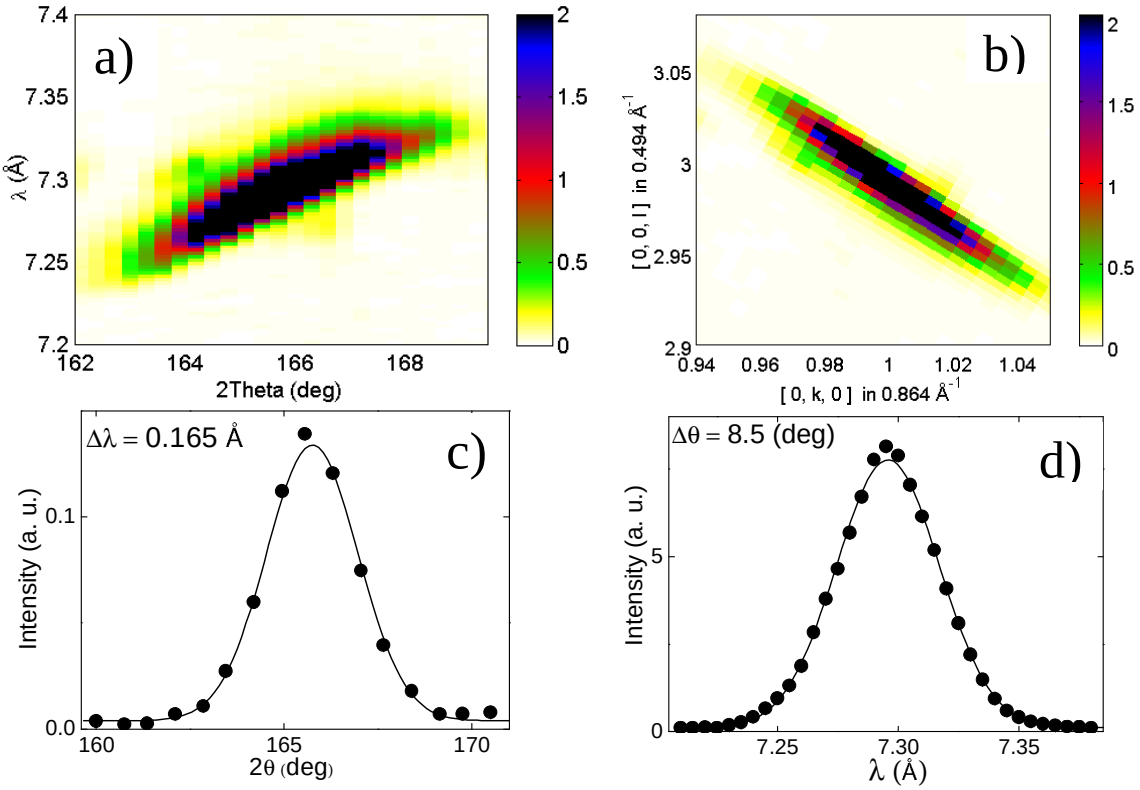

Figure 6.4 (a) 2D map of the (0, 1, 3) Bragg peak intensity as a function of the wavelength λ and the scattering angle 2θ; (b) 2D map of the same peak converted in the **bc** reciprocal plane axis; scans along 2θ and λ are shown in panel (c) and (d).

intensities of the Bragg peaks in the $(\lambda, 2\theta)$ plane,

$$I(\lambda_0) = \sum_{2\theta} \int_{\lambda} I(\lambda, 2\theta) d\lambda = \sum_{\lambda} \int_{2\theta} I(\lambda, 2\theta) d2\theta \tag{6.5}$$

are related to the Bragg peak structure factors by [88]:

$$I(\lambda_0) = C\Phi(\lambda_0)\varepsilon(\lambda_0)\varepsilon(\theta_B)A(\lambda_0, \theta_B)y(\lambda_0)|F|^2 \frac{\lambda_0^4}{\sin^2 \theta_B} + b \tag{6.6}$$

Where C is a overall scale factor, $2\theta_B$ is the nominal total Bragg scattering angle, $\lambda_0 = 4\pi \sin\theta_B/|\mathbf{Q}|_0$ is the nominal scattering wavelength and F is the nuclear/magnetic structure factor; F is the most important quantity we want to extract from the data because it is directly related to the crystal/magnetic structure. The peak center (λ_0, $2\theta_B$) was determined from fitting Gaussians to scans along λ and 2θ, see Figure - 6.4 (c) and (d). The wavelength dependent factors are: the incident flux $\Phi(\lambda_0)$; the detector efficiencies $\varepsilon(\lambda_0)$; the transmission factor $A(\lambda_0, \theta_B)$ which characterize the absorption effects in the sample; the extinction corrections $y(\lambda_0)$ and the Lorentz factor which for the time-of-flight neutron diffraction technique is $\frac{\lambda_0^4}{\sin^2\theta_B}$ [89]. The last term b, is the non-magnetic background which has contributions from both the empty sample holder as well as the sample itself (incoherent scattering). Due to the size of the crystal we expect significant extinction effects which will reduce the intensity of the strongest nuclear Bragg reflections. To extract F in absolute units of barns, we have to determine the scale constant C and to correct the data for all the wavelength dependent factors. Further we will describe the corrections done to the data:

1) To determine the wavelength dependence of the detector efficiency $\varepsilon(\lambda)$ (see Eq. 6.5) we measured the incoherent scattering from a standard vanadium sample (a solid cylinder of radius R = 0.25 cm). Because the incoherent scattering is isotopic the measured intensity will be wavelength dependent, due to the term like $\varepsilon(\lambda)$ and absorption effects in the vanadium sample. The vanadium intensity measured in each detector elements is given by:

$$I_i^V(\lambda) = C_V \Phi(\lambda)\varepsilon_i(\lambda)\varepsilon_i(\theta_B)A^V(\lambda, \theta_B) + B \tag{6.7}$$

The raw intensities of the incoherent vanadium scattering as a function of time of flight were converted to intensity as a function of neutron wavelength for each detector, thus obtaining two dimensional maps in the (λ, detector) plane, see Figure - 6.5 a). After the background (measured for the empty instrument) was extracted from all the 2D maps of vanadium intensity vs. wavelength and detector number, the detector efficiencies $\varepsilon_i(\theta_B)$ (see Eq. 6.7) were obtained from the vanadium data in the following way: we selected a narrow wavelength range (which didn't contain

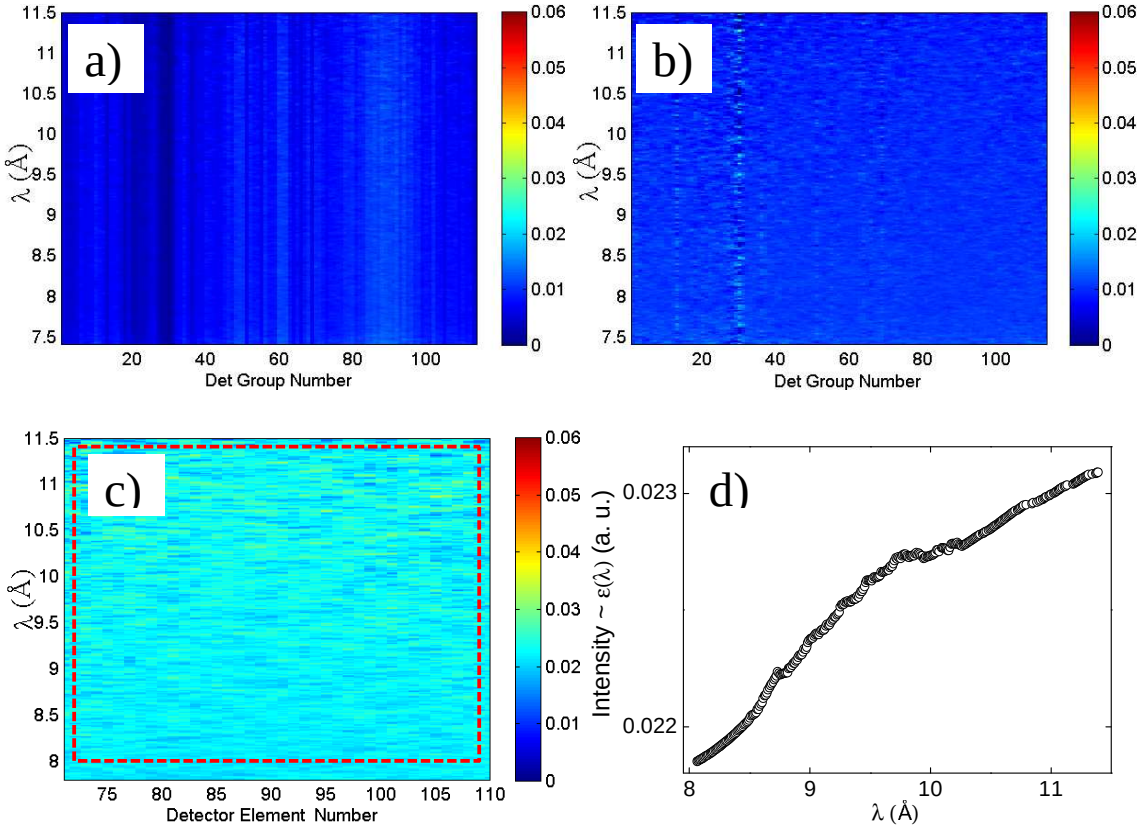

Figure 6.5 2D maps of the incoherent intensity scattered from vanadium as function of the wavelength and detector number; (a) raw intensity (b) intensity corrected for relative efficiencies between detectors $\varepsilon(\theta)$; (c) intensity corrected for $\varepsilon(\theta)$ and absorption A^V ; (d) scan along λ averaged between detectors; the intensity is proportional with $\varepsilon(\lambda)$.

any Bragg reflections from the vanadium sample or from the sample holder) and we averaged the intensity along the wavelength direction thus obtaining a one dimensional vector with the length equal with the number of the detector elements. Each number from the vector is proportional with the corresponding $\varepsilon(\theta_B)$. Finally to correct the intensity for $\varepsilon(\theta_B)$, we divided the vanadium intensity vs. wavelength by the corresponding number from the vector; by doing this type of correction we also corrected for any solid angle dependence. After this correction was done, the intensity was scaled with a constant such that the order of magnitude of the intensity didn't change, see Figure see Figure - 6.5 b). The data was also corrected for absorption effects; transmission factors for a cylindrical crystal were calculated in the literature [90] as a function of scattering angle θ and the dimensionless parameter μR, where μ is the linear absorption coefficient and R is the cylinder radius. The linear absorption coefficient [91] for vanadium is given by:

$$\mu_{vanadium}[cm^{-1}] = 0.20518\lambda + 0.36892 \tag{6.8}$$

where λ is in Å. μ was calculated using the absorption and incoherent cross section given in the literature [4]. By inspecting the transmission factors for fixed scattering angle ($A^V(\lambda, \theta_B$=fixed)), in the wavelength range where we want to extract the detector efficiencies we observe that the absorption effects are very important (there is a 40% decrease in the transmission factor between the extreme wavelength, 3 and 15 Å). The changes in transmission factors for fixed wavelength, in the range of the accessible scattering angles where we did measurements during the experiment are less than 5%. After all these corrections have done, the vanadium intensity vs. wavelength in each detector element is proportional with $\varepsilon(\lambda)$, see Figure 6.5 c); by inspecting the intensity in all the elements of a detector banks we see that they are approximately the same, as expected. We averaged the intensity over all the detector elements in a detector bank, see Figure - 6.5 d). The detectors efficiency $\varepsilon(\lambda)$ extracted from the vanadium data in consistent between the two detector banks as is shown in Figure - 6.6.

2) The intensity measured for Cs_2CoCl_4 was corrected for the wavelength dependence of the

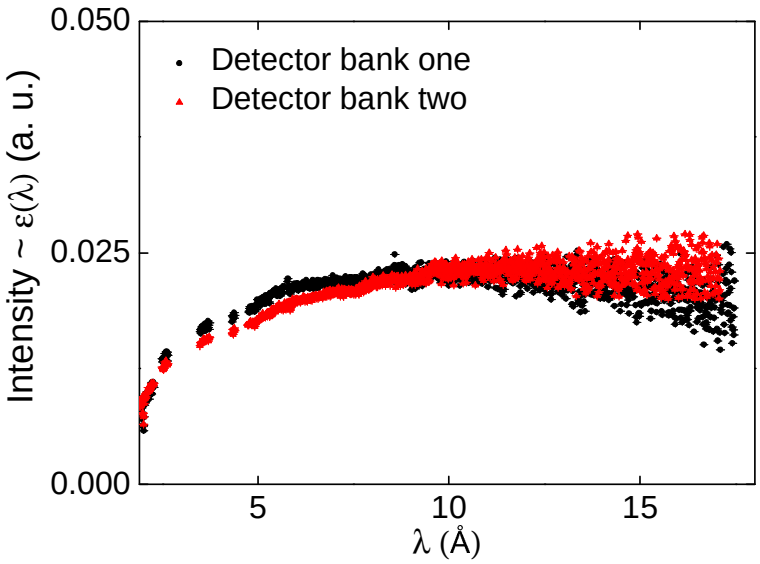

Figure 6.6 Vanadium intensity vs. lambda for the two detector banks after normalization by $\varepsilon(\theta)$ and absorption $A^V(\mu, \theta)$; the resulting values are proportional to the detector efficiencies as a function of wavelength.

detector efficiencies using $\varepsilon(\lambda)$ determined from the vanadium measurements ($\varepsilon(\lambda)$ are shown in Figure 6.6). The relative efficiencies of the various detectors $\varepsilon(\theta)$, was determined in the same way as for vanadium data but the one dimensional vector was obtained by averaging 14 different measurements with the same wavelength range on different orientations of the sample.

3) All integrated intensities for the nuclear and magnetic reflections calculated in the $(\lambda, 2\theta)$ plane as in Figure - 6.4 were corrected for neutron absorption effects using a Monte Carlo code for a rectangular sample of the same size as the actual crystal, taking into account the orientation of the sample with respect to the incident beam. The linear absorption coefficient used in modelling the neutron absorption in the sample was calculated using:

$$\mu_{Cs_2CoCl_4}[cm^{-1}] = 0.1176\lambda + 0.56729 \tag{6.9}$$

the formula was calculated using the absorption and incoherent absorption cross section given in the literature for Co, Cs and Cl atoms [4].

4) After all these corrections were done, the final integrated intensities were proportional with the structure factors squared $|F|^2$; in order to find the scale constant, C which transform the final integrated intensities into structure factors squared in absolute units of barns squared, we had to calculate the nuclear structure factors squared $|F_{calc}|^2$; for the calculations of the $|F_{calc}|^2$ we used the atomic positions from [92] and the nuclear scattering lengths for Cs, Co and Cl found in the literature [91]. A comparison between the theoretical and experimental structure factors is shown in Figure - 6.7 a). The same scaling constant was used to obtain the structure factors for the commensurate and incommensurate magnetic structures on an absolute scale. As a consistency

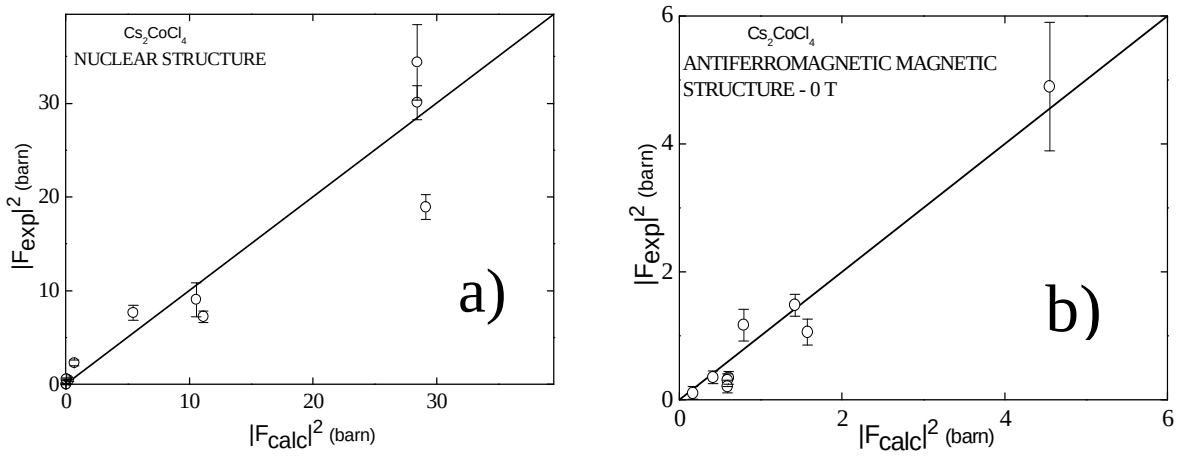

Figure 6.7 Experimental vs. calculated structure factors squared for (a) the nuclear and (b) zero field magnetic peaks. The solid line has unit slope.

check of the scaling constant and various corrections we calculated the expected magnetic structure factors for the zero field AF structure as determined previously [78] and compared them with the experimental structure factors extracted from the data on absolute scale, using the spherical form factors for Co^{2+} ions [4] and we obtained a very good agreement as shown in Figure - 6.7 b), which give us confidence about the scaling constant and all the corrections performed on the data in order to bring the structure factors squared in absolute units of barn.

In order to study the evolution of the zero field magnetic structure vs. field, we measured

the order parameter (integrated intensity vs. field) below T_N for different temperatures, with the magnetic field applied along the **a** axis. At each field (for fixed temperature) we determined the integrated intensity (by fitting Gaussians to the data) of the antiferromagnetic Bragg peak, from the 2D intensity maps in the (Q, 2θ) plane; for example in Figure - 6.8 we show the order parameter for the most intense magnetic diffraction peak of the AF structure, (0, 0.5, 1.5). This figure shows that the zero field magnetic order is suppressed by the quantum fluctuations in a first order phase transition.

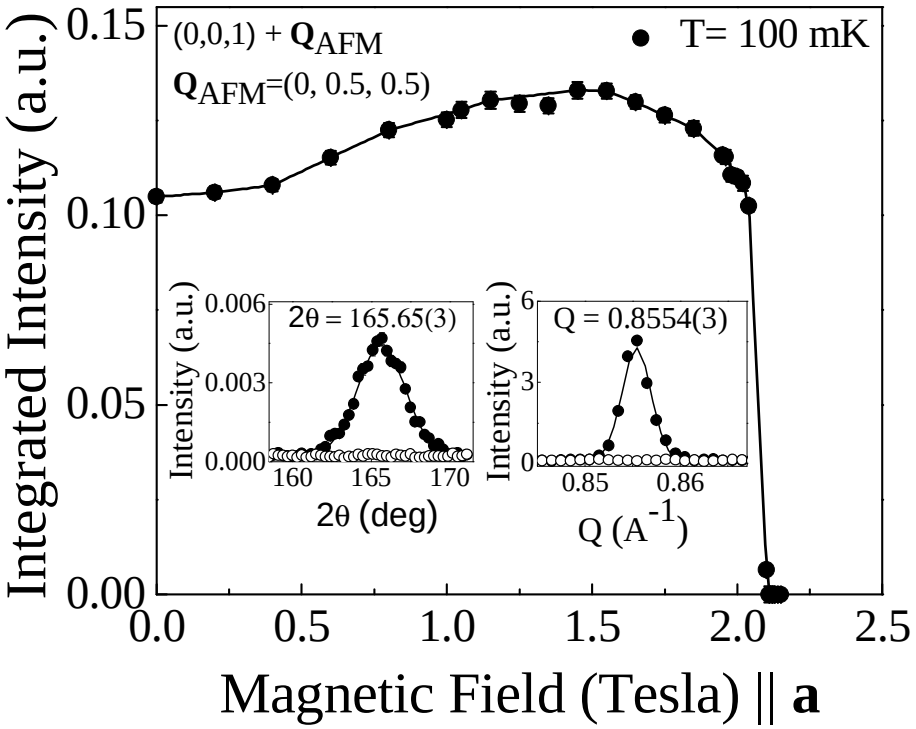

Figure 6.8 Intensity of the (0, 0.5, 1.5) AF Bragg reflection. The solid lines are guide for the eye. The insets show scans along Q = |**Q**| and 2θ for magnetic field below 2.1 T (solid symbols) and above (open symbols). The value of 2.1 T is the value of the magnetic field where the zero field AF order is suppressed.

6.4 Phase Diagram in applied magnetic field along the a - axis

In zero field the magnetic moments order antiferromagnetically and due to the competition between the antiferromagnetic exchange interactions and local anisotropy they are confined in the **bc**-plane, making a small angle with the **b** - axis [78]. The main interest of this project was to learn about the evolution of the AF magnetic order when we apply a magnetic field transverse to the plane of the magnetic moments and to see what happens at the transition field Bc where the magnetic order disappears. To achieve our aim, we measured order parameters at different fields and different temperatures. The results are summarized in Figure - 6.9. The commensurate (CM) magnetic order, a spin-flop like magnetic phase, disappears in a first order phase transition at the critical field 2.1 T and it coexists over a very narrow field range with an incommensurate (INC) magnetic order which is stable from 2.04(3) T up to 2.36(3) T. Typical order parameter plots for the CM and INC magnetic orders are given in Figure - 6.10 a) and b). We observe that in the region where the two phases coexists the CM ordering wave vector (0, 0.5, 0.5) jumps to the INC ordering wave vector (0, 0.5 - ε_0, 0), where ε_0 = 0.055 rlu; Wavevector scan through representative AF and INC phases are given in Figure - 6.11 a). The INC ordering wave vector is constant within errors over the whole field region where the INC phase is stable. as shown in Figure - 6.11 b). Above the critical field B_C the spontaneous magnetic order in the **bc**-plane disappears in a continuous phase transition.

6.5 Magnetic structure in the incommensurate high - field phase

The incommensurate magnetic phase is stable in field range 2.04 T < B < 2.36 T, applied along the **a** axis and is manifested experimentally in magnetic Bragg peaks at satellite positions (H, K, L)$^{\pm}$ = (H, K, L) $\pm$ q, where the incommensurate magnetic wave vector is q = (0, 0.5 - ε_0, 0), with ε_0 = 0.055 rlu being the incommensuration. In total thirteen magnetic Bragg peaks in

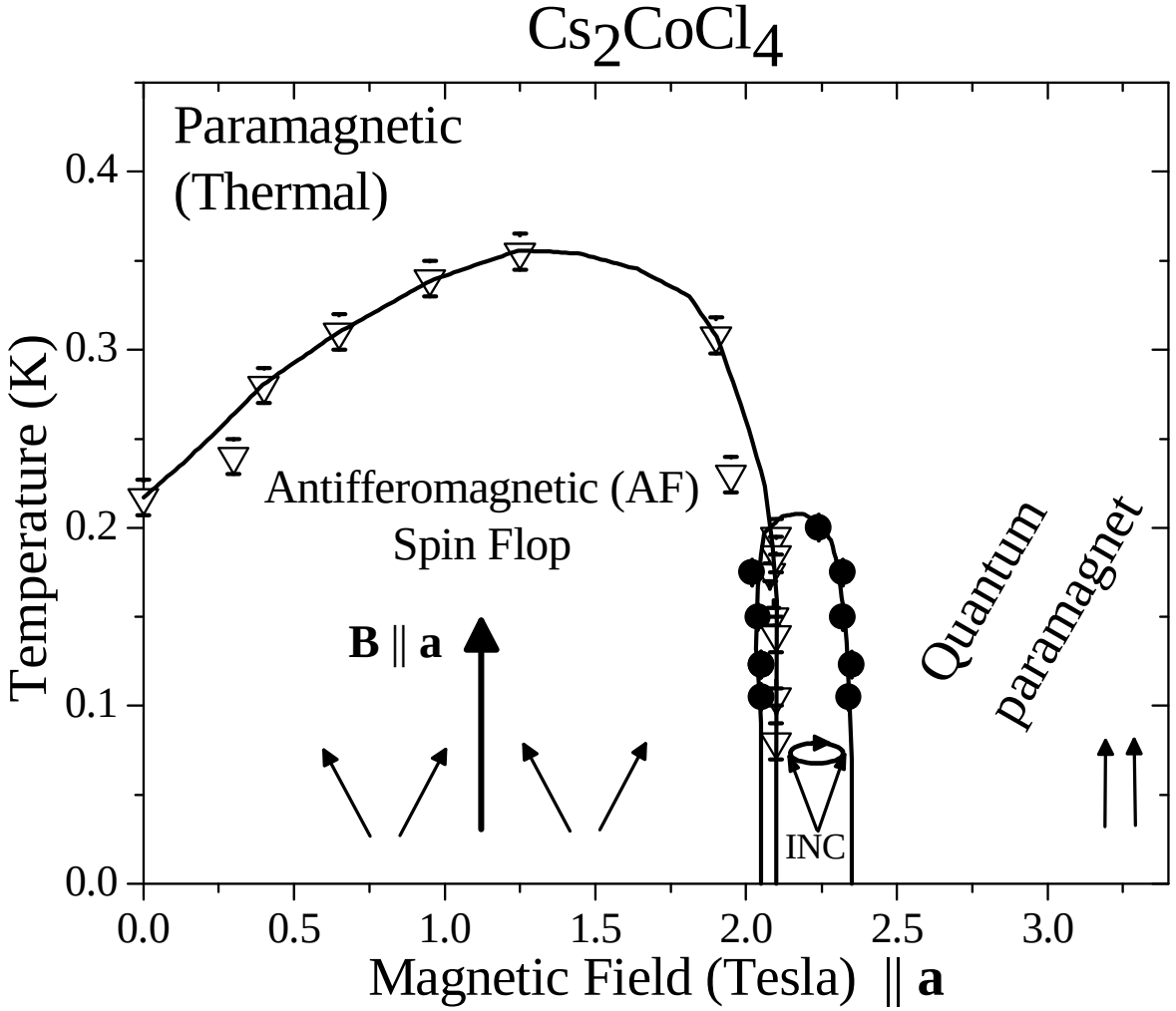

Figure 6.9 Temperature - Field phase diagram for Cs_2CoCl_4 with magnetic field applied along the **a** axis. The data points were found by measuring the intensities of Bragg peaks with varying temperature or applied field. Open triangles denote boundaries of the AF phase. Black circles denote boundaries of the incommensurate magnetic phase. Solid lines are guides to the eye.

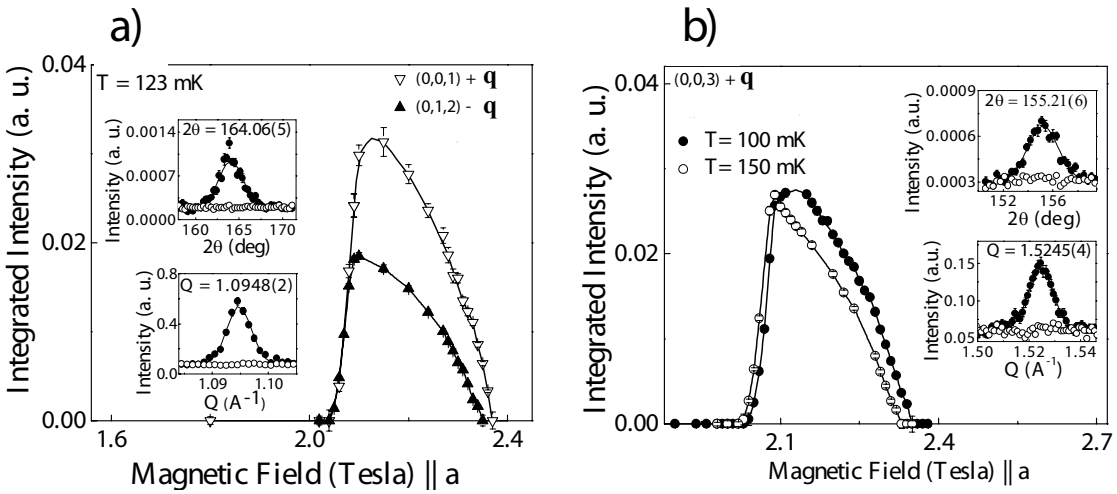

Figure 6.10 (a) Intensity of the [(0, 0, 1) + **q**] and [(0, 1, 2) - **q**] INC Bragg reflections. The insets show scans along Q = |**Q**| and 2θ at the [(0, 1, 2) - **q**] incommensurate position, for 2.02 T (open symbols) and 2.15 T(solid symbols). (b) Intensity of the [(0, 0, 3) + **q**] INC Bragg reflection. The insets show scans along Q = |**Q**| and 2θ at incommensurate position, for 2.38 T (open symbols) and 2.33 T (solid symbols). The solid lines are guide for the eye. The incommensurate phase start appearing at 2.04 T and it disappear at the critical field B_C = 2.36 T.

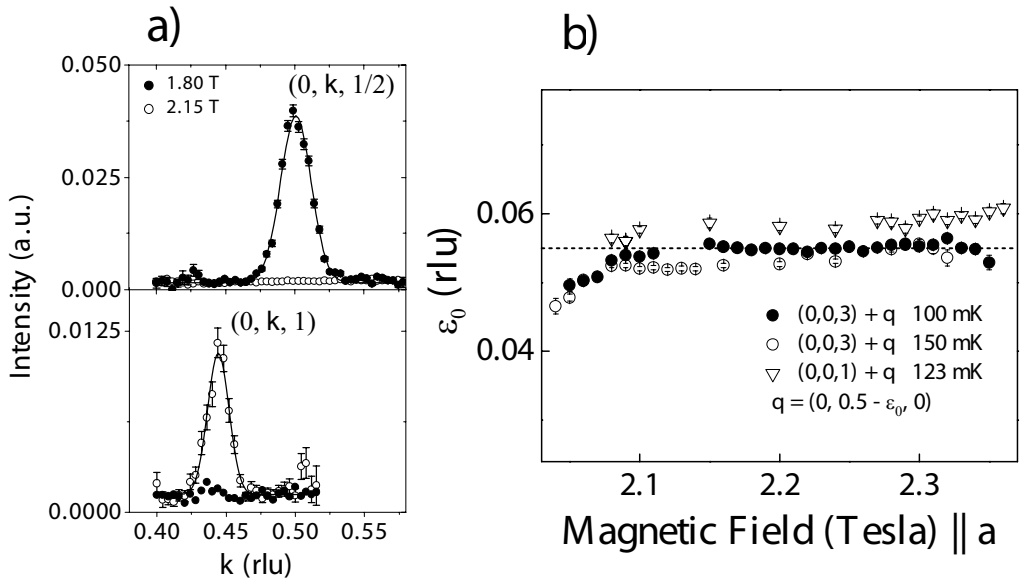

Figure 6.11 (a) wavevector scans through the commensurate (top) and incommensurate (bottom) Bragg positions at 1.8 T in the AF phase (solid symbols) and 2.15 T in INC phase (open circles). (b) Field evolution of the magnetic ordering wave vector for two different INC Bragg reflections at three different temperatures showing a near constant behavior within error. The dashed line is guide for the eye at the optimum values $\varepsilon_0 = 0.055$ rlu .

the **bc**-plane were observed and the results are summarized in Figure - 6.12. Only nuclear peak centers satisfying the selection rule K + L = odd have satellite magnetic Bragg peaks; no magnetic Bragg peaks occur for L = 0. The strongest magnetic Bragg peaks are found for vectors with a large component along **c*** axis compared with the component along **b*** axis. Since neutrons only measure the magnetic moment component transverse to the wavevector transfer **Q** (due to the polarization factor of the cross section Eg. 2.18 in Chapter 2) the above observation indicates that the magnetic structure has a strong component of the magnetic moment along the **b***-axis. Group theory can be used to identify the basis vectors for possible magnetic structures allowed by the symmetry of the space group [93]. For an incommensurate ordering wave vector q = (0, q_y, 0) in the crystal space group Pnma of Cs_2CoCl_4 (four Co^{2+} ions atoms per unit cell) the basis vectors, determined from symmetry analysis [94], describing the allowed magnetic structures are listed in Table - 6.2 and Table - 6.3. Each basis vector, such as C_y corresponds to a sinusoidal

Table 6.2 (a) Irreducible representations of the little group G_q of the ordering wavevector q = (0, q_y, 0); **x**, **y** and **z** are along the crystallographic **a**, **b** and **c** axes.

Irreducible Representation	Basis vectors
Γ_1	$A_x\ G_y\ C_z$
Γ_2	$G_x\ A_y\ F_z$
Γ_3	$C_x\ F_y\ A_z$
Γ_4	$F_x\ C_y\ G_z$

wave modulation of the magnetic moment along a particular direction (here **y** axis) with a certain set of phase factors between the 4 sites in the unit cell. For C_y mode the ordered magnetic moments

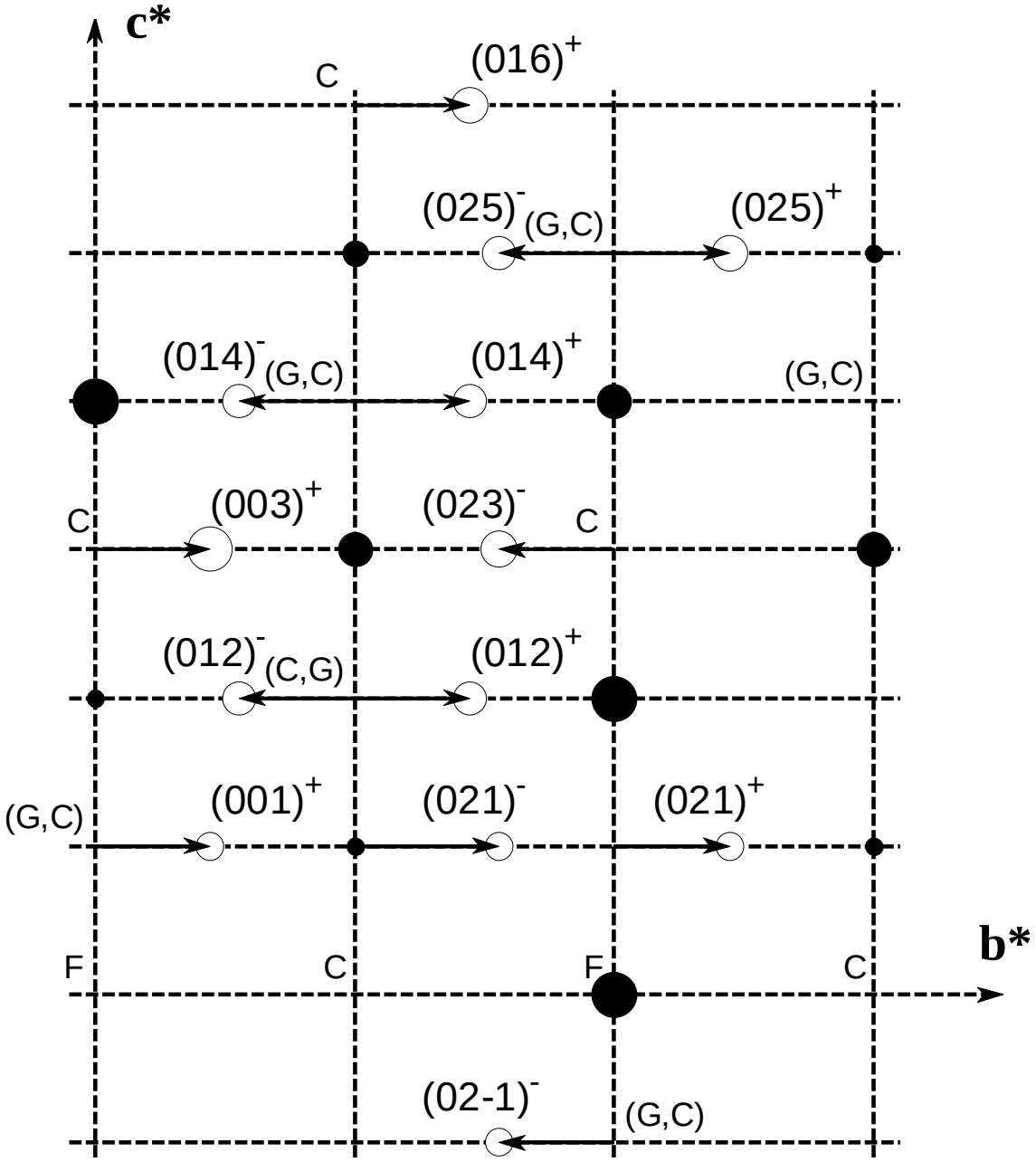

Figure 6.12 Schematic diagram of the (0kl) scattering plane showing the measured nuclear Bragg peaks (black filled circles) and incommensurate magnetic Bragg peaks (open circles), where the size of the circles indicates the intensity. The labels F, C, G and A show the extinction rules associated with the four different types of spin structures allowed by symmetry, as described in the text.

Table 6.3 The four possible basis vectors for the magnetic moments in the four sublattices, (1) to (4), where $\beta = e^{-i\pi q_y}$.

Basis vectors	(1)	(2)	(3)	(4)
F	1	1	β	β
C	1	1	-β	-β
G	1	-1	β	-β
A	1	-1	-β	β

along the **y** axis are given by:

$$\begin{aligned} m^y_{\mathbf{l},1} &= (+1)\ M_y\ sin(\mathbf{q}\cdot\mathbf{r}_{\mathbf{l},1}+\varphi_y) \\ m^y_{\mathbf{l},2} &= (+1)\ M_y\ sin(\mathbf{q}\cdot\mathbf{r}_{\mathbf{l},2}+\varphi_y) \\ m^y_{\mathbf{l},3} &= (-1)\ M_y\ sin(\mathbf{q}\cdot\mathbf{r}_{\mathbf{l},3}+\varphi_y) \\ m^y_{\mathbf{l},4} &= (-1)\ M_y\ sin(\mathbf{q}\cdot\mathbf{r}_{\mathbf{l},4}+\varphi_y) \end{aligned} \tag{6.10}$$

and for a G_z mode

$$\begin{aligned} m^z_{\mathbf{l},1} &= (+1)\ M_z\ sin(\mathbf{q}\cdot\mathbf{r}_{\mathbf{l},1}+\varphi_z) \\ m^z_{\mathbf{l},2} &= (-1)\ M_z\ sin(\mathbf{q}\cdot\mathbf{r}_{\mathbf{l},2}+\varphi_z) \\ m^z_{\mathbf{l},3} &= (+1)\ M_z\ sin(\mathbf{q}\cdot\mathbf{r}_{\mathbf{l},3}+\varphi_z) \\ m^z_{\mathbf{l},4} &= (-1)\ M_z\ sin(\mathbf{q}\cdot\mathbf{r}_{\mathbf{l},4}+\varphi_z) \end{aligned} \tag{6.11}$$

M_y, M_z are the amplitudes of the ordered moments along the **y** and **z** axis, $\mathbf{r}_{\mathbf{l},1}$ is the position in the cell **l** of the atoms Co1 and φ_y and φ_z are arbitrary phases. The combination of two basis vectors such as C_yG_z, leads to an elliptical order with spins at each site rotating in the **bc**-plane, with possibly different amplitudes $M_y \neq M_z$ and with a definite sense of rotations (chirality); for example C_yG_z with φ_z - φ_y = $\pi/2$ has a clockwise rotations for the Co1,4 chain and opposite

rotation for the Co2,3 chains. By comparing the experimental magnetic structure factors squared extracted from the measured magnetic Bragg peaks and the calculated structure factors squared for the different basis vectors we find good agreement with a magnetic structure with basis vector C_y in the Γ_4 irreducible representation with spins along **y** (**b**) axis. To distinguish between the different possibilities we looked carefully at the differences in the magnetic structure factors. For reflections in the (0kl) plane (H = 0) the magnetic structure factor squared in the Γ_4 irreducible representation for a reflection at $(0, K, L)^{\pm}$ is obtained as:

$$|F_{\perp}^{\pm}|^2 = 4\left(a_x^F M_x^2 + a_y^C M_y^2 + a_z^G M_z^2 + a_{yz}^{\pm CG} M_y M_z\right) \tag{6.12}$$

where the prefactors are:

$$a_x^F = \cos^2\left(\pi\frac{K+L}{2}\right)\left[\sin^2(2\pi Lz)\sin^2\left(\pi\frac{L}{2}\right) + \cos^2(2\pi Lz)\cos^2\left(\pi\frac{L}{2}\right)\right] \tag{6.13}$$

$$a_y^C = \sin^2\left(\pi\frac{K+L}{2}\right)\left[\sin^2(2\pi Lz)\sin^2\left(\pi\frac{L}{2}\right) + \cos^2(2\pi Lz)\cos^2\left(\pi\frac{L}{2}\right)\right]\sin^2\alpha \tag{6.14}$$

$$a_z^G = \sin^2\left(\pi\frac{K+L}{2}\right)\left[\sin^2(2\pi Lz)\cos^2\left(\pi\frac{L}{2}\right) + \cos^2(2\pi Lz)\sin^2\left(\pi\frac{L}{2}\right)\right]\cos^2\alpha \tag{6.15}$$

$$a_{yz}^{\pm CG} = -\left(\pm\frac{1}{2}\right)\sin^2\left(\pi\frac{K+L}{2}\right)\sin(4\pi Lz)\left[\cos^2\left(\pi\frac{L}{2}\right) - \sin^2\left(\pi\frac{L}{2}\right)\right]\sin(\varphi_z - \varphi_y)\sin 2\alpha \tag{6.16}$$

where α is the angle between the scattering wave vector **Q**=(0, k$\pm q_y$, l) and the [010] axis (such calculations are explicitly presented in [94]). We observe that the interference term $a_{yz}^{\pm CG}$ changes sign between the two ($\pm q_y$)satellites of the same reciprocal lattice point (0, k, l) and its absolute value is defined by the chirality of the elliptical ordering in the **bc**-plane, the parameter $\varphi_z - \varphi_x (= \pm\pi/2)$. Fits to a longitudinal spin density wave (SDW) model (spin components along y, M_x=M_z=0) are shown in Figure - 6.14. Overall good agreement is obtained; the agreement with the data for the medium-intensity peaks is not improved by allowing a small transverse spin component along the **z** direction (G_z, $M_z \neq 0$), so we conclude that the magnetic structure is an

incommensurate longitudinally-modulated spin density wave (SDW) propagating along the magnetic chain direction **b**, as illustrated in Figure - 6.14. Figure - 6.14 shows that in chains (1) - (4)

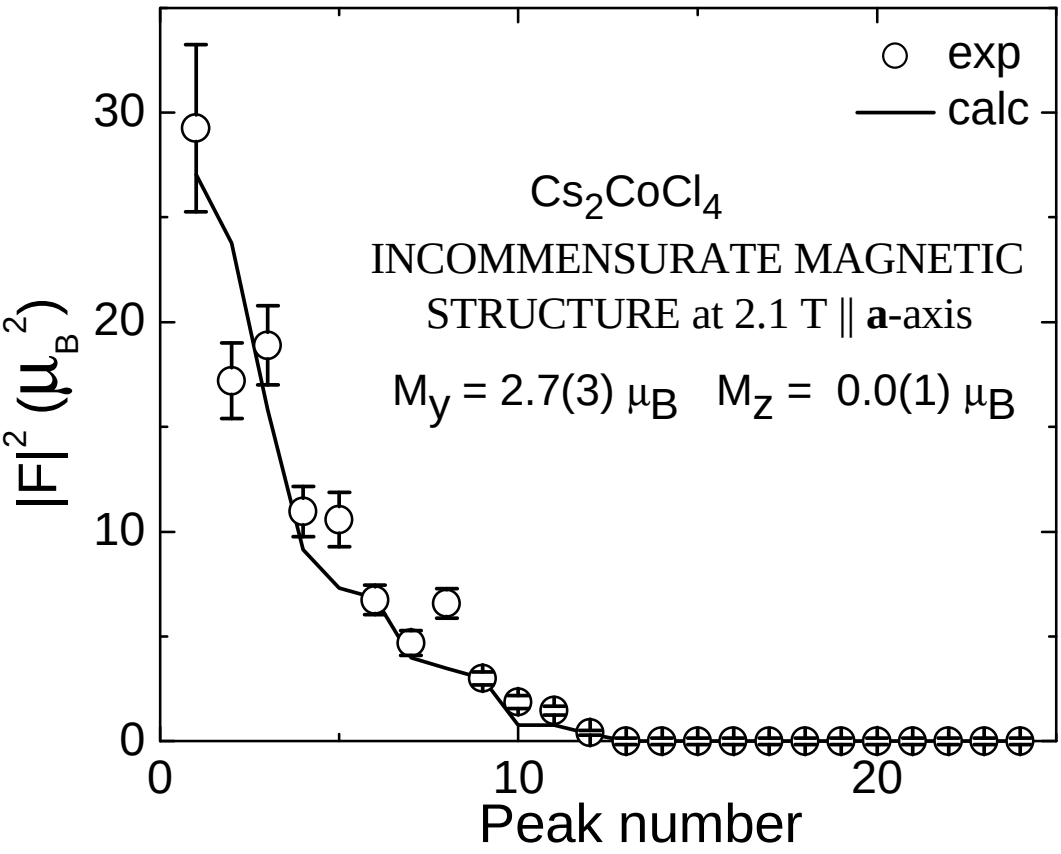

Figure 6.13 . Experimentally observed magnetic structure factors squared (open circles) fitted to the model (solid line) for the magnetic structure of a longitudinal spin-density-wave plotted in Figure - 6.14. Peak numbers are from Table - 6.4.

the large ordered spins are always arranged antiparallel along the chain direction where the antiferromagnetic exchange interaction J, is expected to be the strongest. The phase offset between chains is such that there is an energy gain of energy due to the J_{bc} exchange interaction (which introduce frustration in the system); in each triangle the basal spins arrange themselves antiparallel due to J and the third spins will align itself antiparallel with the largest of the basal spin. There is also a uniform net magnetic moment induced along the magnetic field direction **a** (**x** axis). In Table - 6.4

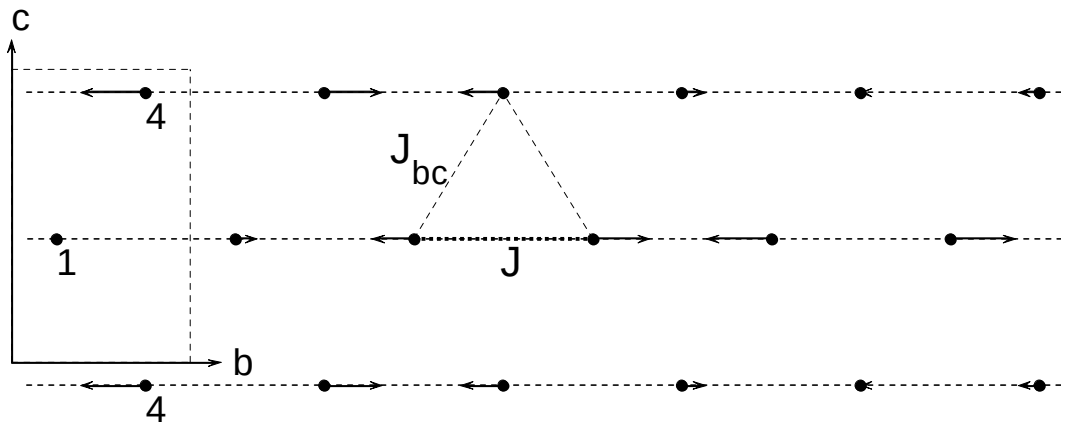

Figure 6.14 Schematic diagram of the parallel chains (1) - (4) showing the SDW ordering propagating along the chains. The external magnetic field is along **a** axis out of the plane of the paper. J is the strongest exchange interaction along the chains direction and J_{bc} is the weakly exchange interactions between the chains.

we show the experimental magnetic structure factors squared and the calculated magnetic structure factors squared for a magnetic structure corresponding to a spin density wave propagating along **b** axis.

6.6 Quantitative parametrization of the exchange Hamiltonian

The spin arrangement corresponding to the interacting chains shown in Figure - 6.3 can be described by a spin exchange model where for simplicity we neglect the easy-plane anisotropy and assume isotropic Heisenberg exchange interactions.

$$H = \sum_{\langle i,j \rangle} J_{ij} \mathbf{S}_i \mathbf{S}_j - g\mu_B \mathbf{B} \sum_i \mathbf{S}_i^z \tag{6.17}$$

where J_{ij} is the exchange interaction between the spin at site i and j, $\hat{S}$ is the spin operator, g is the gyromagnetic factor, μ_B is the Bohr magneton and **B** is the external magnetic field. J_{ij} is J for the Co1 - Co1 atom on the same chain (2 pairs), J_{bc} for the Co1 - Co4 atom (4 pairs), J_{ac} for the Co1 - Co2 atoms (4 pairs) and J_{ab} for the Co1 - Co3 atoms (4 pairs). At very high fields deep in the

Table 6.4 Comparison of the experimentally and calculated structure factors squared for magnetic Bragg peaks in the incommensurate phase at |**B**| = 2.1 T, **B** ∥ **a** axis (visual comparison is in Figure - 6.13); the notation $(003)^+ \Leftrightarrow$ (0 0 3) + (0 0.5-ε_0 0) and $(014)^-$ $\Leftrightarrow$ (0 1 4) - (0 0.5-ε_0 0), where ε_0 = 0.055 rlu; M_z = 2.7(3) μ_B and M_y = 0.0(1) μ_B.

No.	$(hkl)(rlu)$	$\lvert F\rvert^2_{calc}$ (μ_B^2)	$\lvert F\rvert^2_{exp}$ (μ_B^2)
1	$(003)^+$	27.04	29.3(0.4)
2	$(016)^+$	23.76	17.2(1.8)
3	$(023)^-$	15.82	18.9(1.9)
4	$(025)^-$	9.14	11.0(1.2)
5	$(012)^-$	7.31	10.6(1.3)
6	$(025)^+$	6.83	6.7(0.7)
7	$(014)^-$	3.97	4.7(0.6)
8	$(012)^+$	3.48	6.6(0.7)
9	$(014)^+$	3.00	3.0(0.3)
10	$(02-1)^-$	0.77	1.9(0.3)
11	$(021)^-$	0.77	1.5(0.2)
12	$(021)^+$	0.33	0.4(0.1)

paramagnetic phase all the spins are expected to be ferromagnetically align along the field axis. In this case the excitations for Heisenberg interactions only, are exactly given by spin-wave theory as quantum fluctuations are entirely quenched by the large field [95]. A considerable simplification of the problem of 4 sublattices occurs if we approximate the slightly distorted triangular arrangement of chain 1,4 (and 2,3) with perfectly planar structures (Figure - 6.3); chains 1 and 4 are at height 1/4 $\pm$ ξ along the **a** axis (ξ = 1/4 -0.235 = 0.015). For ξ = 0 the problem can be reduced to two triangular lattices in the bc plane offset along the **c** axis. In this case to diagonalize this Hamiltonian

and obtain the dispersion we are using the Holstein and Primakoff formalism and we introduce boson operators a_i^+, b_i^+ to flip spins on the two triangular Co sublattices (where $a_i^+ = S_i^- / \sqrt{2S}$ and S_i^z=S-a_i^+ a_i with S = 1/2); by writing the Hamiltonian in terms of these operators and then by using the Fourier transform of these operators the Hamiltonian (1) becomes:

$$H = E_0 + \sum_Q (a_Q^+ a_Q + b_Q^+ b_Q)(A_0 + A_Q) + (b_Q^+ a_Q e^{i\phi_Q} + a_Q^+ b_Q e^{-i\phi_Q}) B_Q \tag{6.18}$$

$$A_0 = g\mu_B B - J - 2J_{ab} - 2J_{bc} - J_{ac} \tag{6.19}$$

$$A_Q = J\cos(2\pi k) + 2J_{bc}\cos(\pi k)\cos(\pi l) \tag{6.20}$$

$$B_Q = 2J_{ab}\cos(\pi h)\cos(\pi k) + J_{ac}cos(\pi h)\cos(\pi l) \tag{6.21}$$

$$\phi_Q = 2\delta 2\pi l \tag{6.22}$$

where **Q**=(h, k, l) and δ = 0.078 is the offset between successive (b, c) layers. Diagonalization of this Hamiltonian gives the two normal magnon modes with two sinusoidal dispersion relations:

$$\omega_+(Q) = A_0 + A_Q + B_Q \tag{6.23}$$

$$\omega_-(Q) = A_0 + A_Q - B_Q \tag{6.24}$$

corresponding to magnons hopping between the two sublattices. The two dispersion relations are plotted along representative direction in the **bc**-plane in Figure 6.15. The dispersions have incommensurate minima at (0, 1.5 - ε, 0) with ε increasing with increasing J_{ab}/J. The overall shape is modified from a simple sinusoidal from expected in the case of pure 1D chain (g μ_B B - J + J $\cos(2\pi k)$) to have incommensurate minima and non-equivalent minima for k = 1 and 2.

Inelastic scattering data was collected in a field of 4T which is deep in the paramagnetic phase, where the spins are expected to be nearly ferromagnetically aligned along the field direction; at this field there is a significant energy gap of 0.313(5) meV to the first excited states and the thermally induced populations of spin flip at 0.15 K is very small. In order to obtain a good quantitative

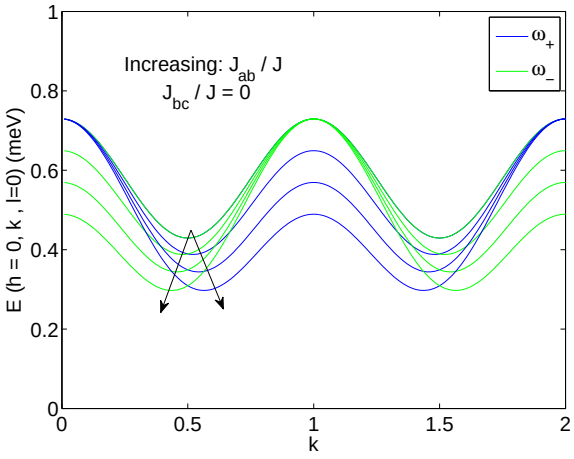

Figure 6.15 Effects of the interchain interaction on the 1D dispersion modes.

parametrization of the Hamiltonian we measured the experimental magnon dispersion for twelve distinct sample orientations which means twelve different cuts through the **bc**-plane. Each data file from OSIRIS comes in the form of a large file containing the intensities as a function of the time-of-arrival in each detector which can be converted to energy transfer. This data can then be projected onto the reciprocal space giving maps of intensities as a function of two of the 3 variables k, l and $\hbar\omega$. For example, plots of the energy transfer as a function of k or l for an orientation of the sample where **b*** is making an angle of Ψ = 48.5 deg with $\mathbf{k}_i$ are given in Figure - 6.16 a) and b). Maps of the neutron scattering intensity as a function of wave vector and energy show a sharp sinusoidally-dispersive gapped mode associated with a magnon spin-flip excitation of the nearly ferromagnetically - aligned ground state (see Figure - 6.16); the presence of the two modes seen experimentally means that there are two types of magnons. The higher modes ($\sim$ 1.21 meV) are attributed to transition to the higher crystal field level (originating from $\tilde{\mathbf{S}}_z = \pm$ 3/2). With the data in the form of intensities versus any two coordinates out of the quartet (h, k, l, $\hbar\omega$) one can create cuts through the data as a function of either h, k, l or $\hbar\omega$ (these cuts mimic the constant energy of momentum scans obtained on triple-axis spectrometer). Typical cuts where we probed the experimental dispersion are presented in Figure 6.17. To find the positions and intensities of

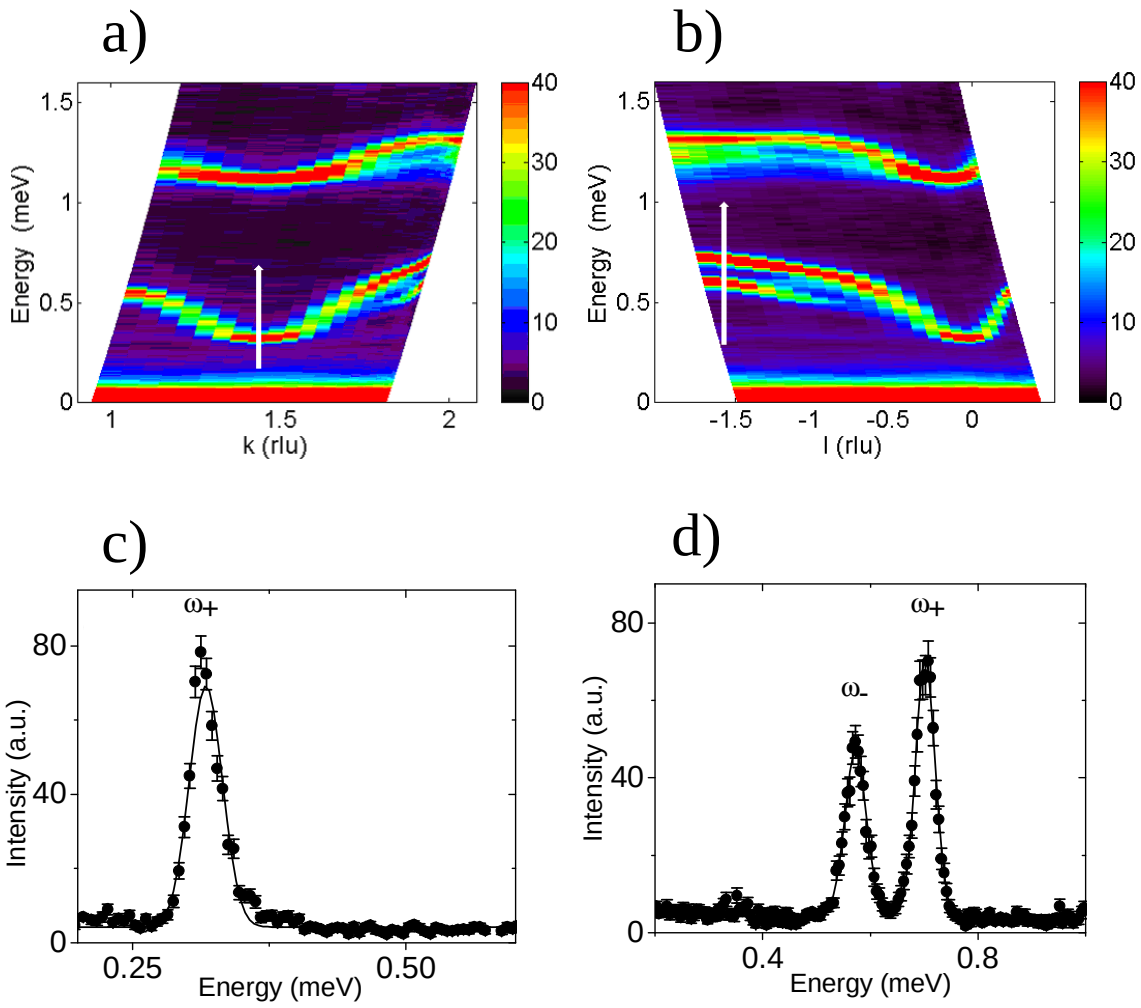

Figure 6.16 Colour maps of the inelastic neutron scattering intensity at 4T as a function of k (a) and l (b) (from magnetization data 2.9 T is the field at which the spins are nearly fully aligned along the field direction). The data is normalized by the integrated elastic line to correct for absorption effects and detector efficiencies. (c) and (d) typical energy cuts (for fixed momentum) used to extract the experimental dispersion. Solid lines are fits to Gaussians.

the single- magnon peaks, in constant-momentum cuts, the data was in a first approximation fitted with Gaussians. Fitting the dispersion relations in Eqs. 6.23 and 6.24 to the measured positions of

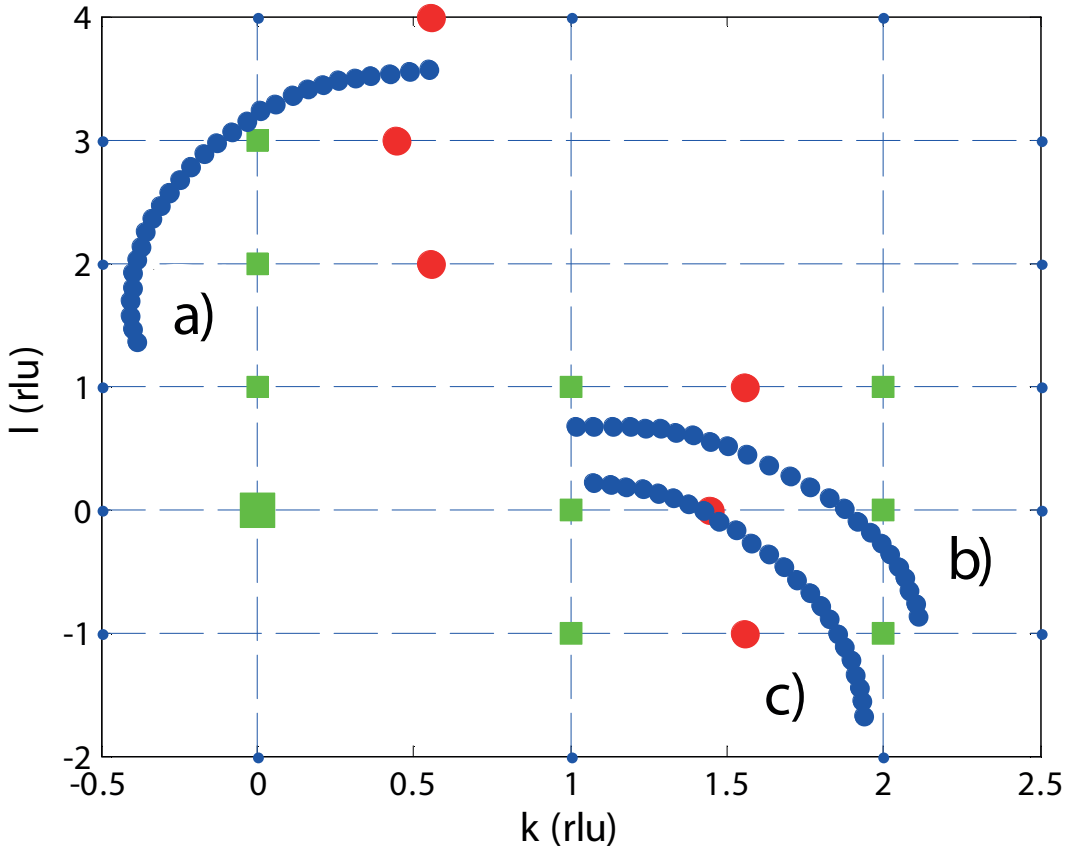

Figure 6.17 Typical cuts through the Brillouin zone; green squares represent the nuclear Bragg peaks and the red circles represent the incommensurate magnetic Bragg peaks. The blue circles show experimentally probed dispersion points.

the magnon peaks we obtain the best fit to the data for J = 0.163(2) meV, J_{ab} = 0.034(2) meV, J_{bc} = 0.018(2) meV, J_{ac} = 0 meV and g =3.32(3). All the interactions are antiferromagnetic. The results confirm that Cs_2CoCl_4 can generally be regarded as a quasi-1D system, with a dominant exchange interaction along the **b** - axis chains as expected, however interchain coupling are also sizeable J_{bc} / J = 11% and J_{ab} / J = 21%, but are frustrated. The agreement between model and data along the 3 directions shown (and several others measured) is very good indicating that this approximate model

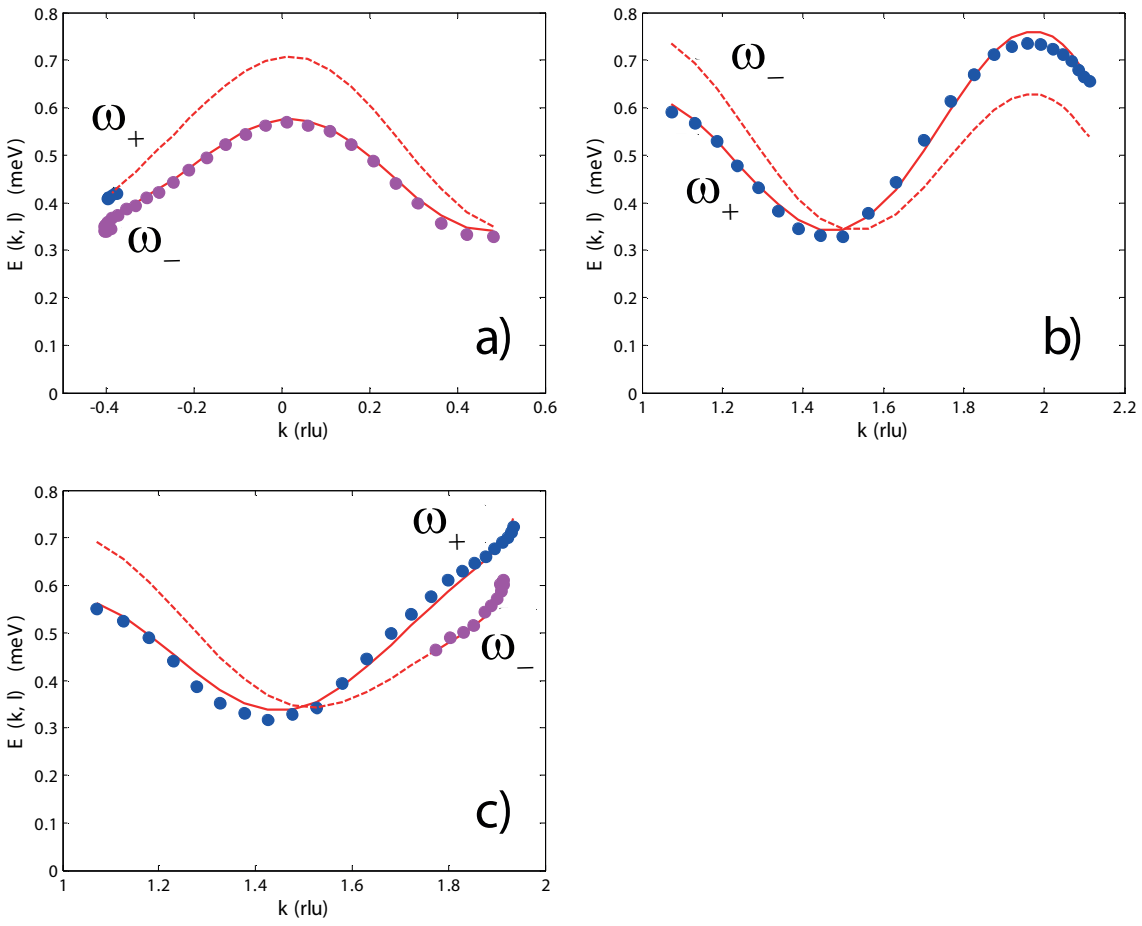

Figure 6.18 Dispersion relations of the magnon excitations at an applied magnetic field of 4 T and temperature 0.15 K, along the solid dotted lines shown in Figure - 6.17 labeled a $\rightarrow$ c, fitted to a spin wave model, Eq. (3). The data points (errors bars smaller than size of the symbol) are extracted from Gaussians fits to the lineshape of constant-momentum cuts (as in Figure - 6.16 (c) and (d)). Blue circles represent the ω_+ mode and magenta circles represent the ω_- mode. Red solid line represents the best fits to the data using the model describe in the text. The dash lines represent the energies where the two dispersions would have been measured if the intensities would have been different from zero.

captures the essential physics of magnon mapping in the high field phase. The fitted dispersion has minimum gap at incommensurate positions very close to the locations of incommensurate Bragg peaks which appear blow B_C, consistent with a continuous (gap closing) transition paramagnetic $\rightarrow$ incommensurate.

6.7 Excitations Energy gap vs. field

At the field of 4 T we measured the gap as close as possible to the incommensurate Bragg peak positions (0, 1.5 - ε_0, 0) on the **b*** axis, near the elastic line (E $\approx$ 0). At this field we observed a large gap of 0.313(2) meV in the magnon dispersion, see Figure - 6.16 c). In order to learn more about how the excitation gap evolves with the field, we measured inelastic data in the range 2.36 T to 6 T (where the lower field gives the transition between incommensurate order and paramagnetic phase at 0.1 K). After analysis of the data, we extracted the gap energy as a function of field, see Figure - 6.19. Above 2.5 T, the gap can be well described by a linear dependence (dot line), where E_{gap}=g μ_B (B - $\tilde{B}_c$) where $\tilde{B}_c$ = 2.26(2) T and g =3.12(8). A linear dependence is expected in the ferromagnetic phase where changing the field, increases the magnon Zeeman energy via, the term g μ_B B , where g is the gyromagnetic factors and B is the external field. Note that this extrapolates to zero to a lower field $\tilde{B}_c$ = (2.26 $\pm$ 0.02) T than the measured critical field where magnetic order disappears at B_c=2.36(2) T. Two scenarios are more likely: either the gap does close at the experimental critical field B_C and the dependence becomes non-linear (subunitary power law) in the close proximity of B_c (solid line in Figure - 6.19) or that the gap persist to be linear and it does not close at the transition which would be consistent with a 1st order phase transition. Experimentally we can put an upper bound on the magnon gap at critical field, as is smaller than 0.02 meV (which is less than 6.4 % of the gap at 4 T), see raw data scans in Figure - 6.20. If the transition is continuous then the gap is expected to close at the dispersion minima **Q** $\pm$ **q**, **q** = (0,

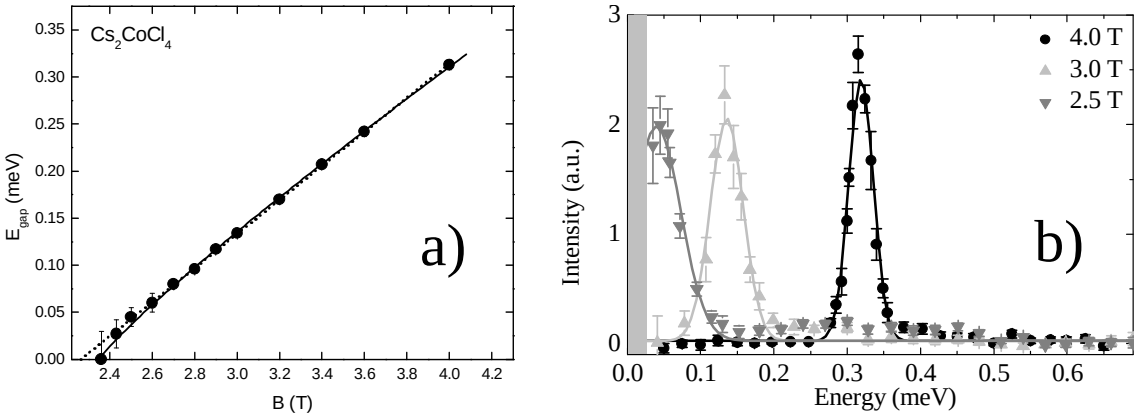

Figure 6.19 (a) Energy gap as a function of field at the (0, 1.5 - ε_0, 0) incommensurate position. The solid line is the best-fit to a power law E_{gap} = a (B - B_c) with the critical field value B_C = 2.36 T where transition to incommensurate order occurs. The dotted line is the best fit to a linear behaviour to data above 2.5 T. (b) typical energy cuts (for fixed momentum) used to extract the energy gap. Solid lines are fits to Gaussians.

0.5 - ε_0), 0) and ε_0 = 0.055(5) where Bragg peaks appear below the critical field 2.36(2) T.

Departures from a perfectly linear dependence very close to B_C might in fact be expected. The purely linear dependence is expected for the case of isotropic Heisenberg system, or systems with rotational symmetry around the field axis and also in the special case of pure 1D systems (for example transverse field-Ising). However for a 3D system with extreme anisotropy (Ising) spin-wave theory predicts a mean-field square root behavior GAP $\sim$ (B - B_C)$^{\frac{1}{2}}$. So it is possible that very close to B_C the scaling form are affected by the strong anisotropy and finite 3D interchain couplings present in the system.

6.8 Continuum Scattering

At higher energies above the one-magnon dispersion, evidence for broad continuum scattering was also observed in the paramagnetic phase for a finite field range above the critical field. Such scattering was seen at 2.5 T and increased upon lowering the field very close to the transition to

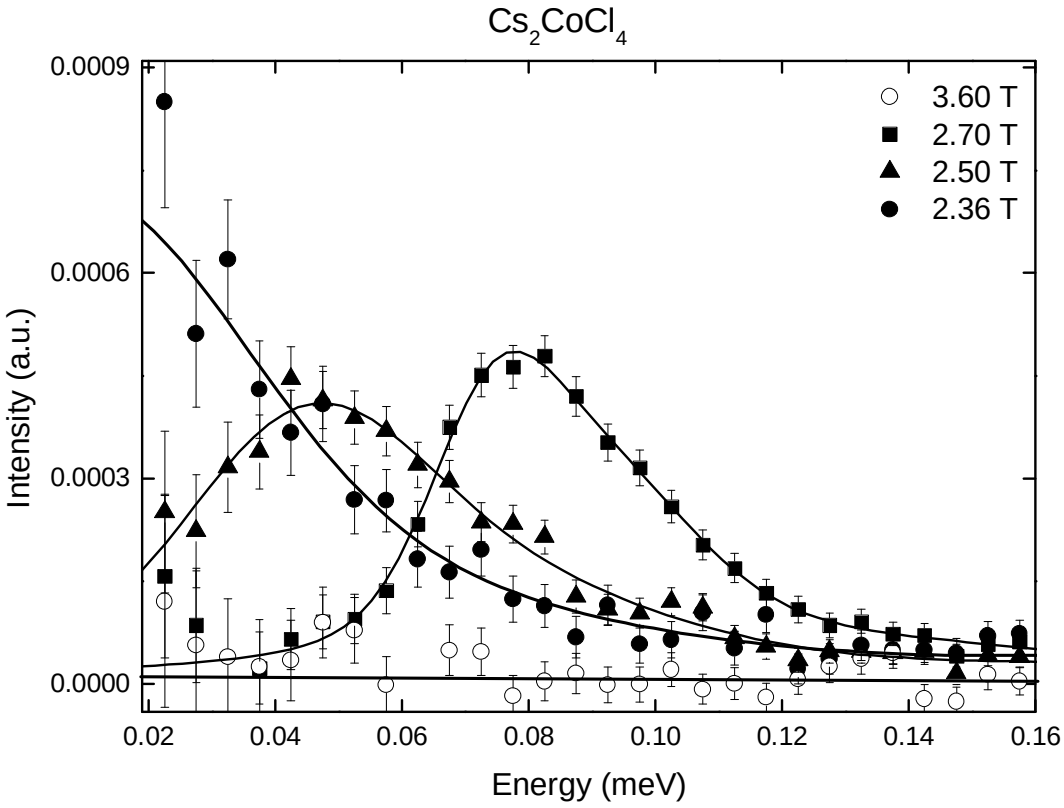

Figure 6.20 Example of energy scans near 0, 1.5 - ε_0, 0) used to extract the energy gap of the magnon dispersion. Lines are guides to the eye. The data was corrected for neutron absorption effects.

magnetic order 2.36 T (see Figure - 6.21) and this continuum scattering could be due to multi - magnon scattering processes which are not expected in pure Heisenberg systems but are expected in the presence of anisotropy, when the spin component along the field direction is not a conserved quantity as in the present case.

The two-magnon scattering continuum can be written as

$$S_{2M}^{|k,\omega\rangle} = \sum_{k_1,k_2} F(k_1,k_2)\delta(k-k_1-k_2)\delta(\omega-\omega(k_1)-\omega(k_2)) \tag{6.25}$$

where the two delta functions represent the conservation of momentum and energy, F(k_1, k_2) are matrix elements and $\omega(k)$ is the dispersion relation. Two magnon scattering is expected to occur in the polarization along the magnetic field direction. Three magnon scattering continuum is expected in the polarization transverse to the field direction and can be written like

$$S_{3M}^{|k,\omega\rangle} = \sum_{k_1,k_2,k_3} F(k_1,k_2,k_3)\delta(k-k_1-k_2-k_3)\delta(\omega-\omega(k_1)-\omega(k_2)-\omega(k_3)) \tag{6.26}$$

A calculation of the accessible phase space for two and three magnons scattering processes is given in Figure - 6.22; we observe that three magnon scattering processes come at lower energies near gap minimas (k $\sim$ 0.5) so is possible that the dominant continuum seen experimentally to be associated to three magnon processes. In order to test this scenario we need quantitative calculations of the expected scattering intensity (not available yet) that include anisotropy effects.

6.9 Conclusions

We observe that the commensurate antiferromagnetic order observed at low fields is stable over a wide field range but is replaced by an incommensurate phase just below the transition to paramagnetic. Using group theory we determined that the magnetic structure inside the incommensurate phase at 2.1 T is a spin density wave propagating along the magnetic chain direction. This new phase is stabilized by the weak frustrated interchain couplings, which become relevant close to

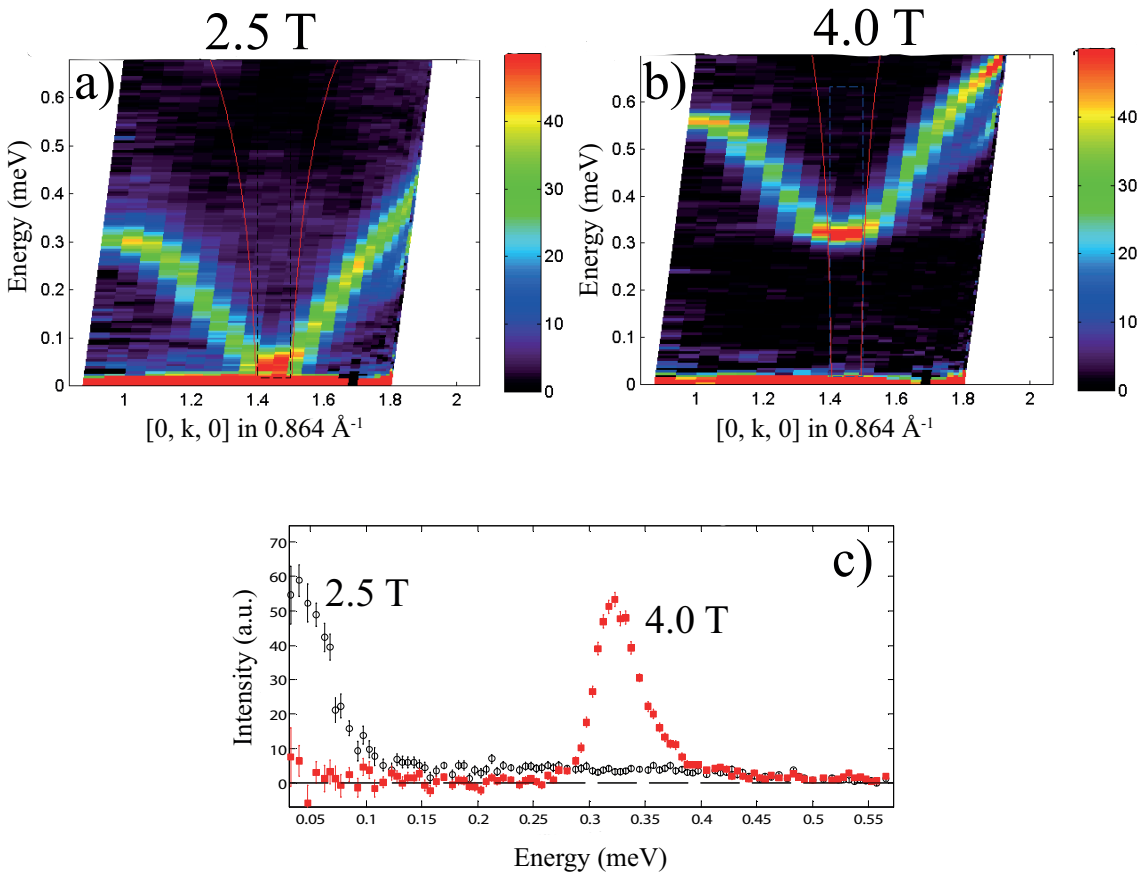

Figure 6.21 (a) and (b) Colour maps of the inelastic neutron scattering intensity at different magnetic fields: 4 T is the field at which the spins are aligned along the field direction and 2.5 T is the field where the transition to the incommensurate magnetic structure occurs. Note the broad continuum scattering filling in the region above the dispersion relations at low energies. (c) Energy scans corresponding to panel (a) and (b); the data points were obtained from averaging the region between the red curve.

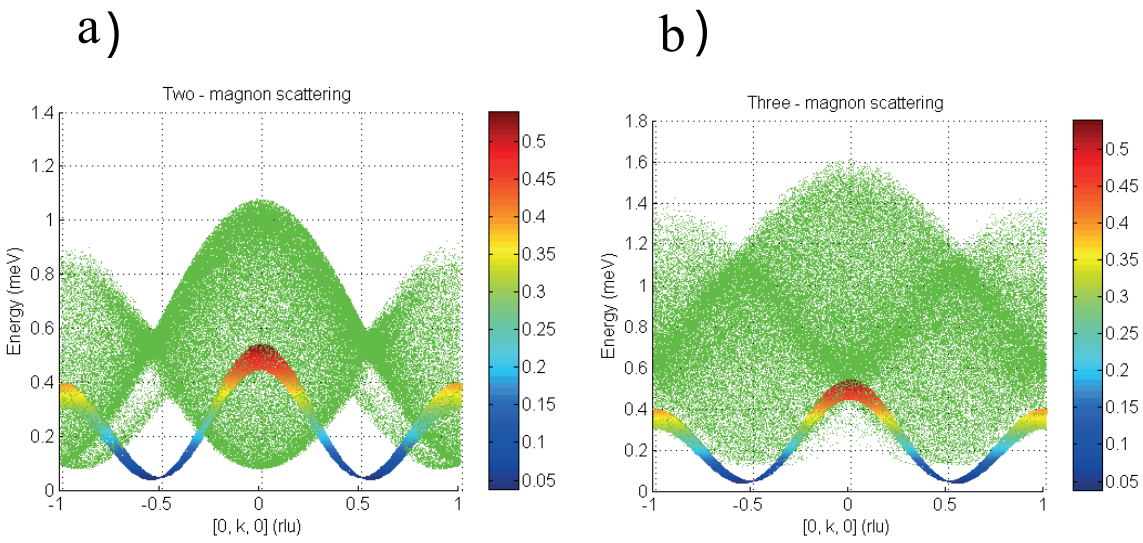

Figure 6.22 Schematic representation of the accessible phase space for multi - magnon scattering processes as a function of wavevector and energy. The solid colored line (at low energies) represents the single magnon branch ω_+; The with comes from a finite integration in the transverse directions. The continuum (green points) above the single magnon branch represent the allowed zone for a) two - magnon and b) three-magnon scattering processes.

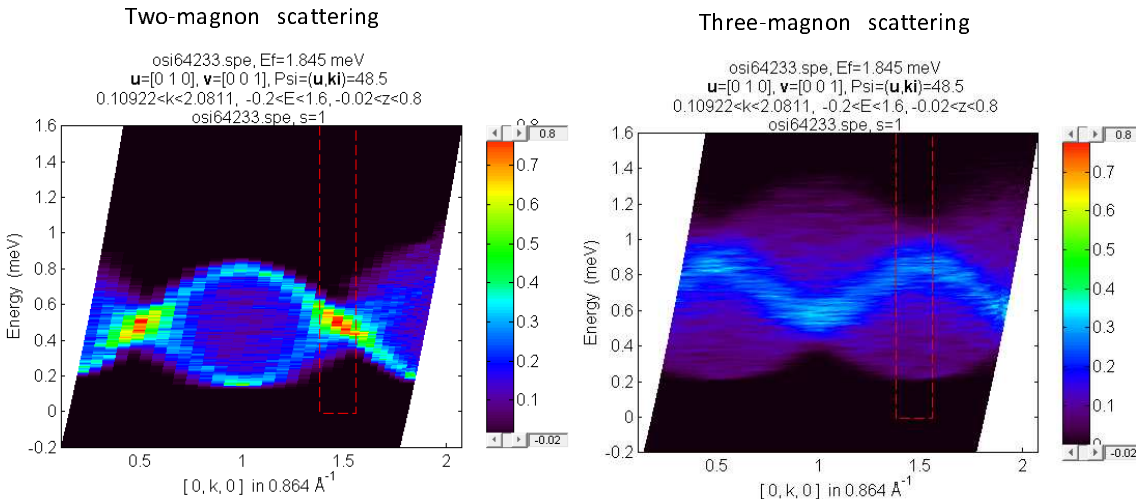

Figure 6.23 Schematic representation of the accessible phase space for multi - magnon scattering processes projected on the experimental axis. These calculations are done using the exchange parameters extracted from the dispersion relations at 2.43 T.

the critical field where the physics is dominated by soft critical fluctuations. Deep in the paramagnetic phase the excitations are sharp, gapped magnons with minima at the incommensurate wavevectors of the magnetic order below B_C = 2.36(2) T and the dispersion relations give values for the intra and inter-chain couplings. In addition to one-magnon excitations at high energies we also observe weak magnetic continuum scattering, which becomes stronger upon approaching the critical field from above and is attributed to three-magnon scattering processes. The data is discussed in terms of an XY magnet with in-plane field where three-magnon processes are allowed because of the non-commutation of the applied field and the exchange Hamiltonian. To confirm this scenario quantitative calculations of the expected scattered intensity that include anisotropy effects are needed.

Bibliography

[1] M. F. Collins, *Magnetic Critical Scattering* (1989).

[2] W. Marshall and S. W. Lovesey, *Theory of Thermal Neutron Scattering* (Oxford University Press, 1971).

[3] G. L. Squires, *Introduction to the Theory of Thermal Neutron Scattering* (1989).

[4] J. Brown, *Neutron Data Booklet - Magnetic Form Factors* (2003).

[5] J. R. D. Copley and T. J. Udovic, "Neutron Time-of-Flight Spectroscopy," Journal of Research of the National Institute of Standards and Technology **98,** 71–87 (1993).

[6] V. L. Aksenov and A. M. Balagurov, "Neutron time-of-flight diffractometry," Physics-Uspekhi **39,** 897–924 (1996).

[7] A. J. Schultz, "Single-crystal time-of-flight neutron diffraction," Trans. Am. Cryst. Assoc. **29,** 29–41 (1993).

[8] M. T. F. Telling and K. H. Andersen, "Spectroscopic characteristics of the OSIRIS near-backscattering crystal analyser spectrometer on the ISIS pulsed neutron source," Phys. Chem. Chem. Phys. **7,** 1255–1261 (2005).

[9] R. W. James, *The Optical Principles Of The Diffraction Of X-Rays* (1954), Vol. 2.

[10] F. de Bergevin, *X-ray and Neutron Reflectivity: Principles and Applications; chapter: The Interaction of X-rays (and Neutrons) with Matter* (2009).

[11] J. Als-Nielsen and D. McMorrow, *Elements of Modern X-ray Physics* (2001).

[12] P. Coppens, *X-ray charge densities and chemical bonding* (1997).

[13] *Handbook on synchrotron radiation*, G. S. Brown and D. Moncton, eds., (1991), Vol. 3.

[14] *Resonant anomalous x-ray scattering: theory and applications*, G. Materlik, C. Sparks, and K. Fischer, eds., (1994).

[15] *International Tables for Crystallography. Chapter: Interpretation of diffracted intensities*, A. J. C. Wilson, ed., (1992).

[16] C. T. Chantler, "Theoretical Form Factor, Attenuation, and Scattering Tabulation for Z = 1-92 from E = 1-10 eV to E = 0.4 Ű 1.0 MeV," J. Phys. Chem. Ref. Data **24,** 71 (1995).

[17] L. Gerward, "X-ray attenuation coefficients: current state of knowledge and avalability," Radiation Physics and Chemistry **41,** 783–789 (1993).

[18] S. M. Seltzer, "Calculation of Photon Mass Energy-Transfer and Mass Energy-Absorption Coefficients," Radiation Research **136,** 147–170 (1993).

[19] J. J. Hoyt, D. de Fontaine, and W. K. Warburton, "Determination of the anomalous scattering factors for Cu, Ni and Ti using the dispersion relation," J. Appl. Cryst. **17,** 344–351 (1984).

[20] J. Wong, F. W. Lytle, R. P. Messmer, and D. H. Maylotte, "K-edge absorption spectra of selected vanadium compounds," Phys. Rev. B **30,** 5596 (1984).

[21] T. Sorgel and M. Jansen, "A New Hexagonal Modification of $AgNiO_2$," Zeitschrift für anorganische und allgemeine Chemie **631,** 2970–2972 (2005).

[22] E. Rossmanith, "Relationship between Lorentz factor and peak width. Development of a new peak-width formula and a generalized Lorentz factor for single and multiple diffraction," Acta Cryst. A **48,** 591–595 (1992).

[23] B. E. Warren, *X-Rays Diffraction* (1968).

[24] A. V. Ryazhkin, Y. A. Babanov, T. Miyanaga, E. D. Crozier, R. A. Gordon, T. Reich, and H. Funke, "Thickness inhomogeneity effect in EXAFS spectroscopy," Physica Scripta **T115,** 197–199 (2005).

[25] L. Ottaviano, A. Filipponi, and A. D. Cicco, "Supercooling of liquid-metal droplets for x-ray-absorption-spectroscopy investigations," Phys. Rev. B **49,** 11749 (1994).

[26] S. Collins and A. Bombardi, "Diamond Beamline I16 - Materials and Magnetism," AIP Conf. Proc. **1234,** 303–306 (2010).

[27] E. Wawrzynska, R. Coldea, and E. M. Wheeler, "Orbital Degeneracy Removed by Charge Order in Triangular Antiferromagnet $AgNiO_2$," Phys. Rev. Lett. **99,** 157204 (2007).

[28] I. I. Mazin, D. I. Khomskii, R. Lengsdorf, J. A. Alonso, W. G. Marshall, R. M. Ibberson, A. Podlesnyak, M. J. Martínez-Lope, and M. M. Abd-Elmeguid, "Charge Ordering as Alternative to Jahn-Teller Distortion," Phys. Rev. Lett. **98,** 176406 (2007).

[29] E. Chappel, M. Nunez-Regueiro, G. Chouteau, O. Isnard, and C. Darie, "Study of the ferrodistorsive orbital ordering in $NaNiO_2$ by neutron diffraction and submillimeter wave ESR," The European Physical Journal B - Condensed Matter and Complex Systems **17,** 615–622 (2000).

[30] H. Meskine and S. Satpathy, "Electronic structure and magnetism in sodium nickelate: Density-functional and model studies," Phys. Rev. B **72,** 224423 (2005).

[31] E. Nazarenko, J. E. Lorenzo, Y. Joly, J. L. Hodeau, D. Mannix, and C. Marin, "Resonant X-Ray Diffraction Studies on the Charge Ordering in Magnetite," Phys. Rev. Lett. **97,** 056403 (2006).

[32] A. M. Mulders, S. M. Lawrence, U. Staub, M. Garcia-Fernandez, V. Scagnoli, C. Mazzoli, E. Pomjakushina, K. Conder, and Y. Wang, "Direct Observation of Charge Order and an Orbital Glass State in Multiferroic $LuFe_2O_4$," Phys. Rev. Lett. **103,** 077602 (2009).

[33] A. N. Mansour and C. A. Melendres, "Analysis of X-ray Absorption Spectra of Some Nickel Oxycompounds Using Theoretical Standards," J. Phys. Chem. A **102,** 65 (1998).

[34] J. ichi Igarashi and M. Takahashi, "4p States and X-Ray Spectroscopy," Physica Scripta **72,** CC1–7 (2005).

[35] Y. Joly, J. E. Lorenzo, E. Nazarenko, J.-L. Hodeau, D. Mannix, and C. Marin, "Low-temperature structure of magnetite studied using resonant x-ray scattering," Phys. Rev. B **78,** 134110 (2008).

[36] E. Wawrzynska, R. Coldea, E. M. Wheeler, T. Sörgel, M. Jansen, R. M. Ibberson, P. G. Radaelli, and M. M. Koza, "Charge disproportionation and collinear magnetic order in the frustrated triangular antiferromagnet $AgNiO_2$," Phys. Rev. B **77,** 094439 (2008).

[37] A. Abragam and B. Bleaney, *Electron paramagnetic resonance of transition ions* (1970), Vol. 1.

[38] K. I. Kugel and D. I. Khomskii, "The Jahn-Teller effect and magnetism: transition metal compounds," Soviet Physics Uspekhi **25,** 231 (1982).

[39] A. Pantelouris, H. Modrow, M. Pantelouris, J. Hormes, and D. Reinen, "The influence of coordination geometry and valency on the K-edge absorption near edge spectra of selected chromium compounds," Chemical Physics **300,** 13–22 (2004).

[40] L. Onsager, "Crystal Statistics. I. A Two-Dimensional Model with an Order-Disorder Transition," Phys. Rev. **65,** 117 (1944).

[41] R. A. Cowley and K. Carneiro, "Critical properties of pure and random antiferromagnets: CoF_2, Co/ZnF_2 and KMn/NiF_3," J. Phys. C: Solid St. Phys. **13,** 3281–3291 (1980).

[42] S. Sachdev, *Quantum Phase Transitions* (1999).

[43] S. Mitsuda, K. Hosoya, T. Wada, H. Yoshizawa, T. Hanawa, M. Ishikawa, K. Miyatani, K. Saito, and K. Kohn, "Magnetic Ordering in One-Dimensional System $CoNb_2O_6$ with Competing Interchain Interactions," J. Phys. Soc. Jpn. **63,** 3568–3571 (1994).

[44] C. Heid, H. Weitzel, P. Burlet, M. Bonnet, W. Gonschorek, T. Vogt, J. Norwig, and H. Fuess, "Magnetic phase diagram of $CoNb_2O_6$: A neutron diffraction study," Journal of Magnetism and Magnetic Materials **151,** 123 – 131 (1995).

[45] W. Scharf, H. Weitzel, I. Yaeger, I. Maartense, and B. Wanklyn, "Magnetic structures of $CoNb_2O_6$," Journal of Magnetism and Magnetic Materials **13,** 121–124 (1979).

[46] T. Hanawa, K. Shinkawa, M. Ishikawa, K. Miyatani, K. Saito, and K. Kohn, "Anisotropic Specific Heat of $CoNb_2O_6$ in Magnetic Fields," J. Phys. Soc. Jpn. **63,** 2706–2715 (1994).

[47] I. Maartense and I. Yaeger, "Field-induced magnetic transitions of $CoNb_2O_6$ in the ordered state," Solid State Communications **21,** 93–96 (1977).

[48] R. Coldea, D. A. Tennant, E. M. Wheeler, E. Wawrzynska, D. Prabhakaran, M. Telling, K. Habicht, P. Smeibidl, and K. Kiefer, "Quantum Criticality in an Ising Chain: Experimental Evidence for Emergent E8 Symmetry," Science **327,** 177 (2010).

[49] D. Dai, H. Xiang, and M. H. Whangbo, "Effects of Spin-Orbit Coupling on Magnetic Properties of Discrete and Extended Magnetic Systems," J. Comput. Chem. **29,** 2187–2209 (2008).

[50] K. H. J. Buschow and F. R. Boer, *Physics of Magnetism and Magnetic Materials - Chapter 5* (2003).

[51] B. N. Figgis and M. A. Hitchman, *Ligand Field Theory and Its Applications - Chapter 5* (New York: Wiley-VCH, 2000).

[52] J. C. Slater, *Quantum Theory of Atomic Structure - Chapter 10* (New York: McGraw-Hill, 1960), Vol. 1.

[53] E. Wheeler and R. Coldea, "Neutron scattering measurements of the crystal field levels were performed at ISIS," Experiment performed at ISIS on HET instrument (2005).

[54] H. Weitzel, "Kristallstrukturverfeinerung von Wolframiten und Columbiten," Zeitschrift fuer Kristallographie, Kristallgeometrie, Kristallphysik, Kristallchemie **144,** 238–258 (1976).

[55] R. Borromei, G. Ingletto, L. Oleari, and P. Day, "Electronic spectrum of NiII in $MgWO_4$, $ZnWO_4$ and $CdWO_4$ at 4.2 K," J. Chem. Soc., Faraday Trans. 2 **77,** 2249 – 2266 (1981).

[56] M. Rotter and A. T. Boothroyd, "Going beyond the dipole approximation to improve the refinement of magnetic structures by neutron diffraction," Phys. Rev. B **79,** 140405 (2009).

[57] D. A. Filippov and I. S. Nikiforov, in *Proceedings of the NATO Advanced Reserch Workshop on Magnetoelectric Interaction Phenomena in Crystals - Theory of the Resonance Magneto-Electric Efect in Iron-Borate*, M. Fiebig, V. V. Eremenko, and I. E. Chupis, eds., (Springer; Kluwer Academic Publishers, 2004).

[58] K. V. Reddy, *Symmetry And Spectroscopy Of Molecules* (1998).

[59] B. Henderson and G. F. Imbusch, *Optical Spectrocopy of Inorganic Solids* (Oxfrod University Press, New York, 1989).

[60] J. A. Sordo and L. Pueyo, "An exercise on the theory of complex spectra," J. Chem. Educ. **62,** 468–472 (1985).

[61] B. Henderson and R. H. Bartram, *Crystal-Field Engineering of Solid-State Laser Materials* (Cambridge University Press, 2000).

[62] Z. Luo, Y. Huang, and X. Chen, *Spectroscopy of solid-state laser and luminescent materials* (Nova Science Publishers, 2007).

[63] J. R. Pilbrow, *Transition Ion Electron Paramagnetic Resonance* (1990).

[64] C. Gorller-Walrand and K. Binnemans, *Handbook on the Physics and Chemistry of rare Earths: rationalization of Crystal-Field Parametrization* (Elsevier Science, 2007), Vol. 23.

[65] J. A. Sordo and L. Pueyo, "An exercise on the theory of complex spectra," J. Chem. Educ. **62,** 468–472 (1985).

[66] J. A. Sordo and L. Pueyo, "An exercise on the theory of complex spectra," J. Chem. Educ. **62,** 468–472 (1985).

[67] R. Borromet, E. Cavalli, and G. Ingletto, "Electronic Spectrum of the Co(II) Ion in the Columbite $CoNb_2O_6$ Host lattice at 4.2 K," Phys. Stat. Sol. (b) **117,** 733–742 (1983).

[68] O. L. Malta, "A Simple Overlap Model in Lanthanide Crystal-Field Theory," Chemical Physics Letters **87,** 27–29 (1982).

[69] O. L. Malta, "Theoretical Crystal-Field Parameters for the YOCl:Eu^{3+} system. A Simple Overlap Model," Chemical Physics Letters **88,** 353–356 (1982).

[70] P. Porcher, M. C. D. Santos, and O. Malta, "Relationship between phenomenological crystal field parameters and the crystal structure: The simple overlap model," Phys. Chem. Chem. Phys. **1,** 397 – 405 (1999).

[71] J. Derouet, L. Beaury, P. Porcher, and P. J. Deren, "Simple overlap model and crystal field analysis of Cs_2ZnCl_4:Co^{2+}. Correlation with optical and magnetic properties," Journal of Alloys and Compounds **300-301,** 242–253 (2000).

[72] J. Derouet, L. Beaury, P. Porcher, R. Olazcuaga, J. M. Dance, G. L. Flem, A. E. Bouari, and A. E. Jazouli, "A New Nasicon-Type Phosphate:$Co_{0.5}Ti_2(PO_4)_3$ II. Simulation of Optical and Magnetic Properties," Journal of Solid State Chemistry **143,** 230–238 (1999).

[73] O. L. Malta, S. J. L. Ribeiro, M. Faucher, and P. Porcher, "Theoretical intensities of 4f-4f transitions between stark levels of the Eu_{3+} ion in crystals," Journal of Physics and Chemistry of Solids **52,** 587–593 (1991).

[74] R. Nistora, L. Andreici, and N. Avram, "Comparative Study between Energy Levels of Cr_{3+} and Co_{2+} Ions Doped in MgF_2 Crystal," Acta Physica Polonica A **116,** 538–540 (2009).

[75] M. Brik, C. Avram, and N. Avram, "Comparative study of crystal field effects for Ni^{2+} ion in $LiGa_5O_8$, MgF_2 and AgCl crystals," Journal of Physics and Chemistry of Solids **69,** 1796–1801 (2008).

[76] C. Kant, T. Rudolf, F. Schrettle, F. Mayr, J. Deisenhofer, P. Lunkenheimer, M. V. Eremin, and A. Loidl, "Optical spectroscopy in CoO: Phononic, electric, and magnetic excitation spectrum within the charge-transfer gap," Phys. Rev. B **78,** 245103 – (2008).

[77] H. Weitzel, H. Ehrenberg, C. Heid, H. Fuess, and P. Burlet, "Lifshitz point in the three-dimensional magnetic phase diagram of $CoNb_2O_6$," Physical Review B **62,** 12146 (2000).

[78] M. Kenzelmann and R. Coldea, "Order-to-disorder transition in the XY-like quantum magnet Cs_2CoCl_4 induced by noncommuting applied fields," Phys. Rev. B 65 **65,** 144432 (2002).

[79] E. Lieb, T. Schultz, and D. Mattis, "Two soluble models of an antiferromagnetic chain," Annals of Physics **62,** 407–466 (1961).

[80] P. Jordan and E. Wigner, "Uber das Paulische Aquivalenzverbot," Zeitschrift für Physik A: Hadrons and Nuclei **47,** 631 (1928).

[81] J. Kurmann, G. Müller, H. Thomas, M. W. Puga, , and H. Beck, "Anisotropic quantum spin chains," J. Appl. Phys. **52,** 1968 (1981).

[82] J. Kurmann and H. Thomas, "Antiferromagnetic long-range order in the anisotropic quantum spin chain," Physica A: Statistical and Theoretical Physics **112,** 235–255 (1982).

[83] D. V. Dmitriev and V. Y. Krivnov, "Quasi-one-dimensional anisotropic Heisenberg model in a transverse magnetic field," JETP Letters **80,** 349 (2004).

[84] H. Yoshizawa, G. Shirane, H. Shiba, and K. Hirakawa, "Neutron scattering study of a one-dimensional XY antiferromagnet Cs_2CoCl_4," Physical Review B **28,** 3904 (1983).

[85] B. N. Figgis, M. Gerloch, and R. Mason, "The Paramagnetic Anisotropies and Ligand Fields of the Tetrahedral Cobaltous Chlorides and Thiocyanate," Proceedings of the Royal Society of London. Series A, Mathematical and Physical Sciences **279,** 210 (1964).

[86] K. N. Shrivastava, "Origin of Superexchange Interactions in 3d Magnetic Solids (I)," Physica Status Solidi (b) **125,** 11 (1984).

[87] K. N. Shrivastava, "Origin of Superexchange Interactions in 3d Magnetic Solids (II)," Physica Status Solidi (b) **125,** 441 (1984).

[88] J. Peters and W. Jauch, "Single crystal time-of-flight neutron diffraction," Science Progress **85,** 297 (2002).

[89] G. L. Squires, *Introduction to the Theory of Thermal Neutron Scattering* (1989).

[90] K. D. Rouse, M. J. Cooper, E. J. York, and A. Chakera, "Absorption corrections for neutron diffraction," Acta Cryst. **A26,** 682 (1970).

[91] J. A. K. Howard, O. Johnson, A. J. Schultz, and A. M. Stringer, "Determination of the neutron absorption cross section for hydrogen as a function of wavelength with a pulsed neutron source," J. Appl. Cryst. **20,** 120 (1987).

[92] P. R. B. Figgis and A. White, "Charge density in the $CoCl_4^2$ ion: a comparison with spin density and theoretical calculations," J. Chem. Soc., Dalton Trans. **7,** 1737 (1987).

[93] E. Bertaut, "Magnetic Structure Analysis and Group Theory," Journal de Physique Colloques **32,** C1 462 (1971).

[94] R. Coldea, D. A. Tennant, R. A. Cowley, D. F. McMorrow, B. Doner, and Z. Tylczynski, "Neutron scattering study of the magnetic structure of Cs_2CuCl_4," J. Phys: Condens. Matter **8,** 7473–7491 (1996).

[95] R. Coldea, D. A. Tennant, K. Habicht, P. Smeibidl, C. Wolters, and Z. Tylczynski, "Direct Measurement of the Spin Hamiltonian and Observation of Condensation of Magnons in the 2D Frustrated Quantum Magnet Cs_2CuCl_4," Phys. Rev. Lett. **88,** 137203 (2002).

[96] C. Gorller-Walrand and K. Binnemans, *Solid State Physics: Point-Charge Calculations of Energy Levels of Magnetic Ions in Crystalline Electric Fields* (1964), Vol. 16.

Appendix A

Crystal Field Hamiltonian in the Point Charge Model

The crystal field Hamiltonian $\mathbf{V}_{cf}$ is explicitly derived below in the approximation of the point charge model (PCM), which assumes that the ligands (arranged in a geometric configuration around the magnetic ion) are point-charges. Let's consider a Cartesian coordinate system which has a magnetic ion (with n unpaired electrons) at the origin and N ligands at positions $\mathbf{R}_j$; these N ligands are the nonmagnetic ions (O^{2-}) from the first neighborhood of the magnetic ion (Co^{2+}) in the crystal. Under the assumptions of the PCM the electrostatic potential due to the surrounding ligands at the position of the ith electron of the magnetic ion is given by

$$\mathbf{V}(\mathbf{r}_i) = -\frac{|e|}{4\pi\varepsilon_0}\sum_{j=1}^{N}\frac{|Z_j|}{|\mathbf{R}_j - \mathbf{r}_i|} \tag{A.1}$$

where $|e|$ is the absolute value of the electron charge, $|Z_j|$ is the number of electrons on the ligands situated at positions $\mathbf{R}_j$ and $\mathbf{r}_i$ is the position of the ith unpaired electron. The summation is carried out over all N ligands. The perturbing crystalline potential energy is obtained from (A.1)

by summing over all n unpaired electrons

$$\mathbf{V}_{CF} = -|e| \sum_{i=1}^{n} V(\mathbf{r}_i) \tag{A.2}$$

In this appendix one can find minimum information necessary to understand the derivation of the Crystal Field Hamiltonian; detailed descriptions of scuh calculations can be found in Ref. [64,96]. The crystalline potential, equation $(A.2)$ may be expressed in Cartesian Coordinates (CC method) or in terms of Spherical Harmonics (SH method). In the case of high symmetry arrangements of the ligands, the CC method can be used, although a tedious amount of work has to be done. In many calculations and especially in the case of low symmetry arrangements of the ligands, the SH method is used because the calculations are easier and a general form for the crystalline potential can be obtained. The first step in the calculation of the crystalline potential in terms of spherical harmonics is to make the assumption that $\mid \mathbf{r}_i \mid < \mid \mathbf{R}_j \mid$ such that $|\mathbf{R}_j - \mathbf{r}_i|^{-1}$ can be expand in terms of the Legendre polynomials P_k; these Legendre polynomials P_k can be expanded further using the spherical harmonics addition theorem; this theorem expresses the angle ω between the two vectors $\mathbf{R}_j$ and $\mathbf{r}_i$ in terms of the individual polar angles (θ_j, φ_j) and (θ_i, φ_i), where (θ_j, φ_j) characterizes the angular position of the ligand change and (θ_i, φ_i) represents the angular position of the ith electron. For the rest of this Appendix we use the following notations $\mathbf{r}_i$=$|\mathbf{r}_i|$ and $\mathbf{R}_j$=$|\mathbf{R}_j|$.

$$\frac{1}{|\mathbf{R}_j - \mathbf{r}_i|} = \sum_{k=0}^{\infty} \frac{r_i^k}{R_j^{k+1}} P_k(\cos\omega), \quad R_j > r_i \tag{A.3}$$

$$\begin{aligned} P_k(\cos\omega) = \frac{4\pi}{2k+1} \{ & Y_k^0(\theta_j, \varphi_j) Y_k^0(\theta_i, \varphi_i) + \\ & + \sum_{q=1}^{k} (-1)^q [Y_k^{-q}(\theta_j, \varphi_j) Y_k^q(\theta_i, \varphi_i) + Y_k^q(\theta_j, \varphi_j) Y_k^{-q}(\theta_i, \varphi_i)] \} \end{aligned} \tag{A.4}$$

The expansion coefficients Y_k^0 are real, but Y_k^q and Y_k^{-q} are complex quantities. In order to avoid the use of imaginary quantities we replace the spherical harmonics Y_k^0, Y_k^q and Y_k^{-q} by the tesseral harmonics Z_{k0}^c, Z_{kq}^c and Z_{kq}^s, which are real quantities. The relations between the spherical and

tesseral harmonics are given below

$$Y_k^0 = Z_{k0}^c, \quad Z_{k0}^c = Y_k^0 \tag{A.5}$$

$$Y_k^q = \frac{(-1)^q}{\sqrt{2}}[Z_{kq}^c + iZ_{kq}^s], \quad Z_{kq}^c = \frac{1}{\sqrt{2}}[Y_k^{-q} + (-1)^q Y_k^q] \tag{A.6}$$

$$Y_k^{-q} = \frac{1}{\sqrt{2}}[Z_{kq}^c - iZ_{kq}^s], \quad Z_{kq}^s = \frac{i}{\sqrt{2}}[Y_k^{-q} - (-1)^q Y_k^q], \quad q > 0 \tag{A.7}$$

The superscripts c and s stand for the presence of the factors $\cos(q\varphi)$ and $\sin(q\varphi)$ in the tesseral harmonics. After the replacement of the spherical harmonics by tesseral harmonics and rearrangement of terms, equation $(A.4)$ can is written as [64]:

$$\begin{aligned} P_k(\cos\omega) = \frac{4\pi}{2k+1}\{&Z_{k0}^c(\theta_j,\varphi_j)Z_{k0}^c(\theta_i,\varphi_i) + \\ &+ \sum_{q=1}^{k}[Z_{kq}^c(\theta_j,\varphi_j)Z_{kq}^c(\theta_i,\varphi_i) + Z_{kq}^s(\theta_j,\varphi_j)Z_{kq}^s(\theta_i,\varphi_i)]\} \end{aligned} \tag{A.8}$$

Now, combination of equations $(A.2)$, $(A.3)$ and $(A.8)$ we obtain for the crystalline potential V_{CF} the following expression

$$\begin{aligned} V_{CF} = \frac{|e|^2}{4\pi\varepsilon_0}\sum_{i=1}^{n}\sum_{j=1}^{N}\sum_{k=0}^{\infty}\frac{Z_j r_i^k}{R_j^{k+1}}\frac{4\pi}{2k+1}&\{Z_{k0}^c(\theta_j,\varphi_j)Z_{k0}^c(\theta_i,\varphi_i) + \\ &+ \sum_{q=1}^{k}[Z_{kq}^c(\theta_j,\varphi_j)Z_{kq}^c(\theta_i,\varphi_i) + Z_{kq}^s(\theta_j,\varphi_j)Z_{kq}^s(\theta_i,\varphi_i)]\} \end{aligned} \tag{A.9}$$

After rearranging terms, an equivalent way to write equation $(A.9)$ is

$$\begin{aligned} V_{CF} = \sum_{k=0}^{\infty}\{&[\frac{|e|^2}{4\pi\varepsilon_0}\frac{4\pi}{2k+1}\sum_{j=1}^{N}\frac{Z_j}{R_j^{k+1}}Z_{k0}^c(\theta_j,\varphi_j)]\,[\sum_{i=1}^{n} r_i^k Z_{k0}^c(\theta_i,\varphi_i)] + \\ &\sum_{q=1}^{k}([\frac{|e|^2}{4\pi\varepsilon_0}\frac{4\pi}{2k+1}\sum_{j=1}^{N}\frac{Z_j}{R_j^{k+1}}Z_{kq}^c(\theta_j,\varphi_j)]\,[\sum_{i=1}^{n} r_i^k Z_{kq}^c(\theta_i,\varphi_i)] + \\ &[\frac{|e|^2}{4\pi\varepsilon_0}\frac{4\pi}{2k+1}\sum_{j=1}^{N}\frac{Z_j}{R_j^{k+1}}Z_{kq}^s(\theta_j,\varphi_j)]\,[\sum_{i=1}^{n} r_i^k Z_{kq}^s(\theta_i,\varphi_i)])\} \end{aligned} \tag{A.10}$$

To simply further this expression we introduce new coefficients A_{k0}^c, A_{kq}^c and A_{kq}^s, that only depend on the position of the ligands (R_j,θ_j,φ_j) with respect to the magnetic ion and their charges Z_j.

$$A_{k0}^c = \frac{|e|^2}{4\pi\varepsilon_0}\frac{4\pi}{2k+1}\sum_{j=1}^{N}\frac{Z_j}{R_j^{k+1}}Z_{k0}^c(\theta_j,\varphi_j) \tag{A.11}$$

$$A_{kq}^{c} = \frac{|e|^2}{4\pi\varepsilon_0}\frac{4\pi}{2k+1}\sum_{j=1}^{N}\frac{Z_j}{R_j^{k+1}}Z_{kq}^{c}(\theta_j,\varphi_j) \tag{A.12}$$

$$A_{kq}^{s} = \frac{|e|^2}{4\pi\varepsilon_0}\frac{4\pi}{2k+1}\sum_{j=1}^{N}\frac{Z_j}{R_j^{k+1}}Z_{kq}^{s}(\theta_j,\varphi_j) \tag{A.13}$$

With knowledge of the crystallographic structure we can obtain numerical values of the (R_j,θ_j,φ_j) for each ligand and we can compute the coefficients A_{k0}^{c}, A_{kq}^{c} and A_{kq}^{s}. Further, the crystalline potential V_{CF} is written in a more compact way by introducing the new coefficientsA_{k0}^{c}, A_{kq}^{c} and A_{kq}^{s}.

$$V_{cf} = \sum_{k=0}^{\infty}\{A_{k0}^{c}\sum_{i=1}^{n}r_i^k Z_{k0}^{c}(\theta_i,\varphi_i) + \sum_{q=1}^{k}[A_{kq}^{c}\sum_{i=1}^{n}r_i^k Z_{kq}^{c}(\theta_i,\varphi_i) + A_{kq}^{s}\sum_{i=1}^{n}r_i^k Z_{kq}^{s}(\theta_i,\varphi_i)]\} \tag{A.14}$$

We would like to mention at this point that in practice k runs only over a limited number of terms, for example for d systems $k \leq 4$. Next we consider the evaluation of the matrix elements of the crystalline potential V_{CF} between free ion states. The matrix thus formed can be diagonalized to find the energy levels and eigenfunctions of the ion in the crystal. Tesseral harmonics can also be written as a function of the cartesian coordinates of the ith electron, for example $Z_{kq}^{c}(\theta_i,\varphi_i) = Z_{kq}^{c}(x_i,y_i,z_i)$. The crystal field perturbing Hamiltonian operator $\hat{V}_{cf}$ is formed by using the classical perturbing crystalline potential energy, equation $(A.14)$, where (θ_i,φ_i) is converted to (x_i,y_i,z_i) and the usual rules quantum mechanics $x_i \to \hat{x}_i$, $y_i \to \hat{y}_i$ and $z_i \to \hat{z}_i$.

Because for transition metals the spin-orbit coupling is much smaller then the electron-electron interaction, in a first approximation we can characterize the eigenfunctions of the free ion by $|L,S,M_L,M_S\rangle$. The matrix elements we have to calculate are of the following form

$$\langle L,S,M_L^n,M_S^n|\hat{V}_{cf}|L,S,M_L^m,M_S^m\rangle_{n,m=1,\ldots,28} \tag{A.15}$$

By an inspection of the equation $(A.14)$ we see that in order to calculate the matrix elements from equation $(A.15)$ we actually have to calculate matrix elements of the following forms

$$\langle L,S,M_L^n,M_S^n|\sum_{i=1}^{n}r_i^k Z_{k0}^{c}(\hat{x}_i,\hat{y}_i,\hat{z}_i)|L,S,M_L^m,M_S^m\rangle_{n,m=1,\ldots,28} \tag{A.16}$$

$$\langle L,S,M_L^n,M_S^n|\sum_{i=1}^{n} r_i^k Z_{kq}^c(\hat{x}_i,\hat{y}_i,\hat{z}_i)|L,S,M_L^m,M_S^m\rangle_{n,m=1,\ldots,28} \tag{A.17}$$

$$\langle L,S,M_L^n,M_S^n|\sum_{i=1}^{n} r_i^k Z_{kq}^s(\hat{x}_i,\hat{y}_i,\hat{z}_i)|L,S,M_L^m,M_S^m\rangle_{n,m=1,\ldots,28} \tag{A.18}$$

The easiest way to calculate the matrix elements from equations $(A.16)$ to $(A.18)$ is by using Steven's "*Operator equivalents*" method [96]. This method makes use of the fact that the $\hat{x}$, $\hat{y}$, $\hat{z}$ operators have matrix elements within the same L manifold which are proportional to those of the $\hat{L}_x$, $\hat{L}_y$ and $\hat{L}_x$ operators. Thus apart from a multiplication constant, matrix elements of $\sum_{i=1}^{n} r_i^k Z_{kq}^{c/s}(\theta_i,\varphi_i) = \sum_{i=1}^{n} r_i^k Z_{kq}^{c/s}(\hat{x}_i,\hat{y}_i,\hat{z}_i)$ in equations $(A.16)$ to $(A.18)$ are proportional to those of a polynomial of angular momentum operators, $\hat{L}_x$, $\hat{L}_y$ and $\hat{L}_x$. Within each manifold of L

$$\begin{gathered}\langle L,S,M_L^n,M_S^n|\sum_{i=1}^{n} r_i^k Z_{kq}^{c/s}(\hat{x}_i,\hat{y}_i,\hat{z}_i)|L,S,M_L^m,M_S^m\rangle = \\ a_k\langle r^k\rangle\langle L,S,M_L^n,M_S^n|\hat{O}_q^k(\hat{L}_x,\hat{L}_y,\hat{L}_z)_{c/s}|L,S,M_L^m,M_S^m\rangle\end{gathered} \tag{A.19}$$

where $\hat{O}_q^k(\hat{L}_x,\hat{L}_y,\hat{L}_z)_{c/s}$ are called Steven$'$s operators and are polynomials of angular momentum operators (their form is given in the Appendix C for relevant k and q values for Co^{2+}), $\langle r^k\rangle$ is a constant equal with the expectation value of the k-th power of the radius of the 3d orbitals for the transition metal ion and finally a_k is a numerical constant depending on l (the orbital quantum number of the electrons in the unfilled shell), n (the number of unpaired electrons) and the total angular momentum L; conventionally they are represented by α_L and β_L for $k = 2$ and $k = 4$ respectively. These constants are obtained by direct calculations of the matrix elements between single electron eigenfunctions (Slater determinants) for each configuration, d^n. Their values are given in Table $A.1$ for a few configurations. Finally putting everything together we can write the crystal field Hamiltonian in the "Operator Equivalent" form:

$$\hat{V}_{cf} = \sum_{k=2,\,4}\{B_0^k\hat{O}_0^k + \sum_{q=1}^{k}[B_q^{k_c}\hat{O}_q^{k_c} + B_q^{k_s}\hat{O}_q^{k_s}]\} \tag{A.20}$$

where B_0^k, $B_q^{k_c}$ and $B_q^{k_s}$ are called "*Crystal Field Parameters*" and are defined as

$$B_0^k = a_k\langle r^k\rangle A_{k0}^c \tag{A.21}$$

Table A.1 Multiplications constant a_k necessary in the calculations of the Crystal Field Parameters used for the Operator Equivalent form of the crystal field Hamiltonian in Eqs. A.21, A.22 and A.23. The values relevant for Co^{2+} ($3d^7$) with the Hund's ground state term ^{4}F are highlighted in bold.

k	a_k	$3d^1$	$3d^2$	$3d^3$	$3d^4$	$3d^6$	$3d^7$	$3d^8$	$3d^9$
^{2S+1}L		^2D	^3F	^4F	^5D	^5D	^4F	^3F	^2D
2	α_L	$-\frac{2}{21}$	$-\frac{2}{105}$	$\frac{2}{105}$	$\frac{2}{21}$	$-\frac{2}{21}$	$\mathbf{-\frac{2}{107}}$	$\frac{2}{108}$	$\frac{2}{21}$
4	β_L	$\frac{2}{63}$	$-\frac{2}{315}$	$\frac{2}{315}$	$-\frac{2}{63}$	$\frac{2}{63}$	$\mathbf{-\frac{2}{315}}$	$\frac{2}{315}$	$-\frac{2}{63}$

$$B_q^{k_c} = a_k \langle r^k \rangle A_{kq}^c \tag{A.22}$$

$$B_q^{k_s} = a_k \langle r^k \rangle A_{kq}^s \tag{A.23}$$

An example of numerical calculations of Crystal Field Parameters is given in Appendix B.

Appendix B

Crystal Field Parameters: Point Charge Model

The crystal field parameters B_q^k can be directly calculated in the point charge model using equations $A.11$, $A.12$ and $A.13$ from *Appendix* A and information about the ligand positions given in Table $B.1$. As an example here we will calculate the crystal field parameters B_1^2 and $B_1^{\prime 2}$ (it is important to mention that: $B_q^{\prime k} = B_q^{sk}$)

$$\begin{aligned} B_q^k &= a_k \langle r^k \rangle \frac{4\pi}{2k+1} \sum_{j=1}^{N} \frac{(-Z_j)|e|^2}{R_j^{k+1}} Z_{kq}^c(\theta_j, \varphi_j) \\ \Rightarrow B_1^2 &= \alpha_L \langle r^2 \rangle \frac{4\pi}{5} \sum_{j=1}^{6} \frac{(-Z_j)|e|^2}{R_j^3} Z_{21}^c(\theta_j, \varphi_j) \end{aligned} \tag{B.1}$$

$$\begin{aligned} B_q^{sk} &= a_k \langle r^k \rangle \frac{4\pi}{2k+1} \sum_{j=1}^{N} \frac{(-Z_j)|e|^2}{R_j^{k+1}} Z_{kq}^s(\theta_j, \varphi_j) \\ \Rightarrow B_1^{s2} &= \alpha_L \langle r^2 \rangle \frac{4\pi}{5} \sum_{j=1}^{6} \frac{(-Z_j)|e|^2}{R_j^3} Z_{21}^s(\theta_j, \varphi_j) \end{aligned} \tag{B.2}$$

where

$$\begin{aligned} Z^c_{21}(\theta_j,\varphi_j) &= \frac{1}{\sqrt{2}}[Y_2^{-1}(\theta_j,\varphi_j) - Y_2^1(\theta_j,\varphi_j)] \\ Z^s_{21}(\theta_j,\varphi_j) &= \frac{i}{\sqrt{2}}[Y_2^{-1}(\theta_j,\varphi_j) + Y_2^1(\theta_j,\varphi_j)] \end{aligned} \tag{B.3}$$

The form of the spherical harmonics has been tabulated for example in [64]. Relevant here are Y_2^{-1} and Y_2^1 given by

$$Y_2^{\pm 1}(\theta_j,\varphi_j) = \mp\frac{1}{2}\sqrt{\frac{15}{2\pi}}\,\cos\theta_j\,\sin\theta_j\,e^{\pm i\varphi_j} \tag{B.4}$$

By replacing the spherical harmonics from equation $B.4$ into equations $B.3$ we obtain the explicit form of the tesseral harmonics as a function of angles (θ_j,φ_j)

$$\begin{aligned} Z^c_{21}(\theta_j,\varphi_j) &= \frac{1}{\sqrt{2}}\sqrt{\frac{15}{2\pi}}\,\cos\theta_j\,\sin\theta_j\,\cos\varphi_j \\ Z^s_{21}(\theta_j,\varphi_j) &= \frac{1}{\sqrt{2}}\sqrt{\frac{15}{2\pi}}\,\cos\theta_j\,\sin\theta_j\,\sin\varphi_j \end{aligned} \tag{B.5}$$

Now in order to calculate the crystal field parameters we have to calculate the sums $\sum_{j=1}^N \frac{Z_j}{R_j^{k+1}} Z^c_{kq}(\theta_j,\varphi_j)$ and $\sum_{j=1}^N \frac{Z_j}{R_j^{k+1}} Z^s_{kq}(\theta_j,\varphi_j)$, where Z_j has the same value (2) for all the 6 oxygen O^{2-} ions, see Table $B.1$;

$$\begin{aligned} \sum_{j=1}^N \frac{Z_j}{R_j^{k+1}} Z^c_{kq}(\theta_j,\varphi_j) = \frac{1}{\sqrt{2}}\sqrt{\frac{15}{2\pi}}[&\frac{\cos\theta_1\,\sin\theta_1\,\cos\varphi_1 + \cos\theta_2\,\sin\theta_2\,\cos\varphi_2}{R_1} \\ &+ \frac{\cos\theta_3\,\sin\theta_3\,\cos\varphi_3 + \cos\theta_4\,\sin\theta_4\,\cos\varphi_4}{R_3} \\ &+ \frac{\cos\theta_5\,\sin\theta_5\,\cos\varphi_5 + \cos\theta_6\,\sin\theta_6\,\cos\varphi_6}{R_5}] \end{aligned} \tag{B.6}$$

and

$$\begin{aligned} \sum_{j=1}^N \frac{Z_j}{R_j^{k+1}} Z^s_{kq}(\theta_j,\varphi_j) = \frac{1}{\sqrt{2}}\sqrt{\frac{15}{2\pi}}[&\frac{\cos\theta_1\,\sin\theta_1\,\sin\varphi_1 + \cos\theta_2\,\sin\theta_2\,\sin\varphi_2}{R_1} \\ &+ \frac{\cos\theta_3\,\sin\theta_3\,\sin\varphi_3 + \cos\theta_4\,\sin\theta_4\,\sin\varphi_4}{R_3} \\ &+ \frac{\cos\theta_5\,\sin\theta_5\,\sin\varphi_5 + \cos\theta_6\,\sin\theta_6\,\sin\varphi_6}{R_5}] \end{aligned} \tag{B.7}$$

From the last two columns of the Table $B.1$, we observe that $(\theta_x = \pi - \theta_{x+1},\ \varphi_x = \pi - \varphi_{x+1})$, where x = 1, 2, 3; using these relations between the angles we simply further the sums in equations $B.6$ and $B.7$ as

$$\sum_{j=1}^{N} \frac{Z_j}{R_j^{k+1}} Z_{kq}^{c}(\theta_j, \varphi_j) = \frac{1}{\sqrt{2}} \sqrt{\frac{15}{2\pi}} \\ [\frac{2\ \cos\theta_2\ \sin\theta_2\ \cos\varphi_2}{R_1} + \frac{2\ \cos\theta_4\ \sin\theta_4\ \cos\varphi_4}{R_3} + \frac{2\ \cos\theta_6\ \sin\theta_6\ \cos\varphi_6}{R_5}] \tag{B.8}$$

and

$$\sum_{j=1}^{N} \frac{Z_j}{R_j^{k+1}} Z_{kq}^{s}(\theta_j, \varphi_j) = \frac{1}{\sqrt{2}} \sqrt{\frac{15}{2\pi}} [\frac{\cos\theta_2\ \sin\theta_2\ (\sin\varphi_2 - \sin\varphi_2)}{R_1} \\ + \frac{\cos\theta_4\ \sin\theta_4\ (\sin\varphi_4 - \sin\varphi_4)}{R_3} \\ + \frac{\cos\theta_6\ \sin\theta_6\ (\sin\varphi_6 - \sin\varphi_6)}{R_5}] \tag{B.9}$$

from equations $B.8$ and $B.9$ we can see that the sum entering in B_1^2 has a finite real value but the sum entering B_1^{s2} cancels out, so there are no complex terms in the crystal field Hamiltonian expressed in the XYZ local reference frame. Similarly all the B_q^{sk} terms in Eq. A.20 cancel out.

Table B.1 crystal parameters used to calculate CFP

Name	Z_j	x(Å)	y(Å)	z(Å)	R_j(Å)	$\theta(deg)$	$\varphi(deg)$
$Co1$		0.0000	0.0000	0.0000	0.0000	0.000	0.000
$O1$	2	1.3469	1.2270	0.9227	2.0423	63.141	42.333
$O2$	2	-1.3468	1.2270	-0.9226	2.0423	116.86	137.66
$O3$	2	1.0653	-1.6970	0.6982	2.1218	70.789	-57.881
$O4$	2	-1.0653	-1.6970	-0.6981	2.1218	109.21	-122.12
$O5$	2	-1.0653	-0.3798	1.8242	2.1463	31.798	-160.38
$O6$	2	1.0653	-0.3798	-1.8241	2.1463	148.20	-19.622

Appendix C

Stevens operators $\hat{O}_q^{kc}$ and their matrix elements in terms of the $|LSM_LM_S\rangle$ base

This Appendix lists the expression of the Sevens operators O_q^k in terms of angular momentum operators from [96].

$$\hat{O}_0^{0c} = 1 \tag{C.1}$$

$$\hat{O}_0^{2c} = 3\hat{L}_z^2 - L(L+1) \tag{C.2}$$

$$\hat{O}_1^{2c} = \frac{1}{4}[(\hat{L}_z\hat{L}_+ + \hat{L}_+\hat{L}_z) + (\hat{L}_z\hat{L}_- + \hat{L}_-\hat{L}_z)] \tag{C.3}$$

$$\hat{O}_2^{2c} = \frac{1}{2}(\hat{L}_+^2 + \hat{L}_-^2) \tag{C.4}$$

$$\hat{O}_0^{4c} = 35\hat{L}_z^4 - [30L(L+1) - 25]\hat{L}_z^2 + 3L^2(L+1)^2 - 6L(L+1) \tag{C.5}$$

$$\hat{O}_2^{4c} = [7\hat{L}_z^4 - L(L+1) - 5](\hat{L}_+^2 + \hat{L}_-^2) + (\hat{L}_+^2 + \hat{L}_-^2)[7\hat{L}_z^4 - L(L+1) - 5] \tag{C.6}$$

$$\hat{O}_3^{4c} = \frac{1}{4}[\hat{L}_z(\hat{L}_+^3 + \hat{L}_-^3) = (\hat{L}_+^3 + \hat{L}_-^3)\hat{L}_z] \tag{C.7}$$

$$\hat{O}_1^{4c} = \frac{1}{2}(\hat{L}_+^4 + \hat{L}_-^4) \tag{C.8}$$

where $\hat{L}_\pm = \hat{L}_x \pm i\hat{L}_y$ are the raising and lowering operators. In terms of orbital angular momentum operators, the orbital states $|LM_L\rangle$ satisfy the following relations

$$\hat{L}_z \, |LM_L\rangle = M_L \, |LM_L\rangle \tag{C.9}$$

$$\hat{L}_\pm \, |LM_L\rangle = \sqrt{L(L+1) - M_L(M_L \pm 1)} \, |LM_L \pm 1\rangle \tag{C.10}$$

Taking into account that the free ion eigenfunctions $|LSM_LM_S\rangle$ are constructed from products of orbital $|LM_L\rangle$ and spin $|SM_S\rangle$ states, the matrix elements of Steven′s operators can be expressed as

$$\begin{aligned} &\langle L,S,M_L^n,M_S^n|\hat{O}_q^k|L,S,M_L^m,M_S^m\rangle_{n,m=1\div 28} = \\ &\langle L,M_L^n|\hat{O}_q^k|L,M_L^m\rangle_{n,m=1\div 28}\delta_{M_S^nM_S^m} \end{aligned} \tag{C.11}$$

The matrix elements of the Steven′s operators in the $|LM_L\rangle$ base, where $M_L = -3,-2,-1,0,1,2,3$ are given below in Tables - C.1 to C.8:

Table C.1 Matrix representation of the $\hat{Q}_0^2$ operator in the $|M_L\rangle$ basis for L = 3

	$\|M_L=-3\rangle$	$\|M_L=-2\rangle$	$\|M_L=-1\rangle$	$\|M_L=0\rangle$	$\|M_L=1\rangle$	$\|M_L=2\rangle$	$\|M_L=3\rangle$
$\langle M_L=-3\|$	15	0	0	0	0	0	0
$\langle M_L=-2\|$	0	0	0	0	0	0	0
$\langle M_L=-1\|$	0	0	-9	0	0	0	0
$\langle M_L=0\|$	0	0	0	-12	0	0	0
$\langle M_L=1\|$	0	0	0	0	-9	0	0
$\langle M_L=2\|$	0	0	0	0	0	0	0
$\langle M_L=3\|$	0	0	0	0	0	0	15

Table C.2 Matrix elements of the $\hat{Q}_1^2$ operator

	$\|M_L=-3\rangle$	$\|M_L=-2\rangle$	$\|M_L=-1\rangle$	$\|M_L=0\rangle$	$\|M_L=1\rangle$	$\|M_L=2\rangle$	$\|M_L=3\rangle$
$\langle M_L=-3\|$	0	$-\frac{5}{4}\sqrt{6}$	0	0	0	0	0
$\langle M_L=-2\|$	$-\frac{5}{4}\sqrt{6}$	0	$-\frac{3}{4}\sqrt{10}$	0	0	0	0
$\langle M_L=-1\|$	0	$-\frac{3}{4}\sqrt{10}$	0	$-\frac{\sqrt{3}}{2}$	0	0	0
$\langle M_L=0\|$	0	0	$-\frac{\sqrt{3}}{2}$	0	$\frac{\sqrt{3}}{2}$	0	0
$\langle M_L=1\|$	0	0	0	$\frac{\sqrt{3}}{2}$	0	$\frac{3}{4}\sqrt{10}$	0
$\langle M_L=2\|$	0	0	0	0	$\frac{3}{4}\sqrt{10}$	0	$\frac{5}{4}\sqrt{6}$
$\langle M_L=3\|$	0	0	0	0	0	$\frac{5}{4}\sqrt{6}$	0

Table C.3 Matrix elements of the $\hat{Q}_2^2$ operator

	$\|M_L=-3\rangle$	$\|M_L=-2\rangle$	$\|M_L=-1\rangle$	$\|M_L=0\rangle$	$\|M_L=1\rangle$	$\|M_L=2\rangle$	$\|M_L=3\rangle$
$\langle M_L=-3\|$	0	0	$\sqrt{15}$	0	0	0	0
$\langle M_L=-2\|$	0	0	0	$\sqrt{30}$	0	0	0
$\langle M_L=-1\|$	$\sqrt{15}$	0	0	0	6	0	0
$\langle M_L=0\|$	0	$\sqrt{30}$	0	0	0	$\sqrt{30}$	0
$\langle M_L=1\|$	0	0	6	0	0	0	$\sqrt{15}$
$\langle M_L=2\|$	0	0	0	0	$\sqrt{30}$	0	0
$\langle M_L=3\|$	0	0	0	0	$\sqrt{15}$	0	0

Table C.4 Matrix elements of the $\hat{Q}_0^4$ operator

	$\|M_L=-3\rangle$	$\|M_L=-2\rangle$	$\|M_L=-1\rangle$	$\|M_L=0\rangle$	$\|M_L=1\rangle$	$\|M_L=2\rangle$	$\|M_L=3\rangle$
$\langle M_L=-3\|$	180	0	0	0	0	0	0
$\langle M_L=-2\|$	0	−420	0	0	0	0	0
$\langle M_L=-1\|$	0	0	60	0	0	0	0
$\langle M_L=0\|$	0	0	0	360	0	0	0
$\langle M_L=1\|$	0	0	0	0	60	0	0
$\langle M_L=2\|$	0	0	0	0	0	−420	0
$\langle M_L=3\|$	0	0	0	0	0	0	180

Table C.5 Matrix elements of the $\hat{Q}_1^4$ operator

	$\|M_L=-3\rangle$	$\|M_L=-2\rangle$	$\|M_L=-1\rangle$	$\|M_L=0\rangle$	$\|M_L=1\rangle$	$\|M_L=2\rangle$	$\|M_L=3\rangle$
$\langle M_L=-3\|$	0	$-15\sqrt{6}$	0	0	0	0	0
$\langle M_L=-2\|$	$-15\sqrt{6}$	0	$12\sqrt{10}$	0	0	0	0
$\langle M_L=-1\|$	0	$12\sqrt{10}$	0	$-15\sqrt{3}$	0	0	0
$\langle M_L=0\|$	0	0	$15\sqrt{3}$	0	$15\sqrt{3}$	0	0
$\langle M_L=1\|$	0	0	0	$-15\sqrt{3}$	0	$-12\sqrt{10}$	0
$\langle M_L=2\|$	0	0	0	0	$-12\sqrt{10}$	0	$15\sqrt{6}$
$\langle M_L=3\|$	0	0	0	0	0	$15\sqrt{6}$	0

Table C.6 Matrix elements of the $\hat{Q}_2^4$ operator

	$\|M_L=-3\rangle$	$\|M_L=-2\rangle$	$\|M_L=-1\rangle$	$\|M_L=0\rangle$	$\|M_L=1\rangle$	$\|M_L=2\rangle$	$\|M_L=3\rangle$
$\langle M_L=-3\|$	0	0	$18\sqrt{15}$	0	0	0	0
$\langle M_L=-2\|$	0	0	0	$-3\sqrt{30}$	0	0	0
$\langle M_L=-1\|$	$18\sqrt{15}$	0	0	0	-60	0	0
$\langle M_L=0\|$	0	$-3\sqrt{30}$	0	0	0	$-3\sqrt{30}$	0
$\langle M_L=1\|$	0	0	-60	0	0	0	$18\sqrt{15}$
$\langle M_L=2\|$	0	0	0	$-3\sqrt{30}$	0	0	0
$\langle M_L=3\|$	0	0	0	0	$18\sqrt{15}$	0	0

Table C.7 Matrix elements of the $\hat{Q}_3^4$ operator

	$\|M_L=-3\rangle$	$\|M_L=-2\rangle$	$\|M_L=-1\rangle$	$\|M_L=0\rangle$	$\|M_L=1\rangle$	$\|M_L=2\rangle$	$\|M_L=3\rangle$
$\langle M_L=-3\|$	0	0	0	$-9\sqrt{5}$	0	0	0
$\langle M_L=-2\|$	0	0	0	0	$-3\sqrt{10}$	0	0
$\langle M_L=-1\|$	0	0	0	0	0	$3\sqrt{10}$	0
$\langle M_L=0\|$	$-9\sqrt{5}$	0	0	0	0	0	$9\sqrt{5}$
$\langle M_L=1\|$	0	$-3\sqrt{10}$	0	0	0	0	0
$\langle M_L=2\|$	0	0	$3\sqrt{10}$	0	0	0	0
$\langle M_L=3\|$	0	0	0	$9\sqrt{5}$	0	0	0

Table C.8 Matrix elements of the $\hat{Q}_4^4$ operator

	$\|M_L=-3\rangle$	$\|M_L=-2\rangle$	$\|M_L=-1\rangle$	$\|M_L=0\rangle$	$\|M_L=1\rangle$	$\|M_L=2\rangle$	$\|M_L=3\rangle$
$\langle M_L=-3\|$	0	0	0	0	$12\sqrt{15}$	0	0
$\langle M_L=-2\|$	0	0	0	0	0	60	0
$\langle M_L=-1\|$	0	0	0	0	0	0	$12\sqrt{15}$
$\langle M_L=0\|$	0	0	0	0	0	0	0
$\langle M_L=1\|$	$12\sqrt{15}$	0	0	0	0	0	0
$\langle M_L=2\|$	0	60	0	0	0	0	0
$\langle M_L=3\|$	0	0	$12\sqrt{15}$	0	0	0	0

Appendix D

Tesseral harmonics

This Appendix lists the explicit expressions of the (real) tesseral harmonics $Z_{kq}^{c/s}$ up to order k=4 from [64]:

$$Z_{kq}^{c} = \frac{1}{\sqrt{2}}[Y_k^{-q} + (-1)^q Y_k^q] \qquad Z_{kq}^{s} = \frac{i}{\sqrt{2}}[Y_k^{-q} - (-1)^q Y_k^q], \quad q > 0 \tag{D.1}$$

$$\begin{aligned} Z_{21}^{c} &= \frac{1}{\sqrt{2}}\sqrt{\frac{15}{2\pi}}\ \sin\theta\ \cos\theta\ \cos\varphi \\ Z_{21}^{s} &= \frac{1}{\sqrt{2}}\sqrt{\frac{15}{2\pi}}\ \sin\theta\ \cos\theta\ \sin\varphi \end{aligned} \tag{D.2}$$

$$\begin{aligned} Z_{22}^{c} &= \frac{1}{2\sqrt{2}}\sqrt{\frac{15}{2\pi}}\ \sin\theta^2\ \cos 2\varphi \\ Z_{22}^{s} &= \frac{1}{2\sqrt{2}}\sqrt{\frac{15}{2\pi}}\ \sin\theta^2\ \sin 2\varphi \end{aligned} \tag{D.3}$$

$$\begin{aligned} Z_{41}^{c} &= \frac{3}{4\sqrt{2}}\sqrt{\frac{5}{\pi}}\ \sin\theta\ (7\cos\theta^3 - 3\cos\theta)\ \cos\varphi \\ Z_{41}^{s} &= \frac{3}{4\sqrt{2}}\sqrt{\frac{5}{\pi}}\ \sin\theta\ (7\cos\theta^3 - 3\cos\theta)\ \sin\varphi \end{aligned} \tag{D.4}$$

$$
\begin{aligned}
Z_{42}^{c} &= \frac{3}{4\sqrt{2}}\sqrt{\frac{5}{2\pi}}\ \sin\theta^{2}\ (7\cos\theta^{2}-1)\ \cos 2\varphi \\
Z_{42}^{s} &= \frac{3}{4\sqrt{2}}\sqrt{\frac{5}{2\pi}}\ \sin\theta^{2}\ (7\cos\theta^{2}-1)\ \sin 2\varphi
\end{aligned}
\tag{D.5}
$$

$$
\begin{aligned}
Z_{43}^{c} &= \frac{3}{4\sqrt{2}}\sqrt{\frac{35}{\pi}}\ \sin\theta^{3}\ \cos\theta\ \cos 3\varphi \\
Z_{43}^{s} &= \frac{3}{4\sqrt{2}}\sqrt{\frac{35}{\pi}}\ \sin\theta^{3}\ \cos\theta\ \sin 3\varphi
\end{aligned}
\tag{D.6}
$$

$$
\begin{aligned}
Z_{44}^{c} &= \frac{3}{8}\sqrt{\frac{35}{2\pi}}\ \sin\theta^{4}\ \cos 4\varphi \\
Z_{44}^{s} &= \frac{3}{8}\sqrt{\frac{35}{2\pi}}\ \sin\theta^{4}\ \sin 4\varphi
\end{aligned}
\tag{D.7}
$$